U.PORTO

FEUP FACULDADE DE ENGENHARIA
UNIVERSIDADE DO PORTO

Hugo Faria

Analytical and Numerical Modelling of the Filament Winding Process

PhD Thesis

U.PORTO
FEUP FACULDADE DE ENGENHARIA
UNIVERSIDADE DO PORTO

PhD Thesis

Hugo Faria

Analytical and Numerical Modelling of the Filament Winding Process

Supervisor: Professor António Torres Marques
Co-Supervisor: Prof. Francisco M. Andrade Pires

April 2013

This thesis is submitted in partial fulfilment of the requirements for the degree of Doctor of Philosophy in Mechanical Engineering

Abstract

The filament winding process, used for the manufacture of a wide variety of composite parts and components, is being increasingly applied in structurally demanding applications. In such cases, the ability to accurately control the manufacturing parameters and their specific influence on the final quality of the laminates becomes increasingly more relevant as well.

In this research program, the filament winding process was studied and modelled in detail. The several physical phenomena interacting at the layer/laminate level were analytically described independently and a meso-scale overall decoupled original model was proposed. Namely, the consolidation pressure, the resin flow, the resin mixing between adjacent layers, the resin cure kinetics and rheology, the fibre bed compaction and the varying layers' stiffness were attained. The stress-strain constitutive relations were modelled taking into account the influence of the thermal, chemical and mechanical effects of all the interacting phenomena. Also, process-intrinsic specific features like fibre misalignment, through-the-thickness gradients and incremental discrete lay-up were included in the analyses. A modular approach, based on sub-models each referring to a relevant group of physical phenomena acting at the layer-laminate level, was designed. This option allowed settling a model applicable to a broader range of real configurations and applications of the filament winding manufacturing process as is required by the industry. The methodology used is suitable both for thermosetting and thermoplastic resin systems, as well as for any geometry or lay-up. In addition, the decoupled structure foresees easier improvements in the future due to the independent analyses of each relevant phenomenon.

In order to evaluate the multi-physical descriptions and interactions, a numerical code was devised and implemented that simulated prescribed winding conditions. This code followed the same modular structure and dedicated sub-routines were written for each sub-model. A FORTRAN® user-routine was associated an ABAQUS® explicit formulation in which the former contained the constitutive model of the consolidating material. An input library was written to include different matrix material possibilities, thus accounting for both previously established and original kinetic and rheological models. Alternative formulations for the stress-strain constitutive relations were also coded in view of further testing those. A fully functional numerical program was, thus, established.

Finally, a comprehensive experimental program was conducted to measure and evaluate all the process variables under certain processing conditions. This program aimed at reliably validating the process model, thus adding relevance and utility to the study. Several experimental procedures and techniques were used and new sub-techniques were developed to retrieve the necessary data. Namely, innovative differential scanning calorimetry and rheology tests under manufacturer's recommended cure cycles, complementary thermography analysis, monitored filament winding setup or even resin colourizing techniques to measure in-situ flow. Partial and full validations of the process model were, thus, progressively achieved.

The validated process model is described, step by step, throughout the thesis, together with the analytical, numerical and experimental procedures conducted to accomplish it. Desirably, the reader is given a deep but logical gradual insight to the modelling strategy and results.

Resumo

O processo de enrolamento filamentar, utilizado no fabrico de vários componentes compósitos, está a ser cada vez mais empregue em aplicações estruturalmente exigentes. Nestes casos, a capacidade de controlar com precisão os parâmetros de produção e a sua influência na qualidade final dos laminados torna-se mais relevante também.

Neste estudo, o processo de enrolamento filamentar, foi estudado e modelado em detalhe. Os diversos fenómenos físicos que interagem ao nível da camada/laminado foram descritos analiticamente de forma independente e um novo modelo mesoscópico desacoplado do processo global foi proposto. Designadamente, a pressão de consolidação, o escoamento da resina, a mistura de resina entre camadas adjacentes, a cinética e reologia de cura da resina, a compactação da malha de fibras e a rigidez variável das camadas foram atentados. As relações constitutivas tensão-deformação foram modeladas tendo em conta a influência dos efeitos térmicos, químicos e mecânicos de todos os fenómenos com interação. Além disso, características intrínsecas ao próprio processo, tais como desalinhamento das fibras, gradientes ao longo da espessura e laminação incremental discreta das camadas foram incluídas nas análises. Uma abordagem modular, baseada em sub-modelos, cada um referente a um grupo relevante de fenómenos físicos, foi desenhada. Esta opção permitiu alargar a gama de configurações e aplicações modeláveis pela ferramenta desenvolvida, como é exigido pela indústria. A metodologia utilizada é adequada para resinas termoendurecíveis e termoplásticos, bem como para qualquer geometria ou sequência de laminação. Além disso, a estrutura desacoplada prevê maior facilidade em futuros desenvolvimentos e melhorias devido às análises independentes de cada um fenómeno relevante.

A fim de avaliar as descrições e interações multi-físicas, um código numérico foi implementado para simular certas condições prescritas. Este código seguiu a mesma estrutura modular com sub-rotinas dedicadas a cada sub-modelo. Uma rotina em FORTRAN® contendo o modelo constitutivo do material em consolidação foi associada a uma formulação explícita do software ABAQUS®. Uma biblioteca de entrada foi escrita para incluir diferentes possibilidades matrizes, com modelos cinéticos e reológicos previamente estabelecidos e modelos originais. Formulações constitutivas tensão-deformação alternativas foram codificadas com vista ao seu teste e comparação. Um programa numérico totalmente funcional foi, assim, estabelecido.

Finalmente, um amplo programa experimental foi realizado para medir todas as variáveis do processo sob determinadas condições de fabrico. Este programa visou validar o modelo de processo, conferindo-lhe relevância e utilidade. Vários procedimentos experimentais foram usados e novas sub-técnicas foram desenvolvidas para obter os dados necessários. Entre eles a calorimetria diferencial e reometria usadas em ciclos de cura recomendados pelo fabricante, análise de termografia complementar, desenvolvimento de vários elementos de monitorização do processo de enrolamento filamentar ou mesmo a técnica de coloração local de resina medir o seu fluxo *in-situ*. Validações parciais e totais do modelo foram, assim, progressivamente alcançadas.

O modelo de processo validado é descrito, passo a passo, ao longo da tese, juntamente com os procedimentos analíticos, numéricos e experimentais realizados para o atingir. Desejavelmente, ao leitor é dada uma visão gradualmente profunda, mas lógica, para a estratégia de modelação e os resultados.

Acknowledgements

This thesis is the visible expression of a deep, long and mostly lonely journey in which several personal frontiers have been approached, eventually touched, surely enriching myself as a person and, hopefully, as an engineer and researcher. Along this path, the support given by Rosinda, substantiated in true care and understanding was invaluable. To her, I am truly grateful.

The work itself, benefited, in several points, of the collaboration and/or assistance of colleagues and organizations, whom I would like to acknowledge:

- INEGI administration board, for allowing my partial dedication to this programme and also for the highly valuable conditions provided in laboratorial means and facilities;
- Agnieszka Żmijewska Rocha, David Miranda and Henrique Neves, for their valuable contributions in the early identification of relevant phenomena, in the development of the numerical code and in its early debugging, respectively;
- Vanessa Silva Gomes, for the valuable contribution in the analysis and review of available stress-strain and micro-mechanical models;
- Gilmar Pereira, for the support in early experimental trials for resin flow analyses;
- Prof. Luisa Madureira, for the intensive help with the analytical solving and manipulation of complex mathematical descriptions, within the stress-strain averaging analyses;
- Dr. Alex Skordos, for the breakthrough help with the early kinetics modelling phase;
- Dr. Celeste Pereira, for the assistance in the DSC tests program.

The collaboration or help of the following people and organizations was also gratefully appreciated:

João Rodrigues (INEGI); Loic Hilliou (DEP UMinho); Armanda Teixeira (INEGI); Dr. David Ayre (Cranfield University); Prof. Andrew Long (University of Nottingham).

To my supervisors, I would also like to thank the continuous availability to follow the incidences of the work and advise me. Whenever asked or needed, their support was effective and, therefore, I am grateful. It has been a pleasure and an advantage to work with both.

List of Symbols

a	characteristic amplitude of the sinusoidal pattern of the fibres // constant (viscosity/curing sub-model)
A_i	constants (crystallization/curing sub-model)
A_{rr}	area of resin mixing (transverse to flow) around the point of interest
α	degree of cure of resin
α_0	initial degree of cure
α_{gel} // $\alpha_{\lim}$	degree of cure at which gelation occurs (gel point)
b	tow bandwidth (multiple rovings, complete bundle) // constant (viscosity/curing sub-model)
B	constant (curing sub-model)
β_{ij}^{c}	thermal expansion coefficient in the *ij*th direction in cured state
β_{ij}^{uc}	thermal expansion coefficient in the *ij*th direction in uncured (initial) state
c	crystallinity // constant (curing sub-model)
C	specific heat of composite
C^f	specific heat of fibres
C^r	specific heat of resin
$\overline{C}_{ij}$	components of the on-axis (1,2,3) stiffness matrix
C_{ij}	components of the off-axis (1,2,3) stiffness matrix
$\tilde{C}_{ij}$	components of the off-axis (1,2,3) stiffness matrix
c_r	relative crystallinity
d	constant (curing sub-model)
E_i // U_i	activation energies for curing/crystallization/viscosity sub-models
E^f	Young’s modulus of fibres
E^m	YOUNG’s modulus of resin (Matrix)
E_c^m	Young’s modulus of resin (matrix) in cured state
E_{uc}^m	Young’s modulus of resin (matrix) in uncured state
E_{ii}	Young’s moduli in the *ii*th principal material axis
E_1^{fb}	Young’s modulus of the fibre bed in direction 1
E_b^{fb}	Young’s modulus of the fibre bed in direction b (bulk)
ε_{ij}	components of the on-axis ($1,2,3$) strains // components of the off-axis (z , θ , r) strains
ϕ'	fibre misalignment angle
$F_{winding}$	winding force
ϕ	winding angle
G_{ij}	shear moduli
G_{ij}^{c}	shear modulus of the resin in cured state
G_{ij}^{uc}	shear modulus of the resin in uncured state
H_t	total heat of crystallization/curing
H_u	ultimate heat of crystallization of polymer
η_{ij}^{c}	chemical change coefficient in the *ij*th direction in cured state

η_{ij}^{uc}	chemical change coefficient in the *ij*th direction in cured state
k	thermal conductivity of the composite
k^{f}	thermal conductivity of fibres
k^{m}	thermal conductivity of resin (matrix)
k_{c}^{m}	thermal conductivity of resin (matrix) in cured state
k_{uc}^{m}	thermal conductivity of resin (matrix) in uncured state
k'	modified Kozeny constant
k_{i}	constants (curing sub-model)
L	characteristic length of the sinusoidal pattern of the fibres
L/a	buckling ratio (waviness ratio)
μ	resin (matrix) viscosity
μ_{ch}	resin (matrix) chemical viscosity
μ_{gel}	viscosity at gel point
μ_{∞}	constant (viscosity sub-model)
n	order of curing reaction (curing sub-model)
ν_{ij}	Poisson’s ratio in *ij*th direction
ν_{ij}^{c}	Poisson’s ratio in *ij*th direction in cured state
ν_{ij}^{uc}	Poisson’s ratio in *ij*th direction in uncured state
p^{f}	pressure hold by the fibres
p^{r}	pressure hold by the resin (matrix)
$p_{winding}$	winding pressure (radial)
$\frac{dP}{dr}$	radial pressure gradient
$\dot{Q}$	rate at which heat is generated by the curing or crystallizing resin (matrix)
R	universal gas constant
r^{f}	radius of the fibres (filaments)
r^{fs}	radial position of the fibre sheet (layer)
$r^{mandrel}$	radius of the mandrel
ρ^{c}	density of composite
ρ^{f}	density of fibres
ρ^{m}	density of resin (matrix)
ρ_{c}^{m}	density of matrix in cured state
ρ_{uc}^{m}	density of matrix in uncured state
S	apparent permeability of the fibre sheet
σ_{ij}	stress in the in *ij*th direction
t^{l}	layer thickness
t_{0}^{l}	initial layer thickness of the (outer) layers
T	temperature
T_{0}	initial temperature
$\dot{u}_{r}^{r}$	resin (matrix) radial velocity

V_0	initial fibre volume fraction
V_f	fibre volume fraction
V_m	resin (matrix) volume fraction
V_r^j	volume of resin from the *j*th ply into the “current” layer
V_a	maximum achievable fibre volume fraction
V'_a	modified maximum achievable fibre volume fraction
U	constant independent of temperature (viscosity sub-model)
Ψ_j^m	relative concentration of different constituents in the *m*th layer

Table of Contents

CHAPTER 1

INTRODUCTION

1.1. Motivations and Objectives

The filament winding (FW) process, used for the manufacture of a wide variety of composite parts and components, has proved to be technically effective and cost competitive through the last few decades. For specific emergent and high demanding applications, it turns to be the most appropriate manufacturing process. Axis-symmetric composite parts like sewage or supply piping systems, high pressure vessels, water storage tanks, aircraft fuselage sections, transmission shafts, fishing rods, golf club shafts but also non axis-symmetric ones like wind turbine blades, buses chassis are among these identified applications.

The FW manufacturing process consists of an automated process in which an impregnated continuous filament (or tape) tow is wound over a rotating mandrel. The synchronized movement of both this mandrel and the delivery head in its moving carriage controls the fibre path, leading to the desired pattern. In Figure 1 the typical configuration of this process (wet winding) is schematically represented. In it, one may observe that in the case of axis-symmetric parts, in such typical process configuration, the main axis of symmetry of the composite component is coincident with the rotation axis of the mandrel. Different process configurations mainly differ in the type of material used (thermosetting prepregs, thermoplastic prepregs, etc) for which different impregnation and feeding systems may be designed.

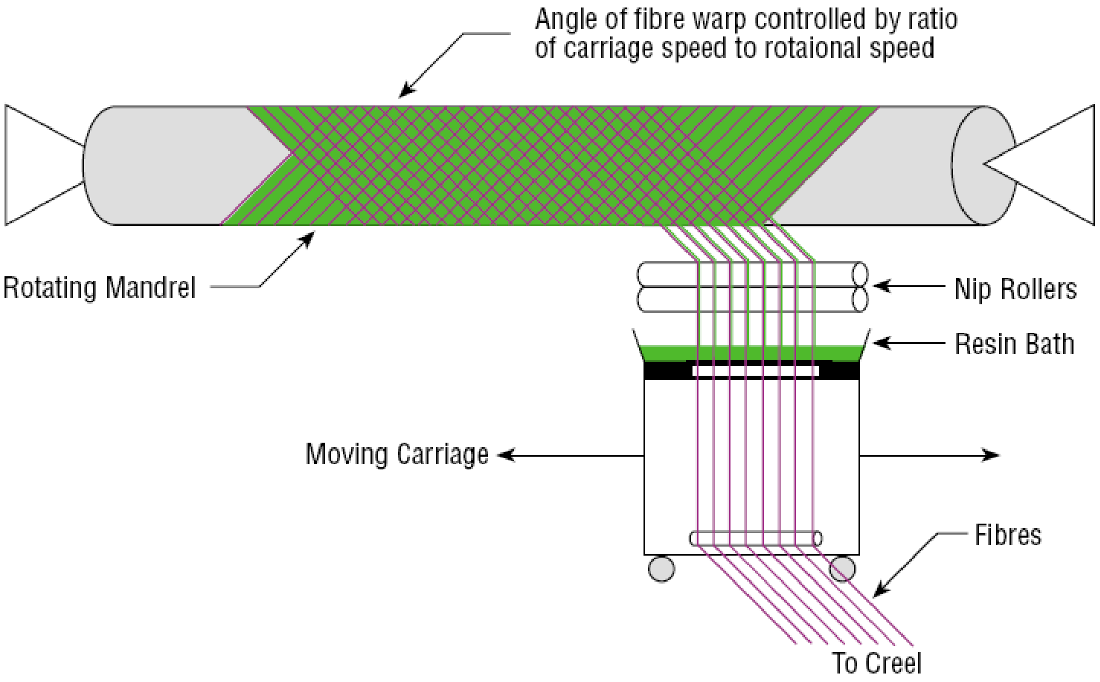

Figure 1 – Schematic view of wet FW process [1].

By controlling the relative amounts of resin and reinforcement, the winding pattern, the fibre’s tension, the cure of the resin system, as well as other important variables of the process, the strength of the filament wound parts may be improved to resist stresses and/or strains in specific directions. Thus, the simultaneous interaction of a great number of complex physical phenomena is of difficult assessment in terms of its modelling and precise measurement. However, with the increasing demands on safety and reliability issues, in short- as well as in long-term applications, it is of absolute need to achieve better knowledge and more accurate models of the physical phenomena acting in the FW process. Only realistic models, capable of relating the input with the output relevant parameters of this multi-physical process will allow a reliable design and control of the FW manufacturing process for each application. A better understanding of the coupled behaviour of those phenomena and of their influence on the final quality of the manufactured parts will, ultimately, allow to optimize them and achieve weight and costs savings in the final products. Questions on the level of reproducibility, predictability and dimensional tolerances may also be further addressed.

This study aimed at developing and validating a multi-physical process model for the FW manufacturing technique. A modular approach, based on sub-models each referring to a relevant group of physical phenomena acting at the layer-laminate level, was designed. This option allowed to settle a model applicable to a broader range of real configurations and applications of the FW manufacturing process as it is now required by the industry.

1.2. Thesis Organization

This thesis is divided into six chapters, each addressing a relevant stage within the development and analysis of the present process model. Each chapter is built independently both thematically and in the logical arguments construction. However, the six chapters report the natural sequence of the whole study, from the problem identification, to the proposition of a solution and its validation.

After this introductory chapter (chapter 1) a comprehensive literature review is set in chapter 2. In this review, the available knowledge on processes and/or sub-processes that correlate with the FW process are identified. Several works published by different authors in the past are critically analysed and the background for this study is therefore enriched. In chapter 3 the FW process model is established. The several physical phenomena acting within the laminate being manufactured are analytically modelled. Each decoupled group of phenomena is described in a dedicated sub-model. The overall architecture of the multi-physical process model is also presented. The experimental tests conducted to assess and measure the evolution of the several physical parameters during the FW process are fully addressed in chapter 4. This chapter holds the detailed description of the experimental procedures and respective results, covering the main process input and output variables. Critical analysis of these results is produced in view of comparing with the numerical ones. Chapter 5 covers the numerical implementation of the process model. Several sub-routines, each relating to a sub-model, are coded into numerical algorithms. These are assembled through a main routine that guarantees the proper flow of variables information and interaction between the several sub-routines accordingly with the model architecture defined. At the end of this chapter, critical comparisons between numerical and experimental results are presented and the validation of the process model is, thus, discussed. In chapter 6, the conclusions are drawn for the entire study. The degree of accomplishment of the objectives and thus the usefulness and validity of the present work are discussed. Future improvements and developments to be further addressed are identified as well.

CHAPTER 2

LITERATURE REVIEW

2.1. Scope of the Review

In this chapter the state of the art referred to the FW process modelling and characterization is addressed through a comprehensive literature review of relevant technical and scientific papers and thesis published in the last four decades. Previous works covering all the relevant fields related to the modelling of this process were studied. Very few researchers focused strictly in the FW process. On the other hand, however, a considerable number of studies led on other processes and/or the detailed characterization of several of the physical and chemical phenomena acting within consolidating composite laminates have been published.

The review is divided in the main sub-themes that correspond to the different physical phenomena governing the consolidation and behaviour of composite laminates. Namely, identification of the FW process parameters, fibre's compaction, resin flow, resin kinetics, stress-strain and global process models are critically identified and described in separated sections. Despite the coupled nature of some mechanisms in the consolidation of composite laminates, independent sections deal with each group of phenomena identified in order to allow a deep understanding of them. Since different authors referred to similar phenomena with different nomenclature or even mathematical symbols, effort is made in homogenizing the relevant information and presenting it in the symbology and nomenclature adopted in the present work. For clarity, the matrix is frequently named resin, independently of thermosetting and/or thermoplastic being considered throughout this chapter. Experimental techniques for the measurement of parameters and/or model validation which are thought relevant for the present study were also reviewed from the literature.

Since the scope of the present thesis is to model a multi-physical process that involves a broad range of correlated research fields, contributions from a wide range of sources are studied. Therefore, although the following literature review may appear reasonably extensive, it strictly covers the relevant knowledge that supports the strategy for the development and establishment of the present FW process model. Further detailed analysis is addressed in chapter 3, when setting the assumptions and formulations of each sub-model.

2.2. Process Modelling in Composites Manufacturing

In this section, the literature addressing the theoretical modelling of each phenomenon governing the behaviour of composite laminates under consolidation is critically reviewed. An overview of the main studies published in the last four decades is drawn. As far as possible, the review is divided in the relevant sub-themes as mentioned above. The sub-themes were chosen upon identification of the process parameters and/or variables which govern it.

2.2.1. Process Parameters

In the FW manufacturing process there are several physical parameters whose different combinations allow a wide range of mechanical and geometrical results. These parameters may be divided into two categories: the user-controllable process parameters and the other process parameters inherent to the physics of the process. By user it is meant the designer and/or operator of the manufacturing process. In a process model development, the final objective is to get the user-controllable process parameters to be the input variables and the inherent variables (which are not directly controllable throughout the process) to be the output ones. Only with sound and correct physical descriptions of each phenomenon one may get a profitable tool for design and process optimization purposes.

The main user-controllable process parameters are:

- the choice of the material system (the reinforcing fibres and the matrix);
- the geometry of the mandrel;
- the initial fibre’s tension;
- the cross-section of the fibre’s bundle (incl. bandwidth and/or thickness);
- the path of the fibres onto the mandrel;
- the winding angle;
- the initial fibre’s degree of impregnation;
- the processing temperature;
- the winding speed;
- the lay-up sequence; and
- the curing time after winding.

The main process inherent parameters or phenomena are typically variable during the process, may vary with time and space, and are:

- the fibre’s motion;
- the matrix flow through the fibre’s bed;
- the matrix degree of conversion (cure/crystallization);
- the matrix viscosity;
- the stresses and strains in the fibres;
- the temperature;
- the fibre’s, resin and void’s volume fraction; and
- the fibre characteristic waviness.

A few more parameters could be pointed out, such as the permeability of the fibre bed to the resin and air, or the layer’s interaction by way of the compaction pressure and resin mixing. However, these may be identified as sub-parameters that influence the main ones previously identified. Moreover, these sub-parameters need to be specifically analysed in each case as they are highly dependent on the material system used together with other main configuration options for the FW process.

Lee and Springer [2] summarized the critical issues to consider when selecting the proper combination of the input variables. Thus, for most of the applications, the values of the controllable process variables must be selected such that:

- the temperature inside the material is below the maximum allowable value at any time during processing;
- the material is cured completely and uniformly;
- at the end of the cure the fibre distribution is uniform and has the desired value;
- the fibre tension is positive, but doesn’t exceed prescribed limits at any time during processing;
- the cured composite has the lowest possible residual stresses;
- the cured composite’s total residual strains are within the prescribed limits;
- the cured composite has the lowest possible void content;
- the processing is executed in the shortest possible time.

It becomes clear that, either for process model validation or manufacturing purposes, considerable set of measuring devices is needed in order to guarantee that the user-controllable process variables really are within the admissible ranges and combinations that lead the outputs to the desired optimum values.

Relatively to the winding patterns, there are mainly three types of winding: circumferential (hoop), polar (longitudinal) and helical winding (Figure 2). The helical winding, if neglecting shear strength between surfaces (friction factor virtually null), implies the deposition of the fibres along a geodesic isotensional trajectory. In such condition, Clairaut’s theorem [3] may be expressed as follows:

$$r \sin\phi = constant \ , \tag{2.1}$$

where r is the radial coordinate of the fibre bundle and ϕ is the winding angle. The geodesic trajectories defined as in the equation (2.1) typically don’t correspond to the principal stress directions of the composite part when $0^{\circ} < \phi < 90^{\circ}$. Further attention is given to this problem in section 2.2.5. In polar winding, on the other hand, one may experience considerable difference (from 12% up to 40% of the maximum value) on the fibre’s tension in the edges (callouts or domes) or in the mid-section (cylindrical) of the composite part [4]. In this case the isotensoidal assumption is not valid anymore.

Analytical and numerical solutions for the kinematics of FW have extensively been investigated during the last decades. Koussios *et al.* [5,6] recently proposed consensual and updated kinematical models for ellipsoidal and cylindrical wound parts.

One specific manufacturing effect of the FW process is its mosaic patterned composite layer, as depicted in Figure 3. This particular formation of the lay-up can significantly affect the stress and strain fields in a thin-walled shell. However, it is not considered in the general stress analysis procedures, including the existing finite element software packages [7]. Stress analysis based on the conventional mechanics of laminated structures can underestimate the actual level of stresses in the thin-walled filament-wound composite shells. Pagano and Whitney [8] suggested that the stress field within a highly anisotropic cylinder, even under simple loading conditions, is far from uniform.

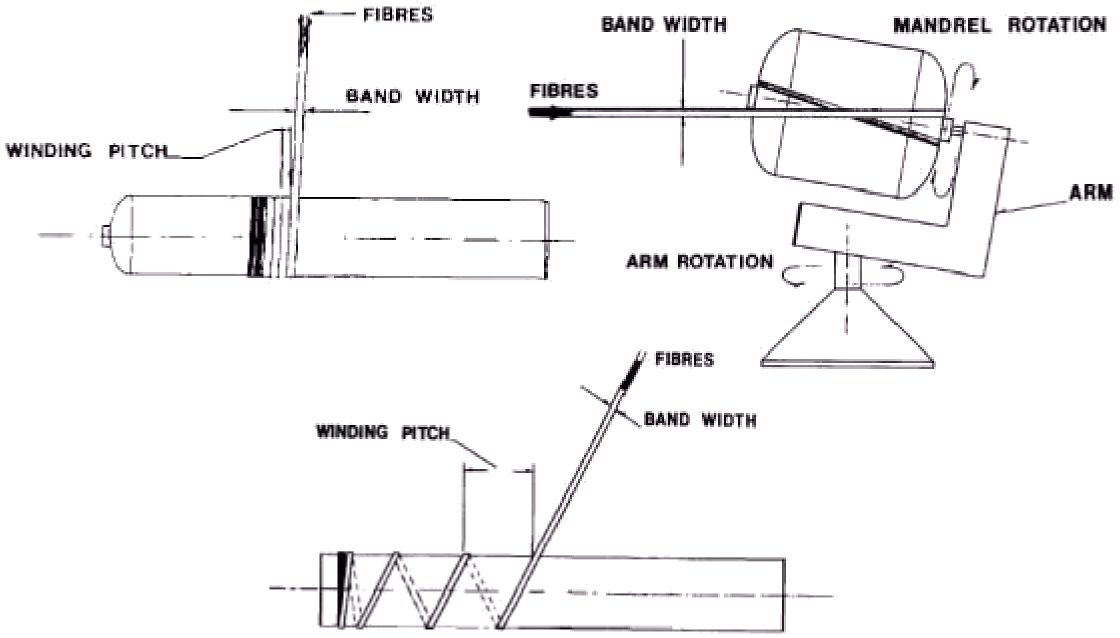

Figure 2 – Schematic representation of circumferential (hoop) winding (top left), polar (longitudinal) winding (top right) and helical winding (bottom) [9].

Each filament-wound layer is typically composed by two plies with $+\phi$ and $-\phi$ fibre’s orientation angles, respectively. As these plies are interlaced throughout the part being wound they are actually identified as a single layer. Morozov [7] studied this characteristic of the FW process and showed how this structural feature affected the strength of the composite parts. He modelled the composite material in a mosaic way where each alternating triangle was defined as either $[+\phi/-\phi]$ or $[-\phi/+\phi]$.

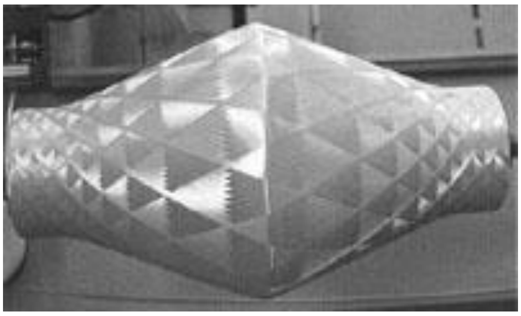

Figure 3 - Angle-ply layer of a filament wound shell [7].

Different configurations of the manufacturing process, whether it is used a thermosetting or a thermoplastic matrix system, will greatly influence the degree of homogeneity of the impregnation as well as the processing temperature. Furthermore, the interaction between layers (adhesion and exchange of mass and heat) and the consolidation of the laminate is strongly dependent of the matrix properties. In the next sections, whenever the choice of the matrix type is critical, it is discussed in detail.

2.2.2. Compaction of the Fibres

The winding tension applied to the fibres during the FW process has an indirect influence on the fibre volume fraction and void content. Higher tension causes higher pressure build-up and as a consequence higher amounts of resin and voids are squeezed through or outwards the laminate. The fibre volume fraction increases and the fibre bed becomes stiffer. However, when the fibres' content is too high there might be lack of matrix to keep fibres together and part performance may decrease significantly.

Several authors studied the pressure build-up phenomenon in self-acting foil bearings in the past century [10-13]. These systems present some similarities with the FW process and are, thus, worth observing. Blok and Rossum [10] have shown that a flexible impermeable tape in contact with a rotating cylinder and lubricating oil would cause the oil pressure to increase between the tape and the cylinder in a wedge-shaped entrance region (Figure 4). Following the wedge-shaped entrance region, the oil was observed to form a constant thickness film gap between tape and cylinder. For a wide range of test conditions, the outward oil pressure, p, in this constant thickness region was observed to be equal to the inward compressive stress, σ, given by:

$$\sigma = \frac{F}{b\,r} \quad , \tag{2.2}$$

where F is the inlet tape force, b is the tape bandwidth and r is the pin radius.

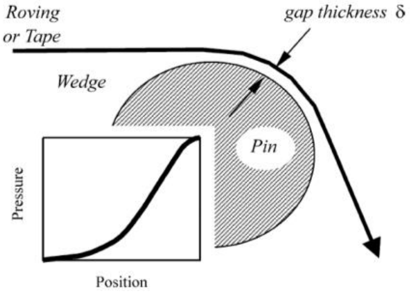

Figure 4 – Schematic cross-sectional of a tape being pulled over a cylindrical pin. The pressure build-up in the wedge entrance is also shown [14].

Similar relations between the constant thickness and processing parameters such as tape tension, width, oil viscosity, relative tape/cylinder speed and cylinder radius were presented by all those researchers. They developed the "lubrication number" concept. It is clear from the preceding analysis that fibre tension plays an important role in pressure build-up in such a fibres/mandrel interaction.

Bates *et al.* [14,15] studied the pressure build-up during melt impregnation of glass-fibre roving. They set the melt pressure at the roving/pin interface to be given by:

$$p = f \frac{F}{b\, r} \ , \tag{2.3}$$

where f is an adjustable fitting parameter that can vary between 0 (no pressure at the interface) and 1 (maximum pressure at the interface). A f value equal to 1 would indicate that the outward melt pressure balances the inward compressive stress. For this value of f, there would be no normal force of the roving against the pin surface. A f value less than 1 would indicate that the roving is in partial contact with the pin. In Figure 5 a schematic view of the roving/pin interaction.

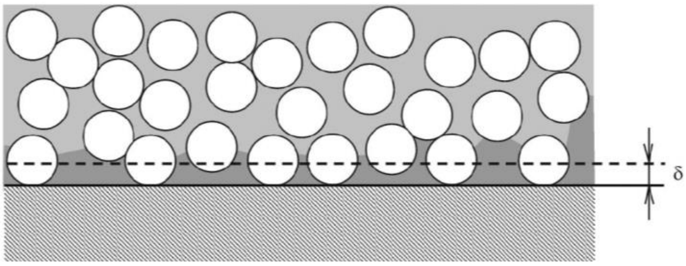

Figure 5 – Schematic transverse cross-section representation of the glass-fibre filaments interacting with the pin and the impregnating melt [14].

In a more general and widely accepted analysis for the pressure born in a composite laminate being processed, the externally applied pressure during its consolidation is shared by the fibre bed and the resin, which can be expressed by [16-22]:

$$\sigma = p_r + p_f \ , \tag{2.4}$$

where σ is now the applied stress, p_r is the resin pressure and p_f is the effective stress sustained by the fibres. A simple viscoelastic system, in which the resin flow and fibre bed compaction are the viscous and the elastic components, respectively, is schematically represented in Figure 6. Theoretically, in a very low fibre volume fraction prepreg, or perhaps in a system with ideal straight fibres, the fibre bed carries no through the thickness stress. In practice, the relatively high fibre volume fraction, and the wavy geometry of real fibre beds mean, significant stress can be borne by the fibre bed, especially if there is any loss of resin [18].

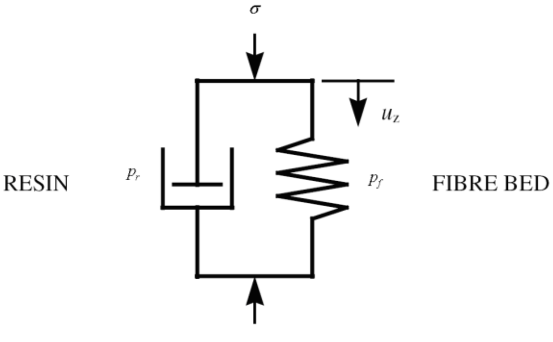

Figure 6 – Analogue representation of composite laminate with elastic (fibre) and viscous (resin) response [18].

The compaction curve of the fibre bed is the relationship between the effective stress, p_f, and the degree of fibre bed deformation, which is typically associated to the fibre bed thickness, t^{fb}, and fibre volume fraction, V_f. Experimental techniques and methods previously published are reviewed in section 2.3.1.

Lee and Springer [23] retrieved from the physics of winding that the pressure applied by the $j+1$ layer to the outside of the previously wound layer, j, is given by:

$$p_{out}^{j} = \frac{F^{j+1}\sin^2\phi}{r_f^{j+1} b^{j+1}} \quad , \tag{2.5}$$

where F is the winding fibre tension, ϕ is the layer winding angle, r_f is the fibre radial position (radius to the middle of the layer) and b is the tow/bundle bandwidth. In modelling the successive deposition of n new layers in the FW process, incremental application of the pressure in each deposed layer can be done with a series of n equal increments or other criteria can be adopted. Banerjee *et al.* [24] coded this phenomena numerically and found several restrictions to the size of each increment to compute.

During the FW process, the fibre's tension may vary from the initial winding tension due to [23]:

- inward radial motion of the fibres through the resin resulting in a reduction in fibre tension;
- radial and axial expansions or contractions of the composite due to thermal or shrinkage effects resulting in an increase or decrease in fibre tension.

The second group of causes is further reviewed in sections 2.2.4 and 2.2.5. Concerning the fibre motion in each layer, it occurs during the winding process from the deposition of the layer up to the moment in which fibres either are fully accommodated or cannot accommodate further due to the pressure gradient and/or matrix state. If the matrix reaches a certain level of viscosity that hinders fibres to move before the pressure drop is complete, then a resin pressure gradient will remain in the laminate at and after this point [25]. In thermosetting resin systems this would be the gelation point.

Banerjee *et al.* [24] developed a fibre motion model for wet FW which described the motion of each layer of the cylinder during winding. This model was based on the assumption that resin reached gelation prior to eventual oven curing phase, i.e., that the fibres motion ceased prior to any external thermal loading that would affect the behaviour of the accommodating laminate. In particular, a process model relating the winding processing conditions (user-controllable parameters) to the fibre volume fraction was presented. According to their study, two phenomena are acting together in the fibre motion:

- as a new layer is wound, an external pressure is applied, creating a pressure gradient in the previously wound layers (equation (2.5)); this load is shared between the fibre and the resin (equation (2.4));
- the fibre bed behaves as a nonlinear spring and when compressed by the external force applied when a layer is wound, it compacts itself (Figure 6).

A specific case of sponge squeeze model, previously developed by Gutowski *et al.* [26] (and reviewed in section 2.2.6), was considered in their study:

- as the resin cured, fibre motion ceased in a particular layer;
- resin in adjacent layers had different viscosities;
- a modified stiffness formulation was adopted.

In Figure 7 the fibre bed compaction mechanism, as considered to occur by these authors, is schematically represented.

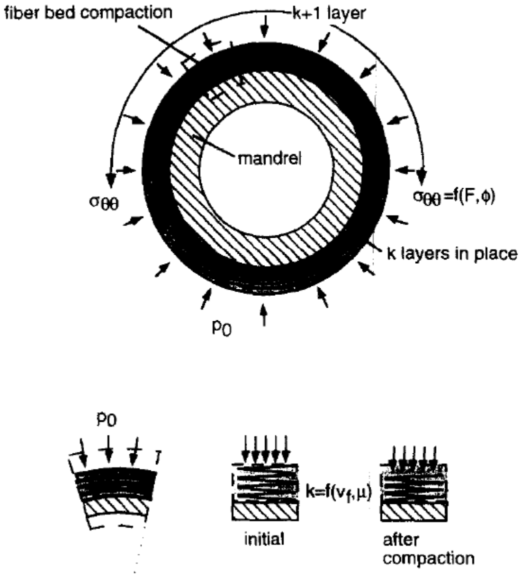

Figure 7 - Compaction during FW. When the k+1 layer is wound, the layers beneath are subjected to a compressive load [24].

The fibre bed stiffness is a function of the fibre volume fraction which changes as the bed compacts, the stiffness must be re-evaluated. The evaluation of the fiber bed stiffness was done through a modified formulation presented by Cai and Gutowski [16,27] in which the fibre volume fraction, V_f, is the only variable influencing its evolution during the consolidation phase. The longitudinal, E_{xx}^{fb}, and transverse (bulk), E_{bb}, on-axis stiffnesses were then expressed as:

$$E_{xx}^{fb} = V_f E^f \frac{\pi/4}{V_a}$$

$$E_{bb} = E_{yy}^{fb} = E_{zz}^{fb} = \frac{\dfrac{\sqrt{V_a}}{\sqrt{V_f}}\left[5 - \dfrac{\sqrt{V_f}}{\sqrt{V_a}} - 4\dfrac{\sqrt{V_0}}{\sqrt{V_f}}\right]}{\dfrac{\beta^4}{3\pi E^f}\left[\dfrac{\sqrt{V_a}}{\sqrt{V_f}} - 1\right]^5}, \qquad (2.6)$$

where E_{yy}^{fb} and E_{zz}^{fb} are, respectively, the in-plane and out-of-plane transverse stiffnesses of the fibre bed, E^f is the Young's modulus of the fibre, and V_0, V_a and β are constants dependent on the state of the fibre bundle.

Once the layer displacements Δu^j are determined for the mth load increment, the radial positions of the layers in place $j = l..k$ are updated as follows:

$$\begin{aligned} \left(r_o^j\right)^m &= \left(r_o^j\right)^{m-1} + \left(\Delta u^{(j)}\right)^m \\ \left(r_i^j\right)^m &= \left(r_i^j\right)^{m-1} + \left(\Delta u^{(j-1)}\right)^m \end{aligned} , \tag{2.7}$$

where r_o^j and r_i^j are the outer and inner radii of the jth layer, respectively.

Figure 8 schematically represents the fibre motion model philosophy developed by Banerjee *et al.*[24].

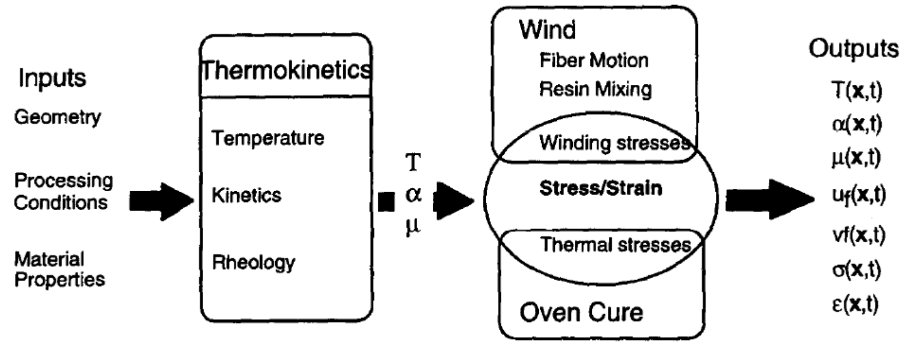

Figure 8 - Schematic showing the inputs and outputs of the FW model and the relationships among sub-models [24].

Gutowski and Dillon [28] proposed a fibre bed compaction model that fitted all the compaction curves previously published by different authors for different laminates. These experimental studies are reviewed in section 2.3.2.

Dave *et al.* [29,30] divided the process of (graphite) fibre bed compaction into three different deformation behaviours. They plotted void ratio as a function of the effective stress for effective stress range of 0 to 1.7MPa. In the range of 0 to 0.07MPa fibre bed has a linear behaviour, which is called “immediate or distortion settlement” behaviour. It occurs together with load application, primarily as a consequence of distortion within the packed fibre bed. In range of 0.07MPa to 1.03MPa the fibre bed has a semi-logarithmic behaviour. It is called “primary compression” or “normal consolidation”. Afterwards, over the range of 1.03MPa, bed fibre behaves like a rapidly stiffening spring. It is called “secondary compression” or “over consolidation” and is described as being due to plastic flow and gradual adjustment under imposed load.

They presented a relationship between the fibre volume fraction, V_f, and the effective stress sustained by the fibre bed, p_f, that in the range $0 \le p_f \le 0.0687MPa$ had the following form [30]:

$$V_f = \frac{1}{1 - 1.5519 \times 10^{-6} p_f + e_0} , \tag{2.8}$$

where e_0 is an empirical constant.

Following Cai and Gutowski's work [16,26,27,31], Agah-Tehrani and Teng [32] proposed a continuum consolidation model for macroscopic analysis of fibre motion during FW of thermosetting cylinders of arbitrary thickness. Their model was limited to winding at a constant (hoop) winding angle throughout the process and constant viscosity resins. The model indicated one zone in which consolidation has ceased and one other in which fibre bundles were continuing to compact due to the applied tension. Hojjati and Hoa [33] and Shin and Hahn [20] also followed and applied Gutowski's continuum equation governing the through-the-thickness compaction behaviour (one-dimensional, r) of consolidating laminates as follows:

$$\frac{\partial p_r}{\partial t} = \frac{V_f}{W} \frac{S}{\mu} \frac{\partial^2 p_r}{\partial^2 r^2} , \tag{2.9}$$

where p_r is the resin pressure, W and S are the tangent compliance and the permeability of the fibre bed, respectively, μ is the resin viscosity. The tangent compliance described a change in the fibre volume fraction resulting from a change in the effective compressive fibre stress.

Gutowski *et al.* [34] derived several alternative expressions relating fibre effective stress, p_f, to the fibre volume fraction, V_f, based upon the assumption that the fibre network stiffness was governed by the bending beam behaviour of the fibre between multiple contact points. The most widely used by several authors is the following formulation:

$$p_f = \frac{3\pi E}{\beta^4} \frac{\sqrt{\frac{V_f}{V_0}} - 1}{\left(\sqrt{\frac{V_a}{V_f}} - 1 \right)^4} , \tag{2.10}$$

where V_0 is a certain "minimum" fibre volume fraction bellow which the fibres carry no load, V_a is the maximum available fibre volume fraction at which resin flow stops, β is the typical waviness ratio (span length/span height) of the fibres and E is the flexural modulus of the fibres.

The lamina stress-strain behaviour has been found to greatly influence the compaction behaviour of the laminate during its consolidation. Laminae with hardening stress-strain behaviour, which is characteristic of real composite layered laminates, have the fastest compaction times [35]. Although this output comes from studies conducted in autoclave/vacuum degassing processes, attention must be given to it. Specific stress-strain constitutive relations are discussed in section 2.2.5.

2.2.3. Resin Flow

Resin flow is the other mechanism (adding to those described in the previous section) that greatly influences the fibre motion and positioning within the layers during FW process. Although in the FW process modelling the resin (matrix) flow and/or cure phenomenological sub-models cannot be separated from the fibre motion sub-models, here we try to summarize them in a decoupled manner. This option is supported by the fact that the resin flow is itself a physical process that can be independently described analytically.

The fluid flow through porous media has been extensively studied in the past. Numerous studies have been published concerning the modelling and characterization of such phenomenon. Among those, soils consolidation, filters behaviour and impregnation of fibrous beds were the most studied. From them, relevant knowledge was gathered to the “recent” composites manufacturing processes.

Ó Brádaigh *et al.* [36] divided the flow in composites during consolidation in two major mechanisms: percolation flow and shear flow. These mechanisms are schematically depicted in Figure 9. For percolation flow, applying pressure to the laminate is similar to squeezing a sponge that causes the fluid to bleed out. For shear flow, the composite behaves as a very viscous fluid filled with inextensible fibres. In this case the resin and fibres move together and the driving force is the deviatoric component of the stress applied to the laminate.

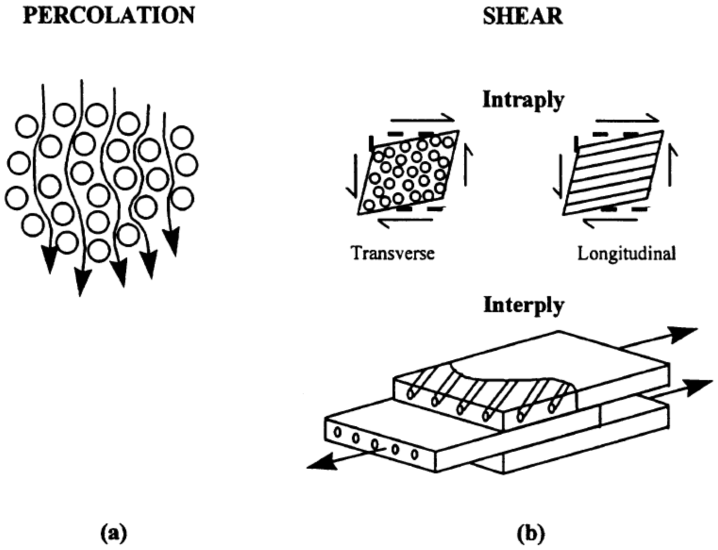

Figure 9 - Flow mechanisms during processing: (a) percolation and (b) shear [36].

Typically, the percolation flow approach is used to model the flow and compaction of thermosetting matrix composites and the shear flow approach is applied to thermoplastic matrix composites [37].

Kyan *et al.* [38] modelled the resin flow through a fibre bed, using a geometrical model of the fibrous bed and assuming that, despite the level of porosity, the fluid was not flowing through a significant portion of the pores space.

Lindt [39] presented analytical descriptions of the slow consolidation of fibres in a Newtonian fluid. He developed the lubrication theory, in which, for low Reynolds and narrow channels flow through the fibre bed, the mechanisms of squeezing and drag flow may be separated as they govern the flow in different regions of the porous media. However, several assumptions were made that do not comply with typical composite fibre beds properties. Namely the assumptions that the cylinders (fibres) must be in pure translation and have smooth surfaces.

Bear [40] suggested that there are two equations describing the unidirectional flow mechanism in porous media: the Darcy's (1856) and the Forchheimer's (1901) equations. These can be expressed as:

$$\dot{u} = -\frac{S}{\mu}\frac{dp}{dr} \ , \tag{2.11}$$

$$d_1\dot{u} + d_2\dot{u}^2 = \frac{dp}{dr} \ , \tag{2.12}$$

where $\dot{u}$ is the fluid velocity, S is the permeability of the medium, μ is the fluid viscosity, $\frac{dp}{dr}$ is the pressure gradient in the direction of the flow. The terms $d_1\dot{u}$ and $d_2\dot{u}^2$ vary with viscous and inertia effects, respectively. After the establishment of the Darcy's [41] model for flow in porous media, Dupuit [42] and Forchheimer [43] included inertia effects for higher flow velocities.

Although the permeability tensor, S_{ij}, is anisotropic for most fibre reinforcements it may be viewed as a scalar quantity, S, in one-dimensional (unidirectional) flow condition [21]. The use of Darcy's type equation as presented above is, thus, suitable for one-dimensional, low Reynolds number flow through a fully saturated porous medium [44]. Flow throughout a fibre sheet in tension is a low Reynolds number flow ($\mathrm{Re} \le 10$). This equation can also be extended and applied to two- and three-dimensional flows [29]. The friction losses related to the superficial velocity of the fluid (resin) are inversely proportional to the aspect ratio of the obstacle (fibre). For high aspect ratios, $r^f / L \ge 0.05$, of the fibre, the relationship between the pressure gradient and the fluid velocity is nearly linear as the inertia effects are not significant at these low velocities. However, when the aspect ratio decreases (and thus the porosity increases) inertial effects become considerable [45].

Due to the increasing importance of composite manufacturing techniques, modelling the permeability of fibre beds was addressed by several research groups through the years. In fact, the parameters that govern the resin flow mechanism are the resin viscosity, the specific permeability of the media and the temperature [29,30]. The parameters related with the thermo-kinetics of the matrix are reviewed in section 2.2.4. The specific permeability, S_i, in the *i*th direction for anisotropic materials can be expressed as:

$$S_i = \frac{\in r_H^2}{K_i} \ , \tag{2.13}$$

where $\in$ is the porosity of the porous medium, r_H is the mean hydraulic radius of the porous medium (cross-sectional area normal to flow divided by the perimeter wetted by the fluid), K_i is the corresponding Kozeny constant. The mean hydraulic radius of the porous medium is given by [35]:

$$r_H = \frac{r^f \in}{2(1-\in)} = \frac{r^f V_m}{2V_f} \ . \tag{2.14}$$

From equations (2.13) and (2.14) the following expression for the through-the-thickness permeability of the fibre bed is obtained:

$$S = \frac{\in^3 {r^f}^2}{4K(1-\in)^2} \quad . \tag{2.15}$$

Equation (2.15) is actually the Kozeny-Carman model [46], originally developed for granular beds showing isotropic distribution, which can also be expressed as:

$$S = \frac{{r^f}^2}{4K}\frac{(1-V_f)^3}{{V_f}^2} \quad . \tag{2.16}$$

This model was extended to flow across arrays of cylinders by Gutowski and co-workers [27,47]. They suggested that once the $j+1$ layer had passed through the resin rich region, the layer itself compacts. The flow resistance of the fibre network increased and the permeability dropped substantially. At a certain point before $V_f = 1$ the flow must stop and this was not accomplished by the Kozeny-Carman model. Therefore, Gutowski and co-workers measured the maximum fibre volume fraction at which resin flow is no longer possible, V_a', and a relationship between the transverse permeability, S, and fibre volume fraction, V_f, was developed as follows:

$$S = \frac{{r^f}^2}{4K'}\frac{\left(\frac{\sqrt{V_a'}}{\sqrt{V_f}}-1\right)^3}{\left[\frac{\sqrt{V_a'}}{\sqrt{V_f}}+1\right]} \quad , \tag{2.17}$$

where r^f is the radius of the fibres, K' is a modified Kozeny constant. Kozeny constant, K, depends on tortuosity, defined as $(Le/L)^2$, where Le is the average effective path length that fluid particle passes from one end to the other end of the porous bed and L is the actual distance between two ends of the bed. Therefore, for flow through an anisotropic porous medium, like a bed of aligned fibres, the value of Kozeny constant in the direction of the fibres is quite different from that in the direction perpendicular to the fibres because the tortuosities in the two directions are different. This led these authors to obtain a modified value for the Kozeny constant by fitting of experimental data.

Several authors presented considerably different values for the non-dimensional Kozeny constant related to the through-the-thickness flow direction. Dave *et al.* [29,30] utilized the value previously presented by Sullivan [48] of $K \approx 6$. Using this value, Smith [35] calculated a permeability of $S = 4.33\times10^{-13} m^2$ from equation (2.15). The value previously reported by Loos and Springer [49] of $S = 5.8\times10^{-16} m^2$ (10^{-3} lower) suggests that the Kozeny's constant must be much higher than $K \approx 6$. Gutowski *et al.* [47] and Lam and Kardos [50] reported $K \approx 11$ and $K \approx 150$ as the reference values, thus supporting this observance.

Springer [51] studied the relationship between the applied pressure and the resin flow during the cure of fibre-reinforced composites, where the layers were found to consolidate in a wavelike manner. Loos and Springer [49] developed resin flow and void models of the curing process. The resin velocity was related to the pressure gradient, fibre permeability and resin viscosity through the Darcy's type equation for flow in porous media (equation (2.11)).

For aligned cylinders, analytical models based on drag, or on the lubrication approach, were developed for Newtonian and generalized fluids by several authors [52-58]. Some of these are available for low porosity, others for high porosity values.

Happel and Brenner [54] developed analytical solutions of the Navier-Stokes equation for flows parallel and normal to an array of cylinders of a given diameter. Sahraoui and Kaviany [57] used a finite-difference numerical method to solve the same equation for a two-dimensional (simultaneous) flow through an array of cylinders. They presented a relation between the permeability of the porous media, S, and its porosity, $\in$, as follows:

$$\frac{S}{4{r^f}^2} = 0.0606\frac{\pi}{4}\frac{\in^{5.1}}{(1-\in)} \qquad 0.4 \leq \in \leq 0.8 \ , \tag{2.18}$$

where r^f is the radius of the fibres.

Sangani and Acrivos [55] established the following relationship between the transverse permeability, S, of circular tows arranged in hexagonal arrays and the fibre volume fraction, V_f:

$$\frac{S}{{r^f}^2} = \frac{1}{27V_f\sqrt{2}}\left(1-\frac{\sqrt{2V_f\sqrt{3}}}{\pi}\right)^{5/2} . \tag{2.19}$$

These models have shown a rather good agreement with experiments [59,60].

The correct modelling of the tow cross-section is also of great importance because of its influence on the resin flow and, consequently, in the fibre's compaction behaviour and interaction between layers. Sherrer [61] compared both the rectangular fibre model of Cutler (1961) and the hexagonally arranged Hashin's fibre model (1964) with experimental data obtained in his compression, torsion and tension tests conducted on cylindrical wound specimens. Both Cutler's and Hashin's models presented relevant limitations due to their restrictive assumptions and results were not satisfactory.

Looking to the topology of the fibre tows when being wound, it is commonly accepted that they present an elliptical cross-section shape. In conventional FW configurations, the fibre bundle incorporates several fibre tows each including several hundreds or thousands of individual filaments. The higher the winding force is, the cross-sectional shape of each tow becomes more flattened, thus approximating the bundle cross-section to a homogenous random distribution of individual cylindrical filaments. However, in the conventional range of winding forces, the tow elliptical cross-section and individuality may govern the permeability characteristic of the fibre bed. Some studies intended to approach these topologies. Epstein and Masliyah [62] numerically solved the problem of normal flow through elliptical fibres by extending both the Happel and Brenner [54] free surface and the Kuwabara [52] zero vorticity cell models. They showed that fibres with an aspect ratio of 5:1 have a permeability that is 75% lower than obtained for circular fibres when the major axis is perpendicular to the flow as is the case in transverse permeability measurements (and of FW). The volume fractions studied were above 10%, since for lower volume fractions the cross-section exerted a minor effect.

Later, the increasing importance of liquid moulding techniques using fabrics led to the development of further models, which took into account not only the ellipticity of the fibre tows, but also their intrinsic permeability. Phelan and Wise [63] proposed a semi-analytical model based on lubrication approximation, and validated it with computational fluid dynamics, and a few experimental observations. Ranganathan *et al.* [64] extended this model and proposed for a solid ellipse an empirical relationship of the form:

$$\frac{S}{ab} = A\left(\sqrt{\frac{V_f^{\max}}{V_f}} - 1\right)^B , \tag{2.20}$$

where a and b are the axes of the ellipse, $V_f^{\max}$ the maximum packing fraction for a given packing geometry and A and B depend on the axes ratio. For example, $V_f^{\max} = (\pi/2)/\sqrt{3}$ for a proportionally hexagonal packing. For the flow perpendicular to the large axis of the elliptical fibres, and a shape factor greater than 5, they proposed the following relationship:

$$\frac{S}{b^2} = 0.67\left(\sqrt{\frac{V_f^{\max}}{V_f}} - 1\right)^{2.62} . \tag{2.21}$$

They extended this approach to porous tows, pointing out the use of a ‘‘nominal volume fraction’’, $V_f^{nominal}$, which refers to the volume occupied by the ellipses, and is related to the actual volume fraction, V_f^{actual}, by:

$$V_f^{actual} = V_f^{nominal} V_f^{tow} , \tag{0.22}$$

where V_f^{tow} is the volume fraction of fibres within a single tow. They showed that the intrinsic porosity of the elliptical tows does not exert much of an influence, until the ratio of the tow permeability over the overall permeability is greater than 0.001. This was later confirmed using boundary element methods (BEM) and computational fluid dynamics (CFD) calculations [65,66]. Extension of these models to the flow of non-Newtonian fluids was also presented [67].

In the FW process the phenomenon of resin flow is strongly related with tension applied to the fibre bundle during the winding that creates compaction gradient pressure in previously wound layers. This causes resin to squeeze and flow through the porous fibre bed [24]. As the fibre bed below compacts, the fibre volume fraction increases and uncured excess resin from previously wound layers bleeds through the surface. When pressure inside laminate becomes equal to the pressure on its boundaries, there is no more resin flow, no further compaction of the bed, and the specific permeability in any particular direction is constant throughout the bed.

As Cai *et al.* [16] identified fibre bed compaction as being a dominant process in wet FW, they also defined the time required for the resin to flow through a certain ply/layer, t_f. It was defined as:

$$t_f = t^* \left(\frac{4K\mu h_0^2}{A_s r^{f\,2}} \right), \tag{2.23}$$

where t^* is a dimensionless time at which the fluid pressure drops substantially, r^f is the radius of the fibres, K is the Kozeny constant, μ is the fluid viscosity, h_0 is the layer thickness and A_s is a fibre bed spring constant. For processing conditions in which the flow time, t_f, is less than the winding time, t_w, for a layer, the fluid (matrix) would have ample time to flow through the compacting fibre bed.

Undulating channels (tubes) have also been used to model pore geometry in the study of flow through porous media. With its converging and diverging character, this model may avoid the difficulty of selecting representative fibre bed structures (Figure 10). Following previous work of Hjelming and Walker [68], Cheng and Chiao [69] simulated the fibre/resin system with two types of flow cells: the through-flow cell (Figure 11 a) and the squeezing-flow cell (Figure 11 b). The forces acting on the fibres were discriminated into a shear force due to resin flow and a hydrodynamic squeezing force caused by fibre compaction. Main assumptions adopted were:

- the resin was considered a Newtonian fluid;
- no flow along occurred the fibres;
- no slippage occurred at the resin/fibre interface;
- inertial and gravitational forces were negligible;
- if using a very viscous resin the flow was treated as a two-dimensional quasi-steady state motion.

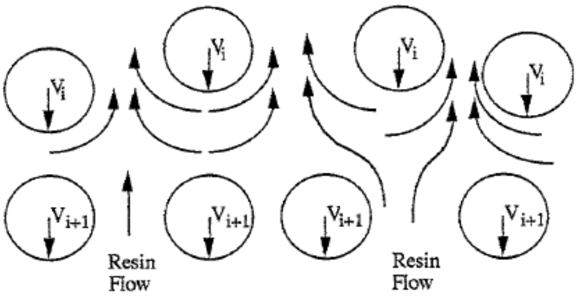

Figure 10 - Structure of random cylinder arrays during consolidation process [69].

The geometric parameters used in this undulating channels model need to be justified further to compare with experimental results.

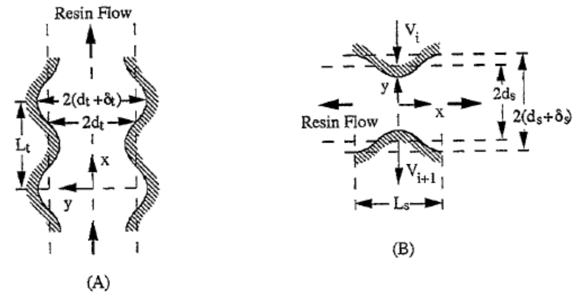

Figure 11 - Geometry of the undulating channel for (a) through-flow cell, and (b) squeezing-flow cell [69].

Few models have been also presented to predict the impregnation and consolidation of thermoplastic composites [70-75]. These models typically applied the Darcy's type equation (equation (2.11)) to model the flow of molten resin within the tows, with the flow direction assumed perpendicular to the fibres direction. All published models ignored void migration and dissolving of entrapped air into the thermoplastic matrix.

One interesting set of assumptions made on the impregnation sub-model developed by Sala and Cutolo [76,77], for thermoplastic powder-impregnated material winding, was that the overall resin movement consisted of three elementary fluxes:

- an isotropic flux induced by a pressure gradient at the boundary of bundles;
- a relative radial flux originated from inwards accommodation of the fibres towards the mandrel;
- a tangential flux produced by bundle deformation due to external pressure.

Part of this flow participated in the impregnation while part of it percolated through the interstices between the tows of fibres composing the bundle. The percentage of flow penetrating the fibre bundle was estimated by computing the ratio of permeabilities outside and inside the bundle (rich in filaments).

2.2.4. Resin Kinetics

In the composites manufacturing, the cure/crystallization kinetic characterization of the matrix have the main purpose of assessing its intrinsic properties such like the degree of cure/crystallization, α or c, and the viscosity, μ. These properties are, typically, inter-related and depend on the thermal conditions and the state of the chemical cure (thermosettings) or re-crystallization (semi-crystalline thermoplastics). Therefore, heat transfer analysis and kinetic formulations for typical matrix systems have been studied by several authors and are reviewed herewith.

The degree of cure of a thermosetting resin, α, is defined as the extent to which curing or hardening of a thermosetting resin has progressed, i.e., the degree of conversion of the resin molecules. It can be evaluated by the relative heat of reaction evolved until a certain time in the curing process and expressed as follows [49]:

$$\alpha = \frac{H}{H_u} , \tag{2.24}$$

where H is the heat evolved from time $t = 0$ to time t, H_u is the total (ultimate) heat of reaction of the resin. Alternatively, it may be expressed as [78]:

$$\alpha = 1 - \frac{H_r}{H_u} \ , \tag{2.25}$$

where H_r is the residual and/or remaining heat of reaction.

In order to model the cure (in the case of thermosetting systems) or crystallization (in the case of semi-crystalline thermoplastic systems) of composite laminates, the energy conservation principle must be considered. Following previous works presented by Springer and co-workers [49,2,79], Zhao *et al.* [80] modelled the through-the-thickness heat transfer in cylindrical wound composites by neglecting convection heat and thus applying the one-dimensional heat conduction equation in the form:

$$\rho C \frac{\partial T}{\partial t} = \frac{1}{r}\frac{\partial}{\partial r}\left(k_r \frac{\partial T}{\partial r} \right) + \rho \dot{Q} \ , \tag{2.26}$$

where $\frac{\partial T}{\partial t}$ and $\frac{\partial T}{\partial r}$ are the thermal gradients in time and space, respectively, r is the radial coordinate, ρ is the density of the composite, C is the specific heat of the composite, k_r is the thermal conductivity of the composite in the radial direction and $\dot{Q}$ is the heat generation rate.

For thermosetting resins, the heat generation term was typically described as a function of the rate of cure, $\frac{d\alpha}{dt}$, accordingly to the following relation [34]:

$$\rho \dot{Q} = \rho^m V_m \left(\frac{d\alpha}{dt} \right) H_u \ , \tag{2.27}$$

where ρ^m and V_m are the density and volume fraction of the matrix, respectively, H_u, is the total heat of reaction. Alternatively, this term has also been described as [81]:

$$\rho \dot{Q} = \rho^m \in \left(\frac{d\alpha}{dt} \right) H_u \ , \tag{2.28}$$

where $\in$ is the porosity of the fibre bed. From equations (2.27) and (2.28) it is clear that the porosity of the fibre bed is intimately related with the matrix volume fraction within the laminate.

Shin and Hahn [20] simulated the heat transfer and compaction along a bleeder-composite laminate assembly processed in autoclave. They used the cure kinetics model of Lee *et al.* [82] for the Hercules® 3501-6 epoxy resin. Their results showed that using variable resin properties instead of constant ones, better predictions of through-the-thickness temperature distribution were achieved. Namely, the resin density, ρ^m, specific heat, C^m, and thermal conductivity, k^m, during its curing process were calculated through the following equations [83]:

$$\rho^m = \begin{cases} 0.09\alpha + 1.232 & \alpha \le 0.45 \\ 1.272 & \alpha > 0.45 \end{cases} , \tag{2.29}$$

$$C^m = 4.184\left(0.468 + 5.975\times10^{-4}T - 0.141\alpha\right) , \tag{2.30}$$

$$k^m = 0.04184\left(3.85 + \left(0.035T - 0.41\right)\alpha\right) , \tag{2.31}$$

where T is the temperature and α is the degree of cure.

For thermoplastic resins, Lee and Springer [84] utilized the same heat conduction equation and associated $\dot{Q}$ to the rate at which heat was released or absorbed by the composite during heating and cooling, thus expressing the heat generation term as:

$$\rho\dot{Q} = \rho^m V_m \left(\frac{dc}{dt}\right) H_u , \tag{2.32}$$

where dc/dt is the rate of change of crystallinity, conceptually identical to the curing rate in thermosetting resins.

Several semi-empirical analytical models were established and presented for the isothermal curing process of epoxy resin systems in the last decades. Most of the models were devised from curve-fitting of experimental differential scanning calorimetry (DSC) tests.

Early studies conducted by Horie *et al.* [85] suggested an autocatalytic four-parameter model describing rate of cure for an isothermal curing reaction without consideration of diffusion control as follows:

$$\frac{d\alpha}{dt} = (k_1 + k_2\alpha^m)(1-\alpha)^n , \tag{2.33}$$

where $\frac{d\alpha}{dt}$ is the curing rate, k_1 and k_2 are the rate constants, m and n are the orders of cure reaction. m and n are related, respectively, to the initiation and propagation of the cure reaction [86]. Later, Chern and Poehlein [87] modified this autocatalytic four-parameter model in order to account for the effect of the diffusion, by including a diffusion factor as follows:

$$\frac{d\alpha}{dt} = \frac{1}{1 + e^{(C(\alpha - \alpha_c))}}(k_1 + k_2\alpha^m)(1-\alpha)^n , \tag{2.34}$$

where C and α_c are temperature-dependent empirical constants. These constants were experimentally determined for different temperatures through nonlinear least squares curve fitting of the $\alpha(t)$ curve. The denominator of the expression takes into account the slowing down of the reaction at high degrees of cure due to the onset of diffusion control at a temperature-dependent critical degree of cure, α_C. Cole *et al.* [88] proposed a similar modelling approach to account for the shift from kinetics to diffusion control in the curing process, developing the following relation:

$$\frac{d\alpha}{dt} = \frac{1}{1+e^{(C(\alpha-\alpha_C))}} K\alpha^m (1-\alpha)^n \ , \tag{2.35}$$

$$K = Ae^{\frac{-\Delta E}{RT}} \ . \tag{2.36}$$

During the curing process of thermosetting resins, the glass transition temperature, T_g, of the system gradually increases. When the isothermal cure reaction reaches a certain stage, the T_g of the system changes from below the cure reaction to equal or above the cure temperature, and vitrification (glassy state) occurs. At this stage, the mobility of the system decreases dramatically. Therefore, the rate of the curing reaction undergoes a significant decrease and falls below the kinetic rate as the curing reaction becomes diffusion controlled [89]. Accordingly, the degree of curing increases very little in the glassy state.

Sourour and Kamal [90] presented a mechanistic model for the early stages of cure of an epoxy-diamine resin system. However, it was clearly not valid for the later stages of cure. Lee *et al.* [82] studied the epoxy resin Hercules® 3501-6 and, based on that model, proposed a piece-wise relationship between the rate of cure, $\frac{d\alpha}{dt}$, and the degree of cure, α, as follows:

$$\begin{aligned} &\frac{d\alpha}{dt} = (K_1 + K_2\alpha)(1-\alpha)(B-\alpha) && \alpha \le 0.3 \\ &\frac{d\alpha}{dt} = K_3(1-\alpha) && \alpha > 0.3 \end{aligned} \ , \tag{2.37}$$

$$K_i = A_i e^{\frac{-\Delta E_i}{RT}} \qquad i = 1,2,3 \ , \tag{2.38}$$

where A_i are the pre-exponential constants, ΔE_i is the activation energy, B is a constant, R is the universal gas constant and T is the absolute temperature.

Ng *et al.* [91] tested two resin systems, 8552 and 977-3 HM® epoxies, and found the following equation describing the kinetic behaviour of both:

$$\frac{d\alpha}{dt} = K_1\alpha^3 - K_2\alpha^2 + K_3\alpha + K_4\alpha \ , \tag{2.39}$$

$$K_i = A_i e^{\frac{-\Delta E_i}{RT}} \qquad i = 1,2,3,4 \ . \tag{2.40}$$

Banerjee *et al.* [24] and Zhao *et al.* [80] used an isothermal analytical model of HBRF 55-A epoxy resin, firstly developed by Pearce and Mijovic [92], in order to model the process of FW. The equation was as follows:

$$\frac{d\alpha}{dt} = (K_1 + K_2\alpha^a)(B-\alpha)^b(1-\alpha)^c \quad , \tag{2.41}$$

$$K_i = A_i e^{\frac{E_i}{RT}} \qquad i = 1{,}2 \quad , \tag{2.42}$$

where a, b and c are the orders of cure. The other kinetic parameters are as defined previously.

In dynamic curing processes, the cure temperature is typically higher than T_g of the curing system during most or all the curing stage. In such cases, glassy state doesn’t occur, diffusion control is negligible and the analytical models may not include diffusion factor. The relationship between the rate of cure, $\frac{d\alpha}{dt}$, and the degree of cure, α, can be described in different forms, such as [86,89]:

$$\frac{d\alpha}{dt} = K(1-\alpha)^n \quad , \tag{2.43}$$

$$\frac{d\alpha}{dt} = K\alpha^m(1-\alpha)^n \quad , \tag{2.44}$$

$$K = Ae^{\frac{E}{RT}} \quad . \tag{2.45}$$

Ersoy *et al.* [78,93] proposed a phenomenological model for the kinetics of Hexcel® 8552 resin within a AS4/8552 carbon/epoxy prepreg. In their study, they replicated the manufacturer’s recommended cure cycle (MRCC) for the resin and determined the evolution of the degree of cure under such cycle. Also, the gel point was defined as the point until when the composite prepreg was able to withstand in-plane shear stresses. The vitrification point was considered as when the instantaneous glass transition temperature reached the process temperature. In Figure 12 these results and definitions are clearly summarized.

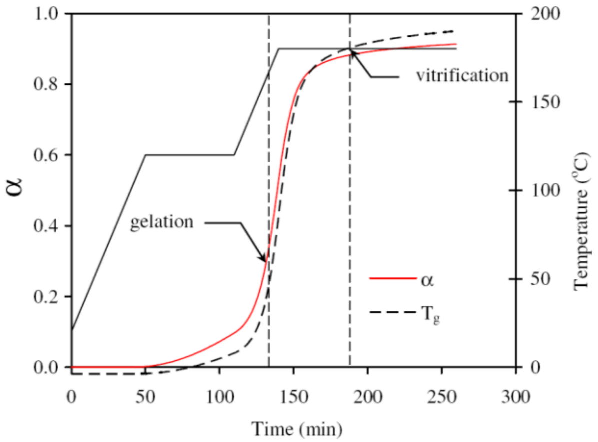

Figure 12 – Development of the degree of cure and the glass transition temperature in a AS4/8552 prepreg laminate during the MRCC [78,93].

Yousefi *et al.* [94] presented a review of kinetic studies conducted on thermosetting resin systems.

Within the composites research field, the cure kinetics of thermosetting resins has been far more studied than the crystallization process of thermoplastic resins. Few studies and models were, however, established for the thermoplastic-based composites.

Mantell and Springer [95] presented a general model for manufacturing processes of thermoplastic composites. They used a crystallinity function proposed by Maffezzoli *et al.* [96] for the modelling of APC-2/AS4 resin during the heating stage, expressed as:

$$\frac{dc}{dt} = -c_{in}\frac{dX_f}{dt} \ , \tag{2.46}$$

$$\frac{dX_f}{dt} = K\left(1 - X_f\right)^n \ , \tag{2.47}$$

$$X_f = \frac{\left(c_{in} - c\right)}{c_{in}} \ , \tag{2.48}$$

$$K = A_0 e^{\left(\frac{E_a}{RT}\right)} \ , \tag{2.49}$$

where $\frac{dc}{dt}$ is the rate of change of crystallinity, c_{in} and c are the crystallinity at initial and “current” stages, respectively, A_0 is a pre-exponential constant, E_a is the activation energy, R is the universal gas constant and T is the absolute temperature. To describe the evolution of the crystallinity of APC-2/AS4 resin during the cooling stage they applied two models, one developed by Lee and Springer [84] which was formulated as:

$$\frac{dc}{dt} = \frac{H_t}{H_u}\frac{dc_r}{dt} \ , \tag{2.50}$$

$$\frac{H_t}{H_u} = A_1 \ln\left(\frac{dT}{dt}\right) + A_2 \ , \tag{2.51}$$

$$\frac{dc_r}{dt} = -\left(1 - c_r\right)\frac{\frac{d\phi}{dT}}{\left(\frac{dT}{dt}\right)^{n-1}} \ , \tag{2.52}$$

$$\phi = e^{\left(A_3 T + A_4\right)} \ , \tag{2.53}$$

and the other developed by Seferis and Velisaris [97,98] with the following relations:

$$\frac{dc}{dt} = c_\infty \frac{d}{dt}\left(W_1 F_{VC1} + W_2 F_{VC2}\right) \ , \tag{2.54}$$

$$W_1 + W_2 = 1 \ , \tag{2.55}$$

$$F_{VCi} = 1 - \exp\left[-C_{1i}\int_0^{t_i} T e^{-\left[\frac{C_{2i}}{T - T_g + 51{,}6} + \frac{C_{3i}}{T\left(T_{mi} - T\right)^2}\right]} n_i t_i^{\left(n_i - 1\right)} dt_i\right] \quad i = 1{,}2 \ , \tag{2.56}$$

where c_r is the relative crystallinity, c_∞ is the equilibrium volume fraction crystallinity, A_i, C_i, n_i and t_i are constants, H_t is the heat evolved until "current" time t, H_u is the theoretical ultimate heat of crystallinity. The quantities T and T_g are the absolute and the glass-transition temperatures, respectively, $\frac{dT}{dt}$ is the cooling rate.

The rigorous way to include crystallization in a heat transfer model would be to solve simultaneously a kinetic equation for crystallization (similarly to equations (2.50)-(2.53)) and the energy equation for temperature (equation (2.26)). Hwang and Tucker III [99], however, modelled the crystallization during cooling of carbon/PEEK laminates through a simpler method by replacing the actual specific heat, C^m, of the matrix with an effective value, C_{eff}, given by:

$$C_{eff} = C^m + H_u \frac{\partial c/\partial t}{\partial T/\partial t} \quad , \tag{2.57}$$

If the crystallization rate, $\frac{dc}{dt}$, was known exactly, this method would be exact. Since the crystallization rate for each material point in the composite laminate is hardly assessed, this method was only approximate.

Within the scope of composites process modelling, the main purpose of the studies on the kinetics and rheology of the matrix systems is to assess their viscosities, since this is a governing parameter for the flow and the mechanical properties of the laminate during its consolidation. Resin (matrix) viscosity, μ, has been described as a function of temperature and degree of curing/crystallization by several authors [24,80,82,84,91,95,100-102]. In thermoplastic resin systems, as the temperature increases, the viscosity decreases. Although different behaviours are observed in different types of thermoplastic, this qualitative relationship is always applicable. On the other hand, in thermosetting resin systems, the viscosity shows an additional dependency on the extension of the curing reaction, which makes their viscosity models more complex and sensitive.

An analytical model for the viscosity of Hercules® 3501-6 was developed by Lee *et al.* [82] and expressed as:

$$\mu = \mu_\infty e^{\frac{U}{RT} + K\alpha} \quad , \tag{2.58}$$

where μ_∞ is a constant, U is the activation energy, K is a constant independent of temperature, T, and R is the universal gas constant. At degrees of cure higher than 0.5 ($\alpha > 0.5$), equation (2.58) wasn't applicable due to gelation of the resin.

The applicability of the analytical model for 8552 and 977-3 HM® resins presented by Ng *et al.* [91] was also limited to the middle stage of the curing reaction. It took the following form:

$$\mu = \mu_\infty e^{\frac{U}{RT} + K_1\alpha^2 + K_2\alpha} \quad . \tag{2.59}$$

In order to model the viscosity of thermosetting resins in the FW process Zhao *et al.* [80] used an equation developed by Macosko [100] for resins typically used in another manufacturing process. They utilized, thus, the following expression:

$$\mu = \mu_{\infty} e^{\frac{U}{RT}} \left(\frac{\alpha_{gel}}{\alpha_{gel} - \alpha} \right)^{(a+b\alpha)} , \tag{2.60}$$

where the constants μ_{∞}, U, a and b were obtained by curve fitting to the experimental resin viscosity data, α_{gel} is the degree of cure at which gelation point occurs. In this model the resin viscosity at the beginning of gelation is captured by the $\left(\frac{\alpha_{gel}}{\alpha_{gel} - \alpha} \right)^{(a+b\alpha)}$ term. The effect of temperature is dual in this model: an increase of the temperature lowers the viscosity of the resin but simultaneously promotes the cure reaction and therefore increases the viscosity.

Although Banerjee *et al.* [24] also used HBRF-55A resin in their studies, the analytical model utilized for the viscosity was different than the one used by Zhao *et al.* [80]. In fact they found the previous model of Lee *et al.* [82] to reasonably fit this specific resin system, with the following expression:

$$\mu = \mu_{\infty} e^{\frac{U}{RT} + K\alpha} \qquad \alpha < \alpha_{gel} , \tag{2.61}$$

where α_{gel} is the degree of cure at which resin gels.

Most of the isothermal models presented above are not able to reasonably predict rheological behaviour during initial reaction and heating stages nor after resin gelation.

The classical concept of thermoplastic polymer crystallization involves two independent phenomena: nucleation and growth of the crystalline forms. The crystallization kinetics has been defined by several methods and models, depending on the regime (isothermal or non-isothermal), [103,104] but the most frequently used expression is the Avrami equation, that can be expressed as [105]:

$$X_f = 1 - e^{\left(-k(T)t^n\right)} , \tag{2.62}$$

where $k(T)$ is a rate constant and n is the Avrami exponent. In highly filled systems (as is the case of fibre reinforced thermoplastic polymers) the original three-dimensional geometry of the polymer spherulites can be changed to two- or one-dimensional entities and a lower growth order leads to lower value for the exponent n. These effects influence the validity of the simple form of the Avrami equation.

The spherulite growth rate and the nucleous density data obtained by light microscopy were used to model the rheological results of thermoplastics at a given temperature. Under the assumption that the density remained constant during crystallization of filled thermoplastic composites, van Ruth *et al.* [101] utilized the Krieger-Dougherty model to determine the viscosity of the laminate (matrix filled with short fibres/inclusions). This model was expressed as:

$$\mu = \mu_s \left(1 - \frac{\varphi}{\varphi_m}\right)^{-[\mu]\varphi_m} , \tag{2.63}$$

where μ_s is the viscosity of the suspending medium (inclusions), φ is the filler content, φ_m is the maximum fully packed filler content and $[\mu]$ is the intrinsic viscosity. The parameters φ_m and $[\mu]$ were found to be strongly dependent on the particle shape.

Fits for two crystallization temperatures of isotactic polypropylene (iPP), at 132ºC and 137ºC, are shown in Figure 13. The agreement between microscopy modelled and experimental rheological results were very good [102].

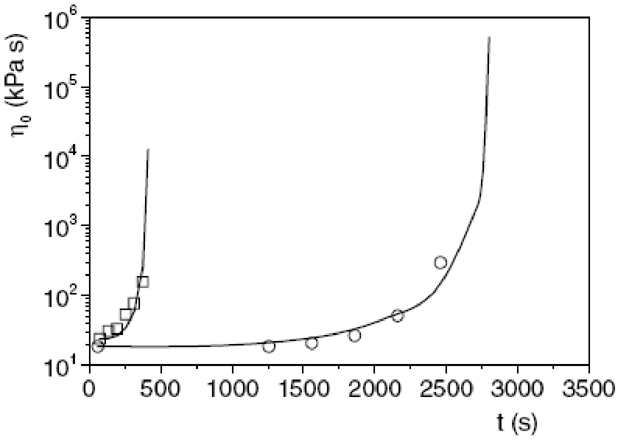

Figure 13 - Time evolution of Newtonian viscosity during crystallization at (□)132ºC and (O)137ºC [102].

These modelling approaches and results, although having been made under pressurized forced flow of polypropylene, may be useful when considering the shear effect between the fibres and the surrounding matrix polymer in the FW process.

In order to model the viscosity of PEEK matrix, Mantell and Springer [95] used the equation previously proposed by Lee and Springer [84] as follows:

$$\mu_m = K e^{\frac{A}{T}} , \tag{2.64}$$

where T is the temperature and the constants K and A were determined by curve fitting. The viscosity of the APC-2/AS4® prepreg laminate was provided by the manufacturer and presented a similar form, though referring to the laminate's viscosity and not only to the matrix viscosity.

Banerjee *et al.* [24] included in their fibre motion model, reviewed in section 2.2.2, a specific feature for the analysis of the effect of resin mixing between adjacent layers. During the FW process uncured resin from previously wound layers can flow into the newly wound layer and the effective viscosity can be calculated by a rule of mixtures. In the *m*th layer, the viscosity, μ, was calculated by the following linear combination:

$$\mu = \sum_{j=1}^{m} \Psi_j^m \, \mu_j \ , \tag{2.65}$$

where μ_j are the viscosities of the constituents (from all contributing layers) and Ψ_j^m is the relative concentration of the different constituents in the *m*th layer, given by:

$$\Psi_j^m = \frac{V_r^j}{V_r^m} \ , \tag{2.66}$$

where V_r^j is the volume of resin from the *j*th layer into the *m*th layer and V_r^m is the total volume of resin in the *m*th layer. In this mixing formulation the phenomenon was viewed as being sequential but some authors cite both sequential and parallel mixing rules as being acceptable.

In trying to globally summarize the specificities and differences between the kinetic behaviours of thermosetting and thermoplastic systems one may attend to the fact that for thermosettings the viscosity of the resin depends on temperature and polymer reactivity, but in the case of thermoplastic matrices the latter contribution can be neglected.

2.2.5. Stress-Strain

The problem of determining the stress (and/or strain) field within a fibre bundle under processing conditions consists in analysing its response, both elastic and viscous, to the solicitations due to the process mechanics. Figure 14 sketches a volume element of aligned lubricated fibres and the various components of the total stress tensor.

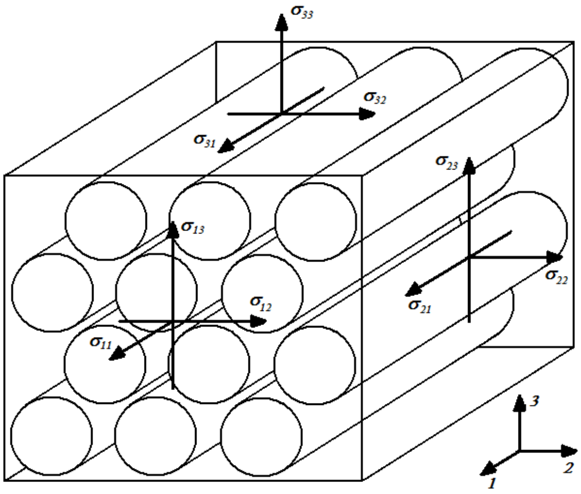

Figure 14 – Stress components applied to a fibre bundle element.

Following the consensual assumption that the externally applied stress is borne by both the fibres and the matrix, Cai and Gutowski [16,27] proposed a generalized three-dimensional description of equation (2.4) in the form:

$$\sigma_{ij} = p_{f\,ij} + p_r \delta_{ij} \ , \tag{2.67}$$

where σ_{ij} are the components of the total applied stress, $p_{f\,ij}$ are the stresses carried by the fibres, p_r is the resin pressure and δ_{ij} is the Kronecker delta ($\delta_{ij} = 1$ for $i = j$ and $\delta_{ij} = 0$ for $i \neq j$). In this model, the shear stresses were assumed to be completely carried by the fibre bundle. This was only valid for low viscosity matrices, which might be consistent with the early stages of the curing/consolidation process.

The validity of micromechanical models for the prediction of composite constitutive properties have been discussed [106]. Namely, their intrinsic assumption that the fibres are dispersed evenly in the matrix and that they are perfectly aligned along the fibre direction was criticized.

The shear stresses and strains that are present in a composite laminate have different effects in its behaviour. At the on-axis local level, the longitudinal shear mode allows aligned fibres to accommodate the complex curvature of the real parts while the transverse shear mode is often unwanted as it can lead to fibre waviness [27].

Even observations on virgin prepregs showed that the fibres have an initial waviness that may be exacerbated by forcing them to conform to the moulding tools or to the fibre bed beneath. Gutowski *et al.* [34], based upon experimental measurements, suggested that fibres do, in fact, have a slight waviness of sinusoidal character. Figure 15 schematically depicts an hypothetical waved configuration and straightening behaviour of a single fibre within the fibre bundle, with characteristic amplitude, a, and length, L. The scalar quantity a/L was defined by several authors as the waviness ratio (if a regular and periodic characteristic is considered) or marcel (if only localized "defects" are considered). Marcel has been defined as fabrication induced defects in composite materials [107]. Terms like "fibre waviness", "fibre wrinkles" or "fibre imperfections" have also been used to refer to these manufacturing defects. They have been observed to occur on, or through the thickness of, the plane of lamination [108].

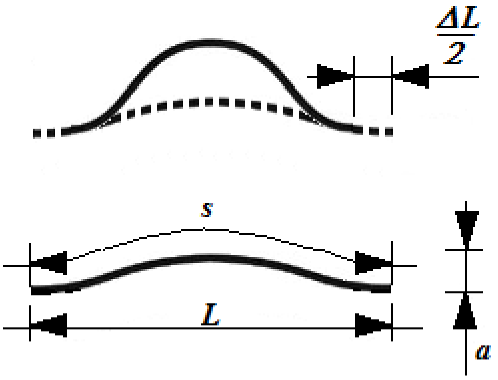

Figure 15 – Straightening of a single fibre.

Moreover, fibre waviness is a type of manufacturing defect that occurs especially during the FW process [109] given the specific constraints applied to the fibre bundles being wound and overwrapped by newly wound layers.

Also, fibres are grouped in tows within the laminate where the fibre fraction is higher. Furthermore, fibre waviness and intermingling may result in higher shear moduli. Nevertheless, the properties predicted by micromechanics are typically close to the experimental values where available, and so if the micromechanical analysis is carried out with appropriate boundary conditions and constituent properties, the validity of those assumptions may be assured.

2.2.5.1. Stress-Strain Constitutive Relations

The constitutive behaviour of a composite lamina at the meso- and macro-scale has been established by several authors in a unique form for every material point within the physical domain of the lamina. For engineering purposes, this has been a consensual approach and is based on the assumption that the composite material can be modelled as a homogeneous material from the properties of its constituents. In some cases, however, authors neglected the contribution of one of the constituents (typically the matrix) in their models.

In this section, the most relevant approaches and steps towards the establishment of valid stress-strain constitutive relations are reviewed. Most of the constitutive models described hereafter were developed for consolidated laminates rather than for laminates under consolidation.

Hofeditz [110] presented design methods for fibrous glass filament-wound pressure vessels, in which both the netting and orthotropic analyses were discussed. In the netting analysis theory, the resin was assumed to have no load carrying ability (simply holding the fibres in position) and the stress in each fibre was assumed to be equal and constant along its length. The basics of this modelling approach is outlined in Figure 16 and the following set of equations:

$$\begin{aligned} \sigma_{axial} &= p_f \cos^2\phi \ , \\ \sigma_{hoop} &= p_f \sin^2\phi \ , \\ \frac{\sigma_{hoop}}{\sigma_{axial}} &= \tan^2\phi \ , \end{aligned} \tag{2.68}$$

where p_f is the stress carried by the fibres, σ_{axial} and σ_{hoop} are the fibre's stress components in the axial and hoop directions, respectively, and ϕ is the winding angle.

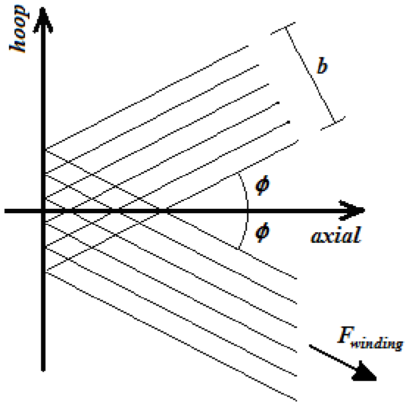

Figure 16 - Geometrical scheme for the netting analysis.

In the orthotropic analysis theory, for tensile stress applied in the longitudinal and transversal directions of the fibres, it was assumed that fibres and matrix undergone the same strain in the longitudinal direction and the same stress in the transversal one. In other words, the fibres and matrix behaved as springs in parallel, when stressed in the fibre's longitudinal direction, and as springs in series, when stressed in the fibre's transversal direction or when subjected to shear stresses.

Jones [111], Tsai [112] and Vinson and Sierakowski [113] applied the generalized Hooke's law to composite anisotropic materials (no planes of symmetry for the material properties) establishing the following stress-strain constitutive relations, in the on-axis $(1,2,3)$ principal material directions:

$$\begin{Bmatrix}\sigma_{11}\\\sigma_{22}\\\sigma_{33}\\\tau_{23}\\\tau_{31}\\\tau_{12}\end{Bmatrix}=\begin{bmatrix}C_{11}&C_{12}&C_{13}&C_{14}&C_{15}&C_{16}\\C_{12}&C_{22}&C_{23}&C_{24}&C_{25}&C_{26}\\C_{13}&C_{23}&C_{33}&C_{34}&C_{35}&C_{36}\\C_{14}&C_{24}&C_{34}&C_{44}&C_{45}&C_{46}\\C_{15}&C_{25}&C_{35}&C_{45}&C_{55}&C_{56}\\C_{16}&C_{26}&C_{36}&C_{46}&C_{56}&C_{66}\end{bmatrix}\begin{Bmatrix}\varepsilon_{11}\\\varepsilon_{22}\\\varepsilon_{33}\\\gamma_{23}\\\gamma_{31}\\\gamma_{12}\end{Bmatrix}, \tag{2.69}$$

where σ_{ii} and τ_{ij} are the normal and shear stresses, ε_{ii} and γ_{ij} are normal and engineering shear strains. C_{ij} are the components of the stiffness matrix, $[C]$. The stiffness matrix $[C]$ is symmetric and so, only 21 of the constants are independent.

For the cases in which the material presented planes of symmetry in its properties, it was demonstrated that this relation would simplify. Particularly, if two orthogonal planes of material property symmetry exist for a given material, symmetry will exist relatively to a third mutually orthogonal plane. In such case, the material is said orthotropic and the stress-strain constitutive relations in the on-axis $(1,2,3)$ principal material directions are given by [111-113]:

$$\begin{Bmatrix}\sigma_{11}\\\sigma_{22}\\\sigma_{33}\\\tau_{23}\\\tau_{31}\\\tau_{12}\end{Bmatrix}=\begin{bmatrix}C_{11}&C_{12}&C_{13}&0&0&0\\C_{12}&C_{22}&C_{23}&0&0&0\\C_{13}&C_{23}&C_{33}&0&0&0\\0&0&0&C_{44}&0&0\\0&0&0&0&C_{55}&0\\0&0&0&0&0&C_{66}\end{bmatrix}\begin{Bmatrix}\varepsilon_{11}\\\varepsilon_{22}\\\varepsilon_{33}\\\gamma_{23}\\\gamma_{31}\\\gamma_{12}\end{Bmatrix}. \tag{2.70}$$

In this case, there are no interactions between normal stresses σ_{ii} and shear strains γ_{ij} as well as between shear stresses τ_{ij} and normal strains ε_{ii}. The stiffness matrix contains only 9 independent constants.

The nonzero components, C_{ij}, of this local stiffness matrix for orthotropic materials were determined and expressed as a function of the material engineering constants. The following expressions were achieved for their determination [112,113]:

$$
\begin{gathered}
C_{11} = E_{11}\left(1-\nu_{23}\nu_{32}\right)/\Delta \quad , \\
C_{22} = E_{22}\left(1-\nu_{31}\nu_{13}\right)/\Delta \quad , \\
C_{33} = E_{33}\left(1-\nu_{12}\nu_{21}\right)/\Delta \quad , \\
C_{44} = G_{23} \quad , \\
C_{55} = G_{13} \quad , \\
C_{66} = G_{12} \quad , \\
C_{12} = E_{11}\left(\nu_{21}+\nu_{31}\nu_{23}\right)/\Delta = E_{22}\left(\nu_{12}+\nu_{32}\nu_{13}\right)/\Delta \quad , \\
C_{13} = E_{11}\left(\nu_{31}+\nu_{21}\nu_{32}\right)/\Delta = E_{33}\left(\nu_{13}+\nu_{12}\nu_{23}\right)/\Delta \quad , \\
C_{23} = E_{22}\left(\nu_{32}+\nu_{12}\nu_{31}\right)/\Delta = E_{33}\left(\nu_{23}+\nu_{21}\nu_{13}\right)/\Delta \quad , \\
\\
\Delta = 1-\nu_{12}\nu_{21}-\nu_{23}\nu_{32}-\nu_{13}\nu_{31}-2\nu_{21}\nu_{32}\nu_{13} \ ,
\end{gathered}
\tag{2.71}
$$

where E_{ii} are the Young moduli in the three principal local material axis, ν_{ij} are Poisson’s ratios and G_{ij} are the shear moduli.

If a plane where the material properties are equal in all directions exists, the material is said transversely isotropic. Assuming, for convenience, that the $2-3$ plane is the plane of such isotropy, Jones [111] simplified the constitutive relations to:

$$
\begin{Bmatrix} \sigma_{11} \\ \sigma_{22} \\ \sigma_{33} \\ \tau_{23} \\ \tau_{31} \\ \tau_{12} \end{Bmatrix} =
\begin{bmatrix}
C_{11} & C_{12} & C_{12} & 0 & 0 & 0 \\
C_{12} & C_{22} & C_{23} & 0 & 0 & 0 \\
C_{12} & C_{23} & C_{22} & 0 & 0 & 0 \\
0 & 0 & 0 & \left(C_{22}-C_{23}\right)/2 & 0 & 0 \\
0 & 0 & 0 & 0 & C_{55} & 0 \\
0 & 0 & 0 & 0 & 0 & C_{55}
\end{bmatrix}
\begin{Bmatrix} \varepsilon_{11} \\ \varepsilon_{22} \\ \varepsilon_{33} \\ \gamma_{23} \\ \gamma_{31} \\ \gamma_{12} \end{Bmatrix} ,
\tag{2.72}
$$

and only 5 independent constants are thus considered. In this case, the 2 and 3 subscripts in the stiffness coefficients are interchangeable and their calculation through equations (2.71) is simplified.

Lee and Springer [23] applied the stress-strain constitutive relations presented by Jones [111] in a off-axis cylindrical coordinate system (Figure 17) to model the *j*th layer of a transversely isotropic cylindrical composite laminate (typical in FW), as:

$$
\begin{Bmatrix} \sigma^j_{zz} \\ \sigma^j_{\theta\theta} \\ \sigma^j_{rr} \\ \tau^j_{r\theta} \\ \tau^j_{rz} \\ \tau^j_{z\theta} \end{Bmatrix} =
\begin{bmatrix}
\overline{C}_{11} & \overline{C}_{12} & \overline{C}_{13} & 0 & 0 & \overline{C}_{16} \\
\overline{C}_{12} & \overline{C}_{22} & \overline{C}_{23} & 0 & 0 & \overline{C}_{26} \\
\overline{C}_{13} & \overline{C}_{23} & \overline{C}_{33} & 0 & 0 & \overline{C}_{36} \\
0 & 0 & 0 & \overline{C}_{44} & \overline{C}_{45} & 0 \\
0 & 0 & 0 & \overline{C}_{45} & \overline{C}_{55} & 0 \\
\overline{C}_{16} & \overline{C}_{26} & \overline{C}_{36} & 0 & 0 & \overline{C}_{66}
\end{bmatrix}
\begin{Bmatrix} \varepsilon^j_{zz} \\ \varepsilon^j_{\theta\theta} \\ \varepsilon^j_{rr} \\ \gamma^j_{r\theta} \\ \gamma^j_{rz} \\ \gamma^j_{z\theta} \end{Bmatrix} ,
\tag{2.73}
$$

where σ^j_{rr}, $\sigma^j_{\theta\theta}$, σ^j_{zz} are the radial, circumferential and axial normal stresses in the *j*th layer, $\tau^j_{r\theta}$, τ^j_{rz}, $\tau^j_{z\theta}$ are the shear stresses in the *j*th layer, ε^j_{rr}, $\varepsilon^j_{\theta\theta}$, ε^j_{zz} are the radial, circumferential and axial normal strains in the *j*th layer, $\gamma^j_{r\theta}$, γ^j_{rz}, $\gamma^j_{z\theta}$ are the engineering shear strains in the *j*th layer and $\overline{C}_{ij}$ are the components of the off-axis

(z, θ, r) stiffness matrix for the *j*th layer. $\overline{C}_{ij}$ are calculated from C_{ij} using the proper $(1, 2, 3)$-(z, θ, r) transformation.

Assuming transverse isotropy in the $2-3$ plane, Cai and Gutowski [27] developed a local stress-strain constitutive relationship for a lubricated fibre bundle where only two material directions are considered, the longitudinal (parallel to the fibres) and the bulk (any direction in the $2-3$ plane). Their empirical formulation was developed under the main assumptions that

- the aligned fibre bundles behaved as nonlinear elastic, porous networks with no shear strength in the $2-3$ plane,
- the fibres had a slight waviness of sinusoidal character and made multiple contacts between them,
- the relevant quantities appearing in the $2-3$ plane could be reduced to one single transverse equivalent quantity Y (denoted by Y_b where the subscript b referred to "bulk"),
- the fibres were lubricated but in drained state,

and allowed to include directly the fibre volume fraction, V_f, in the constitutive matrix. It can be expressed as [27]:

$$\begin{Bmatrix} \varepsilon_1^b \\ \varepsilon_b^b \end{Bmatrix} = \begin{bmatrix} \dfrac{4}{\pi}\dfrac{1}{E^f}\dfrac{V_a}{V_f}\left[\left(1+2\left(\sqrt{\dfrac{V_a}{V_f}}-1\right)\right)^2 - \dfrac{\left[1+2\left(\sqrt{\dfrac{V_a}{V_f}}-1\right)\left(2\sqrt{\dfrac{V_a}{V_f}}-1\right)\left(1-\sqrt{\dfrac{V_f}{V_0}}\right)\left(\sqrt{\dfrac{V_a}{V_f}}-1\right)\right]}{\left(\dfrac{1}{2}-\sqrt{\dfrac{V_f}{V_0}}\right)\left(\sqrt{\dfrac{V_a}{V_f}}-1\right)+\dfrac{3}{2}\sqrt{\dfrac{V_a}{V_f}}\left(1-\sqrt{\dfrac{V_f}{V_0}}\right)} \right] & \dfrac{-\dfrac{16}{\pi^3}\dfrac{L^2}{E^f\,a^2}\sqrt{\dfrac{V_a}{V_f}}\left(\sqrt{\dfrac{V_a}{V_f}}-1\right)^3}{1+\dfrac{\left(1-\sqrt{\dfrac{V_0}{V_f}}\right)\left(4\sqrt{\dfrac{V_a}{V_f}}-1\right)}{\left(\sqrt{\dfrac{V_a}{V_f}}-1\right)}} \\ -\dfrac{16}{\pi^3}\dfrac{L^2}{E^f\,a^2}\sqrt{\dfrac{V_a}{V_f}}\left(\sqrt{\dfrac{V_a}{V_f}}-1\right)^3\left[1-\dfrac{\left(1-\sqrt{\dfrac{V_f}{V_0}}\right)\left(4\sqrt{\dfrac{V_a}{V_f}}-1\right)}{\left(4\sqrt{\dfrac{V_a}{V_f}}-5\sqrt{\dfrac{V_a}{V_0}}+\sqrt{\dfrac{V_f}{V_0}}\right)}\right] & \dfrac{\dfrac{L^4}{3\pi E^f\,a^4}\left(\sqrt{\dfrac{V_a}{V_f}}-1\right)^5}{\sqrt{\dfrac{V_a}{V_f}}\left(5-\sqrt{\dfrac{V_f}{V_a}}-4\sqrt{\dfrac{V_0}{V_f}}\right)} \end{bmatrix} \begin{Bmatrix} \sigma_1^b \\ \sigma_b^b \end{Bmatrix} , \tag{2.74}$$

where ε_1^b, ε_b^b, σ_1^b, σ_b^b are the local (on-axis) strains and stresses in the 1 and b directions, respectively. V_a is the maximum available fibre volume fraction at which the resin flow is not possible, V_0 is the minimum volume fraction of fibres below which fibres do not carry transverse load, $\beta = L/a$ is the ratio between the characteristic length, L, and amplitude, a, of the fibre waviness pattern and E^f is the fibre's flexural modulus. These authors also developed empirical relations to evaluate the layer's elastic properties. Although one may find empirical values for V_a, V_0 and β in the literature, they shall be assessed experimentally for each case since they strongly depend on the material system to consider. These parameters are unique to a particular fibre/sizing [80].

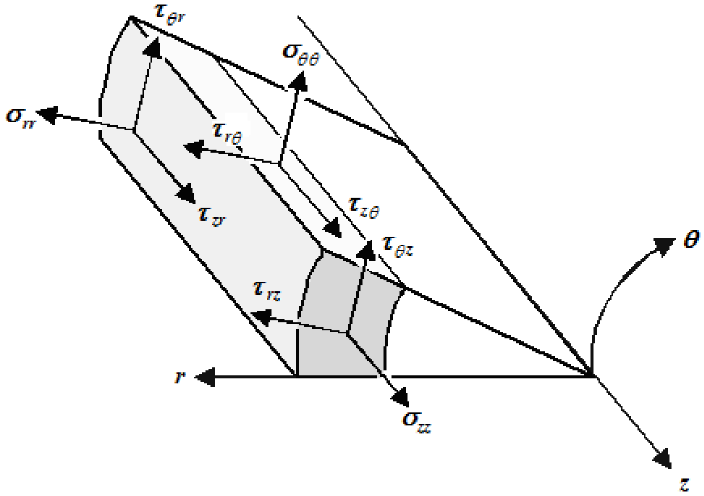

Figure 17 – Stress components in a volume element in cylindrical coordinate system.

Hsiao and Daniel [114], also studied the constitutive behaviour of composite laminates containing fibre waviness. They presented a different approach in which the regular local on-axis compliance matrix, $[S]$, was transformed to follow the fibres waved path. The transformed local compliance matrix, $[S^{wav}]$, was given at each point of the waved path by:

$$[S^{wav}] = [R][T^{wav}]^{-1}[R]^{-1}[S][T^{wav}]^{-T} \;, \tag{2.75}$$

where $[T^{wav}]$ is the waviness transformation matrix for each misalignment angle, θ, at each point of the waved path and $[R]$ is the Reuter matrix (to compatibilize the strain tensorial notation). Note that $[S]$ is the inverse matrix of the stiffness matrix, $[C]$, presented in equations (2.69), (2.70) or (2.72). This method was broadly applicable to materials with any degree of anisotropy, as long as the waved path was known.

In order to account for the effect of the waviness, the components of the constitutive local on-axis compliance matrix of a waved composite were, in fact, assessed from averaging the components of the transformed local compliance matrix, $[S^{wav}]$, over one wavelength of the fibres' path, L, as follows:

$$\tilde{S}_{ij}^{wav} = \frac{1}{L}\int_0^L S_{ij}^{wav}\,dx \;, \tag{2.76}$$

where x is the fibre "ideal" axis.

2.2.5.2. Thermal and Chemical Induced Stresses and Strains

During curing of thermosetting composites the resin undergoes cross-linking reactions that may lead to an increase of material density and reduction in volume. The process of volume reduction, the so-called chemical shrinkage, together with thermal effects can lead to development of high locked-in stresses where there is constraint [115,106]. Several authors studied the effect of these phenomena in the structural behaviour and quality of the consolidated laminates [116-119]. In Figure 18 schematic representations of the cross-linking and volume change are drawn. In this example, an external heating source imposes a curing temperature, thus forcing the composite to go through a certain cure cycle. However, when using thermosetting resins curing at low temperature, similar effects are found.

Due to the isotropic nature of the resins, the contribution of these effects to the stress-strain state of the laminate in each moment is also isotropic.

Johnston *et al.* [120,121] presented a plane strain finite element model for simulation of the development of process-induced deformation during autoclave processing of complex-shaped composite structures. A “cure-hardening, instantaneously linear elastic” constitutive model was employed to represent the mechanical behaviour of the composite matrix (resin), and micromechanical models were used to determine composite ply mechanical properties and behaviour, including thermal expansion and cure-shrinkage.

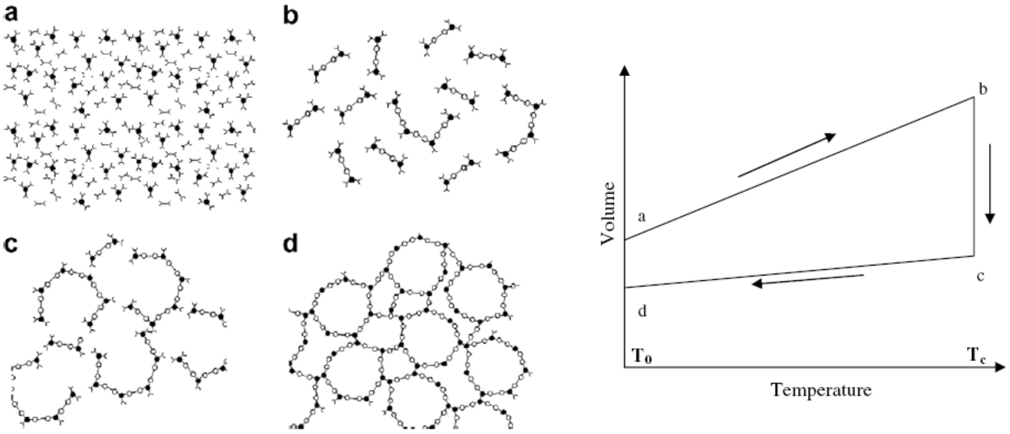

Figure 18 – Schematic representation of cross-linking and volume change phenomena during the curing process of thermosetting resins [122].

In this self consistent field micromechanics (SCFM) method, the elastic constants and strains for unidirectional plies were determined from the mechanical properties of their constituent resin and fibres. A set of equations was established as follows:

$$\begin{gathered}
\varepsilon_{ii}^{th} = \beta_{ii}\Delta T \quad , \\
\varepsilon_{ii}^{ch} = \eta_{ii}\Delta\alpha \quad , \\
\left\{\varepsilon_{ij}^{e}\right\} = \left\{\varepsilon_{ij}^{T}\right\} - \left\{\varepsilon_{ij}^{th}\right\} - \left\{\varepsilon_{ij}^{ch}\right\} \quad , \\
\beta_{11} = \frac{\beta_{11}^{f}E_{11}^{f}V_f + \beta^{r}E^{r}\left(1-V_f\right)}{E_{11}^{f}V_f + E^{r}\left(1-V_f\right)} \quad , \\
\beta_{22} = \beta_{33} = \left(\beta_{22}^{f} + \nu_{13}^{f}\beta_{11}^{f}\right)V_f + \left(\beta^{r} + \nu_{r}\beta^{r}\right)\left(1-V_f\right) - \left[\nu_{13}^{f}V_f + \nu^{r}\left(1-V_f\right)\right]\beta_{11} \quad , \\
\varepsilon_{11} = \frac{\varepsilon_{11}^{f}E_{11}^{f}V_f + \varepsilon^{r}E^{r}\left(1-V_f\right)}{E_{11}^{f}V_f + E^{r}\left(1-V_f\right)} \quad , \\
\varepsilon_{22} = \varepsilon_{33} = \left(\varepsilon_{22}^{f} + \nu_{13}^{f}\varepsilon_{11}^{f}\right)V_f + \left(\varepsilon^{r} + \nu_{r}\varepsilon^{r}\right)\left(1-V_f\right) - \left[\nu_{13}^{f}V_f + \nu^{r}\left(1-V_f\right)\right]\varepsilon_{11} \quad ,
\end{gathered} \tag{2.77}$$

where ε, β and η are strains, thermal expansion coefficient (CTE) and chemical shrinkage coefficient, respectively. Subscripts i and j refer to the local principal material directions and superscripts th, ch, e and T refer to thermal, chemical, elastic-constrained and total, respectively. ΔT and $\Delta\alpha$ are the variations in temperature and degree of cure, respectively. E and ν are the elastic moduli and Poisson's coefficients, V_f is the fibre volume fraction.

Ersoy *et al.* [106] adopted a finite element analysis based micromechanics (FEBM) to predict the composite properties from the constituents properties and to verify if the predictions of SCFM [121] were still valid in the case when the properties of the constituents differ in a few orders of magnitude. Such differences are characteristic of the rubbery stage (previously to vitrification of the resin). Assuming a hexagonal packing arrangement of carbon fibres, they developed finite element models based on the unit cell depicted in Figure 19. The close predictions of the glassy properties (consolidated composite laminate) by both methods demonstrated their validity when the resin is cured and thus in the glassy state. However, for the rubbery properties, out-of-plane Poisson's ratio, ν_{23}, transverse modulus, E_{22}, and out-of-plane modulus, E_{33}, were significantly unpredicted by SCFM. This showed that this method (SCFM) couldn't accurately predict the composite "elastic-apparent" properties when a large difference between the reinforcing and the matrix properties existed, as is the case when the matrix is in a rubbery state (before vitrification). For curing stages previous to resin gelation, the inaccuracy might be even greater.

Several authors have tried to approximate the residual stress state by assuming the stress relaxation to be much quicker than the evolution of chemical shrinkage. Under this assumption incremental linear elastic simulations were performed, by using so called 'equilibrium moduli', i.e. the moduli just after transient relaxation [123]. Process-dependent isotropic linear visco-elastic models were thus assumed. Kim and White [124] approximated the relaxation shear modulus with Prony series, while the Poisson's ratio was assumed to be constant. The influence of ongoing cure was treated like long-term chemical ageing by applying shift factors on the relaxation times. Relaxation measurements were carried out on partially cured specimens ($\alpha \geq 0.57$) at different temperatures.

Lange *et al.* [125] proposed a model for the build-up of cure stresses, in which stresses are generated by the cure shrinkage and decay by viscoelastic relaxation. The relaxation is described by a modified Maxwell model. Again, the Poisson's ratios were assumed constants. It was found that the amount of stress build-up during cure varied greatly between the different resin systems studied. In general, higher crosslink density results in higher stress build-up. However, the model results did not give sufficient improvement compared to their earlier published incremental elastic model [126].

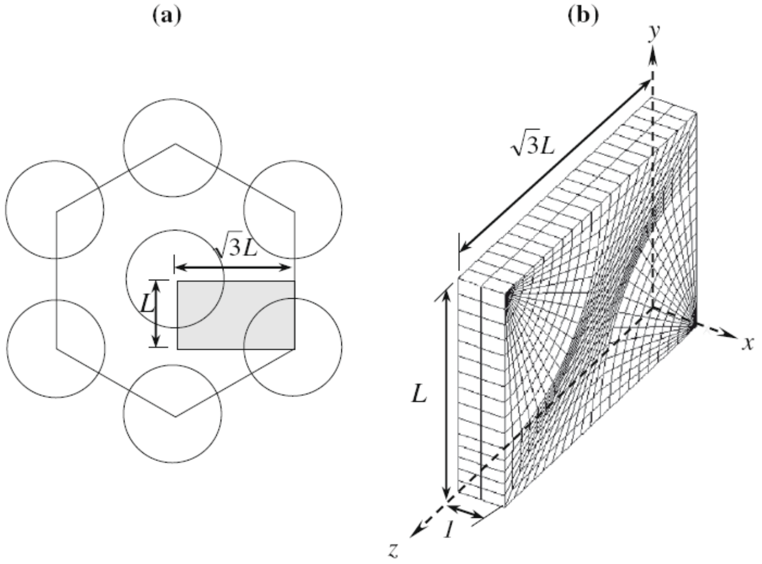

Figure 19 – Unit cell for hexagonal packing of fibres (a) and its meshing (b) [106].

Lee and Springer [23] and Vinson and Sierakowski [113] presented stress-strain constitutive relations in a off-axis cylindrical coordinate system (Figure 17) to model the *j*th layer of transversely isotropic cylindrical composite laminates. In this approach, the authors added to equations (2.73) the strains components due to thermal expansion and chemical shrinkage as follows:

$$\begin{Bmatrix} \sigma_{zz}^{j} \\ \sigma_{\theta\theta}^{j} \\ \sigma_{rr}^{j} \\ \tau_{r\theta}^{j} \\ \tau_{rz}^{j} \\ \tau_{z\theta}^{j} \end{Bmatrix} = \begin{bmatrix} \overline{C}_{11} & \overline{C}_{12} & \overline{C}_{13} & 0 & 0 & \overline{C}_{16} \\ \overline{C}_{12} & \overline{C}_{22} & \overline{C}_{23} & 0 & 0 & \overline{C}_{26} \\ \overline{C}_{13} & \overline{C}_{23} & \overline{C}_{33} & 0 & 0 & \overline{C}_{36} \\ 0 & 0 & 0 & \overline{C}_{44} & \overline{C}_{45} & 0 \\ 0 & 0 & 0 & \overline{C}_{45} & \overline{C}_{55} & 0 \\ \overline{C}_{16} & \overline{C}_{26} & \overline{C}_{36} & 0 & 0 & \overline{C}_{66} \end{bmatrix} \begin{Bmatrix} \varepsilon_{zz}^{j} - \overline{\beta}_{zz}^{j}\Delta T^{j} - \overline{\eta}_{zz}^{j}\Delta\alpha^{j} \\ \varepsilon_{\theta\theta}^{j} - \overline{\beta}_{\theta\theta}^{j}\Delta T^{j} - \overline{\eta}_{\theta\theta}^{j}\Delta\alpha^{j} \\ \varepsilon_{rr}^{j} - \overline{\beta}_{rr}^{j}\Delta T^{j} - \overline{\eta}_{rr}^{j}\Delta\alpha^{j} \\ \gamma_{r\theta}^{j} \\ \gamma_{rz}^{j} \\ \gamma_{z\theta}^{j} - \overline{\beta}_{z\theta}^{j}\Delta T^{j} - \overline{\eta}_{z\theta}^{j}\Delta\alpha^{j} \end{Bmatrix}, \tag{2.78}$$

where $\overline{\beta}_{rr}^{j}$, $\overline{\beta}_{\theta\theta}^{j}$, $\overline{\beta}_{zz}^{j}$ are radial, circumferential and axial thermal expansion coefficients (CTE) for the *j*th layer, $\overline{\beta}_{z\theta}^{j}$ is the thermal expansion coefficient in the $z-\theta$ plane for the *j*th layer, $\overline{\eta}_{rr}^{j}$, $\overline{\eta}_{\theta\theta}^{j}$, $\overline{\eta}_{zz}^{j}$ are the radial, circumferential and axial chemical change ("shrinkage") coefficients for the *j*th layer, $\overline{\eta}_{z\theta}^{j}$ is the chemical change ("shrinkage") coefficient in the $z-\theta$ plane for the *j*th layer. T^{j} is the temperature in the point of interest in the *j*th layer and α^{j} is the degree of cure in the point of interest in the *j*th layer. The variations of some variables with time are denoted with Δ.

Sproewitz *et al.* [127] proposed to consider the chemical change ("shrinkage") as an equivalent thermal matrix expansion, as a useful concept for modelling purposes.

The equivalent CTE, CTE_{eq}, was defined as the sum of thermal and chemical expansion according to the following relation:

$$CTE_{eq} = \beta + \eta = \beta + \frac{\Delta V}{3\Delta T} \ , \tag{2.79}$$

where β is the thermal expansion coefficient, η is the chemical change (“shrinkage”) coefficient, ΔV is the volumetric shrinkage and ΔT is the temperature difference between curing and room temperature. The volumetric isotropic nature of these coefficients suggested that in equation $\bar{\beta}_{rr}^{j} = \bar{\beta}_{\theta\theta}^{j} = \bar{\beta}_{zz}^{j} = \bar{\beta}_{z\theta}^{j}$ and $\bar{\eta}_{rr}^{j} = \bar{\eta}_{\theta\theta}^{j} = \bar{\eta}_{zz}^{j} = \bar{\eta}_{z\theta}^{j}$.

2.2.6. Global Process Models

One- and two-dimensional resin flow/fibre compaction process models have been developed in the last three decades. Most of the studies were not specifically dedicated to the FW process. Nevertheless, their assumptions, modelling strategies and specific features are of great interest in gathering the sense and knowledge to develop this multi-physical process model, since many of the interacting phenomena are common to several of these manufacturing processes. Three-dimensional approaches are much less available in the literature, mainly due to the orthotropic and thin-walled characteristics of most of the composite applications.

In the past, two well-established flow/compaction models were developed and published. They were named the squeezed sponge (sometimes referred as the effective stress model) and sequential compaction models, respectively. Although the sequential and the squeezed sponge (effective stress) models based on different assumptions, they predicted essentially the same results in the regime when the fibre bed carries no load [37]. In the next sections, these two models are reviewed.

2.2.6.1. Sequential Compaction Model

Lee and Springer [23] presented a process model for FW of composite cylinders with thermosetting resin systems. The model related the significant process variables, such as

- the winding speed,
- the initial fibre tension (winding force),
- the winding angle, and
- the applied temperature,

to the thermal, chemical and mechanical behaviour of the composite cylinder and the mandrel. Based on Loos and Springer previous work for flat laminates [49] and Calius and Springer for thin cylinders [79], this study focused on relatively thick cylinders. A user-friendly code (WINDTHICK®) was written and used to calculate

- the temperature in the cylinder and the mandrel,
- the degree of cure and viscosity in the cylinder,
- the viscosity through the cylinder,
- the fibre tensions and positions,
- the stresses and strains throughout the cylinder and in the mandrel, and

- the void diameters in the cylinder.

The model was developed in five parts (sub-models):

- the thermo-chemical sub-model
  - outputs: temperature, degree of cure and viscosity,
- the fibre motion sub-model
  - outputs: radial fibre position,
- the stress-strain sub-model
  - outputs: stresses and strains in composite laminate,
- the void growth sub-model
  - outputs: size of a void at a given location as function of time,
- the strength sub-model
  - outputs: strength of the composite cylinder.

The thermo-chemical sub-model was based on the energy equation for the two-dimensional heat flow, written in the form:

$$\rho C\frac{\partial T}{\partial t}=\frac{1}{r}\frac{\partial}{\partial r}\left(k_r r\frac{\partial T}{\partial r}\right)+\frac{\partial}{\partial z}\left(k_z\frac{\partial T}{\partial z}\right)+\rho\dot{Q}\ , \tag{2.80}$$

where ρ is the density, C is the specific heat of the composite or the mandrel, T is the temperature, t is time, r and z are the radial and axial coordinates, k_r and k_z are the thermal conductivities in the r and z directions and $\dot{Q}$ is the rate at which heat is generated or absorbed by chemical reactions.

Since chemical reactions occurred only in the matrix, i.e., no heat generation or absorption was attributed to the fibres nor to the mandrel, the last term of the energy equation was re-written as:

$$\rho\dot{Q}=\rho^m V_m\dot{Q}^m\ , \tag{2.81}$$

where ρ^m, V_m and $\dot{Q}^m$ are the density, volume fraction and heat generation rate of the matrix, respectively.

Following previous works [49,82] the heating rate was assumed to be a function of the degree of cure (or its rate), and the energy equation, for composites with non-reacting fibres, became:

$$\rho C\frac{\partial T}{\partial t}=\frac{1}{r}\frac{\partial}{\partial r}\left(k_r r\frac{\partial T}{\partial r}\right)+\frac{\partial}{\partial z}\left(k_z\frac{\partial T}{\partial z}\right)+\rho^m V_m H_u\frac{d\alpha}{dt}\ , \tag{2.82}$$

where H_u is the total heat of reaction and $\frac{d\alpha}{dt}$ is the rate of degree of cure.

As discussed in section 2.2.4 several empirical expressions, relating $\frac{d\alpha}{dt}$ to the degree of cure, α, and time, t, were established in the literature for several commercial thermosetting resin systems [49,78,82,85-93,128-131]. Most of these studies also expressed empirically the resin viscosity, μ, as a function of the degree of cure, α, and temperature, T.

The fibre motion sub-model assumed that the fibres orientation angles remained constant during the compaction of the laminate. Motion of fibres in axial and hoop (circumferential) directions was not considered due to the balanced state in which the laminate is in those directions.

The radial velocity of the fibre bundles, $\dot{u}_f$, relative to resin, was computed as:

$$\dot{u}_f = -\frac{S}{\mu}\frac{\sigma_f}{r_f}\sin^2\phi_0 \ , \tag{2.83}$$

where σ_f is the fibre bundle's tension, r_f is the fibre's radial position, ϕ_0 is the initial winding angle, ϕ is the transverse permeability of the fibre bed and μ is the viscosity of the resin. This expression was simply derived from the combination of the Darcy's type equation (equation (2.11)) with the decomposition of the winding force, $F_{winding}$, in the circumferential direction.

Computing data incrementally and using the following expression for fibre stress at time $t+\Delta t$:

$$\sigma_f^{t+\Delta t} = \sigma_f^0\left[1-\frac{E^f S\,\Delta t}{\mu}\frac{\sin^4\phi_0}{r_f^2}\right] , \tag{2.84}$$

where E^f is the fibre's Young modulus, the fibre bundle position and the stress (fibre tension) at time $t+\Delta t$ was obtained.

The stress-strain sub-model considered that the total stresses, σ^T, and strains, ε^T, in the composite laminate are a sum of the contributions of

- stresses and strains due to initial fibre tension, σ^e and ε^e,
- stresses and strains due to changes in fibre tension, and
- stresses and strains due to thermal expansion or contraction and chemical changes, $\sigma^{(th+ch)}$ and $\varepsilon^{(th+ch)}$,

and, therefore, it was stated that:

$$\begin{aligned}\sigma^T &= \sigma^e + \sigma^{(th+ch)} \quad ,\\ \varepsilon^T &= \varepsilon^e + \varepsilon^{(th+ch)} \quad .\end{aligned} \tag{2.85}$$

The void sub-model was similar to the previously developed by Loos and Springer [49] for laminated composites made of prepreg tape. The strength sub-model estimated failures in the cylinder incorporating the Tsai-Wu and the Tsai-Hill failure criterions.

A schematic view of the model architecture is presented in Figure 20.

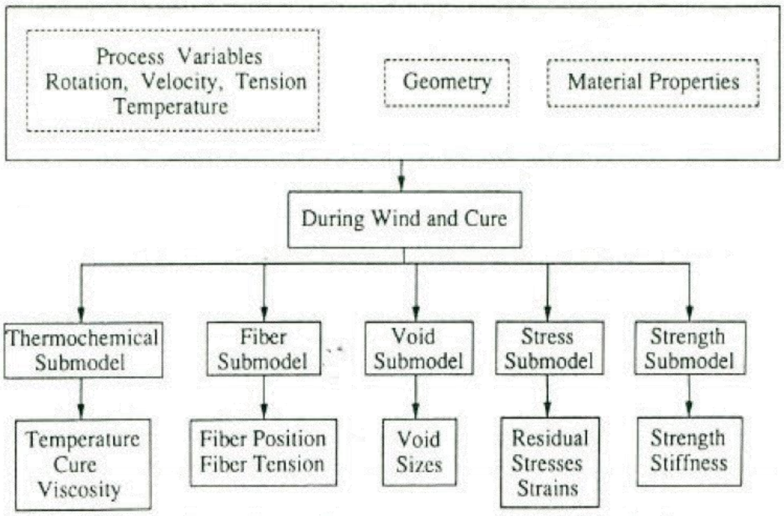

Figure 20 - Outputs provided by the WINDTHICK® code [2].

2.2.6.2. Squeezed Sponge Model

Based on experimental data on compaction of fibre beds, Gutowski *et al.* [26] applied the effective stress (squeeze sponge) theory to the consolidation of composites during cure. This theory formulation stated that at any point in the laminate the stress was borne by both the fibres and the resin, accordingly with equation (2.4).

Given the continuity equation:

$$\frac{\partial \in}{\partial t} = -\frac{\in}{\mu}\left[\frac{\partial}{\partial r}\left(k_r \frac{\partial p_r}{\partial r}\right) + \frac{\partial}{\partial z}\left(k_z \frac{\partial p_r}{\partial z}\right)\right] , \tag{2.86}$$

where $\in$ is the fibre bed porosity $(\in = 1 - V_f)$, p_r is the resin pressure, is the resin viscosity and k_r and k_z are the specific permeabilities of the fibre bed in the r and z directions, respectively, Dave *et al.* [29,30] and Gutowski *et al.* [47] presented solutions for their laminate consolidation models by solving it together with the stress equilibrium equation (equation (2.4)). An important aspect of equation (2.86) was that it accounted for resin mass loss due to resin flow out of the laminate. It also assumed that the fibre bed was fully saturated, i.e., no voids were considered.

A key feature of Gutowski's modelling approach for consolidation in FW of cylinders, was that it included the elastic deformation of the fibre bundle. In [16] two different cases (both typical in FW) were discussed. In one case, the resin flow time was short compared to the winding time. Hence, the fibre distribution and other important parameters were determined almost solely by the fibre deformation behaviour. In the other case, the resin flow time was long compared to the winding time. Here, a quasi-elastic analysis was used to determine the fibre distribution and stresses during winding. These conditions were then used as inputs for the consolidation process model. The winding and consolidation process was sought as a dynamic process involving fibre bundle deformation and fluid mass flow. This process model predicted the time history of process variables, such as fluid pressure, fibre distribution and structural dimensions.

2.2.6.3. Other Modelling Approaches

Spencer [132] established an analytical model to predict the resin cure state, layers' locations and residual stress state in orthotropic filament-wound composite cylinders. The study was focused in thermosetting resins based composites and axis-symmetric cylinders. His model was mainly divided into four sub-models: composite layer stiffness, resin flow, cure kinetics and heat transfer, each modelling the corresponding group of physical phenomena. Three stages of fabrication were considered and analysed separately: winding, curing and mandrel removal. Simplifying assumptions were made as follows:

- all the resin properties rather than elastic modulus and viscosity remained constant during the curing process;
- the resin and fibres' properties were independent of the stress level;
- as the plies were wound, the contribution of the resin to the stiffness and pressure build-up were negligible;
- the coefficients of thermal expansion (CTE) of the laminate were considered linear and constants over the processing temperature range;
- the shear stresses $\tau_{z\theta}$ in each ply $(\pm\phi)$ were assumed to be equal and opposite, producing negligible shear strain $\gamma_{z\theta}$;
- $\frac{\nu_{ij}}{E_i} = \frac{\nu_{ji}}{E_j}, \quad i, j = z, \theta, r$;

From the classical orthotropic stress-strain constitutive relationship as defined in [23,113], considering the abovementioned assumptions, Spencer deduced the following constitutive relationship for each $\pm\phi$ layer expressed in cylindrical coordinates:

$$\begin{Bmatrix} \varepsilon_{rr} \\ \varepsilon_{\theta\theta} \\ \varepsilon_{zz} \end{Bmatrix} = \begin{bmatrix} 1/E_r & -\nu_{\theta r}/E_\theta & -\nu_{zr}/E_z \\ -\nu_{r\theta}/E_r & 1/E_\theta & -\nu_{z\theta}/E_z \\ -\nu_{rz}/E_r & -\nu_{\theta z}/E_\theta & 1/E_z \end{bmatrix} \begin{Bmatrix} \sigma_{rr} \\ \sigma_{\theta\theta} \\ \sigma_{zz} \end{Bmatrix} + \begin{Bmatrix} \beta_{rr}\Delta T \\ \beta_{\theta\theta}\Delta T \\ \beta_{zz}\Delta T \end{Bmatrix} , \tag{2.87}$$

where ε_{ii} and σ_{ii} are the normal strains and stresses in the referred layer, E_i are the elastic modulus of the referred layer, ν_{ij} are the Poisson's ratios, β_{ii} are the linear CTE and T is the temperature.

The changes in the fibre tension due to radial and axial displacements of the fibres were defined as:

$$\Delta F_{winding} = \frac{\left(\frac{u_r^{fb}}{r^{fb}} + \frac{2\pi u_z^{fb} \cos\phi}{Z} \right)}{\frac{F_{winding}}{A^{fb} E^f}} , \tag{2.88}$$

where $F_{winding}$ is the winding tension, u_r^{fb} and u_z^{fb} are the radial and axial displacements of the fibre bundle, r^{fb} is its radial position, Z is the length of the composite cylinder being wound, A^{fb} is the cross-sectional area of the fibre bundle, E^f is the fibre elastic modulus and ϕ is the winding angle. The calculation of the resin modulus, E^r, in each moment during cure was made by assuming its proportionality to the viscosity, μ, as:

$$E^r = \propto \mu \ , \tag{2.89}$$

Using the easily known values for E^r and μ in the fully cured state, and assuming that at the initial state of cure both values are zero, the proportionality is easy applied. This assumption was based on previous indicative results presented by Maximovich and Galeos [133]. The resin flow, the resin kinetics and the heat transfer modelling approaches were developed in a similar way of the ones discussed in previous sections of this text.

Ikonomopoulos and Marchetti [134] coded a process model for the FW process, based on the analytical descriptions of Lee and Springer [23]. The architecture of their model accounted for six sub-models: (1) fibre motion, (2) heat transmission, (3) chemical kinetic, (4) rheological, (5) winding stress-strain and (6) thermo-chemical stress-strain. Olofsson [135,136] also presented a numerical code to predict the temperature and stresses in filament-wound composite cylinders during the manufacturing stage. Again, this work was based on previous models published by Lee and Springer [23].

Hubert and Poursartip [37] provided a comprehensive review of flow and compaction models for thermosetting matrix composites during curing. They divided the review into the resin behaviour during cure, the fibre bed behaviour, and the flow-compaction models.

Darcy’s type equation is the most used governing equation for analyze flow through the laminate. However, Lindt [39] proposed a different approach to solve the consolidation of composites using lubrication theory in his percolation flow model. Lindt assumed the fibres to be straight parallel cylinders suspended in a viscous incompressible fluid. From a force equilibrium involving drag and squeeze flow, the motion of the fibre layers were calculated. This model predicts a symmetrical consolidation from the laminate centre. Such behaviour has not been observed experimentally.

Gutowski and co-workers [26,34] also described the compaction behaviour of composite laminates (for autoclave processing) by applying the effective stress formulation used in soil mechanics.

Loos and William [137] measured the resin flow from laminates with different ply thicknesses, dimensions and ply-stacking sequences. They used the sequential model and outputted that the ply-stacking sequence for flat laminates does not affect significantly the total resin mass loss. Converting these results to wound laminates is not straight forward.

Few models have been developed for FW process of thermoplastic-based composites. Shih and Loos [138] and Toso *et al.* [139] studied the heat transfer of the thermoplastic FW, considering a specific configuration of the process in which a gas torch heats the fibres and resin immediately before the deposition onto the mandrel surface. Song [140] modelled the heat transfer, the crystallization and the consolidation of this process configuration using the finite element method (FEM). The theoretical background supporting these models is the one previously discussed in section 2.2.4.

Either in partial or global process modelling, not much literature can be found relating specifically to the FW process. Most of the assumptions made for other manufacturing processes may, however, be adapted and so, provide useful information for the present study.

Mantell and Springer [95] presented a study on manufacturing process models for thermoplastic composites relating the applied temperature, pressure, speed and time to the temperature, crystallinity, consolidation, interlaminar bonding and residual stresses and strains inside the composite. For that they followed the models proposed by Springer, Loos and their co-workers for manufacturing plates in a press or autoclave, but they extended it to include cylindrical geometries, variations in the applied temperatures and pressures with position and time and rapid bonding.

While presenting a promising method for manufacturing wound artefacts using thermoplastic powder-impregnated material systems, Sala and Cutolo [76,77] developed a simulation model of their manufacturing process setup as they felt the specificity of their apparatus (accounting for a heated chamber). Actually, the necessity of controlling the temperature during all the phases of the process is the main difference between thermosetting and thermoplastic based models.

As so, they divided their model into five sub-models:

- the winding sub-model
    - inputs: winding tensile load, temperature, degree of crystallization and viscosity updated by the other sub-models,
    - outputs: bundle position, tension of layers, layer and laminate thicknesses,
- the thermal sub-model
    - inputs: material characteristics, temperature cycle and crystallization heat computed by the chemical sub-model,
    - outputs: through-the-thickness temperature distribution,
- the chemical sub-model
    - inputs: through-the-thickness temperature distribution,
    - outputs: viscosity and degree of crystallization of each layer,
- the impregnation sub-model
    - inputs: layers stresses, physical and chemical material properties, temperature distributions and geometry,
    - outputs: degree of impregnation and void content for each layer,
- the mechanical sub-model
    - inputs: physical and chemical material properties, geometry, stacking sequence and temperature distribution,
    - outputs: interlaminar stresses at the interface and average residual stresses in the layers due to thermoelastic effects.

In their analytical approach several assumptions were made, such as that the flow was Newtonian, the Darcy’s type equation properly described the one-dimensional resin flow, fibre’s velocity could be assessed through inverting the permeability concept, etc. There were obvious similarities between this approach and other modelling approaches, either for fibre’s motion or resin flow and cure, developed for thermosetting based systems.

2.3. Experimental Procedures and Measuring Techniques

In this section the few experimental techniques presented by other authors within the scope of measuring and/or evaluating process relevant are identified and described. Emphasis is given to those procedures that, even if not directly applied to the FW manufacturing process, may be of interest for the purpose of experimentally validate the present process model. As in the previous section, the text is divided, as much as possible, in accordance with the different physical phenomena that one may identify and study independently.

2.3.1. Compaction of the Fibres

One of the approaches to understand the resin flow and thus the compaction of the fibre bed is to determine the resin pressure within the laminate. As discussed in the section 2.2.2, it corresponds to the portion of the externally applied stress that is sustained by the resin. Measuring pressure in a laminate is difficult, mainly due to the size restrictions [31]. Typical thicknesses of carbon/epoxy plies in different manufacturing processes range from 0.125 mm up to 0.900 mm. Thus, any of the most common sensor types may be excessively intrusive and disturb the resin flow and fibres rearrangement that it is meant to investigate [25].

Smith [141] measured the resin pressure within composite laminates using flat resistive sensors of the size 0.34 mm × 15 mm × 20 mm. In these sensors, as the applied pressure increase, interdigitated conductive fingers are forced against a semi-conductive material, making its electrical resistance to decrease. In Figure 21 these sensors are schematically represented. Results from three carbon/epoxy laminates, with sensors embedded in multiple spots along the thickness, were presented. The accuracy and reliability of the measurements was far from satisfactory due to many factors. Namely, it is not clear what the sensors measured: if the hydrostatic resin pressure, the fibre bed pressure, or both. Also, the large area of the sensors and their opacity obstructed and affected the regular accommodation of fibres and resin flow within the laminate. Minor problems, such as creeping of the polymeric substrate at high temperatures, hysteric responses to pressure variations and noisy outputs, were also reported. The method seems, though, applicable for qualitative sensing of whether the pressure is increasing or decreasing in particular regions of the laminate.

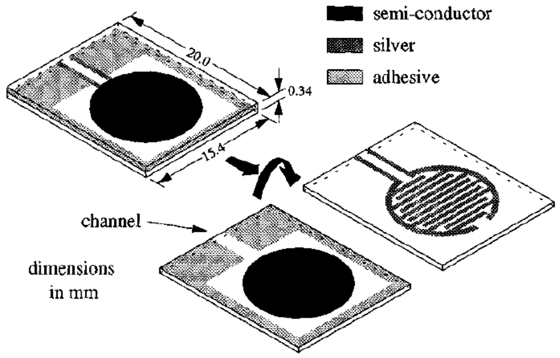

Figure 21 – Schematics of the flat resistive sensors used by Smith [141].

Mackenzie [25] developed sensor assemblies with operation principle similar to static pressure taps. Small fluid-filled tubes extend to the composite laminate spots. The hydrostatic pressure at the tip of each tube is transmitted by the fluid inside to an absolute pressure diaphragm sensor that is outside the laminate. The benefits are evident: the sensors have the ability to measure only the resin hydrostatic pressure and the size and shape of the sensor assembly is virtually non-intrusive to the laminate. In Figure 22 a schematics of the tube sensor assembly is shown. In her work, the absolute pressure sensors were connected as resistors, energized by a constant current of 1mA. The pressure transmission fluid was uncatalysed resin of the same type of the one present in the laminates to measure. Results compared well with the simulations ran with the LamCure® algorithm presented by Smith [141]. However, the good agreement only occurred by assuming, with no sufficient supporting evidence, an initial degree of cure of $0.35 \leq \alpha_0 \leq 0.40$. Using other values for α_0 the agreement was considerably deteriorated. A quite similar sensor type was used by Xin *et al.* [142] based on the technologies previously presented by Lynch *et al.* [143] and Gu *et al.* [144]. Accurate resin pressure measurements within consolidating laminates were achieved. The sensitivity and resolution of such technique was not discussed.

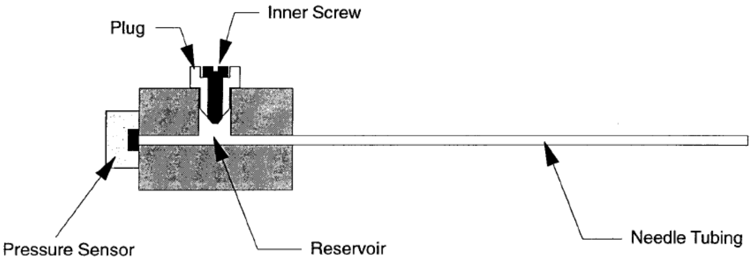

Figure 22 – Schematic representation of the tube sensor assembly [25].

A few experimental studies have been conducted with the objective of measure the compaction curves of carbon fibre [30,34,145-147] and glass fibre [146,148-149] fabrics. Since the measurement of the fibre bed curve alone and the resin pressure are of difficult assessment, the fibre bed was typically tested in a dry form or impregnated with silicone oil after dissolving out the polymer matrix. However, the act of dissolving the resin out of the prepreg can change the fibre arrangement and could affect the fibre bed compaction behaviour. It is also a time-consuming and tricky operation. The use of a very low viscosity fluid or no fluid, and the loading of the specimen at a very low rate were steps normally taken to minimize the viscous response effects caused by the fluid flow out of the sample. When a wetting fluid is used, the fluid pressure is measured and subtracted from the total applied stress to obtain the fibre bed effective stress.

Hubert and Poursartip [18] measured the fibre bed compaction curve directly for AS4/3501-6 composite prepreg. The unidirectional composite specimen was loaded in the through-thickness direction, which was the main deformation mode of the fibre bed, using a piston-mould setup. A uniaxial testing condition was obtained by preventing the distortion in the transverse direction by the mould walls. This technique allowed the measurement of the composite laminate as is, without any steps or indirect measurements that could alter the fibre arrangement in the matrix. The compaction curve of the fibre bed was extracted from the measured displacement and applied load. Their test setup needed a temperature-controlled environmental chamber and the testing conditions were very sensitive and critical as not to cure significantly the resin during the measurement.

Li *et al.* [21] developed a perforated (highly porous) press platens tool to measure the compaction curve of a consolidating laminate subjected to through the thickness squeezing and flow. In their experiment, the fibre bed is compressed with a constant compaction pressure and the thickness variation measured simultaneously. By using a low viscosity fluid that easily flows out through the perforated platens, an equilibrium in which resin pressure decreases to zero and the fibre bed bears the entire compacting pressure is achieved ($\sigma = p_f$). The steady fibre bed thickness with no resin pressure was obtained for each value of externally applied pressure.

Using a setup to reproduce the effect depicted in Figure 4, Bates *et al.* [14] measured the pressure build-up at the interface between glass-fibre roving and cylindrical pins. A radial hole in the pin, connected to a pressure transducer gave a direct insight to the pressure developed. Figure 23 shows a scheme of the test apparatus. They concluded that the maximum pressure (developed at the wedge entrance region) attained approximately 60%-70% of the theoretical value, given in equation (2.2). These results imply that glass-fibre filaments are in contact with the pin and that the resin doesn't balance all the inward stresses. This is in accordance with the widely accepted pressure sharing assumption.

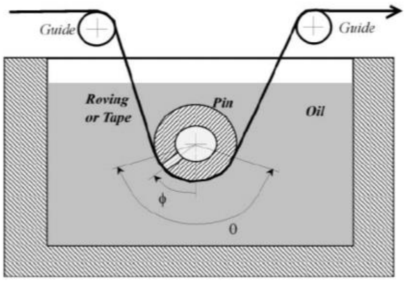

Figure 23 – Schematic cross-sectional representation of the instrumented pin immersed in the oil bath [14].

2.3.2. Resin Flow

Several methods were developed through the last thirty years to characterize and measure the fluid flow in composite laminates during their manufacturing processes. However, due to the small scale at which this phenomenon occurs, the fibres arrangement, the effect of factors such as temperature, heat transfer, pressure gradients and resin changing properties, to date, no method has been entirely satisfactory.

Resin flow has been typically assessed through mass measurements of bleeder layers before and after the cure and consolidation of the laminates [49,137,150]. Measurements of the laminate's initial and final mass were also used with the same objective [141].

Shin and Hahn [20] used a bleeder ply in top of AS4/3501-6 prepreg laminates to confirm the excess resin flowing out during an autoclave processing cycle on carbon/epoxy prepregs. By estimating the bleeder porosity, $\in_b$, using the relation:

$$\in_b = 1 - \frac{m_b}{\rho_b A_b h_b} \ , \tag{2.90}$$

where m_b, ρ_b, A_b and h_b denote mass, density, surface area and thickness of the bleeder ply, respectively, the number of plies to put in top of the laminate was such that the previously estimated resin excess would fully fill the empty space in the bleeder plies. This bleeder mass method is useful for verifying model results. The need for relevant pressure values and confinement to a hot press or equivalent setup, however, turns this procedure non-attractive for free-surfaces processes as is the case of FW. Moreover it doesn't give any insight into the source and path of the resin flow during the consolidation process.

Poursartip *et al.* [151] presented an improved method in which bromine atoms were chemically attached to the molecules of epoxy resin in certain plies of prepreg laminates. After the cure and consolidation, the laminate is sectioned and a contour map of the brominated resin is drawn by wavelength dispersive X-ray (WDX) analysis on a scanning electron microscope. This method allows to assess the flow within the laminate, even for zero-bleeding ones. Again, the evolution of the resin flow during the process is not assessed.

Thomas *et al.* [152] used ultrasonic imaging in the C-scan mode to measure the flow rate of an epoxy resin film penetrating through the thickness of a single layer of woven carbon fabric. A vacuum bag moulding apparatus was immersed in hot water while producing a density map or profile of the scanned material. The method relied on the acoustic contrast of the reflection of wetted and dry regions. Air coupled ultrasonic experiments had been conducted before to characterize the in-plane flow front in RTM processes [153,154] but these authors. Wu and Li [155] demonstrated a simple method to measure the transverse (through the thickness) flow in which fibrous material was wound in a coil and resin was injected through the centre. By observing the flow front, the flow rate and permeability could be determined. These methods are limited to dry fibre (unsaturated) beds being impregnated for the first time during the experiment so that a resin flow front could be observed.

Endruweit *et al.* [156] mapped the fluid distribution within laminates using magnet resonance imaging. They used a reference test fluid and were mainly able to identify and localize eventual dry spots in the impregnated laminate. This heavy and expensive method is mostly suitable for inspection of composite parts after manufacture.

Transverse permeability measurements have been performed and reported in the literature for mats and fabrics. Most measurements are carried out by inducing a steady unidirectional flow across the porous medium, which is stacked into a cylinder.

In order to determine the transverse permeability of fibrous porous media, Rahli *et al.* [157] conducted a series of experiments with rigid fibres (bronze and copper wires with diameter of 150µm) randomly stacked in a measuring cell. Forcing water to flow through the fibre bed with a constant pressure drop, $\Delta p / \Delta h$, for each series of data and measuring its flow, q, the superficial velocity, $\dot{u}$, was deduced. In Figure 24 the experimental apparatus is represented. The relation between the pressure drop and the superficial fluid velocity was determined for several fibre aspect ratios, r^f / L, ranging from 0.0075 up to 0.111. When compared with previously published models [40,54,57] their results present significant deviation [45]. However, this is mainly justified by the fact that this study was conducted in monodispersed randomly packed short fibres while those models refer to fibre beds arranged in simple, ordered patterns and don't even account for the fibre aspect ratio.

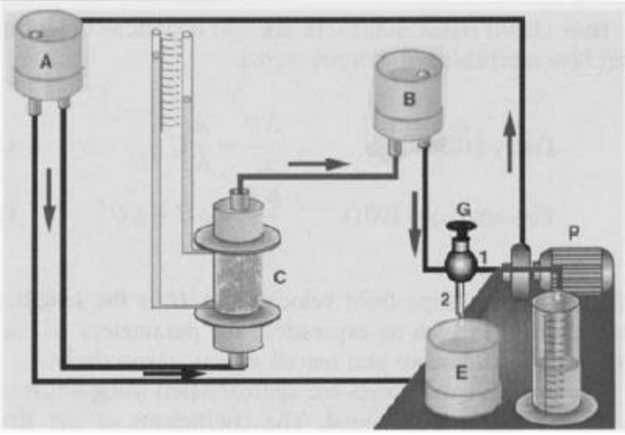

Figure 24 – Schematic representation of the experimental apparatus used by Rahli *et al.* for the determination of the permeability of fibrous media [45].

Similar approaches were recently addressed by Scholz *et al.* [158] and Elbouazzaoui *et al.* [159] by forcing the through the thickness fluid flow on porous samples at prescribed rates. Permeabilities were determined from linear relations between the pressure gradients (pressure drop) and the flow rate.

Buntain and Bickerton [160] compressed fibre beds in a press tool platens arrangement and back-calculated the permeability from the pressure and height measurements. Despite their work was focused in the in-plane permeability, applicability to through the thickness characterization is foreseen. Li *et al.* [21] and Comas-Cardona *et al.* [161] used a similar setup to measure transverse permeability. For each material sample, their press platens enclosure was firstly utilized to measure the compaction behaviour (see section 2.3.2) and then to determine the saturated permeability by fixing the platens and pressurizing the remaining resin in a similar approach to the others described herewith.

In these methods the fibre volume fraction was fixed by the height of the stack of fibres, maintained between the lower and upper limits of the stacking cell. References were made to that the pressure and fluid viscosity were be kept low enough not to further compress the fibres during measurement. By knowing the value of the fluid viscosity, μ, the cross-section of the flowing region, A_{flow}, the height of the stack of fibres, h, and then measuring the pressure drop, Δp, and the fluid flow rate, q, at the outlet, the transverse permeability, S, is obtained simply by applying Darcy's type equation, in the following adapted form [40,60,157,162]:

$$\frac{q}{A_{flow}} = -\frac{S}{\mu}\frac{\Delta p}{h} \ . \tag{2.91}$$

Skartsis *et al.* [147] studied the flow of distilled water and silicone oil through ideal cylinder beds and sheets of aligned carbon fibres (actual fibre beds) in different stacking sequences. In their experimental tests the fibres were held in their positions and thus not allowed to rearrange and accommodate. The measured permeabilities for various pressure drop differences across the “real” carbon fibre bed showed significant deviations from the results of tests with ideal cylinder beds.

Loos and Springer [49] described an iterative numerical-experimental procedure for determining the permeability, S, of prepreg laminates in the through the thickness direction. In it, the curing process of a given laminate is interrupted to measure the resin outflow and achieve a first estimation of the permeability. For this purpose, the top bleeder approach is used as referred above. This value is then inputted to the flow model, and the permeability value is adjusted until masses agree. The main drawback of this procedure is its dependence on the correct knowledge of all other influencing variables, such as resin velocity, $\dot{u}$, or thickness of the layers, t^l, in order to allow such a parametric adjustment of the model.

Morren *et al.* [163] designed and used a textile-like solid specimen with anisotropic permeability, fabricated by stereolithography, for calibration and comparison of permeability measurement setups and model validation. Their work was focused in the characterization of dry fibre beds in the in-plane resin flow in resin transfer moulding (RTM) manufacturing.

An international benchmark exercise to measure and value in-plane permeability of composite textiles was recently done [162]. No equivalent studies were addressed for transverse or through the thickness permeability of fibre beds.

Very few experimental results were presented to complete the validation of the models accounting for the ellipiticity of the fibre tows within a fibre bundle. These were referred in the section 2.2.3. Labrecque [164] showed that the fibre cross-section starts to play a significant role on the infiltration process when the aspect ratio is greater than 3:1. For larger ratios with the flat side facing the flow, the permeability was significantly lower than that for circular fibres in similar conditions. Feuillade *et al.* [165] and Merhi *et al.* [60] measured the out-of-plane permeability of chopped elliptical strands using air and polyethylene-glycol as reference fluids, respectively. In Figure 25 the experimental setup used by the latter research group is schematically represented. The main improved feature in their permeameter was that the fibre bed could be larger than the area of forced flow, in order to minimize the effect of decreased volume fraction near the walls.

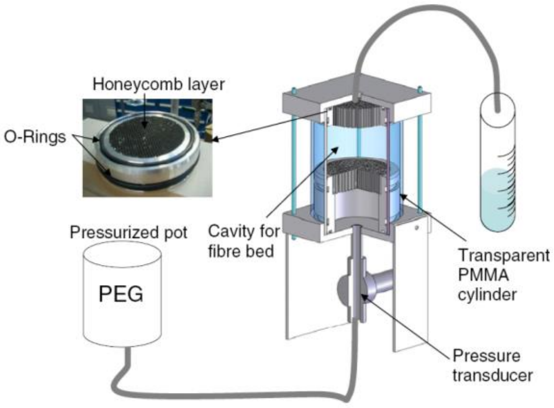

Figure 25 – Schematics of the experimental setup used by Merhi *et al.* for the determination of the transverse permeability of chopped elliptical fibres [60].

The experimental results were compared to theoretical predictions for equivalent fibre beds with circular cross-sections, and for elliptical cross-sections. The effect of an elliptical cross-section of the tows led to transverse permeability values that were much lower than those predicted for circular fibres/tows.

2.3.3. Resin Kinetics

As mentioned in section 2.2.4, several works have been published reporting the characterization of the degree of cure evolution during cure of various thermosetting resin systems [78,82,85-87,89,91-93,166-168]. Several techniques have been used such as spectroscopic analysis, torsional braid analysis (TBA), differential thermal analysis (DTA) and differential scanning calorimetry (DSC). The latter have been applied in more extension through the years. Chen *et al.* [166] used DSC to evaluate the degree of cure of curing composites. Khoun *et al.* [168,169] applied both dynamical and isothermal DSC tests to evaluate the cure behaviour of unsaturated polyester resins.

Heba *et al.* [86] studied the kinetics of an autocatalyzed epoxy resin, assuming a *n*th order reaction, as modelled in equation (2.43), and applied the Freeman-Carrol relation [170] to compute the activation energy, E, and the reaction order, n. The Freeman Carrol relation is expressed as:

$$-\frac{\Delta\ln\left(dH/dt\right)}{\Delta\ln\left(H_u-H\right)}=n-\frac{E/R\times\Delta\left(1/T\right)}{\Delta\ln\left(H_u-H\right)}\ , \tag{2.92}$$

where dH/dt is the heat flow, generated in the curing reaction, H_u is the total heat of curing, H is the heat of cure at given time, n is the reaction order, E is the activation energy, R is the universal gas constant and T is the absolute temperature. Assuming that the hardening reaction proceeded in accordance with the Arrhenius law, a straight line is described by the equation (2.92) rearranged in the following form:

$$\frac{\Delta\ln\left(dH/dt\right)}{\Delta\ln\left(H_u-H\right)}=\frac{E}{R}\frac{\Delta\left(1/T\right)}{\Delta\ln\left(H_u-H\right)}-n\ , \tag{2.93}$$

relating $\frac{\Delta\ln\left(dH/dt\right)}{\Delta\ln\left(H_u-H\right)}$ with $\frac{\Delta\left(1/T\right)}{\Delta\ln\left(H_u-H\right)}$ through a linear relation in which E/R is the slope and n is the interception.

Sun *et al.* [89,171] determined the parameters in equation (2.44) by two methods. The first method, based on early kinetic models of Kissinger [172] and Ozawa [173], consisted in expressing the heating rate, $\frac{dT}{dt}$, as a function of the exothermic peak temperature, T_p, by transformation of equation (2.44). The parameters were, then, obtained from several DSC runs at different heating rates and a linear relationship between the peak temperature and the heating rate was identified. The activation energy was assumed to be the same at different heating rates and was determined from the slope of the curve. The pre-exponential factor and the orders of the curing reaction at each heating rate were determined by a multiple nonlinear least-squares regression. The second method was based on the approach of Borchardt and Daniels [174] and the parameters were obtained from only a single DSC run. By taking the logarithm of both sides of equation (2.44), a linear expression for the logarithm of the curing rate was obtained. The parameters were then determined by a multiple linear regression analysis.

Chen *et al.* [175] used the Kissinger [172] and the isoconversional equations to calculate the activation energies, E_a, of four different epoxy resin systems from dynamic and isothermal curing DSC analyses. These equations are as follows:

$$E_a = -R \frac{\Delta \ln\left(dH/dt/T_p^2\right)}{\Delta\left(1/T_p\right)} \quad , \tag{2.94}$$

$$E_a = -R \frac{\Delta \ln\left(dH/dt\right)}{\Delta\left(1/T\right)} \quad . \tag{2.95}$$

The equation (2.95) allowed more complete assessments of activation energies throughout the entire conversion stage.

Hsiao *et al.* [176] developed a genetic algorithm optimizer to determine the cure kinetic parameters by matching the simulated temperature field through the curing process based on guessed cure parameters with the actual temperature field, measured during real composite parts manufacturing. In each genetic algorithm-based fitting process the best combination of parameters was chosen that minimized the objective function. They concluded that online cure kinetics characterization could be realized with this technique as long as the heating cycle and the fitting time period were carefully chosen.

As for thermoplastic resin systems, little information on experimental characterization studies is available. Bogoeva-Gaceva and Grozdanov [177] ran isothermal DSC analyses in isotactic and homo-polypropylenes (iPP and hPP), in neat form and filled with glass and carbon fibres, and assessed the Avrami exponent, n, and rate constant, K, from the plot of the Avrami equation (equation (2.62)).

In-situ measurements of the resin cure behaviour in composite laminates have been attempted by several authors using different available sensor technologies. Namely, dielectric [178], optical fibre [179], ultrasonic characterization [180], near infrared (NIR) spectroscopy [181] and piezoelectric [182] sensors were proposed. Their application requires the embedment in the mould or tool and considerable number of sensors in order to measure in more than one single point of the laminate. Moreover, in some cases, the resin degree of cure is not measured directly but through indirect correlation with other physical parameters. Multiplexed optical fibre grating sensors were also suggested [183] in order to have distributional measurement of the resin degree of cure.

Kobayashi *et al.* [184] proposed a patch-type flexible matrix sensor based on pemittivity measurements to assess the curing state of the resin in multiple spots along the laminate. Due to its working principle (relation between permittivity and rheology), the method is not affected by sensor deformation or even fibres movement. It is also independent of temperature changes during the process. In Figure 26, the multiple sensor arrangement and the testing apparatus are schematically represented. The effectiveness of the method was confirmed by comparing its results with more conventional differential scanning calorimeter (DSC) study.

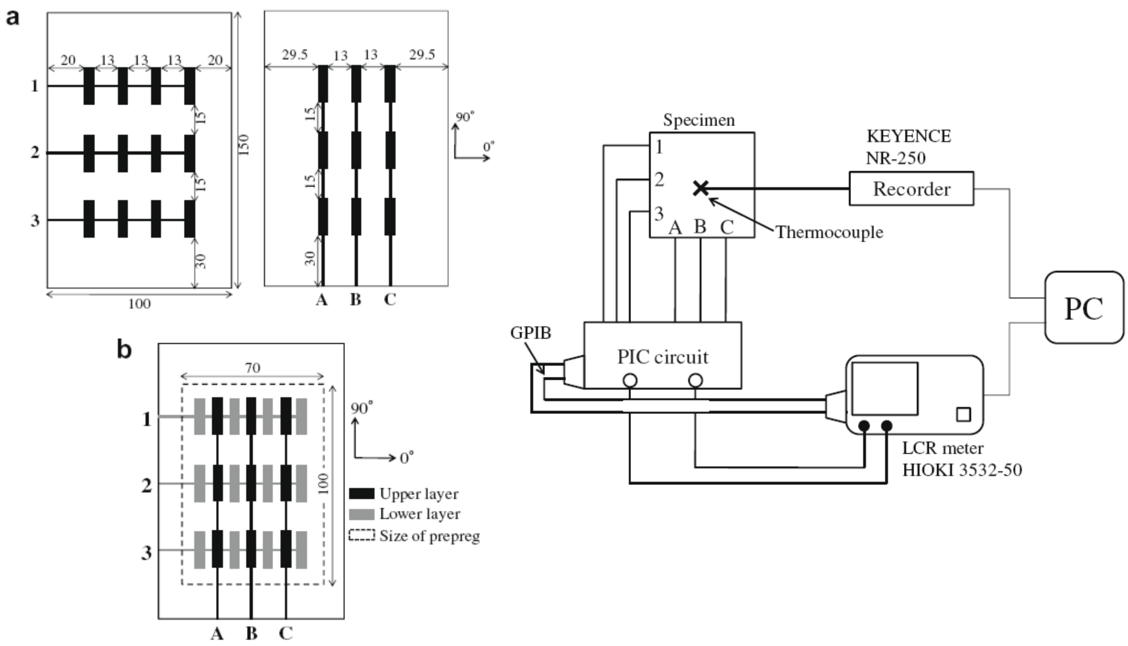

Figure 26 – Schematics of the flexible matrix sensor build-up (left) and test apparatus (right) [184].

2.3.4. Stress-Strain

The stresses and strains fields in consolidating laminates have been typically assessed through direct measurement of the strains and indirect calculation of the stresses. Through constitutive stress-strain relations able to describe the behaviour of the composite under consolidation the assessment to the strains as well as material properties during the process the stress fields could be determined..

Fibre Bragg grating (FBG) sensors are a powerful measurement tool that allows internal and superficial monitoring of strain and temperature. Several authors used this type of sensors in experimental characterization of the process-induced strains and/or temperatures in different composites manufacturing processes [166,185-188].

The sensor working principle is reflected in the following relation [186]:

$$\lambda_B = 2n_{eff}\Lambda \ , \qquad (2.96)$$

where λ_B, n_{eff}, and Λ are the reflected Bragg wavelength, effective refractive index, and the grating period respectively. A change in the effective refractive index and/or the grating period will cause a shift in the reflected Bragg wavelength. This is the measuring principle upon which physical quantities such as strain, temperature, force, and pressure can be measured by the FBG.

Early research works in this field focused mainly in the measurement of a wavelength shift which was attributed to longitudinal strain, and temperature using FBG sensors fabricated in single mode (SM) [185,189,190]. The effects of temperature are often compensated using a reference grating. This compensation technique is similar to the one applied in the long established electrical resistive extensometry measuring technique. Other physical quantities may be inferred indirectly, as well.

Optical FBG sensors capable of measuring two (or more) independent components of transverse strain were developed and experimentally applied [191,192]. The sensors consist of a single Bragg grating written into highly linear birefringent (HiBi), polarization-maintaining optical fibre. When light from a broadband source is used to illuminate the sensor, the spectra of light reflected from the Bragg grating contain two peaks corresponding to the two orthogonal polarization modes of the fibre. Two independent components of transverse strain in the core of the fiber can be computed from the changes in wavelength of the two peaks if axial strain and temperature changes in the fibre are zero or known.

Giordano *et al.* [185] applied a single FBG sensor to monitor significant phenomena occurring during and after the curing stage of a model epoxy system. Both the thermal and the strain effects on sensor response have been used to characterize the curing process as well as the cooling down stage, the de-molding phase and the residual stresses relaxation. In a non-isothermal curing test setup, the gelation onset was identified and the strain build up in the cooling down stage was measured. Additionally, the relaxation of the locked-in strain was measured in repeated heating/cooling cycles through the evolution of the glass transition temperature in the aged sample.

Chehura *et al.* [186] experimentally monitored the chemical shrinkage and thermal expansions/contractions in glass-fibre composites and neat resins with FBG sensors written in HiBi optical fibre using a specific demodulation system. They neglected the presence of possible shear strain under the assumptions that it is small during the initial and gelation phases of the curing.

Casari *et al.* [187] utilized optical FBG sensors to measure the cure shrinkage and residual stresses and strains in a consolidating laminate in the through the thickness direction. Choosing different orientations of the sensors within the laminate, they identified opportunities for 3D measurements using this technique. In Figure 27 a scheme of the sensors embedment apparatus is shown. Optical fibres are less intrusive than other sensor types and present a promising technique for the direct measurement of strain (and indirect measurement of other physical parameters). However, better signal processing is still required in order to achieve accurate measurements and understand the significance of the observed noise. Also, the decoupling of the several phenomena inducing the wavelength changes in the sensor is a challenge.

Several works involving extrinsic Fabry Perot optical fibre (EFPI) sensors have been presented [193,194] to perform residual strain monitoring in the different phases of the curing process of composite laminates. In these applications, the EFPI operation relies on both the strong dependence of interferometer response to local strain fields and the great insensitivity to thermal changes due to the low thermo-optic effect associated to in air cavities.

Yates *et al.* [195] measured the cure shrinkage of four epoxy resin systems using a manometer dilatometer. The overall percentage of final volume contraction as well as its evolution and relationship with the degree of cure were assessed. Daniel *et al.* [196] recorded the chemical shrinkage in assembled laminates by applying the shadow Moiré method. Russel [197] compared the shrinkage measured in several carbon/epoxy prepregs with results from dynamic mechanical analysis (DMA) and dielectric cure monitoring. Maximum volume corresponds to minimum storage and loss modulus in DMA and maximum in dielectric loss factor. Johnston [120] compared results from continuous measurements using thermo-mechanical analysis (TMA) with effective cure shrinkage strain examination at the end of each test conducted in instrumented specimens and found the latter measurements to be more than an order of magnitude lower than the former ones. Prasatya *et al.* [198] used a pressurisable bellows dilatometer to measure chemical shrinkage a an epoxy resin system. Bilyeu *et al.* [199] measured the volume changes in test specimens using a quartz dilatometry cell inside a TMA system. Void elimination and chemical shrinkage were separately quantified. Zarrely *et al.* [200] measured the coefficient of chemical shrinkage using liquid dilatometry at different curing temperatures and established linear relationship between chemical shrinkage and degree of cure. Results tend to show that major shrinkage occurs in the early stages of curing. Results also suggest that chemical shrinkage is only a function of the degree of cure regardless of time and temperature. The same observation was drawn by Li *et al.* [201] after the results obtained by monitoring the density variation of a resin sample through capturing the buoyancy of the sample in a constant density silicon environment.

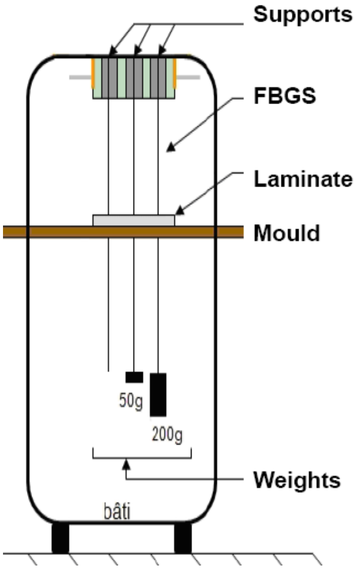

Figure 27 – Schematic view of the optical sensors embedment apparatus [187].

Lange *et al.* [126] obtained cure-dependent relaxation times and (elastic) shear moduli of thermosetting based specimens through torsional DMA measurements.

Garstka *et al.* [115] presented a novel technique to measure the through the thickness strains during processing of epoxy composites. A non-contact video extensometer was used to capture the thermal expansion (during heating stages) the laminate consolidation and the cure shrinkage. In Figure 28 the setup is schematically represented.

The results obtained for the through the thickness strains measured during the cure of a unidirectional laminate are summarized in Figure 29. One may observe that the strains are zeroed at the peak during the second heating ramp of the specific curing cycle applied.

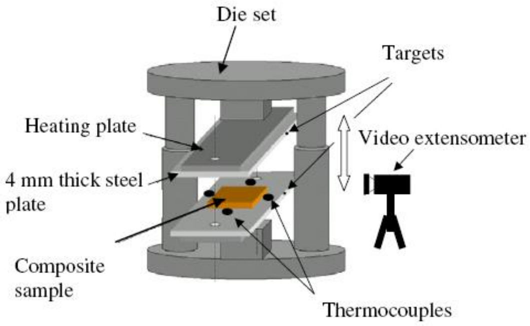

Figure 28 – Schematic view of the experimental setup used for cure shrinkage measurements [115].

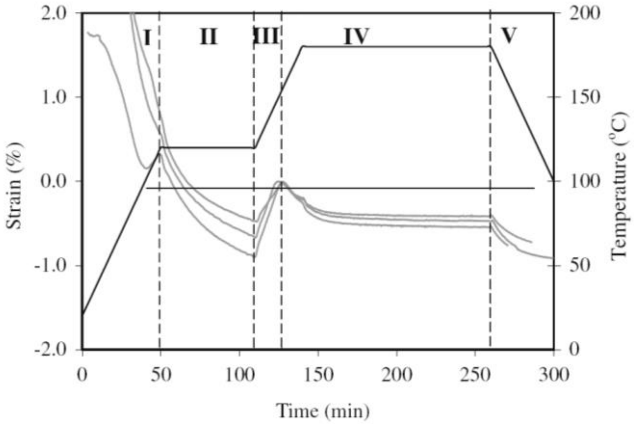

Figure 29 – Through-the thickness strains measured during cure of a unidirectional laminate [115].

Khoun *et al.* measured the chemical shrinkage of a one part epoxy [168] and unsaturated polyester [169] resins using a modified rheology test. This technique measures the gap variation between the rheometer parallel plates after the gel point. The test was conducted at constant temperature to avoid having thermal expansion/contraction effects. The linear shrinkage, $\eta_L \varepsilon_{ch}$, was calculated assuming that the resin was incompressible with a constant Poisson's ratio of 0.5, through the following equation [202]:

$$\eta_L \varepsilon_{ch} = \left((1+\nu)\left(\frac{\nu}{1-\nu} \right) + 1 \right)^{-1} \left(\frac{h-h_0}{h_0} \right) , \tag{2.97}$$

where ν is the Poisson's ration, h_0 and h are the values of the gap between the parallel plates at the initial and at a given time, respectively. Assuming that the through-the-thickness strain is the only non-zero component of the "chemical strain" tensor in the resin, the volumetric shrinkage was calculated through the following relation:

$$\eta_v \varepsilon_{ch} = \left[1 + \frac{1}{3} \left(\frac{h-h_0}{h_0} \right) \right]^3 - 1 \ . \tag{2.98}$$

The same apparatus would be applicable to measure thermal expansion of the resin before and after the gel point. However, the chemical reaction should be somehow freezed not to have the chemical shrinkage effects occurring simultaneously. In the same study [168] the authors characterized the cure shrinkage by a gravimetric method, similarly to what previous authors had presented [201]. They concluded that the applicability of the gravimetric method is limited to higher gel times and degree of cure at gel time than the rheometer method. In Figure 30 schemes of the apparatus used in both methods are presented.

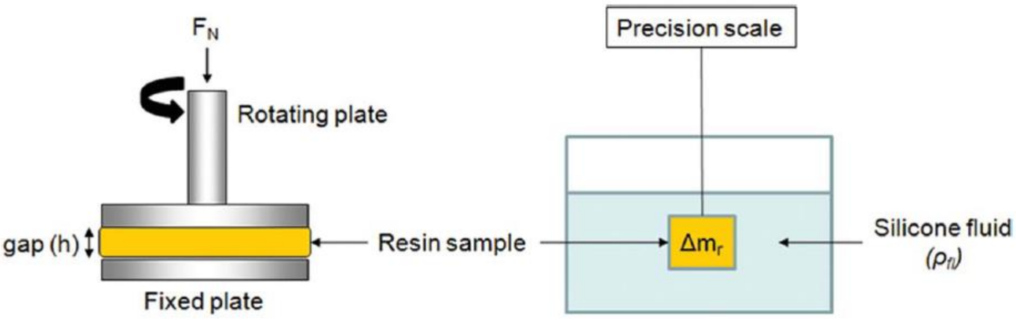

Figure 30 – Schematic representation of the rheometer parallel plates (left) and gravimetric methods setups [168].

In all the abovementioned studies, either a test specimen was used in specific setups, or the *in situ* measurements required physical apparatus that affected the regular composite processing conditions. They all refer to prepreg laminates cured at high temperatures.

Room-temperature-curing resins have not been studied as extensively as higher temperature systems. Gillespie, Bogetti and co-workers [203,204] measured *in situ* the chemical shrinkage of a low temperature vinyl-ester cure resin system after gelation using a density column technique. A bimaterial specimen experiment was developed to isolate the chemical and thermal contribution to curvature. Additionally, the cure reaction has proven to be significantly different than higher temperature reactions and very sensitive to temperature.

Ersoy *et al.* [106] measured the moduli development in carbon/epoxy unidirectional (UD) and cross-ply (XP) prepreg laminates during its curing through dynamic mechanical analysis (DMA) in the transverse shear mode. Since the specimens couldn't be hold by the fixture in early stages of the curing process, due to the liquid nature of the resin in that stage, those were previously pre-cured up to the gel point. So, the shear modulus, G_{23}, was calculated only from the gelation point onwards. Relevant information was, however, assessed, as can be observed in Figure 31. In their work, the coefficients of thermal expansion (CTE) were also measured by two different methods. In the first method, high temperature strain gauges, bonded onto the specimens' flat surface in the transverse direction. Compensation gauges were placed on a block of zero thermal expansion titanium silicate glass. In the second method, thermo-mechanical analyses (TMA) were made on different specimens. This method allowed to assess also to the through the thickness strain developing during the curing of the samples. Characteristic results are plotted in Figure 32.

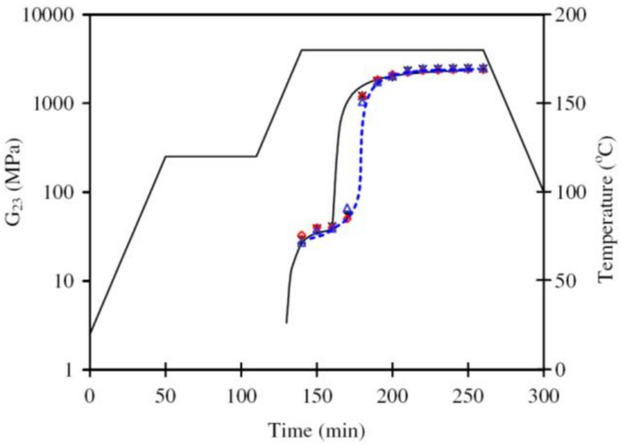

Figure 31 – Development of the shear modulus in a carbon/epoxy prepreg laminate through cure [106].

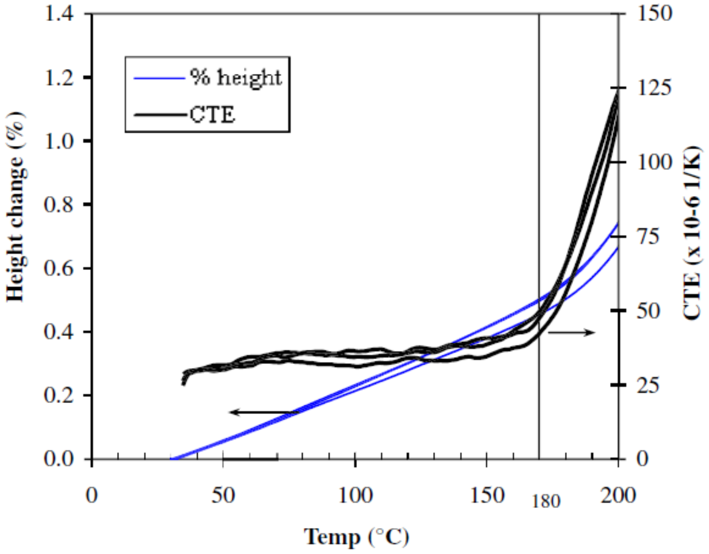

Figure 32 – Thermal expansion behaviour of unidirectional laminate in the through the thickness direction [106].

2.4. Critical Remarks

Within the scope of the FW process model development, a critical analysis of the relevant information and knowledge gathered in the literature review is summarized herewith.

Several authors modelled composites manufacturing processes in the last decades, including a few studies dedicated to the FW process. However, there is still lack of consensual, consolidated and fully validated models for the FW process. The process models developed so far for the FW haven’t been fully validated, since only fibre bed compaction and resin outwards flow have been measured with accuracy but no stresses and strains as well as resin pressure or resin mixing between adjacent layers have been satisfactorily measured. In fact, due to the greater geometrical complexity of the testing apparatus in a typically cylindrical FW laminate, most of the experimental data used to validate the FW process models was gathered out of the real process setup. Namely, compaction and resin bleeding has been measured in autoclave or press platens tools, and fibre volume fraction has been estimated from the final laminate thickness. Moreover, the existing models were dedicated to either thermosetting or thermoplastic based configuration, thus not accounting for a more general applicability.

Among several issues assessed through this review, it was noted that:

- experimental testing of composite samples typically led to great scatter of results, which influenced the quality and adequateness of curve-fitted models (in resin kinetics characterization, for example),
- most of the process models assume the initial degree of cure (conversion) of the resin to be zero, which is far from true,
- most of the kinetic models are valid only within a limited range of degree of cure,
- few information was available on low temperature curing systems,
- for the FW process models,
    - no information was available on the control of the initial fibre volume fraction, as well as the homogeneity of the fibre bundle impregnation,
    - the resin mixing between adjacent layers (as well as its influence on the cure kinetics) was not characterized,
    - the body forces such as gravity were neglected in modelling resin flow,
    - occurrence of the different physical phenomena in the axial and circumferential directions was mostly neglected, thus being most of the models of one-dimensional nature,
    - no relevance was attributed to the fibres interlaced pattern.

Nevertheless, the information and data assessed and published by numerous researchers through the years is of great interest for the present work. This review is mostly a compilation of the relevant studies conducted on specific partial issues and phenomena that interact in the FW process. Each group of previous studies allowed to understand the phenomena, their individual modelling approaches and support, therefore, the strategy in developing further and/or to integrate them into the global process model pursued in the present work. The model to develop shall, therefore, account with the several multi-physical descriptions reviewed herewith, adapting, whenever applicable, to the distinctive characteristics of the FW manufacturing process.

CHAPTER 3

PROCESS MODEL

3.1. Modelling Strategy

In order to model the FW composites manufacturing process, analytical descriptions of the different physical phenomena acting in this process were established and are detailed herewith. The identification of the phenomena governing the consolidation process at the layer/laminate level was achieved by combining the knowledge gathered through a comprehensive literature review (chapter 2), the study of the physics of the process and the practical experience on the process. Upon this, the most relevant assumptions were drawn and a modelling strategy was devised.

The modelling strategy was settled upon the following principles and ideas:

- the physics of the process was analysed and studied in three inter-related groups of phenomena, namely:
    - the “purely” mechanical phenomena, relating forces, pressures, stresses, strains through elastic and/or elastic-apparent properties of the materials and tools,
    - the flow and compaction related phenomena, describing the displacements and motions of the matrix and fibres,
    - the thermo-chemical phenomena, defining the matrix rheological state,
- the model accounted for both thermosetting and thermoplastic matrix based composites,
- each phenomenon (or group of phenomena) corresponding to an identified sub-process was decoupled from the others as much as possible and modelled separately in a dedicated sub-model,
- for the numerical implementation of the model, each sub-process modelled analytically corresponded to a sub-routine and a main routine guaranteed the correct interaction and flow of variables between those,
- the main input variables of the global model corresponded to the main user-controllable process parameters,
- the main output variables of the global model corresponded to the main mechanical and geometrical properties of the produced laminates,
- the global model was built in a modular configuration, grouping and combining every sub-models for each process configuration accounted for.

The sub-division of the analysis in three groups of phenomena, allowed to separate and focus the study of phenomena of different physical natures. The interactions and properties that could be modelled by exact mechanical analytical descriptions were grouped into the mechanical analysis. The other physical phenomena that govern the matrix/fibres interactions and are described by empirical expressions were grouped into the flow/compaction analysis. The thermal and chemical phenomena governing the curing/crystallization and rheology of the matrix were grouped in the thermo-chemical analysis. Although the analyses could be organized differently, this sub-division is the one that better reveals the multi-physical nature of the FW process, thus identifying the main fields of physics to be studied and modelled.

The option of accounting for both thermosetting and thermoplastic matrices, even if slightly increasing the complexity and extent of the study and the model itself, appeared to be of greater usefulness for the present industrial need. In the past, authors treated thermosetting and thermoplastic based materials in different and separated studies. Moreover, thermoplastic composite manufacturing process models have been far less studied than thermosetting ones. However, since both these process configurations are currently widely used in the industry and that a modelling tool with wider and generic applicability is pursued, this option was taken within the strategy established.

Attention was also given to the fact that the process controllable parameters are those variables that the FW process designer and user mostly understands and is actually able to control. Hence, the main input variables of the global process model correspond to these parameters, in view of attributing the greatest usefulness to this tool. The outputs, on the other hand, correspond to the parameters that engineers and physicists analyse when driving a quantitative evaluation of the quality of the composite part produced by this process. Even though it is obvious, the establishment of relationships between the user-controllable variables and the relevant mechanical and geometrical properties of the component was a major driver of this study and is the only way to make this model usable and interesting.

The decoupled modelling approach of the several sub-processes aimed at achieving a modular configuration for the global model. This feature turned the model both intuitive and easy to improve by replacing the module(s) related to the sub-process(es) to be improved or described differently.

Throughout this chapter, the analytical descriptions of the different sub-models, corresponding to the several sub-processes and physical phenomena interacting in the FW process, are presented. As mentioned above, the analysis was grouped into the mechanical, the flow/compaction and the thermo-chemical analyses. The theoretical background supporting each sub-model is also addressed.

3.2. Mechanical Analysis

In this section, the sub-models relating to the general mechanics of the FW process are described in detail. In this analysis, the external forces applied to the laminate being processed are related with the stresses and strains through analytical models derived from solid mechanics and theory of composite laminates. Namely, the consolidation pressure and the stress-strain sub-models are presented.

3.2.1. Consolidation Pressure Sub-Model

During the FW process the initial fibre tension, $F_{winding}$, that is prescribed to the fibre bundle being laid onto the mandrel (or the fibre bed beneath) induces a pressure build-up phenomenon. This phenomenon is herein described and modelled. In a first approach, simplifying assumptions are made so that the fundamentals of the phenomenon are clearly identified and gradually analysed. The objective is that the complexity of the real phenomenon is approximated in a step by step reliable procedure. Firstly, a comprehensive analytical description is drawn. Then, considerations are made concerning the boundary conditions and specificities of this sub-model.

3.2.1.1. Analytical Description

In Figure 33 a cross sectional scheme of the FW process on a cylindrical mandrel is shown. For simplicity, hoop winding is depicted. Therefore, no carriage axial movement exists and layers are continuously wound directly over the previous ones (fibre bed). The winding angle, ϕ, is 90º. This is the simplest kinematical case in FW.

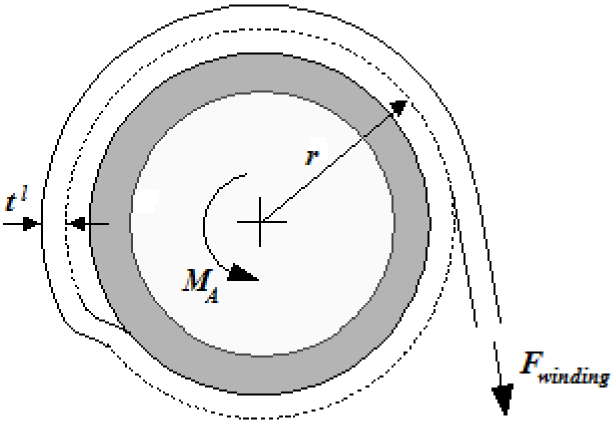

Figure 33 – Schematic cross sectional view of a hoop winding.

An analogous study on thin cylinders subjected to internal pressure allows an easy understanding of the mechanics involved in this part of the process. In such case, the circumferential (hoop) stress, $\sigma_{\theta\theta}$, in the thin wall of the cylinder is given by [205,206]:

$$\sigma_{\theta\theta} = \frac{P\,r}{t^w} \,, \tag{3.1}$$

where P is the internal pressure to which the thin cylinder is subjected, r is the internal radius of the cylinder and t^w is the cylinder wall thickness. Figure 34 helps in understanding this relation. For easiness of perception, only the relevant components of the internal pressure are presented (in reality the pressure acts perpendicularly to the surface).

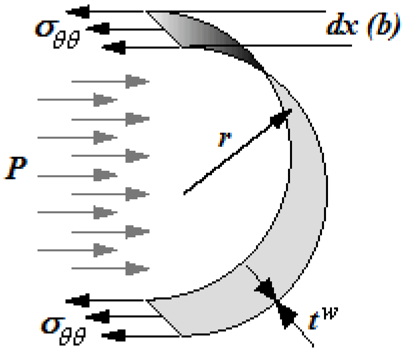

Figure 34 – Cut view of a thin-walled cylinder subjected to internal pressure.

Similarities between the mechanics of both phenomena depicted in Figure 33 and 34 are noticeable. In the problem of a thin cylinder subjected to internal pressure this loading condition, P, causes the cylinder wall to be stressed in circumferential (hoop), radial and longitudinal (axial) directions. Reversely, in the hoop winding is the imposition of a longitudinal stress in the fibre bundle (analogically equivalent to the circumferential stress, $\sigma_{\theta\theta}$, in the thin shell) that causes a pressure, $p_{winding}$, to appear as the bundle is wound over the rigid mandrel. Hence, if one single wound layer is considered, by analogy the pressure, $p_{winding}$, built-up at its inner surface is given by:

$$p_{winding} = \frac{t^l\ \sigma_{\theta\theta}}{r} = \frac{F_{winding}}{r\ b}\ , \tag{3.2}$$

where $\sigma_{\theta\theta}$ is the hoop stress, r is the reference radius of the wound layer, t^l is the thickness of the wound layer, $F_{winding}$ is the winding force imposed to the fibre bundle and b is the fibre bundle bandwidth.

In fact, due to the axisymmetric and constant cross-section characteristics of the laminate, the pressure build-up at the mandrel-layer interface, $p_{winding}$, is statically equilibrated in the longitudinal (axial) and circumferential (hoop) directions. Therefore, only its radial component is considered for modelling purposes hereafter.

As a new layer is wound, additional external pressure is applied to the fibre bed beneath composed by the previously wound layers, thus creating a pressure gradient in the laminate. The radial pressure at the inner surface of the generic *j*th layer, $p^j_{winding}$, is the sum of the pressures acting in the layers that lie on it, which is then given by:

$$p^j_{winding} = \sum_{i=j}^{n} \frac{F_{winding}}{r^i\ b^i}\ , \tag{3.3}$$

where n is the number of wound layers, r^i is the reference radius of the *i*th layer ($j < i \leq n$), b^i is the fibre bundle bandwidth of the *i*th layer.

This simplified analytical model of the radial pressure generated in a hoop winding is valid under several reasonable assumptions, such as:

- the thickness, t^l, of the layers is small when compared to the perimeter;
- the deformability of each layer is negligible;
- the longitudinal stress imposed to the fibre bundles being wound, $\sigma_{\theta\theta}$, is uniformly distributed between resin and fibres composing the bundles;
- friction forces between composite layers and/or mandrel and composite layer as well as interlaminar slippage are negligible;
- thermo-chemical expansions and/or contractions of the laminate have negligible contributions to the build-up of the consolidation pressure;
- inertial and gravitational forces are negligible.

In a more accurate analysis, some of these assumptions might need to be re-evaluated as they coarsely approach the reality.

In fact, when a new layer is wound, the external radial pressure that it builds over the previously wound layers generates two main fibre motion mechanisms. One is the uncured resin viscous flow through the porous fibre bed as it is squeezed. This flow occurs in the radial, longitudinal and transversal directions of fibres, although in most of the modelling approaches only the radial flow is considered, as discussed in chapter 2. The other fibre motion mechanism is the fibre bed compaction itself, behaving as a rapidly stiffening nonlinear spring, which is compressed by the external force applied when a new layer is wound [26]. As the wound lay-up compacts, inner layers have a higher fibre volume fraction and subsequently higher stiffness. These phenomena are detailed and modelled in sections 3.3.1 and 3.3.3, respectively. They oppose, however, the abovementioned assumption that each layer is not deformable.

In early stages of the winding and consolidation process, in which the resin viscosity is low, the interlaminar slippage of adjacent layers may occur due to the inward accommodation of the layers as the resin flows outwards. Low friction factors in such a lubricated system contribute to this mechanism. Moreover, if higher winding tension, $F_{winding}$, is applied more likely it is to occur. This also questions the abovementioned assumption that the interlaminar slippage is negligible. In later stages of the process, thermo-chemical phenomena may induce expansion and/or contraction of the laminate but the higher viscosity of the resin counter-balances these effects.

Equations (3.2) and (3.3) are, thus, reasonably valid for the initial stages of the winding and consolidation process and are considered to properly describe the pressure build-up by the action of the initial winding tension, $F_{winding}$. However, the fibre bed, composed by consolidating resin and fibres, will constantly try to get a new equilibrium state. As said before, after a certain layer being wound, it tends to move inwards and so the circumferential stress initially applied to the fibre bundle may be partially released. The changes in the circumferential (hoop) stress, $\Delta\sigma_{\theta\theta}$, due to the distributed radial displacement of the layer may be evaluated through the following relation:

$$\Delta\sigma_{\theta\theta} = \left(E^f V_f + E^m V_m\right)\Delta\varepsilon_{\theta\theta} \ , \tag{3.4}$$

where E^f is the elastic (Young) modulus of the fibres, V_f is the fibre volume fraction and $\Delta\varepsilon_{\theta\theta}$ is the change in the circumferential (hoop) strain due to the radial displacement of the layer. In this relation, it is assumed that the volume fractions of fibres and resin remain constant, which is of course not accurate. However, this is a reasonable approach to assess the changes in the circumferential (hoop) stresses in each layer from the initial stage in which it is equal to the initial winding tension, $F_{winding}$, to the immediately subsequent stages when new layers are wound over it and the fibre/resin composite is still a lubricated system (resin with low viscosity). The term $E^f V_f + E^m V_m$ represents the composite circumferential (hoop) stiffness.

The change in the circumferential (hoop) strain due to the radial displacement of the layer (homogeneously distributed along its perimeter) is given by:

$$\Delta\varepsilon_{\theta\theta} = -\frac{2\pi r_{initial} - 2\pi r}{2\pi r_{initial}} = \frac{r - r_{initial}}{r_{initial}} , \tag{3.5}$$

where $r_{initial}$ and r are the initial and the actual radial positions of the layer, respectively.

Hence, from equations (3.2), (3.4) and (3.5), the consolidation pressure due to the hoop winding mechanics, $p_{winding}$, is approximated in the early stages of the winding and consolidation process by the following relation:

$$p_{winding} = \frac{F_{winding}}{r_{initial}\, b} + \frac{t^l}{r} \frac{\left(E^f V_f + E^m V_m\right)\left(r - r_{initial}\right)}{r_{initial}} . \tag{3.6}$$

The hoop winding is a particular case of the FW process. It is typically used in sequential combination (or intercalated) with helical and/or polar winding (see Figure 2). In fact, one of the most important parameters in the FW process is the winding angle, ϕ, resulting from the coordinated movement of the rotating mandrel and the moving carriage. In Figure 35 this specificity of FW is schematically depicted.

In consolidated filament-wound laminates it has been observed that the influence of the winding angle on its mechanical properties is not linear within the range $0^\circ \le \phi \le 90^\circ$. For instance, when the in-plane principal stresses are in the ratio 2:1 and the fibres are oriented at an angle close to $\phi \approx \pm \arctan\sqrt{2}$, the stress-strain relations are very sensitive to the value of ϕ and to the relative stiffness of the fibres and matrix [207]. It is, therefore, immediate to observe that the winding angle is a major parameter that influences the physics of the FW process during the winding and consolidation as well.

The effect of the winding angle, ϕ, in the pressure build-up phenomenon may be assessed through the principles of the netting analysis theory [208]. In Figure 36 a schematic representation of the fibre bundles' positioning within the laminate is shown.

From a simple geometrical analysis, the stress components of the composite layer in the circumferential (hoop), $\sigma_{\theta\theta}$, and axial, σ_{zz}, directions generated by the winding tension, $F_{winding}$, imposed to the fibre bundles are retrieved from the equations (2.68) now rewritten as:

$$\begin{aligned}\sigma_{\theta\theta} &= \sigma_{11}\sin^2\phi \quad , \\ \sigma_{zz} &= \sigma_{11}\cos^2\phi \quad ,\end{aligned} \tag{3.7}$$

where σ_{11} is the on-axis local stress imposed to the fibre bundle in its longitudinal direction due to the winding tension and ϕ is the winding angle at which the fibre bundle is wound.

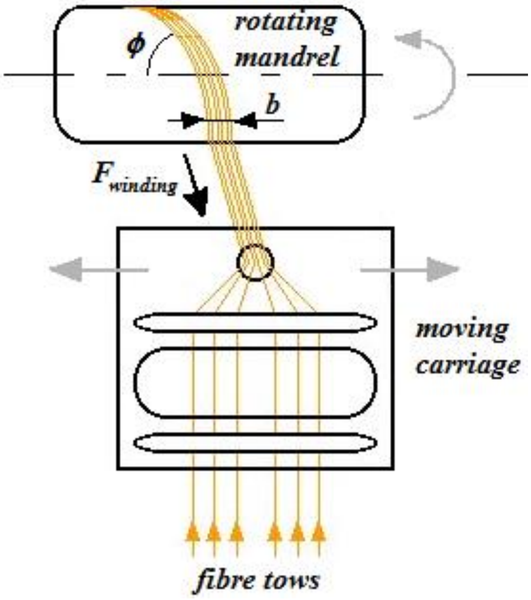

Figure 35 – Schematic representation of FW process.

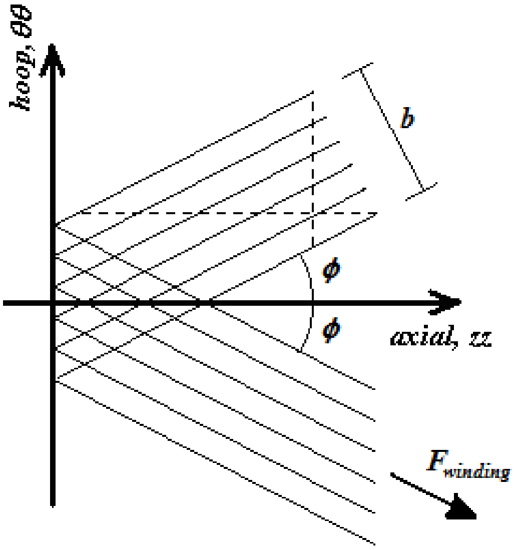

Figure 36 – Scheme of the fibre bundles orientation used in the netting analysis.

While in the netting analysis the resin was assumed to have no load carrying ability, here no such distinction is made since σ_{11} is the local longitudinal stress of the fibre bundle (including the resin). It is obvious that in early stages of the curing/crystallization process both descriptions are reasonably equivalent. However, as the process advances, the latter description (equation (3.7)) is more accurate and, thus, has wider applicability for different process timings and conditions.

Taking the winding angle into consideration and, therefore, generalizing the applicability of this sub-model, from equations (3.6) and (3.7), the consolidation pressure due to the winding mechanics, $p_{winding}$, is approximated in the early stages of the winding and consolidation process by:

$$p_{winding} = \left[\frac{F_{winding} \sin\phi}{r_{initial}\ b} + \frac{t^l}{r} \frac{\left(E^f V_f + E^m V_m\right)\left(r - r_{initial}\right)}{r_{initial}} \right] \sin\phi \ , \tag{3.8}$$

where the circumferential (hoop) stiffness of the composite layer is approximated by the term $\left(E^f V_f + E^m V_m\right)\sin\phi$. This formulation is based on the assumption that the transverse stiffness of the fibre bundle is negligible in the early stages of the process (while the lubricated bundle moves and accommodates).

Consequently, the consolidation pressure in the *j*th layer due to the winding mechanics, $p^j_{winding}$, including the effect of the winding angle, ϕ, and the inward movement of the layer immediately after its winding is calculated as follows:

$$p^j_{winding} = \left[\sum_{i=j}^{n} \frac{F_{winding} \sin^2\phi^i}{r^i\ b^i} \right] + \frac{t^l}{r^j} \frac{\left(E^f V^j_f + E^{m^j} V^j_m\right)\left(r^j - r^j_{initial}\right)}{r^j_{initial}} \sin\phi^j \ , \tag{3.9}$$

where the first term on the right hand side relates to the pressure imposed by newly wound layers that lie on the *j*th layer and the second term relates to the specific radial motion of the *j*th layer.

As discussed in section 2.2.2., the stress externally applied to the composite under consolidation is shared by the fibres and the resin [16-22]. This was expressed in equation (2.4). In equation (2.67) this principle was further generalized for a three-dimensional description [16,27]. In accordance with both descriptions, the consolidation pressure load due to the winding mechanics, $p_{winding}$, is then distributed as:

$$p_{winding} = p_r + p_f \ , \tag{3.10}$$

where p_r is the resin pressure and p_f is the effective stress sustained by the fibres.

The distribution of the pressure built-up during FW at each layer's interface between fibres and resin is governed by the relative content of each within the fibre bundle (and, therefore, in the layer). The higher the fibres volume fraction, V_f, is, higher is their contribution to sustain the applied load and, thus, p_f becomes higher.

For values of V_f below a certain lower limit, V_0, the fibres carry no load since they are separated and fully surrounded by resin and $p_{winding} = p_r$ [18,34]. In such case, the resin flow dominates the consolidation process. On the other hand, if the resin pressure, p_r, is small, fibre deformation becomes the dominant factor in the process. The fibre effective stress, p_f, is then assessed through equation (2.10), discussed and presented in section 2.2.2, now rewritten for the *j*th layer, as follows [34]:

$$p_f^j = \frac{3\pi E}{\beta^4} \frac{\sqrt{\frac{V_f^j}{V_0}} - 1}{\left(\sqrt{\frac{V_a}{V_f^j}} - 1 \right)^4} \, , \tag{3.11}$$

where p_f^j is the effective stress carried by the fibres in the *j*th layer, V_0 is a certain "minimum" fibre volume fraction bellow which the fibres carry no load, V_a is the maximum available fibre volume fraction at which resin flow stops, β is the typical waviness ratio (span length/span height) of the fibres and E is the flexural modulus of the fibres. Since V_0, V_a, β and E are constants assessed experimentally or taken from the available literature for the whole laminate, V_f is the only parameter that changes with position (layers) and time.

From equations (3.9) and (3.11), the consolidation pressure due to the winding mechanics, $p_{winding}^j$, and the effective stress born by the fibres, p_f^j, are calculated for each layer. After knowing those values the resin pressure in each layer interface is easily retrieved from equation (3.10).

3.2.1.2. Boundary Conditions

Typical boundary conditions must be established together with the general modelling description, in order to comply with intrinsic characteristics of the FW process. Different process configurations, such as the geometry and material of the mandrel, the winding angle and speed, may change the proper definition of the boundary conditions to apply to this sub-model.

In the following, a cylindrical mandrel of circular cross-section is considered since this is the most widely used geometry in the FW industry. It is also considered in this model due to its axis-symmetry and, thus, easiness on its mechanical description and experimental utilization for validation purposes. As a consequence, the radial pressure built-up due to the winding mechanics in each composite layer is considered to be of equal value and homogeneous along the circumferential direction of the layer. Additionally, the mandrel material is considered to be "infinitely" rigid and therefore no deformations occur in it. Hence, the radius of the mandrel, $r^{mandrel}$, is constant throughout the duration of the process.

Regarding the winding speed, the process is considered to be reasonably approximated by quasi-static physical analysis and, therefore no dynamic effects are accounted for. Namely, the initial consolidation pressure imposed by the winding of a certain layer is calculated through equation (3.9) and no overshooting of this value is assumed to occur due to eventual high speed contact between the layer being wound and the fibre bed beneath. On the other hand, the time needed to overlap a certain layer, which directly depends on the winding speed and path, is attained in the resin flow sub-model (section 3.3.1).

The winding angle, which may be set within the interval $0^{o} \leq \phi \leq 90^{o}$, imposes that $p_{winding} = 0$ for $\phi = 0^{o}$. For a given winding tension, $F_{winding}$, the consolidation pressure is maximum for $\phi = 90^{o}$. These conditions are easily confirmed by analysing equation (3.9).

When the first layer is wound onto the mandrel the radial pressure (also called consolidation pressure), $p_{winding}$, which is balanced by the winding tension, $F_{winding}$, varies along the layer thickness from one certain finite value at the mandrel/layer interface and the atmospheric pressure at the outer surface. For the determination of the pressure build-up at the mandrel/layer interface due to the winding mechanics when the first layer is wound, equation (3.9) is rewritten as:

$$p_{winding}^{1} = \frac{F_{winding} \sin^{2} \phi}{r^{mandrel} \, b^{1}} \quad , \tag{3.12}$$

where $r^{mandrel}$ is the radius of the mandrel, which is coincident with the inner radius of the first layer during the entire process duration.

Usually, in the FW operation no external pressure is applied and so the boundary condition at the outer surface is that the pressure is zero (or atmospheric pressure). The pressure is assumed to have a linear gradient through the thickness of the first layer and is related to the radial position within the thickness domain as follows:

$$p^{1} = -\frac{p_{winding}^{1}}{t^{l^{1}}} r + p_{winding}^{1} \left(1 + \frac{r^{mandrel}}{t^{l^{1}}} \right) \quad , \qquad r^{mandrel} \leq r \leq r^{mandrel} + t^{l^{1}} \quad , \tag{3.13}$$

where p^{1} is the pressure within the first layer at each radial position r, $p_{winding}^{1}$ is the interface pressure calculated in equation (3.12), $r^{mandrel}$ is the radius of the mandrel and $t^{l^{1}}$ is the thickness of the first layer.

For the *n*th layer being wound the situation is similar to the case of the first layer. In this case, however, due to the winding mechanics, the consolidation pressure, $p_{winding}^{n}$, is established between the newly wound layer and the *n-1* previously wound. In that moment there is a pressure increase at the outer surface of the *n-1* wound layers.

For any other *j*th layer between the first and the nth layer, the inner and outer pressures due to the winding mechanics are easily assessed through equation (3.9), considering the superscripts *j* and *j+1*, respectively.

3.2.2. Stress-Strain Sub-Model

In this section, the stress-strain constitutive relations describing the behaviour of a lamina within a laminate being wound are discussed and the corresponding sub-model is established. The theoretical background supporting the modelling approach is firstly addressed. The sub-model and specific boundary conditions are then analytically described.

3.2.2.1. Theoretical Background

Several stress-strain constitutive relations have been proposed recently for composite laminates. All account for the contribution of the different phases of the composite materials (fibres and matrix, e.g.) thus suggesting a combinatory overall behaviour. Different methods for the determination of the constitutive homogenized elastic properties of the laminates as well as different forms for the constitutive stiffness matrix were studied. Additionally, since the process model intended to define the constitutive behaviour of consolidating laminates, thermo-chemical effects were also reviewed and added to the simple mechanical structural analysis.

3.2.2.1.1. Thermal and Chemical Strains

In a composite laminate under consolidation, there are thermochemical phenomena occurring that influence the stress and/or strain states of the structure. In order to account for these, the total strains to be considered are given by:

$$\varepsilon_T = \varepsilon_e + \varepsilon_{th} + \varepsilon_{ch} \ , \tag{3.14}$$

where ε_e, ε_{th} and ε_{ch} are the elastic-equivalent, the thermal and the chemical strains, respectively.

The elastic-equivalent strains are due to the external mechanical loads applied to the laminate, namely by the winding force, $F_{winding}$. The thermal strains relate directly to the variation of the material temperature, ΔT. The chemical strains relate to the intrinsic shrinkage phenomena occurring in thermosetting curing resins as the degree of cure increases. For thermoplastic resins this last term would be zero.

The local on-axis components of the thermal and chemical strains are calculated as follows:

$$\{\varepsilon_{th}\} = \begin{Bmatrix} \beta_{11}\Delta T \\ \beta_{22}\Delta T \\ \beta_{33}\Delta T \\ 0 \\ 0 \\ 0 \end{Bmatrix} , \qquad \{\varepsilon_{ch}\} = \begin{Bmatrix} \eta_{11}\Delta\alpha \\ \eta_{22}^{j}\Delta\alpha \\ \eta_{33}\Delta\alpha \\ 0 \\ 0 \\ 0 \end{Bmatrix} , \tag{3.15}$$

where β_{ii} are the thermal expansion coefficients of the resin in the ith direction, η_{ii} are the chemical shrinkage coefficients of the resin in the *i*th direction, ΔT and $\Delta\alpha$ are the variation of temperature and degree of cure, respectively, in the material point of interest. The volumetric nature of both the thermal and chemical strains justifies the absence of the distortional components. Moreover, in most cases, both in terms of the type of resin and the processing conditions, the three normal *ii* components of β and η are equal due to the isotropic nature of the resin.

As a result, the total on-axis strain tensor can be calculated as follows:

$$\{\varepsilon_T\} = \begin{Bmatrix} \varepsilon_{11} - \beta_{11}\Delta T \ - \eta_{11}\Delta\alpha \\ \varepsilon_{22} - \beta_{22}\Delta T - \eta_{22}\Delta\alpha \\ \varepsilon_{33} - \beta_{33}\Delta T - \eta_{33}\Delta\alpha \\ \gamma_{23} \\ \gamma_{31} \\ \gamma_{12} \end{Bmatrix} , \tag{3.16}$$

where the engineering shear strains, γ_{ij}, are defined as:

$$\gamma_{ij} = \varepsilon_{ij} + \varepsilon_{ji} = 2\,\varepsilon_{ij} \ . \tag{3.17}$$

3.2.2.1.2. Composite Elastic Properties

The prediction of the elastic-apparent properties of a composite lamina typically involves micromechanical analyses of the fibre bundles geometry, morphology and behaviour. Nevertheless, these analyses are scalable to be used in meso- and/or macro-mechanical analyses of the laminate structure. The elastic-apparent properties of the composite, including the combined contribution of both fibres and matrix, can be predicted by several approaches: analytical, semi-analytical and numerical methods.

The physical symmetry of the fibres and matrix, in a unidirectional composite, enables to infer that there is a plane of isotropy (normal plane to the direction of the aligned fibre reinforcements). Therefore, it is accurate to recognize one lamina as a transversely isotropic material. Assuming, then, transverse isotropy, only five independent elastic constants are necessary to determine the compliance or the stiffness matrix. Some helpful relations are presented to obtain all the properties (dependent and/or independent properties), needed for the determination of the stiffness matrix.

Within the several analytical methods proposed for the prediction of the elastic engineering constants, numerous approaches can be used [209], namely mechanics of materials, netting analysis, self-consistent models, variational techniques using energy bounds principles or exact solutions. On the other hand, semi-analytical or semi-empirical methods contain experimental parameters in order to simplify the analytical equations, include the degree of contiguity of fibres (if they are isolated or if they contact each other, account for imperfections in fibre alignment and/or overcome some limitations of other methods.

Tsai [210], obtained expressions for the longitudinal and transverse Young's moduli, E_1 and E_2, longitudinal Poisson's ratio, ν_{12}, and longitudinal shear modulus, G_{12}, considering the contiguity of fibres, $0 < C < 1$, as depicted in Figure 37.

The Voigt model [211] predicts the independent elastic constants, based on an assumption that the strains are equal for both constituents of the composite (fibres and matrix), when external loading is applied. It is commonly known as the rule of mixtures, and the properties can be estimated through the effective components of the stiffness matrix of the lamina, C_{ij}, which is obtained by a linear combination of the corresponding quantities for the matrix, C_{ij}^{m}, and the fibres, C_{ij}^{f}, weighted by the volume fractions of matrix and fibre, V_m and V_f respectively, as follows:

$$C_{ij} = V_m C_{ij}^{m} + V_f C_{ij}^{f} \quad . \tag{3.18}$$

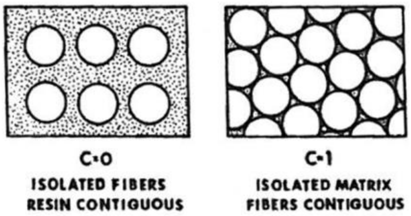

Figure 37 – Fibre contiguity limits [111].

The Reuss model [212] proposes that stresses remain constant throughout the composite. This is the rule of mixtures for the compliance matrix, S_{ij}, or usually known as the inverse rule of mixtures, and is formulated as follows:

$$S_{ij} = V_m S_{ij}^{m} + V_f S_{ij}^{f} \quad . \tag{3.19}$$

Voigt and Reuss models do respectively overestimate and underestimate the stiffness components, as is shown in the comparative analysis for the various methods.

The Hashin-Hill Bounds model determines upper and lower bounds for the independent elastic constants. The basis for the determination of a lower bound on the effective properties is the application of the principle of minimum complementary energy, and for the upper bound is the application of the minimum potential energy.

Hashin and Rosen [213] extended the previous work to fibre-reinforced materials. The composite cylinder assemblage model was then established based on a particular geometric arrangement of the composite material. It is possible to identify two phases on each concentric cylinder, the fibre phase, which is surrounded by an annulus of matrix material. The analysis of a concentric cylinder only allows the determination of four of the five independent elastic constants needed. Thus, a new model was introduced, which is intimately related with the composite cylinders model.

The dilute methods ignored the interaction between particles or phases, which is an unrealistic assumption for random distributions, even at the lower fibre content range. In order to account for these interactions, Mori and Tanaka [214] constructed a fourth order tensor, which is the most widely used approach, that physically represents the relation between the uniform strain in the inclusion (fibre), surrounded by an all-matrix material under an imposed uniform strain at infinity. Benveniste [215] restated the original method, and Dvorak [216] presented explicit expressions for the engineering constants of unidirectional composites, assumed as transversely isotropic materials. The five constants are expressed as [217]:

$$p^* = \frac{2V_f p_f p_m + V_m\left(p_f p_m + p_m^2\right)}{2V_f p_m + V_m\left(p_f + p_m\right)} = G_{12}^* \ , \tag{3.20}$$

$$k^* = \frac{k_f k_m + m_m\left(V_f k_f + V_m k_m\right)}{V_f k_m + V_m k_f + m_m} = -\left(\frac{1}{G_{23}^*} - \frac{4}{E_2^*} + \frac{4\left(\nu_{12}^*\right)^2}{E_1^*}\right)^{-1} \ , \tag{3.21}$$

$$m^* = \frac{m_f m_m\left(k_m + 2m_m\right) + k_m m_m\left(V_f m_f + V_m m_m\right)}{k_m m_m + \left(k_m + 2m_m\right)\left(V_f m_m + V_m m_f\right)} = G_{23}^* \ , \tag{3.22}$$

$$l^* = \frac{V_f l_f\left(k_m + m_m\right) + V_m l_m\left(k_f + m_m\right)}{V_f\left(k_m + m_m\right) + V_m\left(k_f + m_m\right)} = 2k^*\nu_{12}^* \ , \tag{3.23}$$

$$n^* = V_f n_f + V_m n_m + \left(l^* - V_f l_f - V_m l_m\right)\frac{l_f - l_m}{k_f - k_m} = E_1^* + 4k^*\left(\nu_{12}^*\right)^2 = E_1^* + \frac{\left(l^*\right)^2}{k^*} \ . \tag{3.24}$$

In a considerably different and unique approach, a direct relation between the fibre bed stiffness, E^{fb}, and the fibre volume fraction, V_f, was used for stiffness evaluation of the composite by Cai and Gutowski [27]. Assuming as well a transversely isotropic behaviour, the fibre bed stiffnesses in the on-axis local 2-3 plane (Figure 14) are considered to have the same value, E_b^{fb}, in which the subscript b refers to bulk. The layer stiffnesses are then calculated by the following relations:

$$\begin{aligned} E_1^{fb} &= V_f E^f \frac{\pi/4}{V_a} \ , \\ E_b^{fb} = E_2^{fb} = E_3^{fb} &= \frac{\dfrac{\sqrt{V_a}}{\sqrt{V_f}}\left[5 - \dfrac{\sqrt{V_f}}{\sqrt{V_a}} - 4\dfrac{\sqrt{V_0}}{\sqrt{V_f}}\right]}{\dfrac{\beta^4}{3\pi E^f}\left[\dfrac{\sqrt{V_a}}{\sqrt{V_f}} - 1\right]^5} \ , \end{aligned} \tag{3.25}$$

where E_i^{fb} are the fibre bed stiffness in the ith local direction, V_a is the maximum available volume fraction of fibres at which the resin flow stops [34], V_0 is the minimum volume fraction of fibres below which fibres do not carry transverse load, $\beta = L/a$ is the ratio between the characteristic length, L, and amplitude, a, of the fibre waviness pattern, E^f is the fibre's elastic modulus. As previously discussed in chapter 2, this approach was based on the beam theory, and was drawn to specifically attain the waved misalignment of fibres, as an intrinsic characteristic of the FW process. Therefore, this simpler set of equations is very attractive. Despite the fact that it is possible to find in the literature empirical values for V_a, V_0 and β, they shall be assessed experimentally as they strongly depend on the material system and processing conditions used.

3.2.2.1.3. Stress-Strain Constitutive Relations in Composite Lamina

The most commonly accepted constitutive relationships for composite laminates are based on the generalized Hooke's law and were already reviewed in chapter 2. Namely, in equations (2.69), (2.70) and (2.72), the law applied to anisotropic, orthotropic and transversely isotropic materials was respectively expressed. The main challenge is then to select the most correct and adequate form, observing that during the FW process, the compaction mechanisms act almost only in the radial direction. This aspect promotes different stiffening behaviours between the local transverse (2-direction) and radial (3-direction) directions. Such effect tends to attribute a local orthotropic nature, rather than transversely isotropic, to the composite laminate being wound and consolidated. Most previous authors studying the FW process, however, modelled the laminate under assumptions of transverse isotropy.

Nonetheless, two other topics assume greater relevance for the FW process modelling: the correct contemplation of the matrix contribution to the overall behaviour through all the winding and curing/consolidation stages and the introduction of specific features, such as intrinsic defects or variations in properties, which have particular relevance in this process. The contribution of the viscous matrix to the composite behaviour is normally accomplished through its elastic-apparent properties at each moment. Its properties before complete cure/consolidation are almost not studied and no reliable or accepted data exists in literature. Moreover, each matrix system has its own characteristic evolution during curing/consolidation. Regarding the specific defects, fibre waviness is highlighted as an intrinsic phenomenon in the FW process. As mentioned above, some constitutive relations developed in the past accounted for this effect. This will be further addressed herein.

The shear stresses and strains that are present in a composite laminate have different effects in its behaviour. At the on-axis local level, the longitudinal shear mode allows aligned fibres to accommodate the complex curvature of the real parts while the transverse shear mode is often unwanted as it can lead to fibre waviness [27]. Terms like "fibre wrinkles", "fibre imperfections" or "marcel defects" have been used to refer to this manufacturing defect. It has been observed to occur on, or through the thickness of, the plane of lamination [108]. The fibre tows or bundles are not perfectly straight nor perfectly aligned. It is, thus, practically unavoidable to have some waviness, misalignment, entanglement or even breakage within a fibre bundle [16]. Moreover, fibre waviness is a type of manufacturing defect that occurs especially during the FW process [109] given the specific constraints applied to the fibre bundles being wound and overwrapped by newly wound layers.

Since the exact waviness pattern and its degree of regularity is often of difficult assessment, it is reasonable to assume some certain patterns with simple or convenient analytical descriptive expressions. Sinusoidal waviness patterns were suggested as reasonable approximations [27,109,218-220] where the characteristic amplitude, a, and length, L, are the most relevant parameters.

Hsiao and Daniel [109], presented a different approach where the regular local on-axis compliance matrix, $\left[S^{reg}\right]$, is transformed to follow the fibres' path. The transformed local compliance matrix, $\left[S^{wav}\right]$, is, then, given at each point by:

$$\left[S^{wav}\right]=\left[R\right]\left[T^{wav}\right]^{-1}\left[R\right]^{-1}\left[S^{reg}\right]\left[T^{wav}\right]^{-T} , \tag{2.75}$$

where $\left[T^{wav}\right]$ is the waviness transformation matrix for each θ at each point, $[R]$ is the Reuter matrix (to compatibilize the strain tensorial notation). Note that $\left[S^{reg}\right]$ is the inverse matrix of the stiffness matrix presented in equations (2.69), (2.70) and (2.72). The waviness transformation matrix was given by:

$$\left[T^{wav}\right]=\begin{bmatrix} \cos^2\theta & 0 & \sin^2\theta & 0 & 2\cos\theta\sin\theta & 0 \\ 0 & 1 & 0 & 0 & 0 & 0 \\ \sin^2\theta & 0 & \cos^2\theta & 0 & -2\cos\theta\sin\theta & 0 \\ 0 & 0 & 0 & \cos\theta & 0 & -\sin\theta \\ -\cos\theta\sin\theta & 0 & \cos\theta\sin\theta & 0 & \left(\cos^2\theta-\sin^2\theta\right) & 0 \\ 0 & 0 & 0 & \sin\theta & 0 & \cos\theta \end{bmatrix}, \tag{3.26}$$

where θ is the misalignment angle at each point of the assumed fibre waved path.

Then, the components of the constitutive local on-axis compliance matrix of a waved composite were assessed from averaging the components of the transformed local compliance matrix over one wavelength of the fibres' path, as follows:

$$\bar{S}_{ij}^{wav}=\frac{1}{L}\int_0^L S_{ij}^{wav}dx\ , \tag{2.76}$$

where x is the fibre "ideal" axis and L is the wavelength of the sinusoidal pattern of the fibres. In this way, the classical stress-strain constitutive relations used to describe composite laminates' behaviour were adapted to include the effect of fibre waviness.

The adequate transformations to the global coordinate system need to be properly accounted as well, in order to match the stress, strain and stiffness properties with the principal directions used for the other physical phenomena being modelled.

The off-axis quantities of a generic tensor, $\left[\bar{X}\right]$, are then related to its on-axis quantities, $[X]$, as follows [113]:

$$\left[\bar{X}\right]=[T]^{-1}[X][T]^{-T}\ , \tag{3.27}$$

where $[T]$ is the transformation matrix. For the present case, the transformation matrix from the on-axis (1,2,3) coordinate system to the off-axis (z,θ,r) cylindrical coordinate system is given by [113]:

$$[T]=\begin{bmatrix} \cos^2\phi & \sin^2\phi & 0 & 0 & 0 & 2\cos\phi\sin\phi \\ \sin^2\phi & \cos^2\phi & 0 & 0 & 0 & -2\cos\phi\sin\phi \\ 0 & 0 & 1 & 0 & 0 & 0 \\ 0 & 0 & 0 & \cos\phi & -\sin\phi & 0 \\ 0 & 0 & 0 & \sin\phi & \cos\phi & 0 \\ -\cos\phi\sin\phi & \cos\phi\sin\phi & 0 & 0 & 0 & \left(\cos^2\phi-\sin^2\phi\right) \end{bmatrix}, \tag{3.28}$$

where ϕ is the applicable winding angle.

3.2.2.2. Analytical Description

The stress-strain sub-model was developed after the review of the several methods proposed by previous authors for composite laminates and the analysis of the particularities of the FW process. Assumptions were made and a step by step sequence for calculation of the global constitutive relations was settled.

3.2.2.2.1. Modelling Assumptions

The main assumptions and simplifications in this modelling approach are:

- Unlike other approaches available in literature, the fibre bundles are assumed to have an orthotropic behaviour, instead of a transversely isotropic one. The radial compaction that occurs during the process, leads to different elastic properties in the local 2- and 3-directions. Therefore, orthotropic relations are used through the modelling stages and different evolutions for the elastic properties in the 2- and 3-directions are inputted;
- The reference unit cell considered is a portion of the wavy fibre bundle, as depicted in Figure 38;

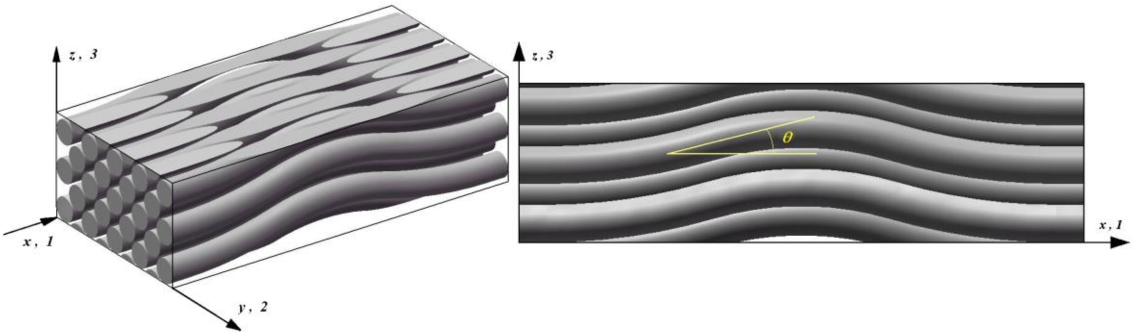

Figure 38 – Representative volume element (RVE) corresponding to a single period of waved fibre bundle portion. Trimetric (left) and lateral (right) views.

- The layers, composed of resin and bundles of oriented fibres, behave as homogeneous material with weighted properties determined from the constituents' properties;
- The local on-axis (1,2,3) stiffness components are assessed from transforming the regular orthotropic stiffness matrix and then averaging its components over one wavelength;
- The transformation of coordinates, from local (1,2,3) to global (z, θ, r), as presented here, is limited to axis-symmetric laminates. However, due to the local nature of the modelling, its suitability to virtually model any other geometry only depends on the definition of the transformation matrix, $[T]$;
- The resin flow and thus the fibre bed compaction phenomena occur only in the radial direction, r, across the laminate's thickness;
- Due to the storage conditions of the dry fibres in rovings, the bundle twisting promoted by this manufacturing technique, their deposition over "rigid" surfaces during the winding operation and the constraints promoted by layer's overwrapping and thermal and chemical effects, the fibres are

assumed to have a waviness pattern characterized by a function of the type [27]:

$$z = \frac{a}{2}\left(1 - \cos\frac{2\,\pi\,x}{L}\right) \,, \tag{3.29}$$

where z is the transversal position measured perpendicularly to the "ideal" axis, x, along the fibre, a and L are, respectively, the characteristic amplitude and length of the sinusoidal pattern of the fibres. For completeness, the fibre misalignment angle at each point is given by:

$$\theta = \tan^{-1}\left(\frac{\pi\,a}{L}\sin\frac{2\pi\,x}{L}\right) \;; \tag{3.30}$$

- Resin intrinsic properties that depend on the degree of cure, such as thermal expansion coefficient, β, chemical shrinkage coefficient, η, and thermal conductivity, k, are assumed to vary linearly between the known initial and final values. Also the "elastic-apparent" constants of the resin, like Young's modulus, E^m, shear modulus, G_{ij} and Poisson's ratios, ν_{ij}, are assumed to vary in the same manner with the degree of cure, α. The following piecewise linear relations are considered to represent the variation of such properties before and after the resin reach gelation, α_{gel}:

$$\begin{cases} Y = \overline{\alpha}\, Y^c + (1-\overline{\alpha}) Y^{uc} & \alpha < \alpha_{gel} \\ Y = Y^c & \alpha \geq \alpha_{gel} \end{cases} \,, \tag{3.31}$$

where Y represents any of the above mentioned material properties, Y^{uc} and Y^c its known values at the initial reference cure state and after cure (consolidation), respectively. The quantity $\overline{\alpha}$ is the ratio defined as:

$$\overline{\alpha} = \frac{\alpha - \alpha_0}{\alpha_{gel} - \alpha_0} \;. \tag{3.32}$$

3.2.2.2.2. Composite elastic properties

The various methods available to determine the composite homogenized properties were compared through evaluating their results for pre-selected cases. The material properties used as constituents are indicated in Table 1. No difference was observed for the longitudinal Young's modulus calculation. In contrast, relevant differences were observed in the other four elastic properties' calculations, which are depicted in Figure 39. The comparative predictions were realized for the range of fibre volume fraction, V_f, between 0.45 and 0.8.

From the results one may observe that the Reuss model typically underestimates the elastic properties, except for the Poisson's ratio. The Voigt model presents consistent overestimations. The Mori-Tanaka method's predictions consistently fitted within the Hashin-Hill bounds and agreed with the concentric cylinders assembly model(s).

Table 1 – Material elastic properties of the constituents used for evaluation of the available methods for determination of the composite homogenized properties.

Constituent	Material	E_1 [GPa]	E_2 [GPa]	G_{12} [GPa]	ν_{12}	G_{23} [GPa]
fibres	AS4	225	15	15	0.2	7
matrix	3501-6	3.35	3.35	1.567	0.34	1.567

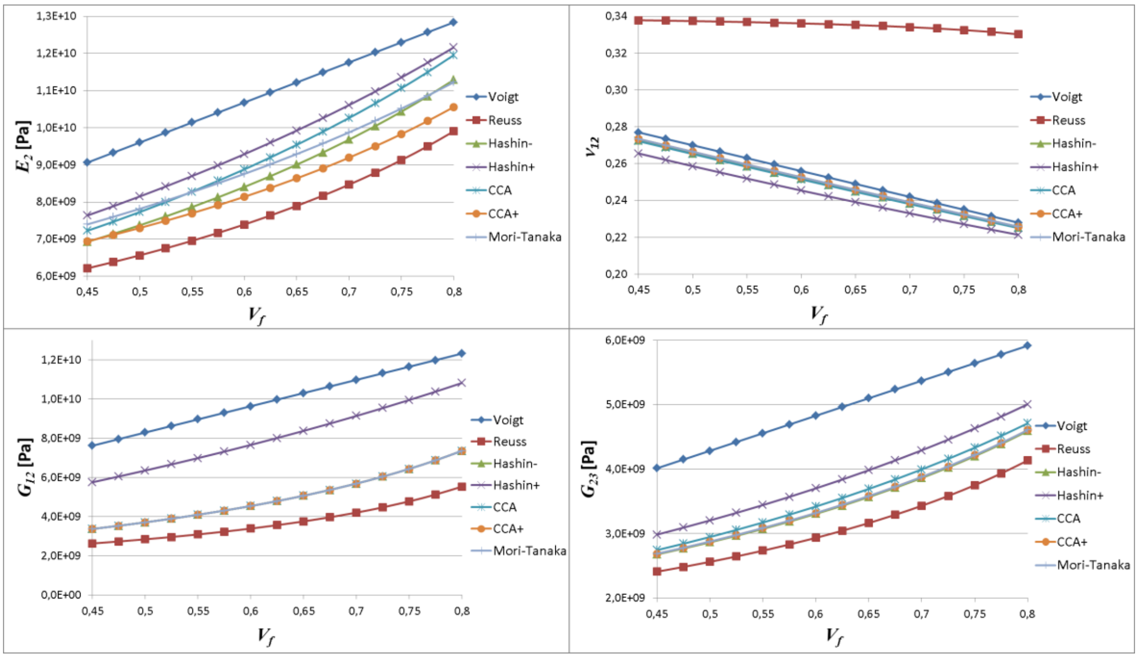

Figure 39 – Prediction of the composite homogenized elastic properties by several methods, for a fibre volume content range between 0.45 and 0.8.

These results enhanced the attractiveness of the Mori-Tanaka method, and are in line with previous analyses and conclusions established by other authors. Namely, looking to the accuracy of this method for periodic and more complex arrangements [221], for cases with aligned inclusions (such as fibres) [222] and its easiness of implementation [223].

Hence, the Mori-Tanaka method was selected and preferentially used in this model to compute the elastic properties of the composite layers at each time instant.

3.2.2.2.3. Local On-axis Stress-Strain Constitutive Relationship

Within the frame of the present process model, the stress-strain constitutive relations are used to calculate the stress components given the strain and stiffness tensors at each instant. The total strain components are calculated as specified in equations (3.14) to (3.17). The local on-axis constitutive orthotropic stiffness matrix, $\left\lfloor C_{ij} \right\rfloor$, defined in equations (2.70) and (2.71), is then populated with the updated layer elastic constants calculated from equations (3.20) to (3.24). The averaged transformed ("waved") local stiffness matrix, $\left[\overline{C}_{ij}^{wav}\right]$, which accounts for the fibre waviness, is calculated as follows:

$$\left[\overline{C}_{ij}^{wav}\right]=\frac{1}{L}\int_{0}^{L}\left[T^{wav}\right]^{-1}\left[C_{ij}\right]\left[R\right]\left[T^{wav}\right]\left[R\right]^{-1}dx \ , \tag{3.33}$$

where $\left[T^{wav}\right]$ is the waviness transformation matrix for each θ at each point, presented in equation (3.26), $\left[R\right]$ is the Reuter matrix, x is the fibre "ideal" axis and L is the wavelength of the sinusoidal pattern of fibres.

The constitutive relationship at the local on-axis coordinate system, keeping the consideration of orthotropic material, is thus given by:

$$\begin{Bmatrix}\sigma_{11}\\ \sigma_{22}\\ \sigma_{33}\\ \tau_{23}\\ \tau_{31}\\ \tau_{12}\end{Bmatrix}=\left[\overline{C}_{ij}^{wav}\right]\begin{Bmatrix}\varepsilon_{11}-\beta_{11}\Delta T-\eta_{11}\Delta\alpha\\ \varepsilon_{22}-\beta_{22}\Delta T-\eta_{22}\Delta\alpha\\ \varepsilon_{33}-\beta_{33}\Delta T-\eta_{33}\Delta\alpha\\ \gamma_{23}\\ \gamma_{31}\\ \gamma_{12}\end{Bmatrix} \ , \tag{3.34}$$

The 21 independent components of the un-averaged waviness transformed local matrix, $\left[C_{ij}^{wav}\right]=\left[T^{wav}\right]^{-1}\left[C_{ij}\right]\left[R\right]\left[T^{wav}\right]\left[R\right]^{-1}$, are expressed as:

$$\begin{gathered}
C_{11}^{wav}=C_{11}m^{4}+C_{33}n^{4}+\left(2C_{13}+4C_{55}\right)m^{2}n^{2} \ , \\
C_{12}^{wav}=C_{12}m^{2}+C_{23}n^{2} \ , \\
C_{13}^{wav}=C_{13}\left(m^{4}+n^{4}\right)+\left(C_{11}+C_{33}-4C_{55}\right)m^{2}n^{2} \ , \\
C_{15}^{wav}=\left(C_{11}-C_{13}\right)m^{3}n+\left(C_{13}-C_{33}\right)mn^{3}-2C_{55}\left(m^{2}-n^{2}\right)mn \ , \\
C_{22}^{wav}=C_{22} \quad , \quad C_{23}^{wav}=C_{12}n^{2}+C_{23}m^{2} \quad , \quad C_{25}^{wav}=C_{12}mn-C_{23}mn \ , \\
C_{33}^{wav}=C_{33}m^{4}+C_{11}n^{4}+\left(2C_{13}+4C_{55}\right)m^{2}n^{2} \ , \\
C_{35}^{wav}=\left(C_{13}-C_{33}\right)m^{3}n+\left(C_{11}-C_{13}\right)mn^{3}+2C_{55}\left(m^{2}-n^{2}\right)mn \ , \\
C_{44}^{wav}=C_{44}m^{2}+C_{66}n^{2} \quad , \quad C_{46}^{wav}=C_{66}mn-C_{44}mn \ , \\
C_{55}^{wav}=\left(C_{11}+C_{33}-2C_{13}\right)m^{2}n^{2}+C_{55}\left(m^{2}+n^{2}\right)^{2} \ , \\
C_{66}^{wav}=C_{66}m^{2}+C_{44}n^{2} \ , \\
C_{14}^{wav}=C_{16}^{wav}=C_{24}^{wav}=C_{26}^{wav}=C_{34}^{wav}=C_{36}^{wav}=C_{45}^{wav}=C_{56}^{wav}=0 \ ,
\end{gathered} \tag{3.35}$$

where m and n are the director cosine and sine of the waviness transformation matrix, respectively, and are assessed from the deformed shape of the chosen sinusoidal path, presented in equation (3.29), written as:

$$m=\cos\theta=\frac{1}{\sqrt{1+\tan^2\theta}}=\frac{1}{\sqrt{1+\frac{A^2\sin^2\left(\frac{2\,\pi\,x}{L}\right)\pi^2}{L^2}}}\ ,$$
$$n=\sin\theta=\frac{\tan\theta}{\sqrt{1+\tan^2\theta}}=\frac{A\sin\left(\frac{2\,\pi\,x}{L}\right)\pi}{L\sqrt{1+\frac{A^2\sin^2\left(\frac{2\,\pi\,x}{L}\right)\pi^2}{L^2}}}\ , \tag{3.36}$$

and the integration terms to calculate the averaged transformed ("waved") local stiffness matrix, $\left[\overline{C}_{ij}^{wav}\right]$ are calculated as follows:

$$\frac{1}{L}\int_0^L m^p n^q=0 \qquad (p,q=odd\ \ integer)\ ,$$
$$\frac{1}{L}\int_0^L m^4=\frac{\alpha^2+2}{2\left(1+\alpha^2\right)^{3/2}}\ ,\qquad \frac{1}{L}\int_0^L n^4=1-\frac{3\alpha^2+2}{2\left(1+\alpha^2\right)^{3/2}}\ ,$$
$$\frac{1}{L}\int_0^L m^2n^2=\frac{\alpha^2}{2\left(1+\alpha^2\right)^{3/2}}\ ,\qquad \frac{1}{L}\int_0^L m^2=\frac{1}{\left(1+\alpha^2\right)^{1/2}}\ , \tag{3.37}$$
$$\frac{1}{L}\int_0^L n^2=1-\frac{1}{\left(1+\alpha^2\right)^{1/2}}\ ,$$
$$\alpha=\pi\,\frac{A}{L}\ .$$

3.2.2.2.4. Global Off-axis Stress-Strain Constitutive Relationship

Within the scope of assessing the stresses in the laminate, it is necessary to represent the stress states of each and all layers in the same coordinate system. Often, the natural geometrical global coordinate system of the laminate/part is the preferred system. In cylindrical laminates, which is often the case in the FW process, the off-axis (z,θ,r) cylindrical coordinate system is the one to work with. Therefore, the local on-axis stresses, as calculated with equation (3.34), are transformed to the global cylindrical coordinates, through:

$$\begin{Bmatrix}\sigma_{zz}^j\\ \sigma_{\theta\theta}^j\\ \sigma_{rr}^j\\ \tau_{r\theta}^j\\ \tau_{rz}^j\\ \tau_{z\theta}^j\end{Bmatrix}=\left[T\right]^{-1}\begin{Bmatrix}\sigma_{11}\\ \sigma_{22}\\ \sigma_{33}\\ \tau_{23}\\ \tau_{31}\\ \tau_{12}\end{Bmatrix}\ , \tag{3.38}$$

where $\left[T\right]$ is the applicable transformation matrix which is defined in equation (3.28).

The full description of the global off-axis constitutive stress-strain relations, with the transformed stiffness components, $\tilde{C}_{ij}$, explicitly expressed, takes the form below:

$$\begin{Bmatrix} \sigma_{zz} \\ \sigma_{\theta\theta} \\ \sigma_{rr} \\ \tau_{r\theta} \\ \tau_{rz} \\ \tau_{z\theta} \end{Bmatrix} = \begin{bmatrix} \tilde{C}_{11} & \tilde{C}_{12} & \tilde{C}_{13} & 0 & 0 & \tilde{C}_{16} \\ \tilde{C}_{12} & \tilde{C}_{22} & \tilde{C}_{23} & 0 & 0 & \tilde{C}_{26} \\ \tilde{C}_{13} & \tilde{C}_{23} & \tilde{C}_{33} & 0 & 0 & \tilde{C}_{36} \\ 0 & 0 & 0 & \tilde{C}_{44} & \tilde{C}_{45} & 0 \\ 0 & 0 & 0 & \tilde{C}_{45} & \tilde{C}_{55} & 0 \\ \tilde{C}_{16} & \tilde{C}_{26} & \tilde{C}_{36} & 0 & 0 & \tilde{C}_{66} \end{bmatrix} \begin{Bmatrix} \varepsilon_{zz} - \beta_{zz}\Delta T - \eta_{zz}\Delta\alpha \\ \varepsilon_{\theta\theta} - \beta_{\theta\theta}\Delta T - \eta_{\theta\theta}\Delta\alpha \\ \varepsilon_{rr} - \beta_{rr}\Delta T - \eta_{rr}\Delta\alpha \\ \gamma_{r\theta} \\ \gamma_{rz} \\ \gamma_{z\theta} - \beta_{z\theta}\Delta T - \eta_{z\theta}\Delta\alpha \end{Bmatrix} . \tag{3.39}$$

3.2.2.3. Boundary Conditions

The stress level within the laminate has an intrinsic relationship with the pressure developed by the action of the winding force. In fact, the value of radial stress, σ_{rr}, is comparable to the pressure, $p_{winding}$, in both magnitude and history. To the through-the-thickness pressure gradient a stress gradient shall correspond. The stresses, along with the applied pressure, build-up as new layers are wound over the previous ones. In the early stages of the winding, the local on-axis longitudinal stress, σ_{11}, in the ultimate (outer-most) layer is equal to the fibre tension induced by the windinf force, $F_{winding}$.

The radial displacements, and thus the radial strains, ε_{rr}, at the inner-most border of the laminate, which corresponds to the mandrel-composite interface, are null during the entire winding and consolidation stages.

Due to the one-dimensional nature of the present model, the artificial assumptions of zero flow in circumferential, $\theta\theta$, and longitudinal, zz, directions imply an artificial enforcement of zero displacement in those directions. Such simplification holds reasonably since the radial phenomena clearly govern the overall mechanisms.

3.3. Flow/Compaction Analysis

The group of physical phenomena associated with the flow mechanisms are the resin flow itself, the resulting resin mixing between adjacent layers and the fibre bed compaction. In this section, analytical descriptions of these phenomena, each corresponding to a dedicated sub-model, are presented.

3.3.1. Resin Flow Sub-Model

The phenomenon of resin flow is inter-related with the tension applied to the fibre bundle during the FW process. As a new layer is wound, it creates a compaction gradient pressure in previously wound layers (fibre bed beneath). This causes resin to be squeezed and flow through the porous fibre bed. As the laminate compacts, uncured excess resin from previously wound layers bleeds through the fibre bed generating a resin rich region at the outer surface of the laminate.

3.3.1.1. Analytical Description

After the review of the main modelling approaches for viscous flow in porous media, discussed in chapter 2, the fundamental descriptions were selected and included in the present model. Since the process model is explicitly defined with time, the adequate variables to describe the resin flow are either the flow rate or velocity. The latter is applicable when quasi-static and unidirectional flow is being considered, which is the case under analysis.

The velocity with which resin flows through the saturated fibre sheet under tension is related to the pressure gradient, dp/dr, fibre bed transverse permeability, S, and resin viscosity, μ, through the Darcy's type equation for flow in porous media as:

$$\dot{u}^r = -\frac{S}{\mu}\frac{dp}{dr} \quad . \tag{2.11}$$

When the pressure inside the laminate becomes equal to the pressure on its boundaries, the resin flow ceases and the kinematic equilibrium of the laminas is reached.

Once the *n*th layer has passed through the resin rich region, the layer itself compacts. As the fibres within the bundles get closer, its flow resistance increases and the permeability decreases substantially. The relation between the transverse permeability, S, and fibre volume fraction, V_f, is given as [24,34,37]:

$$S = \frac{{r^{f}}^{2}}{4k'}\frac{\left(\frac{\sqrt{V'_a}}{\sqrt{V_f}}-1\right)^3}{\frac{V'_a}{V_f}+1} \quad , \tag{2.17}$$

where r^f is the fibre radius, k' is a modified Kozeny constant ($k' \cong 0.2$ for carbon fibre beds [34]) and V'_a is the maximum available fibre volume fraction at which radial flow stops ($0.76 < V'_a < 0.82$ for carbon fibre beds [34]).

3.3.1.2. Boundary Conditions

Due to the geometrical arrangement of the composite laminate onto the cylindrical mandrel, as well as the necessarily negative value of the radial pressure gradient, the resin flow is known to occur only from inner to the outer regions (outward flow). At the composite-mandrel interface no flow occurs. As mentioned previously, the flow ceases when the pressure gradient becomes null. In practical terms, very high resin viscosity and/or very low permeability promote the same effect of flow ceasing.

When the *n*th layer is wound, the thickness of the resin rich layer is assessed through subtracting the *n*th layer inward displacement to the *n*-sum outer radial position. This definition is slightly different from the one proposed by previous authors [24] and comes from experimental evidence and the conservation of mass principle. Since no relevant changes in density occur during the process, the principle of conservation of mass reasonably holds the effective mass transfer events within the laminate’s thickness.

The values of V'_a used to compute the permeability, depend on the type of fibre packing arrangement considered at the micro-scale. These have relevant influence in the calculation of this and sub-sequent parameters. Therefore, they are referred to and assessed in chapter 4, in the experimental validation procedures.

3.3.2. Resin Mixing Sub-Model

In the FW process, resin from one layer can flow to an adjacent layer. Uncured resin from previously wound layers can flow into the newly wound layer and the effective properties of the layer’s matrix may change significantly. This phenomenon is very intrinsic to wet FW and encloses very relevant influence to the cure/consolidation of the composite laminate.

3.3.2.1. Analytical Description

When two portions of resin of the same type but with different curing/consolidation histories mix, the joint behaviour of the blend follows a new (unknown) path. This is valid for the mechanical and chemo-rheological properties. In order to account for this effect in the process model, one or more physical parameters representative of the changes in the behaviour should be modelled.

In the present model, the effective viscosity of the matrix is one of the most relevant parameters, since it affects the flow ability, and therefore the consolidation, but is directly related with the degree of cure/consolidation which is a fast evolving property during the process. Thus, the viscosity was chosen as the reference property to associate with the resin mixing.

The effective viscosity of a blend can be calculated by a rule of mixtures. In the *m*th layer, the viscosity μ can be calculated by a linear combination as [24]:

$$\mu = \sum_{j=1}^{m} \Psi_j^m \mu_j \ , \tag{3.40}$$

where μ_j are the viscosities of the constituents (from all contributing layers), Ψ_j^m is the relative concentration of the different constituents in the *m*th layer, defined as:

$$\Psi_j^m = \frac{V_r^j}{V_r^m} \ , \tag{3.41}$$

where V_r^j is the volume of resin from the *j*th ply into the *m*th layer and V_r^m is the total volume of resin in the *m*th layer. These volumes are readily calculated once the resin velocity at the layer boundaries is known.

3.3.2.2. Boundary Conditions

The validity of the linear combination of the constituent's viscosity, to evaluate the joint viscosity was not questioned before. However, a specific study was carried out and discussion on this aspect is addressed in chapter 4. The overall viscosity of the blend (mixture of resins) evolves through two mechanisms: the update of the constituents' relative concentration in each layer (or material point) and the self-evolution of each constituent's viscosity due to thermo-chemical phenomena.

For long winding times, the viscosity of the resin in adjacent layers can be significantly different. In the case of short winding times, that effect may be nearly neglected. In any case, the history of the effective viscosity of the mixture differs from its "ideal" history if no mixing occurs. The relevance of this phenomenon also varies with the type of resin system: for thermoplastic resin systems, for example, the viscosity of a previously wound layer is so high that mixture with new resin is unlikely to occur. The interchangeable relation between the viscosity and the degree of cure/crystallization of the resin, allows to infer its cure/consolidations state.

3.3.3. Fibre Bed Compaction Sub-Model

One of the immediate effects of the resin transfer between adjacent layers is the correspondent motion of the fibre bed. This accommodation is further enforced by the mechanical action of the incremental external pressure as the laminate is built. Therefore, the radial positions of the layers evolve according with these actions. Their thickness and available volume vary as a consequence, thus also the relative fibre/resin contents. The description of these phenomena is carried out in this section.

3.3.3.1. Background

In typical FW, the radial position of the fibre bed (also called fibre sheet), may be modified due to the following two reasons [23]:

- Fibre tension in the curved fibre tows causes the fibres to move through the resin while the resin viscosity is sufficient low. This is the reverse view of the resin squeezed flow phenomenon. Once the viscosity becomes sufficiently high the fibres become "locked" into the resin and do not move relatively to resin under the action of fibre tension;

- Temperature variations of the mandrel/composite and chemically induced changes ("shrinkage") in the resin may cause expansions or contractions.

From integrating the stress-strain constitutive relations, equation (3.39), Lee and Springer [23] modelled the radial displacement of the fibre bed due to an incremental external pressure originated by the winding of new layers. For the generic *j*th layer, within the fibre bed already in place while the new layer is wound, the radial displacement, u, was expressed as

$$\begin{cases} u^j = a_1^j\, r^{\lambda^j} + b_1^j\, r^{-\lambda^j} + c_1^j \left[\dfrac{\tilde{C}_{26} - 2\tilde{C}_{36}}{4\tilde{C}_{33} - 2\tilde{C}_{22}} \right]^j r^2 + d_1^j \left[\dfrac{\tilde{C}_{12} - \tilde{C}_{13}}{\tilde{C}_{33} - 2\tilde{C}_{22}} \right]^j r \quad , \qquad \lambda^j \neq 1 \\ u^j = a_1^j\, r + b_1^j\, r^{-1} + c_1^j \left[\dfrac{\tilde{C}_{26} - 2\tilde{C}_{36}}{4\tilde{C}_{33} - 2\tilde{C}_{22}} \right]^j r^2 + d_1^j \left[\dfrac{\tilde{C}_{12} - \tilde{C}_{13}}{2\tilde{C}_{33}} \right]^j r \ln r \quad , \qquad \lambda^j = 1 \end{cases} , \tag{3.42}$$

where a_1^j, b_1^j, c_1^j and d_1^j are constants evaluated from the known conditions at each layer interface and at inner and outer surfaces of the composite "cylinder", r is the radial position, $\tilde{C}_{ij}$ are the components of the off-axis (z, θ, r) stiffness matrix and

$$\lambda^j = \sqrt{\frac{\tilde{C}_{22}}{\tilde{C}_{33}^j}} \; . \tag{3.43}$$

For the determination of the constants, continuity of both displacements and radial stresses at the layer's interface was assumed. Similar analyses were made to derive the displacements induced by thermal expansions or contractions and chemical changes ("shrinkage"). These descriptions of the displacements are intrinsically related with the stress and strain states in the laminate.

Cai and Gutowski [16] further modelled the effect of the displacement and deformation of the fibre bed in the relative contents of fibres and matrix. Considering fibre and resin continuity, unidirectional radial flow and taking the volume element sketched in Figure 17 as reference, the mass conservation relationship for the deformed volume element (with thickness of $\partial\xi/\partial r \; dr$ and radial displacement) was described as:

$$\frac{\partial}{\partial t}\left[\left(1 - V_f\right) \xi \frac{\partial \xi}{\partial r} \right] + \frac{\partial}{\partial t}\left(\xi q\right) = 0 \; , \tag{3.44}$$

and the continuity condition for the fibre bundle as:

$$\frac{V_{f0}}{V_f} = \frac{\xi}{r} \frac{\partial \xi}{\partial r} \; , \tag{3.45}$$

where $\xi = r + u$ is the radial position of the volume element after displacement, V_f is the fibre volume fraction, V_{f_0} is the fibre volume fraction at the reference state (when $u = 0$) and q is the flow rate per unit area in the radial direction. Combining equations (3.44), (3.45) and (2.11), the consolidation equation in terms of the deformed variable, ξ, was written as [16]:

$$\frac{1}{V_f}\frac{\partial V_f}{\partial t} + \frac{1}{\xi}\frac{\partial}{\partial \xi}\left(\frac{S}{\mu}\xi\frac{\partial p^r}{\partial \xi}\right) = 0 \ , \tag{3.46}$$

where S is the apparent permeability of the medium, μ is the fluid viscosity and p^r is the resin pressure.

3.3.3.2. Analytical Description

The descriptions of the displacements and deformations of the fibre bed proposed by the two groups of authors cited above are intrinsically coupled with the stress-strain constitutive relations and the overall strain states, respectively. Herewith, for the descriptions of the fibre compaction group of phenomena, simpler analyses were realized, thus obtaining alternative relations which held realistic modelling approaches. The main physical assumptions taken were the following ones:

- The fibres angle remains constant during processing;
- Motion of the fibre sheet in axial, zz, and hoop, $\theta\theta$, directions is not considered once the components of fibre tension in these directions are symmetrically balanced;
- Any inertial effects are negligible;
- The thickness of the fibre sheet is small when compared to the radial positions (cylindrical shell analysis).

Under the assumptions described above, the force equilibrium for a given layer may be expressed as [23]:

$$\frac{\Delta p}{\Delta t^l} = \frac{d\,p}{d\,r} = -\frac{\sigma_{\theta\theta}}{r^{fs}} \ , \tag{3.47}$$

where p is the radial pressure, t^l is the layer thickness, $\sigma_{\theta\theta}$ is the hoop stress.

By combining equations (2.11), (3.7) and (3.47) the following expression is obtained for the radial velocity of the fibre sheet:

$$\dot{u}_r^{fs} = -\frac{S}{\mu}\frac{\sigma_{11}^f}{r^{fs}}\sin^2\phi \ , \tag{3.48}$$

where S is the apparent permeability of the medium, μ is the fluid viscosity, σ_{11}^f is the fibre's stress in the local on-axis longitudinal direction, r^{fs} is the radial position of the fibre sheet and ϕ is the winding angle.

The instantaneous radial position of the fibre sheet, r^{fs}, is given by:

$$r^{fs} = r_0^{fs} + u_r^{fs} \ , \tag{3.49}$$

where r_0^{fs} is the radial position of the fibre sheet at a reference time (deposition time, prior to the displacement) and u_r^{fs} is the radial displacement of the fibre sheet relatively to resin. The relative displacement u_r^{fs} is determined by integrating equation (3.48).

The complementary contribution of the thermo-chemical strains to the motion or displacement of the fibre sheet is evaluated by integrating the thermal and chemical strain components, ε_{th} and ε_{ch}, in the radial direction, to calculate the thermal and chemical displacements, u_{th} and u_{ch}, respectively. Due to the volumetric nature of the thermal and chemical strains, the corresponding radial displacements are:

$$\begin{aligned} u_{th} &= \frac{1}{2}\beta_{rr}\Delta T \ , \\ u_{ch} &= \frac{1}{2}\eta_{rr}\Delta\alpha \ , \end{aligned} \tag{3.50}$$

where β_{rr} and η_{rr} are the thermal expansion and chemical shrinkage coefficients and ΔT and $\Delta\alpha$ are the variations of temperature and degree of cure, respectively. The latter only applies for thermosetting resin systems. Equation (3.49) further completes as:

$$r^{fs} = r_0^{fs} + u_r^{fs} + u_{th} + u_{ch} \ . \tag{3.51}$$

The variation of radial positions of the layers, may alter their thickness, t^l, and thus the relative contents of fibres, V_f. Since only matrix flows in and/or out of each layer (the fibres remain), the thickness variation is directly related with the relative contents. Since only radial flow is considered and that the “circumferential length” of each layer is assumed not to vary ($u_r^{fs} << r^{fs}$), the condition:

$$V_f \, t^l = constant \ , \tag{3.52}$$

holds for the entire consolidation process. The updated contents are then assessed.

3.3.3.2. Boundary Conditions

As in the case of the strains, the displacements at the mandrel-composite interface are null. The mass conservation principle is transformed and used as volume conservation principle throughout the process model. The variations of volume due to thermal and/or chemical effects are ignored in the scope of this simplified principle. Thus, the total thickness of the laminate remains constant after deposition of the ultimate layer. Since no resin loss is admitted in the model, the outer layers will incorporate all the excess of resin squeezed from inner layers. In practice, the so-called resin rich region will be held by the outer layer(s).

3.4. Thermo-Chemical Analysis

The thermo-chemical group of physical phenomena includes the heat transfer, the kinetics and the rheological behaviours of the matrix systems. The relationships between the heat generation, temperature, cure or crystallinity and the viscosity of the matrix are accounted in this group. In this section, analytical models of these sub-processes taking place during resin cure or crystallization in FW are addressed. These phenomena were extensively discussed in chapter 2 and were specifically addressed through experimental procedures described in chapter 4 as well. Therefore, herein, only the relevant equations chosen for the process model are presented.

3.4.1. Heat Transfer Sub-Model

The heat transfer within the laminate and between the laminate and the neighbourhood may assume major relevance in certain process conditions. It allows for the dissipation of the heat generated by chemical reactions, thus helping to maintain a certain prescribed processing temperature that may be enforced from external sources. Additionally, it may induce cure/crystallization accelerations or decelerations.

3.4.1.1. Analytical Description

The basis of this sub-model is the energy conservation equation extended with the energy absorbed or released during cure of the thermoset resin or crystallization/consolidation of the thermoplastic. In this model, only through-the-thickness thermal gradients are considered. Neglecting energy transfer by convection, the one-dimensional energy equation can be expressed as [80]:

$$\rho C \frac{\partial T}{\partial t} = \frac{1}{r}\frac{\partial}{\partial r}\left(k_r \frac{\partial T}{\partial r} \right) + \rho \dot{Q} \ , \tag{2.26}$$

where t is time, r is the radial position, T is the temperature, ρ is the density of the composite, C is the specific heat of the composite, k_r is the thermal conductivity in radial direction and $\dot{Q}$ is the rate at which heat is generated by the curing or crystallizing resin.

For thermosettings, the heat generation term is a function of the change in the resin cure state, $d\alpha/dt$, and takes the following form [27, 80]:

$$\rho \dot{Q} = \rho^m V_m \left(\frac{d\alpha}{dt} \right) H_u \ , \tag{2.27}$$

where ρ^m and V_m are the density and volume fraction of the matrix, respectively, H_u, is the total heat of reaction (characteristic of each system).

For thermoplastics, $\dot{Q}$ is the rate at which heat is generated or absorbed by the composite during heating and cooling and takes the following form [84]:

$$\rho\dot{Q} = \rho^m V_m \left(\frac{dc}{dt}\right) H_u \ , \tag{2.32}$$

where $dc/dt = f_1(c, T, dT/dt)$ is the rate of change of crystallinity (or morphology for amorphous thermoplastics), an empirically derived function of temperature and rate of change of temperature.

3.4.1.2. Boundary Conditions

In the inner limits of the composite laminate, the mandrel exchanges heat with the composite and the inner atmosphere. A simplification was introduced by neglecting this phenomenon. The mandrel is assumed to be at room/processing temperature during the winding and cure/consolidation phases.

The outer surface of the composite laminate is in direct contact with air at room/processing temperature.

In thermosetting resins, the total heat of reaction, used in the determination of the heat generation rate, is a characteristic property/value for each resin system. This is further addressed in chapter 4, where the experimental values are listed.

3.4.2. Resin Cure/Crystallization Sub-Model

Accordingly with the literature review fully addressed in chapter 2, several relationships between the degree of cure/crystallization and the temperature, like:

$$\frac{d\alpha}{dt} = f\,(\alpha, T) \ , \tag{3.53}$$

$$\frac{dc}{dt} = f\,(c, T) \ , \tag{3.54}$$

were chosen and catalogued in the model library, thus accounting for several applicable resin systems. The data for the thermosetting resins pre-selected for this library is summarized in Table 2. Data for thermoplastic systems is less homogeneous (all available equations have different parameters) and less consensual, as well. For this reason these are not listed in the table.

For the specific resin systems used in the experimental validation, the governing kinetic models were fully developed and are described in detail in chapter 4.

3.4.3. Resin Viscosity Sub-Model

The resin viscosity depends on the degree of cure, α, and the temperature, T, in the case of thermosetting systems, while for thermoplastics it is a single function of the temperature, T. Similarly to the cure/crystallization sub-model, several relationships between the degree of cure/crystallization and the temperature, of the types:

$$\mu = f\,(\alpha, T) \ , \tag{3.55}$$

$$\mu = f\,(T) \ , \tag{3.56}$$

were chosen and catalogued in the model library, thus accounting for several applicable resin systems. The data for this library is summarized in Table 3.

For the specific resin systems used in the experimental validation, the governing kinetic models were fully developed and are described in detail in chapter 5.

Table 2 – Kinetic model data for the different thermosetting resin systems selected and included in the process model library.

resin		Epoxy 976	Epoxy 977-3HM	Epoxy HBRF-55A	Epoxy 3501-6
model		$\frac{d\alpha}{dt}=\left(K_1+K_2\alpha^a\right)\left(B-\alpha\right)^b$	$\frac{d\alpha}{dt}=K_1\alpha^3-K_2\alpha^2+K_3\alpha+K_4\alpha$	$\frac{d\alpha}{dt}=(K_1+K_2\alpha^a)(B-\alpha)^b(1-\alpha)^c$	$\frac{d\alpha}{dt}=(K_1+K_2\alpha)(1-\alpha)(B-\alpha) \quad \alpha\leq 0.3$ $\frac{d\alpha}{dt}=K_3(1-\alpha) \quad \alpha>0.3$
K_1	A_1	4.400×10^3	1.640×10^5	4.901×10^2	3.502×10^7
	E_{a1}	6.250×10^4	6.920×10^4	4.471×10^4	8.070×10^4
K_2	A_2	7.500×10^3	-2.190×10^4	2.052×10^3	-3.357×10^7
	E_{a2}	5.680×10^4	6.000×10^4	4.285×10^4	7.780×10^4
K_3	A_3	n/a	1.900×10^2	n/a	3.567×10^3
	E_{a3}	n/a	4.610×10^4	n/a	5.660×10^4
K_4	A_4	n/a	1.020×10^5	n/a	n/a
	E_{a4}	n/a	7.600×10^4	n/a	n/a
m	a	1.03	n/a	0.840	n/a
n	b	1.22	n/a	0.540	n/a
	c	n/a		1.000	n/a
B		1.0	n/a	1.065	0.47

Table 3 – Rheological model data for the different thermosetting resin systems selected and included in the process model library.

resin	Epoxy 976	Epoxy 977-3HM	Epoxy HBRF-55A	Epoxy 3501-6
model	$\mu=\mu_\infty e^{\frac{U}{RT}+K\alpha}$	$\mu=\mu_\infty e^{\frac{U}{RT}+K_1\alpha^2+K_2\alpha}$	$\mu=\mu_\infty e^{\frac{U}{RT}}\left(\frac{\alpha_{gel}}{\alpha_{gel}-\alpha}\right)^{(a+b\alpha)}$	$\mu=\mu_\infty e^{\frac{U}{RT}+K\alpha}$
K_1	1.880×10^1	1.110×10^1	4.901×10^2	14.100 ± 1.2
K_2	n/a	0.810	4.471×10^4	n/a
a	n/a	n/a	0.162	n/a
b	n/a	n/a	2.509	n/a
α_{gel}	n/a	n/a	0.85	n/a
μ_∞	1.060×10^{-6}	3.460×10^{-5}	1.870×10^{-8}	7.930×10^{-14}
U	3.760×10^4	4.620×10^5	4.270×10^4	9.080×10^4

3.5. Main Assumptions and Limitations

Several assumptions and limitations were introduced along with the description of the sub-models. Nevertheless, some remarks have to be made on relevant aspects, aiming and foreseeing the generalization of the FW process modelling. Herewith, the most important aspects are highlighted.

Certain material properties varying during the process were assumed to change linearly with the degree of cure. Some of them were also assumed to change linearly across the layer's thicknesses. It seemed reasonable, given the difficulty in accurately assess those parameters.

No analysis was made to account for the eventual void inclusion and growth during the process, since the FW characteristic of sequential lamination and relatively low velocities make such phenomena nearly absent and therefore negligible even from the theoretical point of view.

Concerning the applicability of the thermo-chemical data, efforts were made to assess the kinetic and rheological behaviour under conditions that would approximate the real ones occurring at the layer/laminate level. The information in the literature is very limited on such conditions.

On the general applicability, this model is of local nature. Moreover, it has a decoupled sub-modelling structure (modular architecture), thus making it virtually applicable to any geometry and material system, provided that the adequate input data is available. It accomplishes, in this way, the main objective of developing a basic framework for further studies and developments, pursuing its usefulness to real applications.

CHAPTER 4

EXPERIMENTAL PROCEDURES

4.1. Validation Methodology

In the previous chapter, the relationships between the several physical variables and parameters acting at the layer/laminate level during the FW process were identified. A modular multi-physical process model was built in which the sub-models (each modelling a specific group of phenomena) interact through the exchange and iterative updating of the evolving variable/quantities. The accuracy (and validity) of this model is, therefore, dependent upon

- the values of the variables and/or properties used in it;
- the correction of the physical descriptions of each phenomenon; and,
- the assumptions made.

The variables and/or properties inputted to the model are divided in three groups: the material thermal and mechanical properties, the input variables of the manufacturing process and the input data that feed (independently) one or more sub-models. The first group of properties is mainly provided by either the material manufacturer's data sheets or literature. The process related inputs are retrieved from process setup, experimental measurements or previous knowledge. Among these are the fibre winding force, $F_{winding}$, winding angle, ϕ, tow bandwidth, b, mandrel radius, $r^{mandrel}$, initial layer's thickness, t_0^l, initial fibre volume fraction, V_0, and processing (room) temperature, T^{pr}. The input data used in specific sub-models, such as resin cure (in the case of thermosetting resins), resin viscosity or resin mixing, is assessed from both previously established models and novel sub-models developed during the present work. These are presented and discussed in the second section (section 4.2) of this chapter.

The correction of the physical descriptions of each phenomenon, i.e., the validity of each of the sub-models established in the framework of the present multi-physical process model, was discussed in the previous chapter, along with their own definitions and theoretical support. Their experimental validation is, however, a very important part of the model development, since it allows the evaluation of the overall applicability and accuracy of the process model, through assessment to reliable "real" data and later comparison with the numerical results simulating similar conditions. Moreover, the difficulty in assessing and measure the relevant variables during the process (which justifies the lack of comprehensive experimental validation of the main process models developed in the last decades) determines the need to develop a few dedicated setups and methods, which are quite unique and interesting *per se*. The measurement of the relevant model outputs is presented and discussed in the third section (section 4.3) of this chapter.

The main assumptions made in the model are related with the initial and boundary conditions as well as with the evolution of properties of the matrix during the process. The former were based on self-evident aspects of the process while the latter were established to approximate matrix properties which are very difficult to assess. Namely, values for matrix Young's modulus, E^m, shear modulus, G^m, Poisson's ratios, ν^m, density, ρ^m, heat conductivity, K^m, heat capacity, C^m, thermal expansion coefficient, β^m, and shrinkage coefficient, η^m, are extremely difficult to assess in practical way (unconsolidated matrix within the composite laminate) and are scarcely available in literature. Thus, these were not specifically validated through external means rather than just by the overall matching of the model results, addressed in chapter 5. Also, eventual formation of voids was not considered, since these were assumed negligible upon the literature review made.

To accomplish the goal of verifying the validity of the process model, a comprehensive experimental programme was followed. It included both the development of new sub-models for the material systems used and measurement of the change in the main process physical variables during the winding trials. Due to the modular (decoupled) nature of the process model developed, the desirable independent validation of each sub-model seemed applicable and was aimed from the beginning. Such an independent validation would allow not only to test and evaluate each of the relevant physical descriptions integrated in the model, but also to divide the experimental programme into several dedicated tests thus attributing greater control and accuracy to the validation procedure.

The methodology used for the experimental validation of the process model consisted in generating sets of reliable data from the measurements done in several winding trials. The value and variations of the main physical variables were assessed using dedicated techniques and parametric configurations of the experiments.

Specifically, the main outputs of the model were measured and/or evaluated through the following experiments:

- an original experimental technique was developed to characterize the resin flow within the laminate during the FW process;
- the compaction of the laminate was measured through the comparison of initial and final radial positions of the layers;
- the variation of the relative phases content (fibre and matrix volume fractions) was assessed both in global terms and through-the-thickness final gradients;
- the fibre waviness was characterized at initial and final stages of the winding in order to support the assumptions made on typical fibres misalignment pattern.

Regarding several other model parameters, which are mainly input values for relevant sub-models, additional experiments were conducted. Based on existing techniques, the following thermo-chemical phenomena were studied and modelled, considering the two resin systems used in the winding trials:

- novel kinetic models of the cure of two different thermosetting systems were developed;
- the rheology (evolution of viscosity during the cure process) was also characterized and modelled for these resin systems;
- the assumptions made in the resin mixing sub-model were evaluated through an original rheological characterization of the two resin systems under certain mixing conditions that reproduced the operating conditions in wet FW.

As mentioned above, the input data relating to initial process conditions, were setup and confirmed in the winding trials.

The experimental validation task conducted within the present study included several dedicated techniques and methods, which are applicable and relevant to many composite manufacturing processes, rather than just to FW. Therefore, the research work and the knowledge gathered through the experimental programme had a greater scope than the sole validation of the process model developed herewith. Moreover, a few original methods and sub-models were developed thus enhancing the relevance and value of this campaign.

In this chapter, the thermo-chemical, mechanical and manufacturing experimental tests are presented. The procedures, results and their analysis are discussed in detail. Throughout the following two sections, these are divided into the experimental assessment to model input data and measurements of output data.

4.2. Experimental Assessment to Model Input Data

In this section, the experimental procedures conducted to either generate reliable input data for the thermo-chemical sub-models or measure main process input parameters are described. Both the procedures and the results are presented.

4.2.1. Resins Cure Kinetics

The cure/consolidation behaviour of the matrix in composites is a major physical phenomenon among those driving the morphological changes in a composite laminate under processing conditions. Its characterization is, therefore, highly relevant for the modelling of the manufacturing process.

In the FW process, the matrix systems used are grouped into thermosetting and thermoplastic resins. When using thermosetting resins, both wet and prepreg dry winding configurations could be setup, while in the case of thermoplastics only prepreg winding may be practically implemented. Due to greater spread and applicability of thermosettings in high-performance parts as well as the complexity of their thermo-chemical behaviour, these were chosen for the experimental validation of the current FW process model. Specifically, two epoxy resin systems used in wet FW were selected and studied in detail and later added to the process model library. The two systems were characterized and modelled through differential scanning calorimetry (DSC) analysis. The kinetic parameters were determined and two original kinetic models were established for these resin systems subjected to “real” processing conditions. The aim was to assess the input data needed for the resin cure process sub-model. Hereafter, the experimental procedure is described, together with its validation and the kinetic models developed.

4.2.1.1. Experimental Procedure

The curing of thermosetting resins is almost invariably characterized by an exothermic chemical reaction where low molecular weight monomers, in a mixture with low weight hardeners and/or accelerators, change from a liquid state into a rubbery and then solid glass states. Covalent crosslinks are formed during this curing process. Although several reactions may take place (simultaneously or sequentially) the overall transformation of reactants into products may be assessed through the global extent of conversion. Since in thermosetting resins this process is accompanied by release of heat, the extent of conversion may be evaluated as a fraction of the total heat released [224]. This quantity is the so-called degree of cure, α, that was previously defined in equation (2.24), recalled as:

$$\alpha = \frac{H}{H_u} \quad , \tag{2.24}$$

where H is the heat evolved from time $t = 0$ to time t and H_u is the total (ultimate) heat of reaction of the resin.

A few experimental techniques have been developed to characterize the behaviour of material samples measurable through changes in temperature and/or other related physical aspects. Thermal analysis (TA) is the group of techniques in which a property of the sample is monitored against time or temperature while the temperature of the sample, in a specified atmosphere, is programmed [225]. Among these, DSC is the most adequate to evaluate and model the cure kinetics of thermosetting resins. In this technique the difference of heat flow, dH/dt, between a material sample and a reference is measured during a temperature or time scan, while temperature of the furnace chamber is varied in a specified program. Most DSC instruments are of the heat-flux design, as is the case of the one used in this experimental procedure.

In Figure 40 the typical DSC test arrangement is schematically depicted, together with the actual setup. The standard procedure consists in containing a small material sample in a shallow pan, assuring good thermal contact between sample, pan and heat flux plate. An empty pan is placed in the remaining heat flux plate so that the differential heat is only due to the material sample behaviour itself. The mass of the material sample is typically required to be within the interval 10-20mg. Homogeneous heating of the cell is achieved by constructing the furnace from a metal of high thermal conductivity. In the case of the equipment used in this experimental campaign (Q20 model from TA Instruments$^{\circledR}$), silver is used. Temperature and/or energy calibration is carried out by running standard materials, usually very pure metals with accurately known melting points and heats of fusion. Particular attention shall be given to the provision for establishing a gas flow through the chamber, to sweep away volatiles, provide the required atmosphere, and to assist in heat transfer [226]. In the experiments conducted and presented hereafter nitrogen was used as purge gas.

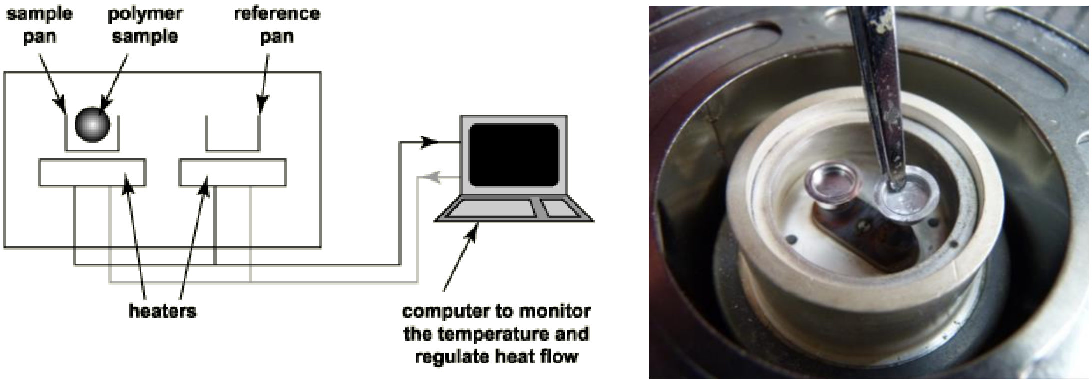

Figure 40 – Schematic representation of the DSC equipment [227] (left) and close view of the resin sample placement in the experimental procedure conducted (right).

As mentioned in chapter 2, kinetic analysis of thermosetting resins has been successfully performed in DSC by several authors. Both isothermal and dynamic scans have been applied. In isothermal tests, the material samples are monitored along with time while being subjected to a constant temperature. On the other hand, in dynamic tests the samples are subjected to a prescribed temperature cycle. Ramps of constant heating rates are the most commonly used cycles in dynamic mode.

In this experimental programme, both isothermal and dynamic tests were carried out. Isothermal tests are more time consuming and, for low temperatures, reaction rates (and, therefore, heat flow rates) may be too slow to be accurately detected by the equipment. Hence, precise and highly sensitive instruments are needed. On the contrary, dynamic scans are prone to achieve higher reaction rates as well as to propitiate complete reactions.

From the DSC isothermal curves outputted, where heat flow, dH/dt, is plotted against time, t, the evolution of the heat released, H, is assessed from integrating the curve data as follows:

$$H(t) = \int_0^t \frac{dH}{dt} dt \ , \tag{4.1}$$

which is graphically represented in Figure 41. The evolution of the degree of cure is then computed from the ratio defined in equation (2.24).

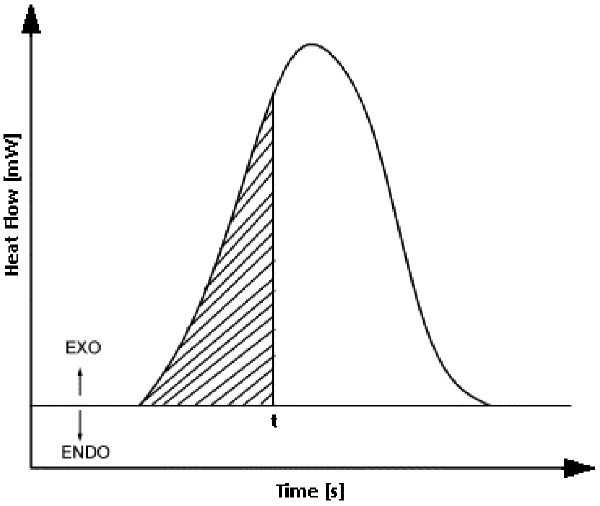

Figure 41 – Typical DSC isothermal curve output for polymers with exothermic reaction.

Being the purpose of these experimental tests focused on simulating the manufacturing conditions, particularly the ones used in the winding trials, the manufacturer's recommended curing cycles (MRCC) were used as the temperature cycles for each specific resin. This approach, rarely used in previous works, allowed to assess and establish novel models for the kinetic behaviour of the resins studied in their real conditions of application. Additionally, the models developed from this study considered temperature stages at room temperature, which is quite unique. Moreover, these were the first comprehensive kinetic characterization studies conducted in the two epoxy systems chosen, SR®1500 and Araldite® LY556.

4.2.1.2. Characterization/Modelling of Two Epoxy Systems

Within the scope of the experimental validation of the FW process model developed herewith, two commercial epoxy resin systems were selected and studied independently. Hereafter, the results of the DSC experiments conducted in both resins are presented and discussed. Two novel kinetic models were established that predict the evolution of the degree of cure, α, of these resins during the manufacturing and curing stages, since "real" working temperatures (MRCC) were considered. Therefore, these kinetic models were implemented in the resin cure sub-model library for the validation of the global model through comparison with the other experimental results discussed in this chapter.

In order to apply these models directly on the experimental validation of the process model, it was assumed that the behaviour of the resins within the laminate during consolidation is similar to their behaviour in neat (un-filled) condition. Despite the coarser approximation that this assumption may represent, it is justified by both the relatively good agreement found by previous researchers and the practical limitations in assessing the *in-situ* curing behaviour.

The two commercial epoxy resin systems chosen were the SR®1500 from Sicomin Composites (France) and Araldite® LY556 from Huntsman (USA). The former was chosen due to its greater availability and “fast” cure at room temperatures, thus allowing to run several parametric winding trials solely in the FW setup. This resin is commonly used in hand lay-up manufacturing rather than in FW. However, it is applicable in FW of smaller parts and represents quite well the typical industrial usage. The latter resin was chosen due to its wide use in highly valued industries, namely in aeronautic and aerospace applications. It represented also a major challenge, since the MRCC is rather more complex than a simple isothermal condition and its modelling became a case study itself. These two resins represent, in terms of process advantages and limitations, a broad number of applications in FW and different industries, which was the underlying reason to choose and study them.

SR® 1500

The formulation bases of SR® 1500 are bisphenol A and F. The resin system used was a mixture of the resin with the amine hardener SD® 2505 in the ratio of 100:33% by weight, respectively. For this epoxy system, the MRCC are those presented in Table 4.

Table 4 – MRCC for SR® 1500 / SD® 2505 and selected curing cycles for DSC tests.

Pre-cure	2 to 4 hours @ 20ºC
Minimum post-cure cycle	2 to 7 days @ 20ºC
Advised post-cure cycle	2 to 7 days @ 20ºC OR 12 hours @ 40ºC OR 6 hours @ 60ºC
Cycle selected for DSC tests	14 hours @ 30ºC; 14 hours @ 40ºC; 14 hours @ 50ºC

As previously mentioned, the MRCC were attained in the selection of the testing temperature cycles. Three isothermal cycles, at 30ºC (303 K), 40ºC (313 K) and 50ºC (323 K) and duration of 14 hours, were, then, defined for the DSC tests conducted with this epoxy system. Two material samples were tested at each temperature. After mixing the resin and the hardener, each sample was carefully placed in the proper aluminium shallow pan and weighted in a microbalance. The mass, pre-conditioning and test temperature of the tested samples is presented in Table 5.

Table 5 – Mass and test condition of the samples of SR® 1500 / SD® 2505 tested.

Sample ID	Mass [mg]	Pre-conditioning	Test Temperature Cycle
SRHF0	15.2	Dry, Dark, 22ºC	14 hours @ 40ºC
SRHF1	13.3	Dry, Dark, 22ºC	14 hours @ 50ºC
SRHF2	14.2	Dry, Dark, 22ºC	14 hours @ 30ºC
SRHF3	20.6	Dry, Dark, 23ºC	14 hours @ 50ºC
SRHF4	12.5	Dry, Dark, 22ºC	14 hours @ 40ºC
SRHF5	11.4	Dry, Dark, 24ºC	14 hours @ 30ºC

The heat flow signals directly outputted from the DSC setup were firstly normalized by the mass of the samples. The specific heat flow is then plotted in the following graphics, for the samples SRHF0, SRHF1 and SRHF2. The mixture of the two constituents of this epoxy system was proceeded at time $t = 0$. From these plots it becomes evident that this resin is highly reactive at room temperatures and that the curing reactions progress mostly in early stages of the curing cycle.

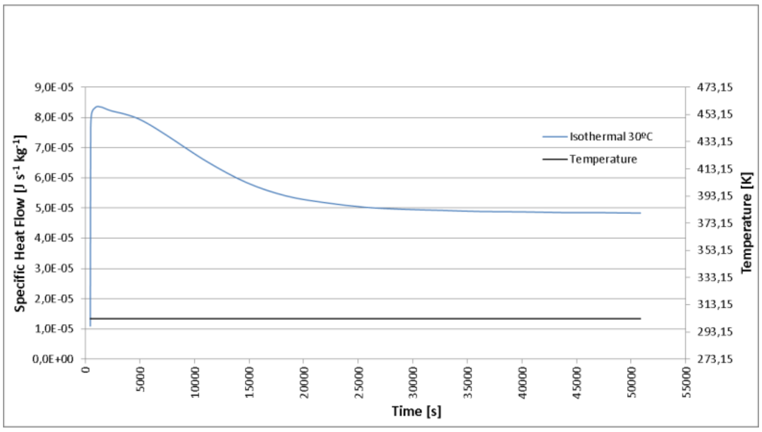

Figure 42 – Plot of specific heat flow for the isothermal DSC test conducted in sample SRHF2 at 30ºC (303 K).

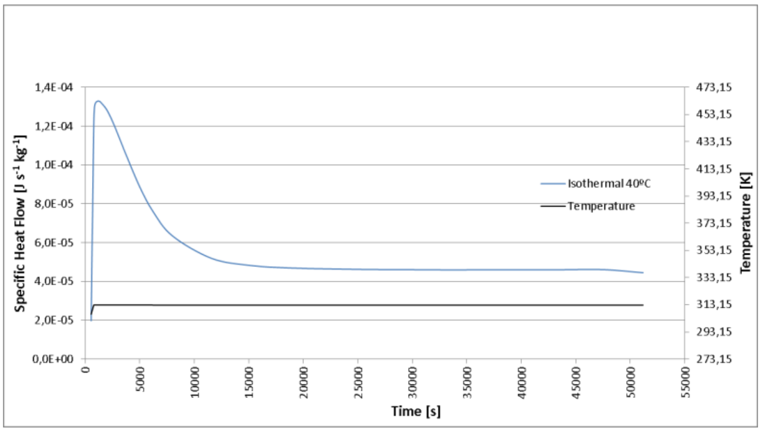

Figure 43 – Plot of specific heat flow for the isothermal DSC test conducted in sample SRHF0 at 40ºC (313 K).

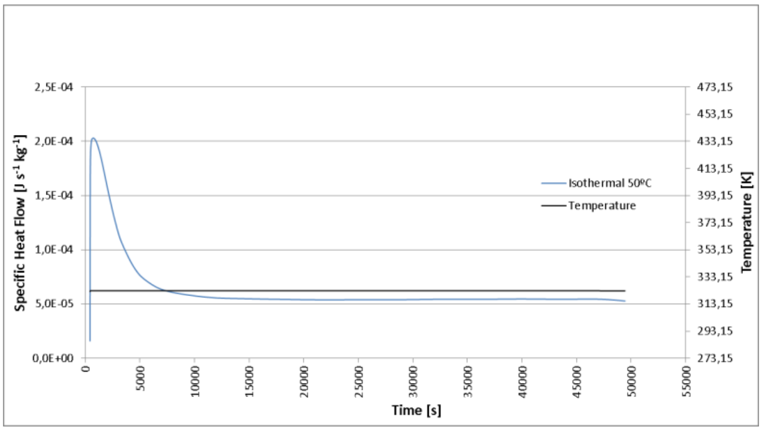

Figure 44 – Plot of specific heat flow for the isothermal DSC test conducted in sample SRHF1 at 50ºC (323 K).

Through integration of these curves, the heat of reaction corresponding to the isothermal test condition, H_{ISO}, could be determined. Since the test temperatures were considerably low (nearly room temperatures were used), the samples were not expected to achieve complete degree of cure in the isothermal conditions. Therefore, two dynamic DSC scans were further conducted in each sample in order to assess the residual heat of reaction, H_r, and consequently, the total (ultimate) heat of reaction, H_u, of this epoxy system. A linear temperature increasing rate of 10ºC/min was applied in each ramp, scanning the material sample from room temperature up to 200ºC (473 K). The first dynamic scan consistently captured the vitrification phenomenon that did not occur during the isothermal tests due to the low temperatures used. This is an endothermic reaction and therefore a heat absorption peak is observed. At the end of the first dynamic scan the samples were fully cured. The second dynamic scans were conducted to set the baseline of the thermal behaviour of the fully cured samples. From the difference in the heat flow observed in the first and second dynamic scans, the residual heat of reaction, H_r, was determined. In the following figures, the outputs of these additional tests are plotted for the samples SRHF0, SRHF1 and SRHF2 in terms of the specific heat flow.

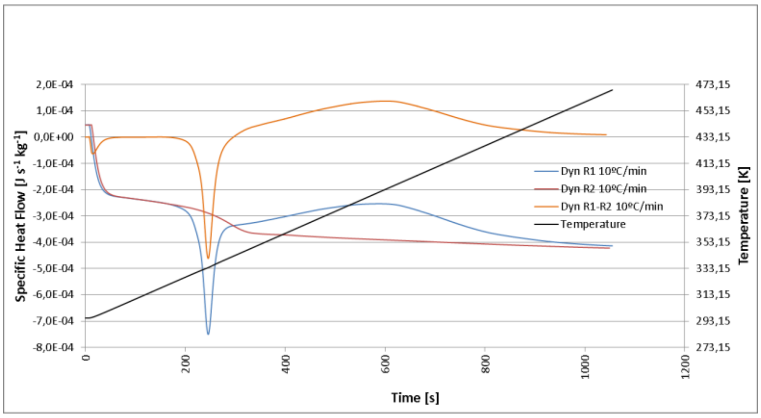

Figure 45 – Plot of specific heat flow for the dynamic DSC tests conducted in sample SRHF2 (previous isothermal test at 303 K).

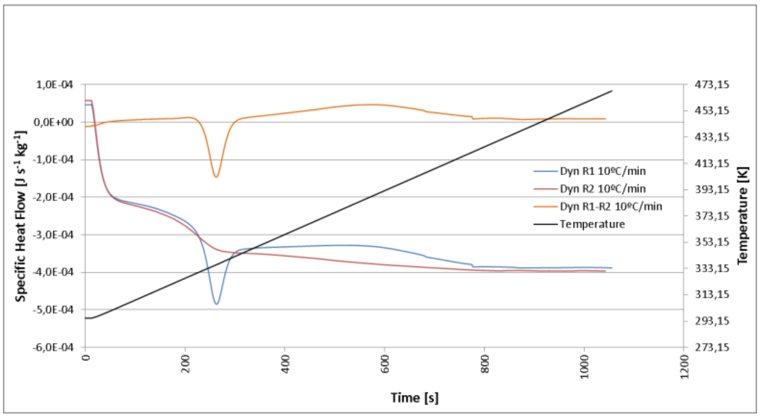

Figure 46 – Plot of specific heat flow for the dynamic DSC test conducted in sample SRHF0 (previous isothermal test at 313 K).

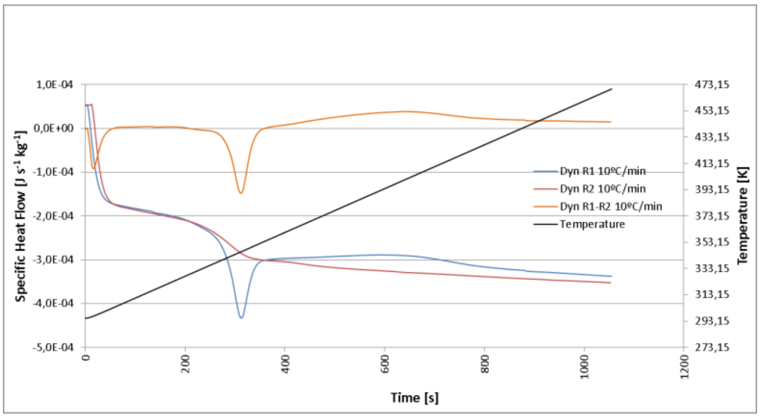

Figure 47 – Plot of specific heat flow for the dynamic DSC test conducted in sample SRHF1 (previous isothermal test at 323 K).

For each resin sample the total (ultimate) heat of reaction, H_u, is the sum of the heat released during the isothermal test, H_{ISO}, and the residual heat, H_r, assessed through the dynamic scans, thus being defined as follows:

$$H_u = H_{ISO} + H_r \ . \tag{4.2}$$

The values of the heats of reaction measured in each sample are listed in Table 6.

Table 6 – Heats of reaction of the samples of SR® 1500 / SD® 2505 tested.

Sample ID	Isothermal Test		Dynamic Scans	H_u [J/kg]	T_g [ºC]
	Temp. [ºC]	H_{ISO} [J/kg]	H_r [J/kg]		
SRHF2	30	0.420	0.0584	0.478	59.7
SRHF5	30	0.378	0.0737	0.452	50.8
SRHF0	40	0.453	0.0192	0.472	60.8
SRHF4	40	0.438	0.0367	0.474	61.7
SRHF1	50	0.447	0.0185	0.465	71.1
SRHF3	50	0.457	0.0192	0.476	70.5

The consistency of the results obtained is easily observable in the following plot of the isothermal heat of reaction, residual heat of reaction and total heat of reaction for all the material samples. One can verify that the total heat remains constant, independently of the isothermal testing temperature. This is in accordance with theory and results from previous authors [228].

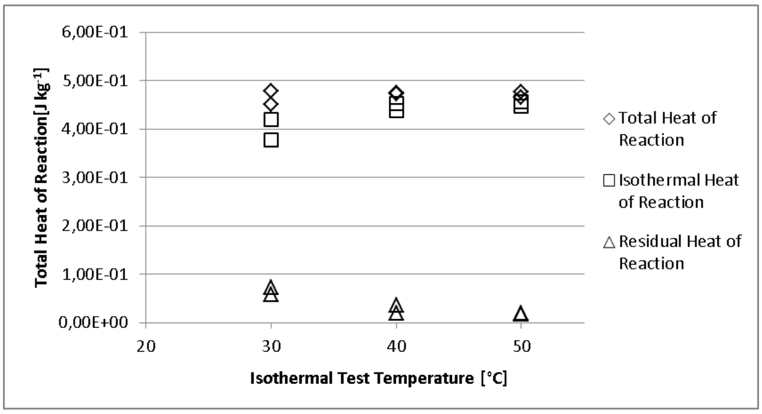

Figure 48 – Isothermal, residual and total heat of reaction of the material samples of SR®1500/SD®2505 tested under different temperatures.

From the definition expressed in equation (2.24), the experimental curves for the evolution of the degree of cure, α, with time were computed. Using a backward Euler numerical integration scheme, the rate of degree of cure, $d\alpha/dt$, was also determined for each test data. These curves are plotted in the following figures for all the tests conducted. As previously mentioned, one can observe that the reaction is not fully completed during the isothermal tests. Specifically, the maximum degree of cure achieved in the tests conducted at 40ºC and 50ºC is of ca. 95% while for those conducted at 30ºC the averaged value is of ca. 86%. This is due to the fact that, as the cure progresses, it becomes gradually governed by diffusion (rather than by the intrinsic polymerization) which further prevents the vitrification stage to be achieved. Later in this section, the influence of this phenomenon in the establishment of a correct model is discussed.

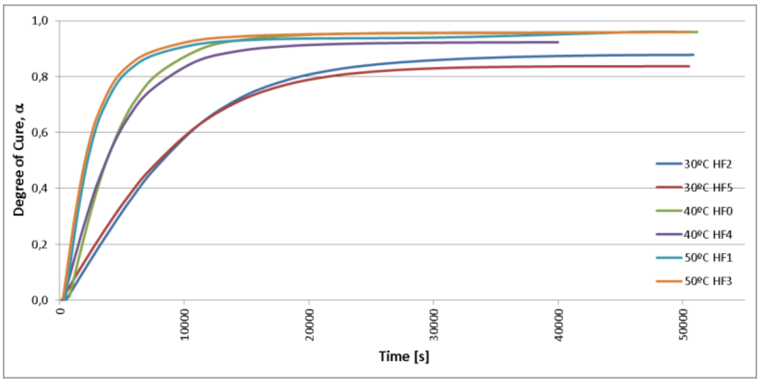

Figure 49 – Evolution of the degree of cure in all the SR®1500/SD®2505 samples during the isothermal tests conducted at different temperatures.

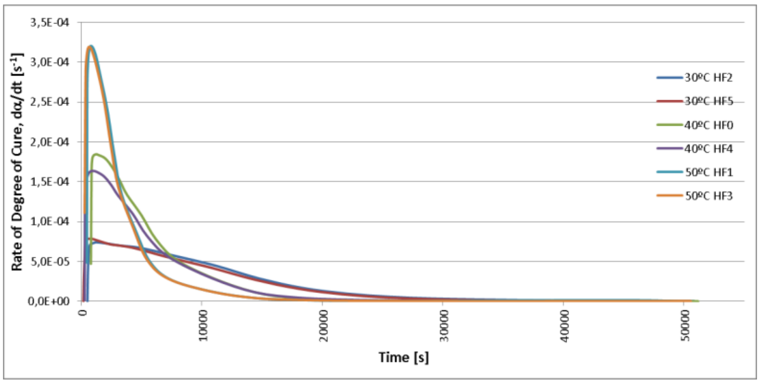

Figure 50 – Evolution of the rate of degree of cure in all the SR® 1500 / SD® 2505 samples during the isothermal tests conducted at different temperatures.

From these plots, it is also observable that the initial rate of conversion increases with temperature. Despite the very low rates of conversion observed after $t = 30000\,s$, the reaction did not stop in any of the samples during the isothermal test. This means that longer stages at these temperatures would promote a greater completion of the curing reaction. However, the ratio between the time needed and the small increase of reaction completeness is highly unfavourable to its practical implementation and therefore this MRCC is quite established and accepted among users.

The kinetic models of polymers are typically established in terms of the relationship between the rate of cure, $d\alpha/dt$, and the degree of cure, α. This is mainly justified by the need of attaining both the initial reactivity of the system and the final degree of cure achieved. Moreover, the $d\alpha/dt - \alpha$ data curves were found to be more reliably fitted by models than $\alpha(t)$ or $d\alpha(t)/dt$. The rate of cure is then parameterized in terms of three major variables as follows [224]:

$$\frac{d\alpha}{dt} = K(T)\ f(\alpha)\,h(p)\ , \tag{4.3}$$

where T is the temperature, α is the degree of cure and p is the pressure. The pressure dependence is ignored in most of semi-empirical kinetic models developed for reactive polymers through thermal analysis (TA). In the case studied herewith, this dependence was also neglected due to the facts that only pressures above 3 MPa have shown to be relevant [224,229,230] and that in wet FW the maximum value of pressures developed within the laminate may barely reach such magnitude, and only for short periods (at the layer's deposition) and considerable drop is expected for the majority of the winding and consolidation period.

Hence, the rate of cure was considered as a function of only the variables temperature, T, and degree of cure, α, and equation (4.3) simplified to:

$$\frac{d\alpha}{dt} = K(T)\ f(\alpha)\ . \tag{4.4}$$

In Figure 51 the experimental data is plotted for all the isothermal tests conducted with SR® 1500 / SD® 2505 resin in terms of the rate of cure *versus* degree of cure. Upon setting of these data, the challenge consisted in establishing an adequate model in the form of equation (4.4) that would properly fit the experimental curves in all the domain of temperature and degree of cure. An additional challenge was added by considering that the model should also represent the main physical phenomena occurred during the curing reaction.

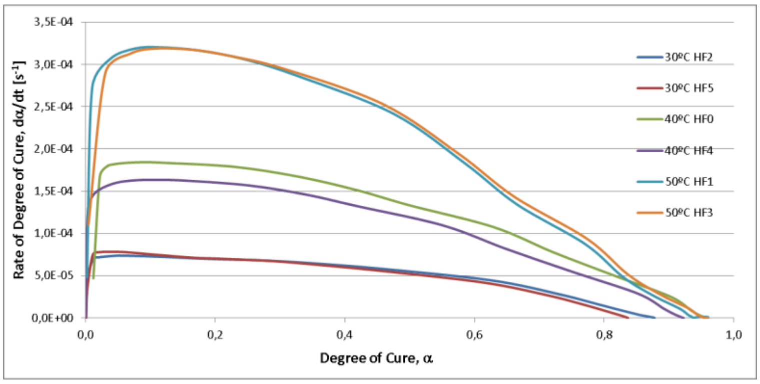

Figure 51 – Plot of the rate of degree of cure *versus* degree of cure for all the SR® 1500 / SD® 2505 samples during the isothermal tests at different temperatures.

Several previously established semi-empirical models were studied and evaluated. All were phenomenological models, since mechanistic ones are rather more complex and require deeper knowledge on the chemistry of the reactants. As referred in chapter 2, phenomenological models proved to represent well the overall behaviour of the reactive polymers.

Due to the apparent single-step decelerating shape of the experimental $\alpha(t)$ curve (Figure 49), a nth order model [231] was firstly fitted to the experimental data using a non-linear least squares minimization technique. This model is described by the following relation:

$$\frac{d\alpha}{dt} = k_1 (1-\alpha)^n \ , \tag{2.43}$$

where k_1 is a rate constant and n is the reaction order. The dependence on temperature of the curing rate is considered to follow an Arrhenius form described as:

$$k_1 = A_1 \, e^{\frac{E_{a1}}{RT}} \ , \tag{2.45}$$

where A is the pre-exponential constant, E_a is the activation energy, R is the universal gas constant and T is the absolute temperature. This model, however, was not able to approximate the kinetic behaviour in early stages of the cure. This was due to the fact that the $\alpha(t)$ curves actually presented a sigmoidal shape, rather than a simply decelerating shape. This became evident only with the plotting of the $d\alpha(t)/dt$ curves (Figure 50) where one may observe a short initial stage in which $d\alpha/dt$ increases from zero to its maximum value. This suggested that the resin had an autocatalytic behaviour despite the considerably fast achievement of a maximum rate of cure.

A second set of models were then studied and fitted to the experimental curves. The so-called Kamal-Sourour autocatalytic model [85,232] was chosen due to its ability to capture the overall decelerating tendency as well as the initial increasing of the rate of cure. It is described by the following relation:

$$\frac{d\alpha}{dt} = (k_1 + k_2\alpha^m)(1-\alpha)^n \ , \tag{2.33}$$

where m is a second reaction order constant. The sum $m+n$ is thus the overall reaction order. The rate constants k_1 and k_2 are defined similarly to k in equation (2.45). Despite the fact that better agreement was found for the initial stage of the cure, a good combination of the estimation of the maximum rate of cure and proper slope in the behaviour after this peak was never achieved.

It was observed that the nth order model could fit better the data after the maximum rate of cure was achieved, while the autocatalytic model allowed to improve the estimation in very early stages of the cure. However, none presented a satisfactory result for the overall domain. In order to combine the advantageous features of the nth order and the autocatalytic models in fitting these experimental curves, a more complex model, developed by Karkanas and Partridge [233] was studied. This model is truly a combination of the nth order and autocatalytic models and is expressed as:

$$\frac{d\alpha}{dt} = k_1(1-\alpha)^{n_1} + k_2\alpha^m(1-\alpha)^{n_2} \ , \tag{4.5}$$

where k_1 and k_2 are the two rate constants as previously defined and n_1, n_2 and m are reaction order constants. This model is a multi-step description of the overall reaction in which two parallel reactions are actually represented by the two terms in the right-hand side. Such model allows not only to fit better the experimental results in the domain of the overall reaction, as it also describes independently the two main chemical reactions that typically occur in epoxy-amine systems. It is well known that the uncatalyzed reaction of an epoxide with a primary amine produces a secondary amine which reacts with another epoxy group to form a tertiary amine. These reactions are auto-accelerated by the hydroxyl groups formed in the reactions [85,234]. Hence, this model was expected to estimate the evolution of the overall rate of cure satisfactorily, since it would be able to enforce each of the two parallel reactions to govern the overall reaction in the adequate stages of it.

The results of the fitting of the three models (nth order, Kamal-Sourour and Karkanas) to the experimental DSC isothermal data obtained for the SR® 1500 / SD® 2505 epoxy resin are shown in Figure 52. The kinetic parameters determined for each model fitting are presented in Table 7. As it is easily observable the agreement of the models with the experimental data improved from the initial trial with the nth order model to the third trial with the Karkanas model. The estimations that the latter produced for the three temperatures studied were acceptable for the majority of the domain of the degree of cure, α. Still, a better fitting, and thus a better model was sought for this particular epoxy system and room temperature conditions.

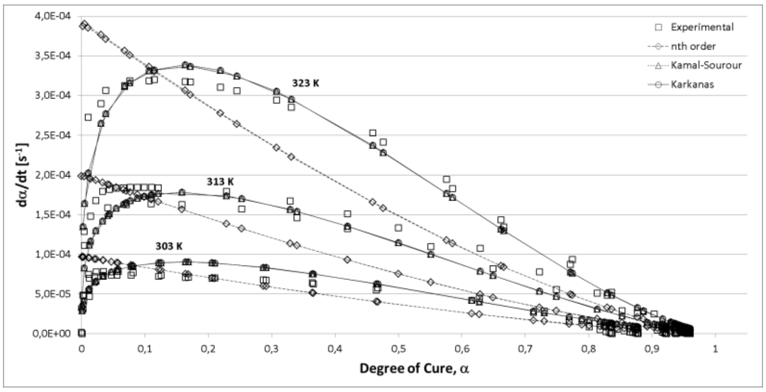

Figure 52 – Fitting of the nth order, Kamal-Sourour and Karkanas models to the experimental DSC isothermal data of SR$^{®}$1500/SD$^{®}$2505 at 30ºC (303K), 40ºC (313K) and 50ºC (323K).

In Figure 53 the final stage of the isothermal cure is plotted (zoomed view of Figure 52). In it one may observe that these models overestimate the rate of cure, $d\alpha/dt$, in the final stage of the cure ($\alpha > 0.8$). In fact, these models tend to the value $\alpha = 1.0$, i.e., to a complete reaction.

Table 7 – Kinetic parameters determined for the fitting of the experimental curves with the nth order, Kamal-Sourour and Karkanas models.

Kinetic Parameters		Kinetic Model		
		nth order $\frac{d\alpha}{dt} = k_1(1-\alpha)^n$	Kamal-Sourour $\frac{d\alpha}{dt} = (k_1 + k_2\alpha^m)(1-\alpha)^n$	Karkanas $\frac{d\alpha}{dt} = k_1(1-\alpha)^{n_1} + k_2\alpha^m(1-\alpha)^{n_2}$
k_1	A_1	5.5380×10^5	2.1732×10^5	2.1699×10^5
	E_{a1}	5.6580×10^4	8.1890×10^4	8.1775×10^4
k_2	A_2	n/a	3.0370×10^5	3.0283×10^5
	E_{a2}	n/a	5.3336×10^4	5.3328×10^4
m		n/a	0.2746	0.2746
n	n_1	1.4033	1.4576	1.4000
	n_2			1.4576

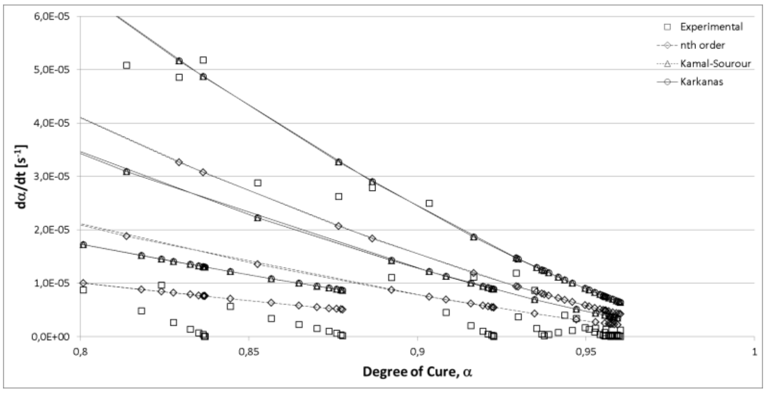

Figure 53 – Detailed plot of the experimental and model curves in the final stage of the isothermal cure.

The inability of the three previously established models to estimate the premature end of reaction, i.e., the incompleteness of the reaction under the specific isothermal conditions studied, suggested that additional thermo-chemical phenomena were playing a relevant role in the overall kinetic behaviour of this resin. Effectively, in the experimental $d\alpha/dt-\alpha$ curves a slight change in the trend slope is observed at degrees of cure in the range of $0.47<\alpha<0.64$. This change in the rate of conversion is associated with the significant decrease of mobility of the reacting species after gelation. At later degrees of cure, the diffusion control of the reacting groups, arising from the densification and increasing viscosity of the network, retards substantially the polymerization process, and the reaction effectively “stops” [235]. In order to account for this phenomenon, a diffusion factor was defined and implemented in the kinetic model of SR® 1500 / SD® 2505. This factor aimed at forcing the model to estimate correctly the maximum degree of cure effectively achieved at each isothermal condition. Better agreement in the entire domain was then pursued.

As discussed in chapter 2, several authors extended a few previously established phenomenological models to take into account the slowing down of the reaction at high degrees of cure due to the onset of diffusion control at a temperature-dependent critical degree of cure, α_c [235-237]. A similar approach was addressed in the specific case under study. The diffusion factor, $f_d(\alpha)$, was defined as:

$$f_d(\alpha)=\frac{1}{1+e^{(C(\alpha-\alpha_{\max}))}} \quad , \tag{4.6}$$

where C is a constant and $\alpha_{\max}$ is the temperature-dependent ultimate degree of cure achieved under isothermal conditions. The dependency of this factor on the temperature was established through the variation of the ultimate degree of cure with the absolute temperature, T, which can be observed in Figure 54. A linear dependence was assumed and thus a linear relationship was determined for $\alpha_{\max}$, presented in equation (4.7).

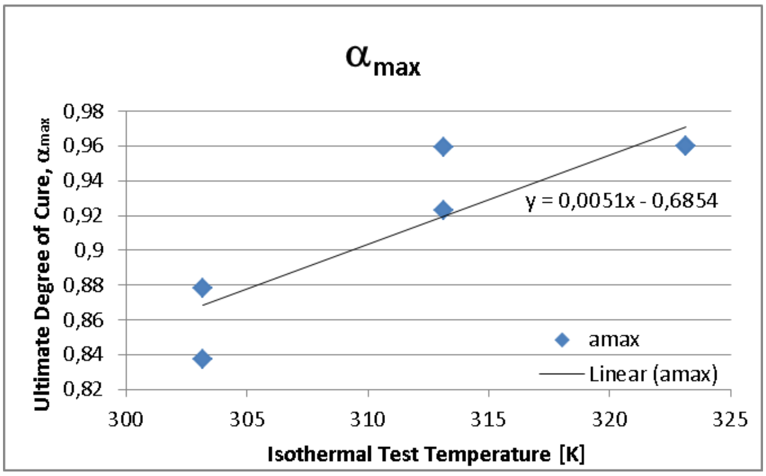

Figure 54 – Maximum (ultimate) degree of cure achieved under isothermal conditions at three different temperatures.

$$\alpha_{\max} = 5.1\times10^{-3}T - 6.854\times10^{-1} \ . \tag{4.7}$$

Since the Karkanas model has shown the best fitting among the three models studied, the diffusion factor was applied to extend and improve this model. An extended model was then established in the form [238]:

$$\frac{d\alpha}{dt} = \frac{1}{1+e^{(C(\alpha-\alpha_{\max}))}}\left[k_1(1-\alpha)^{n_1} + k_2\alpha^{m}(1-\alpha)^{n_2}\right], \tag{4.8}$$

which was fitted to the experimental data using a least squares minimization genetic algorithm (GA). Such algorithm is fairly less dependent on the initial (guess) values of the parameters and allowed to achieve their optimized values without dependency on the previously achieved for the other models. This novel model is hereafter referred to as Karkanas extended model. The agreement of this model with the experimental data is considerably better than the ones obtained with the previously proposed models. Such improvement in the approximation can be observed in Figure 55. It is also clear that the good fitting at the final stages of the cure indicates that this model is able to predict the premature end of conversion ($\alpha_{\max} < 1$). The values of the kinetic parameters obtained for this model are presented in Table 8.

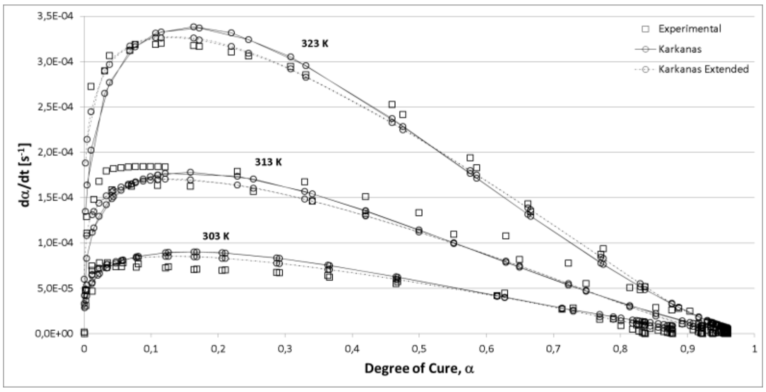

Figure 55 – Fitting of Karkanas extended model to the experimental DSC isothermal data of SR®1500/SD®2505 at 30ºC (303K), 40ºC (313K) and 50ºC (323K).

The Karkanas extended model is, therefore, able to represent the kinetics of the epoxy resin system SR®1500/SD®2505 under isothermal conditions near to room temperature, which are the MRCC chosen for the experimental winding trials with this resin system.

Araldite® LY556

The second resin system studied was a DGEBA-type epoxy system Araldite® LY556 with an anhydride hardener Aradur® 917 (HY917) and the 1-methyl imidazole accelerator DY070. The weight ratio of 100:90:2% (LY556:HY917:DY070) was considered. For this epoxy system, the MRCC are those presented in Table 9.

Table 8 – Kinetic parameters determined for the fitting of the experimental curves with the Karkanas extended model.

Kinetic Parameters		Kinetic Model	
		Karkanas extended $\frac{d\alpha}{dt}=\frac{k_1(1-\alpha)^{n_1}+k_2\alpha^m(1-\alpha)^{n_2}}{1+e^{(C(\alpha-\alpha_c))}}$	Karkanas $\frac{d\alpha}{dt}=k_1(1-\alpha)^{n_1}+k_2\alpha^m(1-\alpha)^{n_2}$
k_1	A_1	9.3347×10^4	2.1699×10^5
	E_{a1}	6.0067×10^4	8.1775×10^4
k_2	A_2	3.4760×10^5	3.0283×10^5
	E_{a2}	5.4284×10^4	5.3328×10^4
m		16.8223	0.2746
n	n_1	1.2286	1.4000
	n_2	0.1993	1.4576
C		14.94384	n/a

Table 9 – MRCC for Araldite® LY556 / Aradur® 917 / accelerator DY070 and selected curing cycles for DSC tests.

Recommended gelation cycle	2 to 4 hours @ 80ºC OR 1 to 3 hours @ 90ºC
Recommended post-cure cycle	4 to 8 hours @ 120ºC OR 2 to 8 hours @ 140ºC OR 2 to 8 hours @ 160ºC
Cycle(s) selected for DSC tests	2 hours @ 30ºC + 4 hours @ 80ºC + 8 hours @ 120ºC; 2 hours @ 30ºC + 4 hours @ 80ºC + 8 hours @ 140ºC; 2 hours @ 30ºC + 4 hours @ 80ºC + 8 hours @ 160ºC.

Similarly to the procedure followed with the SR® 1500 resin system, the MRCC for Araldite® LY556 were accounted in the selection of the testing temperature cycles. Three curing cycles, each composed of three isothermal dwells, were selected and applied. The three consecutive dwells corresponded to the room temperature manufacturing (30ºC), gelation dwell (80ºC) and post-curing (120ºC, 140ºC and 160ºC) isothermal stages, respectively. The first isothermal dwell was intended to approximate the real winding stage which is typically conducted at room temperature. The temperature of 30ºC (303 K) was selected as being the minimum temperature that allowed to have a controlled temperature (stable purge gas and heat flows) in the DSC equipment used, while being the nearest possible to the reference 25ºC corresponding to the average room temperature used in the winding trials. Three material samples were tested, each at one of the three curing cycles selected. Following the standard procedure in DSC analyses, each sample was placed in the aluminium pan and weighted in a microbalance, then placed in the DSC chamber and the test started. The mass, pre-conditioning and temperature cycle of the tested samples is presented in Table 10.

Table 10 – Mass and test condition of the samples of LY556/HY917/DY070 tested.

Sample ID	Mass [mg]	Pre-conditioning	Test Temperature Cycle
LYHF10	21.4	Dry, Dark, 24ºC	2 h @ 30ºC + 4 h @ 80ºC + 8 h @ 120ºC
LYHF11	22.2	Dry, Dark, 22ºC	2 h @ 30ºC + 4 h @ 80ºC + 8 h @ 140ºC
LYHF12	16.0	Dry, Dark, 20ºC	2 h @ 30ºC + 4 h @ 80ºC + 8 h @ 160ºC

The heat flow results directly outputted from the DSC setup were normalized with the mass of the samples. The specific heat flow is plotted in the following graphics, for the three tested samples. As in the case of the other resin system, the mixture of the three constituents of this epoxy system was produced and completed at time $t = 0$. It is observable that at room temperature the reactivity of this resin system remains very low (nearly negligible) for the whole duration of this stage. These results also show that the majority of the conversion progress is achieved during the early stages of the second dwell (80ºC/353 K).

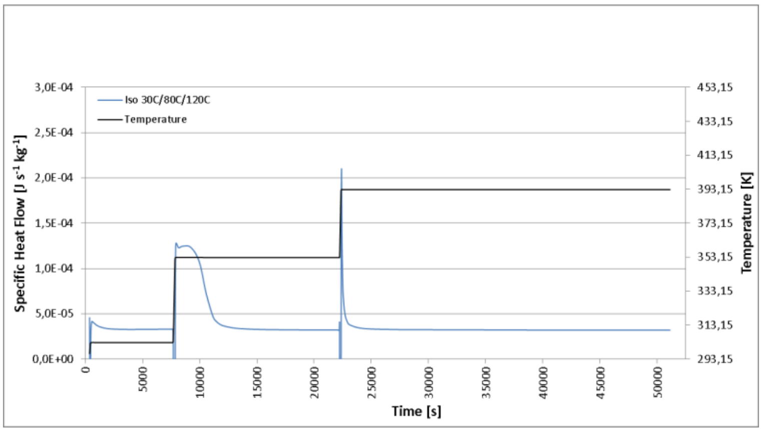

Figure 56 – Plot of specific heat flow for the 3 dwell isothermal DSC test conducted in sample LYHF10 at 30ºC/80ºC/120ºC (303 K/353 K/393 K).

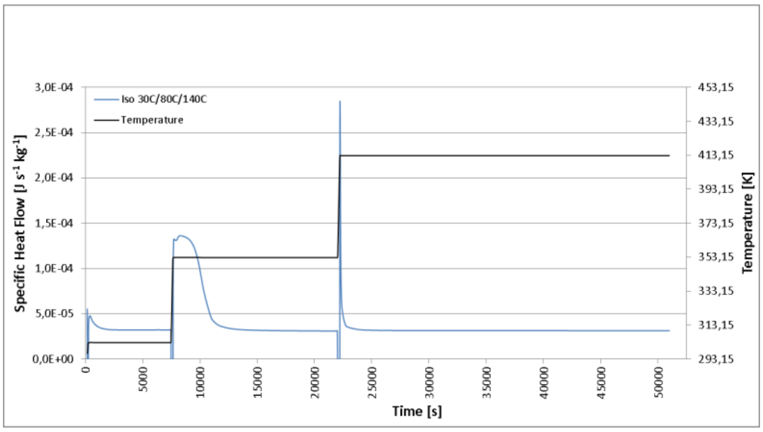

Figure 57 – Plot of specific heat flow for the 3 dwell isothermal DSC test conducted in sample LYHF11 at 30ºC/80ºC/140ºC (303 K/353 K/413 K).

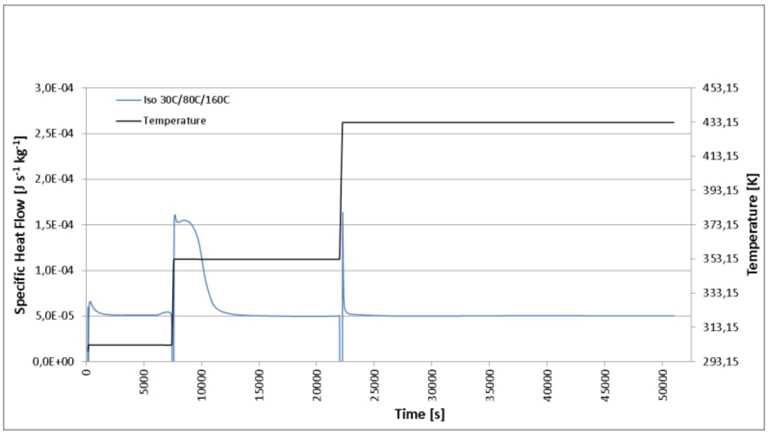

Figure 58 – Plot of specific heat flow for the 3 dwell isothermal DSC test conducted in sample LYHF12 at 30ºC/80ºC/160ºC (303 K/353 K/433 K).

The heats of reaction were determined for the three test curing cycles by integration of these curves. In order to determine and quantify whether or not cure completeness were achieved in the isothermal DSC tests, two dynamic DSC scans were further conducted in each sample. Hence, the heats of reaction under 3 dwells isothermal conditions, $H_{3\times ISO}$, the residual heats of reaction, H_r, and consequently, the total (ultimate) heat of reaction, H_u, of this epoxy system were assessed. In the dynamic scans, the test conditions and procedures applied were similar to those used in the other resin system and were, therefore, described above.

Unlike the other epoxy system studied, the LY556/HY917/DY070 system showed to achieve nearly complete cure after the MRCC. Therefore, the residual heats of reaction returned from the dynamic scans were considerably low as no relevant exothermic peaks were observed. The endothermic vitrification phenomenon was, nevertheless, present and the vitrification temperatures, T_g, were possible to determine. In the following graphics, the outputs of the dynamic tests are plotted for the three samples in terms of the specific heat flow.

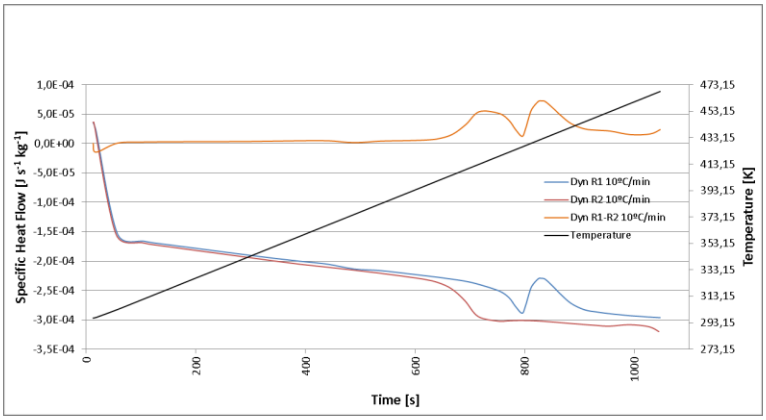

Figure 59 – Plot of specific heat flow for the dynamic DSC tests conducted in sample LYHF10 (previous 3 dwell isothermal test at 303 K/353 K/393 K).

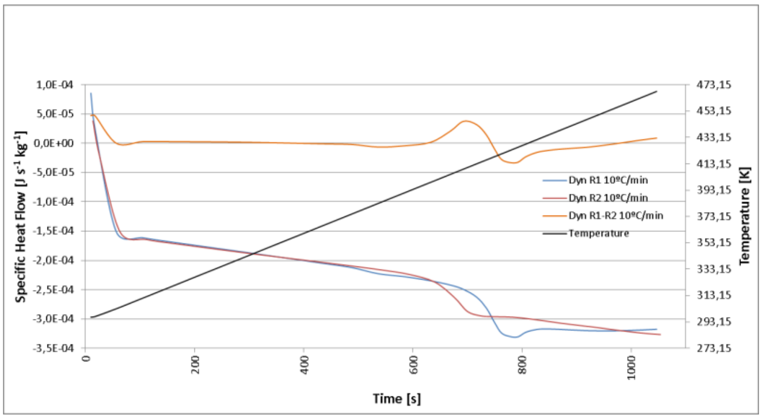

Figure 60 – Plot of specific heat flow for the dynamic DSC test conducted in sample LYHF11 (previous 3 dwell isothermal test at 303 K/353 K/413 K).

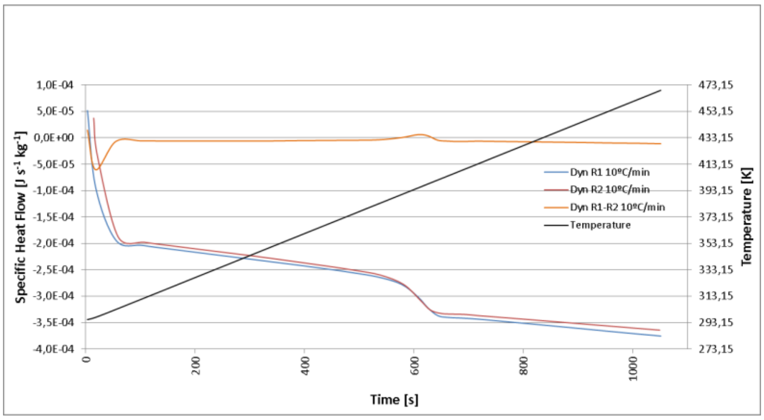

Figure 61 – Plot of specific heat flow for the dynamic DSC test conducted in sample LYHF12 (previous isothermal test at 303 K/353 K/433 K).

The values of the heats of reaction determined for each sample are presented in Table 11. The values determined for the total (ultimate) heat of reaction, H_u, intrinsic to this resin system is in accordance with those previously published by other researchers [239,240], thus indicating the validity of the experimental procedure implemented in this work.

Table 11 – Heats of reaction of the samples of LY556/HY917/DY070 tested.

Sample ID	Isothermal Test		Dynamic Scans	H_u [J/kg]	T_g [ºC]
	Temp. [ºC]	H_{ISO} [J/kg]	H_r [J/kg]		
LYHF10	30/80/120	0,307	0,0141	0,321	151,0
LYHF11	30/80/140	0,337	0,00319	0,340	145,5
LYHF12	30/80/160	0,330	0,000512	0,330	125,0

The heats of reaction obtained for each MRCC condition are also plotted below. It is observable that, as the third dwell temperature increased, the isothermal heat of reaction (the heat released during each MRCC), $H_{3\times ISO}$, increased and the residual heat of reaction, H_r, oppositely decreased. This evolution was expected since the increasing of the curing temperature favours the completeness of the chemical conversion. In fact, the completeness of the reaction of the LY556/HY917/DY070 under these MRCC was considerably high ($H_{3\times ISO} \approx H_u$) and for the temperatures of 140ºC and 160ºC in the third dwell, the reaction nearly concluded and thus the residual heats in those cases were nearly null. One can also verify that the total heat remained constant, independently of the isothermal testing temperature of the third dwell of each MRCC applied. As mentioned above, this is in accordance with theory and principles for polymer curing reactions [228].

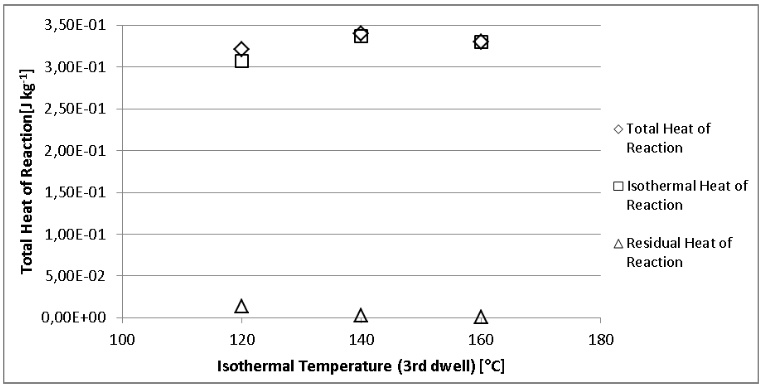

Figure 62 – 3 dwell isothermal, residual and total heat of reaction of the material samples of LY556/HY917/DY070 tested in different MRCC.

Following the same procedure as for the SR® 1500 / SD® 2505 data, the experimental curves for the evolution of the degree of cure, α, and the rate of degree of cure, $d\alpha/dt$, with time were computed and are plotted in the following figures. The maximum degree of cure, $\alpha_{\max}$, achieved in the MRCC with the third dwell temperature at 140ºC (413 K) and 160ºC (433 K) was of ca. 99.2% while for the one at 120ºC (393 K) it was of 95.6%. Comparing to other epoxy resin systems and their corresponding MRCC, the completeness of reaction achieved in this system with the MRCC is very high, nearly maximal.

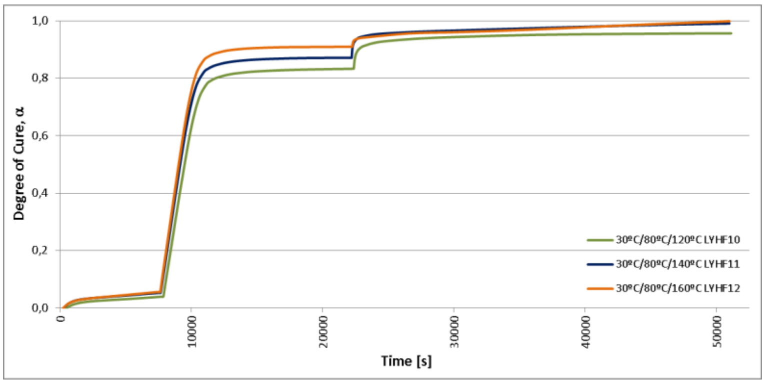

Figure 63 – Evolution of the degree of cure in all the LY556/HY917/DY070 samples during the 3 dwell isothermal tests conducted.

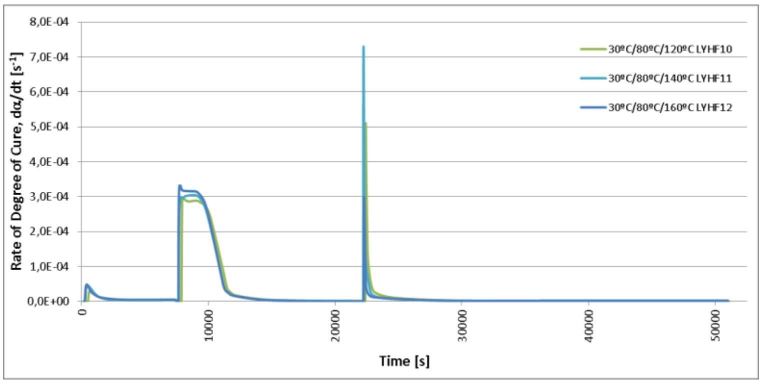

Figure 64 – Evolution of the rate of degree of cure in all the LY556/HY917/DY070 samples during the 3 dwell isothermal tests conducted.

In Figure 65, the experimental data is plotted in terms of the rate of cure *versus* degree of cure. As seen before, this is the relevant relationship to model and, therefore, several equations were analysed and fitted through non-linear least squares minimization techniques.

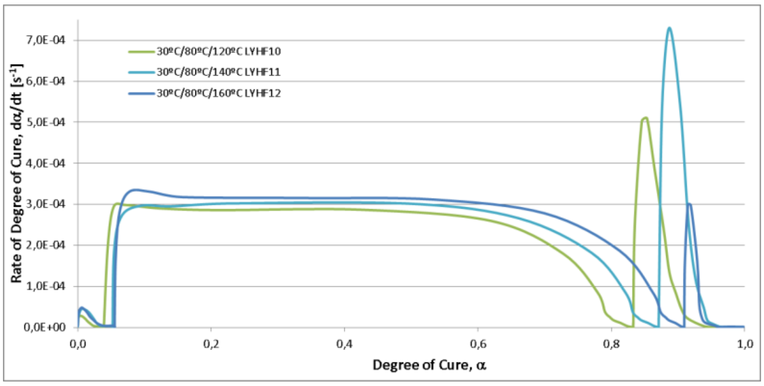

Figure 65 – Plot of the rate of degree of cure *versus* degree of cure for the epoxy system LY556/HY917/DY070 during the 3 dwell isothermal tests.

Unlike the case of the SR® 1500 / SD® 2505, the MRCC for the LY556/HY917/DY070 implied two discontinuous stages corresponding to the different temperature dwells. In the experimental DSC programme, three stages were actually applied by adding an initial near to room temperature dwell. This resulted in a discontinuous multi-step relationship that was hardly modelled by a single equation (model) for the entire applicable domain of α. Nevertheless, since the steps of the function also corresponded to sudden changes in the temperature, a temperature-dependent model could ultimately be able to approach it reasonably. This challenge was addressed and the establishment of an adequate model in the form of equation (4.4) that would properly fit the experimental curves within all the domain of temperature and degree of cure was firstly pursued. Ideally, the model should also represent the main physical phenomena occurring during the curing reaction, thus being a parametrically meaningful kinetic model for this epoxy under these MRCC.

Despite the discontinuities observed at the transitions between the isothermal dwells, the experimental $\alpha(t)$ curves (Figure 63) presented a single-step decelerating shape, thus suggesting a n^{th} order model [231] could be fitted. Here again, several other previously established semi-empirical phenomenological models were fitted to the LY556/HY917/DY070 experimental curves. Namely, the Kamal-Sourour autocatalytic model [85,232] and the Karkanas model [233] were evaluated.

The results of the fitting of the three models (nth order, Kamal-Sourour and Karkanas) to the experimental DSC isothermal data obtained for the LY556/HY917/DY070 epoxy resin are shown in Figure 66. A one shot global fitting of each model to the three isothermal stages was conducted through non-linear least squares minimization. The kinetic parameters determined for each model global fitting are presented in Table 12.

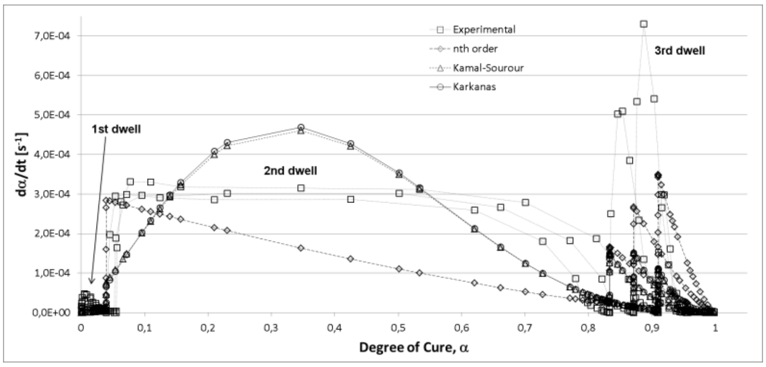

Figure 66 – One shot global fitting of the nth order, Kamal-Sourour and Karkanas models to the experimental DSC 3 dwell isothermal data of LY556/HY917/DY070.

Table 12 – Kinetic parameters determined for the fitting of the experimental curves with the nth order, Kamal-Sourour and Karkanas models.

Kinetic Parameters		Kinetic Model		
		nth order $\frac{d\alpha}{dt}=k_1(1-\alpha)^n$	Kamal-Sourour $\frac{d\alpha}{dt}=(k_1+k_2\alpha^m)(1-\alpha)^n$	Karkanas $\frac{d\alpha}{dt}=k_1(1-\alpha)^{n_1}+k_2\alpha^m(1-\alpha)^{n_2}$
k_1	A_1	1.0000×10^5	1.0483×10^6	1.4810×10^6
	E_{a1}	5.7577×10^4	7.3666×10^4	9.5824×10^4
k_2	A_2	n/a	1.0000×10^5	1.0000×10^5
	E_{a2}	n/a	4.8267×10^4	4.8236×10^4
m		n/a	1.4176	0.0009
n	n_1	1.4441	2.9497	2.9595
	n_2			1.3994

The quality of the model fitting in the first dwell is treated later in this text, since by direct comparison with the second and third ones, it is nearly negligible. Regarding the second and third isothermal dwells, the three models behaved differently. The nth order model showed higher sensitivity to the temperature, thus allowing it to capture the behaviour in the third isothermal dwell for the three temperatures (120ºC/393 K, 140ºC/413 K and 160ºC/433 K). However, its agreement in the second isothermal dwell (80ºC/353 K) was very poor and no acceptable combination of parameters was successfully determined. Oppositely, the Kamal-Sourour and the Karkanas models showed better agreement in the second isothermal dwell.

These results clearly indicated that a good agreement in all the applicable domains of degree of cure and temperatures (three different temperatures were imposed in the third isothermal dwell) would be very difficult to achieve. In other words, keeping the same kinetic parameters for the entire domain led to considerable mismatch between the experimental data and each model in either one or all the isothermal dwells.

Hence, independent analyses and modelling of each isothermal dwell were conducted to achieve an acceptable (and therefore usable) model for the relevant domains. The non-linear least squares minimization technique was applied through both genetic (evolutionary) and non-linear iterative algorithms. The results of the independent fitting to each dwell are shown below for the three models. In the following figures the best fits are graphically plotted and in Table 13 the corresponding kinetic parameters are presented.

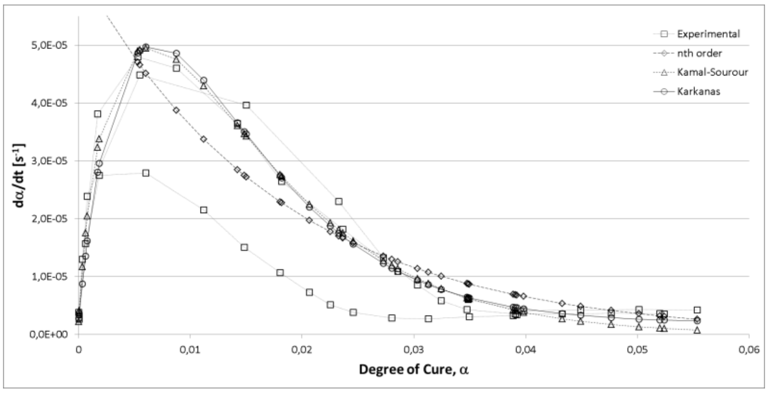

Figure 67 – Fitting of the nth order, Kamal-Sourour and Karkanas models to the experimental DSC data of the 1st isothermal dwell (303 K) on LY556/HY917/DY070.

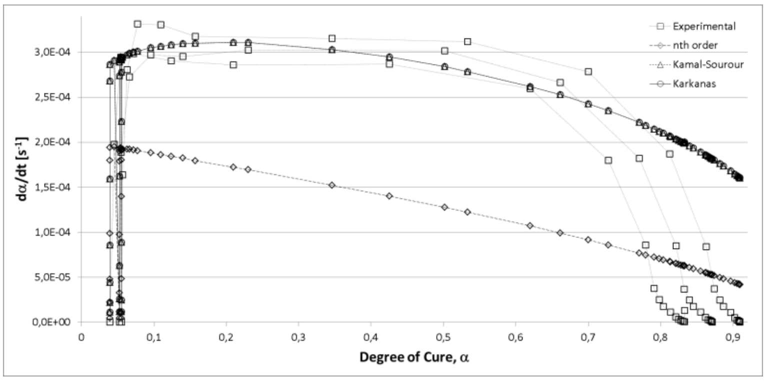

Figure 68 – Fitting of the nth order, Kamal-Sourour and Karkanas models to the experimental DSC data of the 2nd isothermal dwell (353 K) on LY556/HY917/DY070.

Despite the fact that a reasonable agreement was possible to obtain for each isothermal dwell with certain models, strongly different sets of parameters were achieved in each independent fitting. Namely, the reaction order exponents were out of the expected range in the first dwell (30ºC). Moreover, no evidence of a meaningful relationship and/or evolution of each model’s kinetic parameters throughout the interdependent domains (α, T) was found. Nevertheless, several useful indications were assessed with these initial model fitting procedures in view of defining the proper model for this resin system under these MRCC conditions. Hereafter, the analysis of the results is addressed.

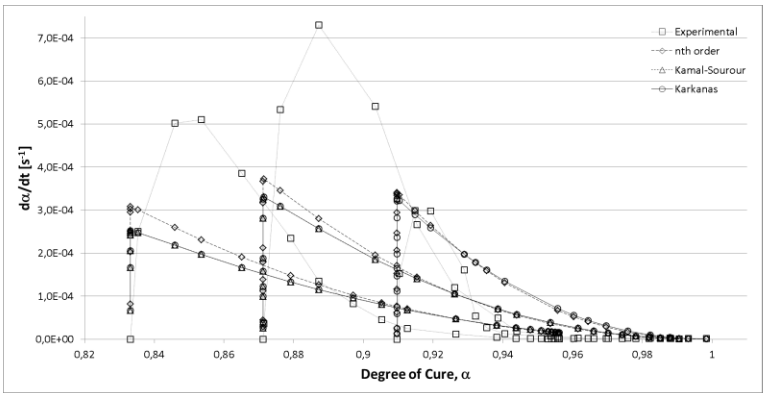

Figure 69 – Fitting of the nth order, Kamal-Sourour and Karkanas models to the experimental DSC data of the 3rd isothermal dwell (393 K/413 K/433 K) on LY556/HY917/DY070.

Table 13 – Kinetic parameters determined for the fitting of the experimental curves with the nth order, Kamal-Sourour and Karkanas models. The optimum combinations of parameters were determined independently for each isothermal dwell.

Kinetic Parameters		Kinetic Model								
		nth order $\frac{d\alpha}{dt}=k_1(1-\alpha)^n$			Kamal-Sourour $\frac{d\alpha}{dt}=(k_1+k_2\alpha^m)(1-\alpha)^n$			Karkanas $\frac{d\alpha}{dt}=k_1(1-\alpha)^{n_1}+k_2\alpha^m(1-\alpha)^{n_2}$		
		1st dwell	2nd dwell	3rd dwell	1st dwell	2nd dwell	3rd dwell	1st dwell	2nd dwell	3rd dwell
k_1	A_1	7.4719×10^5	2.4385×10^6	2.2500×10^5	0.0000	0.0000	0.0000	6.3338×10^5	0.0000	0.0000
	E_{a1}	5.8402×10^4	6.8148×10^4	5.3256×10^4	0.0000	0.0000	0.0000	6.6718×10^4	0.0000	0.0000
k_2	A_2	n/a	n/a	n/a	8.0100×10^5	1.9660×10^5	2.2500×10^5	5.7969×10^5	1.9660×10^5	2.2500×10^5
	E_{a2}	n/a	n/a	n/a	4.8070×10^4	5.8825×10^4	5.3256×10^4	4.4084×10^4	5.8825×10^4	5.3256×10^4
m		n/a	n/a	n/a	0.7299	0.0875	1.5000	0.9553	0.0875	1.5000
n	n_1	55.7349	0.6506	2.2918	113.6903	0.3620	2.2500	0.0000	0.0000	0.0000
	n_2							137.6796	0.3620	2.2500

As previously mentioned, the 1st isothermal dwell (30ºC/303 K) was introduced in the MRCC in order to simulate/approximate the real manufacturing conditions to which the matrix is subjected during the FW stage. The DSC outputs clearly show that the kinetics of this resin at this temperature is nearly negligible compared to the kinetics observed in both the 2nd and 3rd dwells. In fact, most of the models available in literature were developed for specific ranges of temperature (typically between 80ºC and 160ºC) and do not approach reasonably the experimental data at near-to-room temperatures. The range of conversion in this dwell is as small as $0\% < \alpha < 5\%$. However, since the main objective of this work was to model the FW manufacturing process, the ability to model the kinetic behaviour at these low temperatures became crucial and a major challenge.

In the 1st dwell, the models that better fitted the experimental data obtained for the three resin samples tested were the Kamal-Sourour and the Karkanas (Figure 67).

Despite the fact that the exponent n took very high values (Table 13) and therefore the interpretation of the kinetic parameters could be distorted, the determination of a value of $k_1 = 0$ in the Kamal-Sourour model suggested that a simpler autocatalytic model could describe this kinetic behaviour. The equation (2.44) represents a special case of the Kamal-Sourour model when $k_1 = 0$ and may, thus, be rewritten as follows:

$$\frac{d\alpha}{dt} = k_2 \alpha^m (1-\alpha)^n \ . \tag{4.9}$$

Unlike the 1st isothermal dwell, in the 2nd isothermal dwell (80ºC/353 K) the resin kinetics was very expressive and both the rate and the extension of the cure achieved were high. The range of conversion in this dwell was $5\% < \alpha < 90\%$. In fact, during this stage (composite part heated after the winding stage) gelation occurs and the final positions of the fibre bed are achieved upon ceasing of the resin flow. The morphology of the matrix changes considerably and thermo-chemical aspects such as shrinkage become highlighted. For these reasons, the 2nd isothermal dwell was the most relevant for the development of an adequate kinetic model for the LY556/HY917/DY070 epoxy system under MRCC conditions.

Both the Kamal-Sourour and the Karkanas models were able to fit the experimental data of the 2nd dwell similarly (Figure 68). The short initial period of temperature rise and the subsequent plateau of the $d\alpha/dt - \alpha$ curve were positively captured. Since the optimized values returned $k_1 = 0$ for both models, the hypothesis of using the simpler autocatalytic model in equation (4.9) gained even more consistency. However, a discrepancy was obtained in the final decrease of the conversion rate ($\alpha > 75\%$). The sudden drop of the conversion rate suggested, as in the case of the SR®1500/SD®2505 resin, that upon this point the reaction was diffusion-controlled. In the experimental $d\alpha/dt - \alpha$ curves a sudden change in the trend slope is observed at degrees of cure of around $\alpha = 0.75$. As discussed before, this change in the rate of conversion is associated with decrease of mobility of the reacting species after gelation. The diffusion control then retards substantially the polymerization process, and the reaction effectively “stops” if the same isothermal condition is kept [235]. Following the same approach that several authors used to account for the slowing down of the reaction at high degrees of cure [235-237] a novel autocatalytic diffusion-extended model was developed by adding a so-called diffusion factor, $f_d(\alpha)$, to the simplified Kamal-Sourour model ($k_1 = 0$) in the form:

$$f_d(\alpha) = \frac{1}{1 + e^{(C(\alpha - \alpha_{\max} + \alpha_0))}} \ , \tag{4.10}$$

where α_0 and $\alpha_{\max}$ are, respectively, the initial and final degrees of cure observed in the 2nd dwell, thus defining the applicable domain of α, and C is a constant.

The new model was then established as follows [238]:

$$\frac{d\alpha}{dt} = \frac{k_2 \alpha^m (1-\alpha)^n}{1 + e^{(C(\alpha - \alpha_{\max} + \alpha_0))}} \ . \tag{4.11}$$

This model is, in fact, an oriented adaptation of the one proposed by Chern and Poehlein [236] and previously presented in equation (2.34). This diffusion term considers not only the maximum degree of cure for which the curve tends, $\alpha_{\max}$, but also the shifted initial degree of cure, α_0, due to the fact that this isothermal dwell was preceded by another isothermal stage. The result is depicted in Figure 70. The agreement with the experimental data was then successfully improved and the model was able to properly describe the entire curve in the applicable domains (α, T). The kinetic parameters together with the constants of the diffusion factor are presented in Table 14. The quantities α_0 and $\alpha_{\max}$ were determined, respectively, as the averaged values of the initial and final degrees of cure of the three resin samples tested (specifically in the 2nd isothermal dwell).

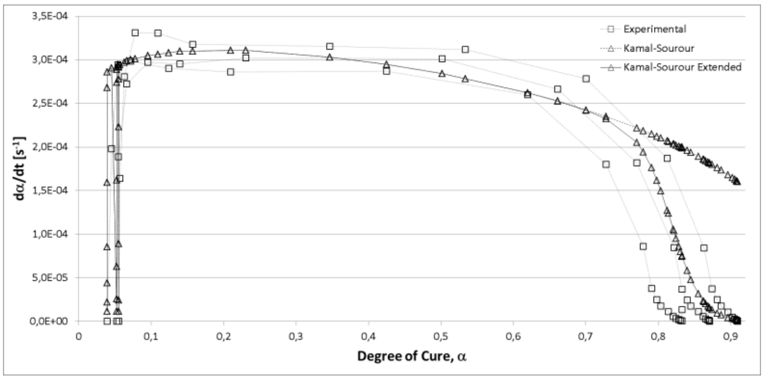

Figure 70 – Fitting of the Kamal-Sourour diffusion-extended model to the experimental DSC data of the 2nd isothermal dwell (393 K/413 K/433 K) on LY556/HY917/DY070.

Table 14 – Kinetic parameters determined for the fitting of the experimental DSC data of LY556/HY917/DY070 in the 2nd isothermal dwell (80ºC/353 K) with the Kamal-Sourour diffusion-extended model.

Kinetic Parameters		Kinetic Model	
		Kamal-Sourour extended $\frac{d\alpha}{dt}=\frac{(k_1+k_2\alpha^m)(1-\alpha)^n}{1+e^{C(\alpha-\alpha_{\max}+\alpha_0)}}$	Kamal-Sourour $\frac{d\alpha}{dt}=(k_1+k_2\alpha^m)(1-\alpha)^n$
k_1	A_1	0.0000	0.0000
	E_{a1}	0.0000	0.0000
k_2	A_2	1.9660×10^5	1.9660×10^5
	E_{a2}	5.8825×10^4	5.8825×10^4
m		0.0875	0.0875
n		0.3620	0.3620
C		48.5000	n/a
α_0		0.0490	n/a
$\alpha_{\max}$		0.8710	n/a

In the 3rd dwell the three models firstly fitted presented similar coarse approximations to the experimental data (Figure 69). A good agreement of the fitting for the three experimental curves (three resin samples - 120ºC/393 K, 140ºC/413 K and 160ºC/433 K) was not expectable, since these presented considerable scatter. The sample tested at 160ºC/433 K presented a lower initial heat release rate (and thus lower conversion rate) than the two other samples, breaking the expectable increasing tendency with the applied temperature [238,240]. Further material samples and tests would be required to evaluate the effective trend. It is worth to notice, however, that the sample tested at 160ºC/433 K was the one that presented greater conversion at the end of the 2nd isothermal dwell (80ºC/353 K) and thus had less cross-links and reactive species available to progress with the cure. This is the suggested reason for the unexpected lower reaction rate observed at the beginning of the 3rd dwell in this sample. Nevertheless, at the start of the 3rd dwell, as $83\% < \alpha < 91\%$, the resin was already almost fully cured in all samples. Therefore, from the manufacturing process model point of view, this was not a relevant stage for modelling since the fibre bed and the matrix (thus, the composite laminate) were already locked in their final positions. However, both for the sake of completeness and due to the fact that thermo-chemical and mechanical phenomena could still occur and influence the final stress condition of the composite, the experimental data of the 3rd isothermal dwell was equally analysed and modelled.

In order to set the applicable domain of α for the model of the 3rd isothermal dwell, α_0 was defined as the averaged value of the initial degrees of cure of the three resin samples tested (specifically in the 3rd isothermal dwell). The final degree of cure, $\alpha_{\max}$, was not averaged, since the three samples were subjected to different temperatures in this dwell. It was therefore established as a temperature-dependent parameter and its evolution is graphically represented in Figure 71. A quadratic dependence was assumed and thus a 2nd order polynomial relationship $\alpha_{\max}(T)$ was determined, taking into account that a maximum value of $\alpha_{\max} = 1.0$ should not be exceeded within a reasonable temperature range above 160ºC/433 K. This condition would not be necessary if the strict domain of $120^{\circ}C < T < 160^{\circ}C$ is considered in the kinetic modelling. However, it allowed to widen the range of applicability of the model to pratical situations in which greater temperatures are applied. The relationship established for $\alpha_{\max}$ is then described as:

$$\alpha_{\max} = -1.711 \times 10^{-5} T^2 + 1.514 \times 10^{-2} T - 2.349 \ . \tag{4.12}$$

In Figure 72, the fitting of the nth order, Kamal-Sourour and Karkanas models to the 3rd dwell experimental data, after definition of the restricted applicable domain $\alpha_0 < \alpha < \alpha_{\max}$, are presented.

All the three models showed similar sensitivity to temperature. Also, the capture of the curve shapes at the maximum conversion rates and the fast slow-down of the reaction were not good for the three models. The corresponding recalculated kinetic parameters are presented in Table 15.

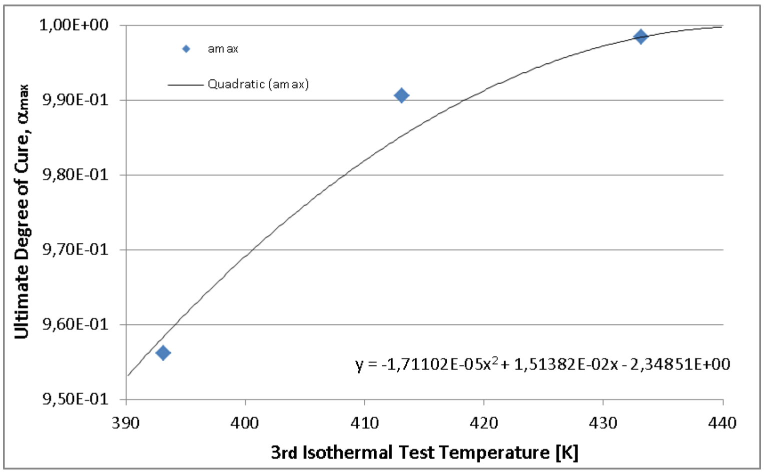

Figure 71 – Maximum (ultimate) degree of cure achieved under the isothermal conditions at three different temperatures in the 3rd dwell for the resin LY556/HY917/DY070.

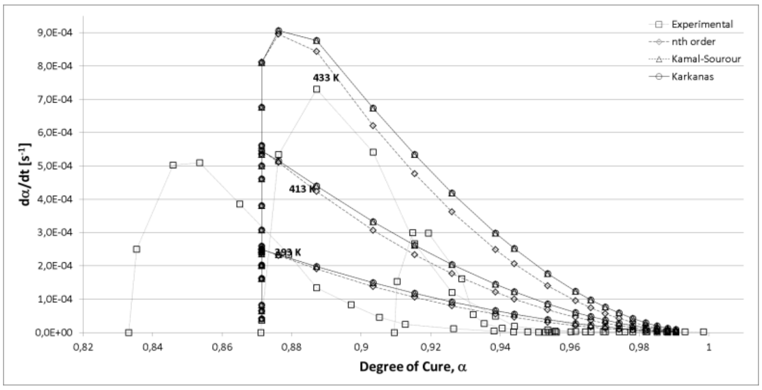

Figure 72 – Fitting of the nth order, Kamal-Sourour and Karkanas models to the experimental DSC data of the 3rd isothermal dwell (393 K/413 K/433 K) on LY556/HY917/DY070 in the applicable domain.

Table 15 – Kinetic parameters determined for the fitting of the experimental curves of the 3rd isothermal dwell with the nth order, Kamal-Sourour and Karkanas models.

Kinetic Parameters		Kinetic Model		
		nth order $\frac{d\alpha}{dt} = k_1(1-\alpha)^n$	Kamal-Sourour $\frac{d\alpha}{dt} = (k_1 + k_2\alpha^m)(1-\alpha)^n$	Karkanas $\frac{d\alpha}{dt} = k_1(1-\alpha)^{n_1} + k_2\alpha^m(1-\alpha)^{n_2}$
k_1	A_1	2.2500×10^5	0.0000	0.0000
	E_{a1}	5.3651×10^4	0.0000	0.0000
k_2	A_2	n/a	2.2500×10^5	2.2500×10^5
	E_{a2}	n/a	5.3651×10^4	5.3651×10^4
m		n/a	1.5000	1.5000
n	n_1	2.0500	1.9500	0.0000
	n_2			1.9500

The apparent disagreement between the models and the experimental data points is inflated by the facts that the latter are not superposed in the same restricted domain

($\alpha_0 < \alpha < \alpha_{\max}$) and the experimental results on the third sample (160ºC/433 K) are not in line with the expectable behaviour/dependence on temperature [238,240]. Hence, the determination of these model curves attained both the magnitude of the experimental data and the increasing tendency with temperature (focusing on the samples tested at 120ºC and 140ºC). From the kinetic parameters found, it was concluded that, similarly to the previous dwells, a simpler form of the Kamal-Sourour model ($k_1 = 0$) was adequate to describe the 3rd dwell. The autocatalytic approach to model this last stage of the MRCC is consistent to the modelling results for the 2nd isothermal dwell. The equation (4.9) was found to model the kinetic behaviour of the epoxy system LY556/HY917/DY070 in the temperature and degree of cure ranges of $120^oC < T < 160^oC$ and $0.871 < \alpha < 1.0$, respectively.

However, as mentioned before, the selected model is not able to follow the strong decrease in reactivity observed for all the three samples after the conversion rate peak. Therefore, the existence of an additional mechanism governing the later stage of the curing process at these temperatures is inferred from the experimental data. Since this occurs at nearly maximum degree of cure for the entire reaction, the sudden drop of reactivity (up to final cease of reaction) could be associated with the completion of the chemical cross-linking polymerization, rather than with the onset of diffusion. Due to the high degree of cure previously achieved at the end of the 2nd isothermal dwell (80ºC), the kinetic behaviour of the resin during the 3rd isothermal dwell (120ºC/393 K, 140ºC/413 K or 160ºC/433 K) was certainly different to the one it would have if subjected to these latter isothermal condition from an initial uncured state ($\alpha \approx 0$). This compromises the comparison with previous isothermal studies conducted with the same epoxy system [240]. In practical terms, however, from the phenomenological modelling point of view, the autocatalytic model should be extended with a factor attributing greater decreasing slope upon reach of the characteristic peak.

In order to improve the quality of the model fitting, firstly a diffusion factor similar to the one developed for the 2nd dwell was applied, thus establishing the same model described in equations (4.10) and (4.11). With both $\alpha_0 = 0.871$ and $\alpha_0 = 0$ (in the latter case ignoring the shifted initial degree of cure of the 3rd dwell) no changes were observed. Secondly, a diffusion factor similar to the one developed by Fournier *et al.* [235] and used by Rabearison *et al.* [240] was considered in the form:

$$f_d(\alpha) = \frac{2}{1 + e^{C(\alpha - \alpha_{\max})}} - 1 \ , \qquad (4.13)$$

and the autocatalytic diffusion-extended model was rewritten as:

$$\frac{d\alpha}{dt} = \left[\frac{2}{1 + e^{C(\alpha - \alpha_{\max})}} - 1 \right] k_2 \alpha^m (1 - \alpha)^n \ , \qquad (4.14)$$

and fitted to the experimental data points. The improved result is depicted in Figure 73. The kinetic parameters together with the constants of the diffusion factor are presented in Table 16.

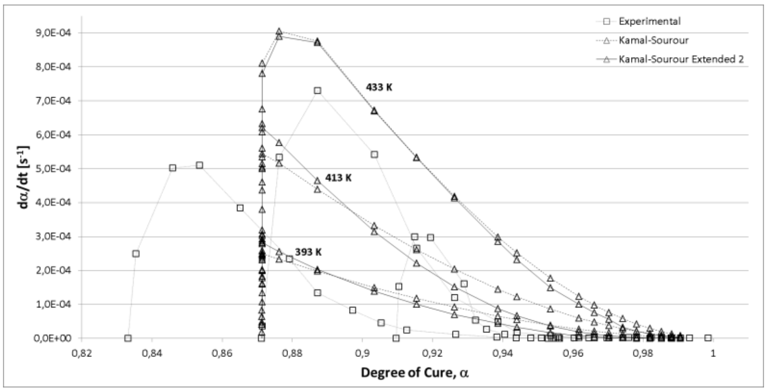

Figure 73 – Fitting of the nth order, Kamal-Sourour and Karkanas models to the experimental DSC data of the 3rd isothermal dwell (393 K/413 K/433 K) on LY556/HY917/DY070 in the applicable domain.

Table 16 – Kinetic parameters determined for the fitting of the experimental DSC data of LY556/HY917/DY070 in the 3rd isothermal dwell (393 K, 413 K and 433 K) with the Kamal-Sourour diffusion-extended 2 model.

Kinetic Parameters		Kinetic Model	
		Kamal-Sourour extended 2 $\frac{d\alpha}{dt}=\left[\frac{2}{1+e^{C(\alpha-\alpha_{\max})}}-1\right](k_1+k_2\alpha^m)(1-\alpha)^n$	Kamal-Sourour $\frac{d\alpha}{dt}=(k_1+k_2\alpha^m)(1-\alpha)^n$
k_1	A_1	0.0000	0.0000
	E_{a1}	0.0000	0.0000
k_2	A_2	3.1562×10^5	2.2500×10^5
	E_{a2}	5.3651×10^4	5.3651×10^4
m		1.5000	1.5000
n		1.9500	1.9500
C		20	n/a
$\alpha_{\max}$		$-1.711\times10^{-5}T^2+1.514\times10^{-2}T-2.349$	n/a

Upon the analyses and development of the best phenomenological models for each isothermal stage of the MRCC, the overall kinetic model for the entire MRCC was obtained by assuming a piece-wise equation along the combined domains of α and T. This overall model is described by the following set of equations:

$$\begin{cases} \frac{d\alpha}{dt}=k_2\alpha^m(1-\alpha)^n & ,0\le\alpha<0.049,\ 298K<T<308K \\ \frac{d\alpha}{dt}=\frac{k_2\alpha^m(1-\alpha)^n}{1+e^{(C(\alpha-\alpha_{\max}+\alpha_0))}} & ,0.049\le\alpha<0.871,\ 333K<T<353K \\ \frac{d\alpha}{dt}=\left[\frac{2}{1+e^{C(\alpha-\alpha_{\max})}}-1\right]k_2\alpha^m(1-\alpha)^n & ,0.871\le\alpha<1,\ 373K<\alpha<433K \end{cases} \quad , \qquad (4.15)$$

and graphically represented in Figure 74. It consisted, then, in a simplified Kamal-Sourour autocatalytic model ($k_1=0$) diffusion-extended for the 2nd and 3rd isothermal dwells. The kinetic parameters obtained for this model are in Table 17.

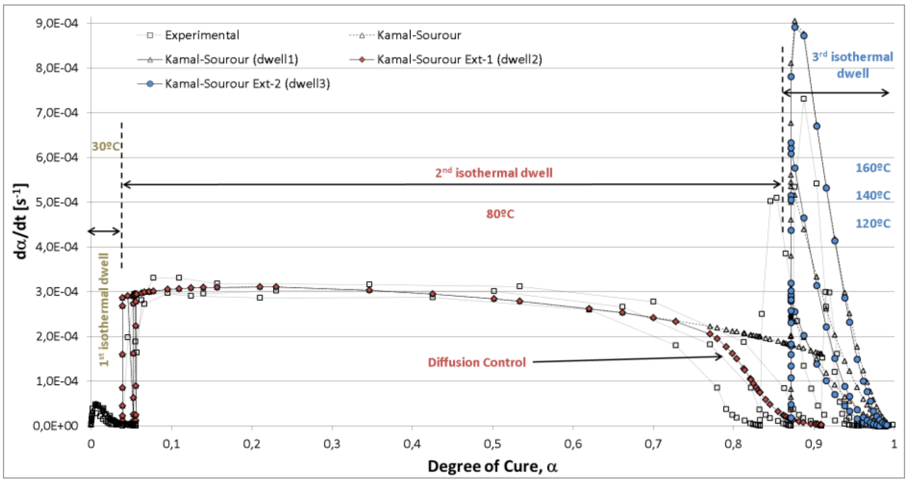

Figure 74 – Graphical representation of the kinetic model for the epoxy system LY556/HY917/DY070 subjected to the MRCC conditions.

Table 17 – Kinetic parameters determined for the kinetic model developed for the three isothermal dwells of the MRCC for the epoxy system LY556/HY917/DY070.

Dwell		1st dwell	2nd dwell	3rd dwell
Duration [h]		2	4	8
Temp. [K]		303	353	393, 413 and 433
Kinetic Parameters		Kinetic Model		
		Kamal-Sourour $\frac{d\alpha}{dt}=(k_1+k_2\alpha^m)(1-\alpha)^n$	Kamal-Sourour extended $\frac{d\alpha}{dt}=\frac{(k_1+k_2\alpha^m)(1-\alpha)^n}{1+e^{C(\alpha-\alpha_{\max}+\alpha_0)}}$	Kamal-Sourour extended 2 $\frac{d\alpha}{dt}=\left[\frac{2}{1+e^{C(\alpha-\alpha_{\max})}}-1\right](k_1+k_2\alpha^m)(1-\alpha)^n$
k_1	A_1 [s^{-1}]	0.0000	0.0000	0.0000
	E_{a1} [Jmol^{-1}]	0.0000	0.0000	0.0000
k_2	A_2 [s^{-1}]	8.0100×10^5	1.9660×10^5	3.1562×10^5
	E_{a2} [Jmol^{-1}]	4.8070×10^4	5.8825×10^4	5.3651×10^4
m		0.7299	0.0875	1.5000
n		113.6903	0.3620	1.9500
C		n/a	48.5000	20
α_0		n/a	0.0490	0.8710
$\alpha_{\max}$		n/a	0.8710	$-1.711\times10^{-5}T^2+1.514\times10^{-2}T-2.349$

The model developed herewith for the LY556/HY917/DY070 was integrated in the global FW process model in the resin cure sub-model library.

4.2.2. Resins Rheological Behaviour

Within the scope of the FW process model, the viscosity of the matrix system, which evolves during the manufacturing and consolidation stage, is a relevant parameter to be assessed. In either the thermoplastic or thermosetting process configuration, this physical characteristic directly affects the stiffness (and thus the stress-strain state) of the composite laminate being wound. More intrinsically, it governs the ability of the matrix to flow through the fibre bed. Rheology is the discipline dealing with deformation and flow of matter under controlled conditions [241]. Using constitutive equations between the stress and strain histories, useful descriptions of the rheological behaviour of industrially relevant materials are obtained.

Following the study presented in the previous section, the two epoxy resin systems selected for the process model validation in wet FW trials were studied in detail. The two systems - SR®1500 from Sicomin Composites (France) and Araldite® LY556 from Huntsman (USA) – were characterized and modelled through rotational viscosimetry and oscillatory rheometry. The establishment of predictive models for the change in the viscosity during the cure, as the degree of conversion progressed from its initial to the final states, was pursued.

Original rheological models were established for these resin systems subjected to the "real" processing conditions, since MRCC were used. These empirically validated sub-models were afterwards included in the resin viscosity process sub-model, as main inputs for the global process model. Hereafter, the experimental and modelling procedures are described and the rheological models developed are presented.

4.2.2.1. Experimental Procedures

The viscosity of thermosetting resins is governed by two different phenomena: the growing size of the molecules during curing, which increases the viscosity of the resin, and the effect of temperature on the molecular mobility [242]. The two phenomena compete throughout the curing process and the predominance of one over the other is highly dependent on the temperature range, concentrated mass and degree of cure (conversion). Due to the intrinsic nature of the polymer cross-linking reactivity, as two or more reacting species are blended, most authors model the viscosity, μ, as a function of the temperature, T, and degree of cure, α, as [82,91,100]:

$$\mu = f(T,\alpha) \ , \tag{4.16}$$

disregarding, thus, the mass as an independent parameter. In fact, the effect of the quantity of concentrated mass freely available in the reacting sample is directly related with the temperature. In fact, since the chemical reaction of thermosetting systems is typically exothermic, upon release of heat at a certain point, the heat is transferred to its vicinity which creates a self-heating phenomenon. So, the effect of mass quantity is limited to whether or not the temperature of every regions of the sample is controllable from sole external heating sources. Intuitively, the greater the available mass is, more relevant is the internal self-heating mechanism.

Rotational viscosimetry and oscillatory rheometry are among the most widely used techniques to assess the change of viscosity in reacting polymers [243,244]. These two techniques were used in this study in view of analysing the resins behaviour under different mass conditions. The use of two different experimental procedures allowed also to achieve additional cross validation of their results.

Since the typical arrangements and procedures associated with these techniques are not suitable to extend the measurements up to and afterwards the gelation of the polymer sample, special care and a few adaptations were implemented to account for this. The two experimental procedures used for the rheological characterization of the SR®1500 and LY556 epoxy systems are described hereafter.

The working principle of rotational viscometers is to measure the torque needed to rotate the measurement instrument (spindle, cylinder or roller), whilst being immersed in the material sample under analysis. When compared with calibrated values, the torque at constant rotational velocity is converted into a measure of the fluid viscosity. A Brookfield viscometer (Visco Basic Plus from Fungilab) was used in the first experiment. A thermostatic bath was added to the apparatus to provide an external heating source. In Figure 75, the schematic representation of the rotational viscometer test setup and the actual experimental apparatus are depicted. The silicon oil thermostatic bath was kept at the prescribed isothermal temperatures using a precision heating plate. The epoxy system components to be mixed were separately pre-heated to the test temperature. Upon completion of the mixture of the epoxy system components initial time of the experiment was set and the resin sample put back in the bath. For each test, the proper spindle was selected by the applicable expectable viscosity range to be measured. Both the thermostatic bath and resin sample temperatures were monitored during the measurement.

One condition for the viscometer to provide correct values was that minimum predefined distances between the rotating spindle and the lateral and bottom surfaces of the sample cup was respected (according to the manufacturer’s recommendations). Also, a minimum height of the spindle should be covered. Following those indications, the masses of the material samples tested with the viscometer were within the range 250 g to 300 g.

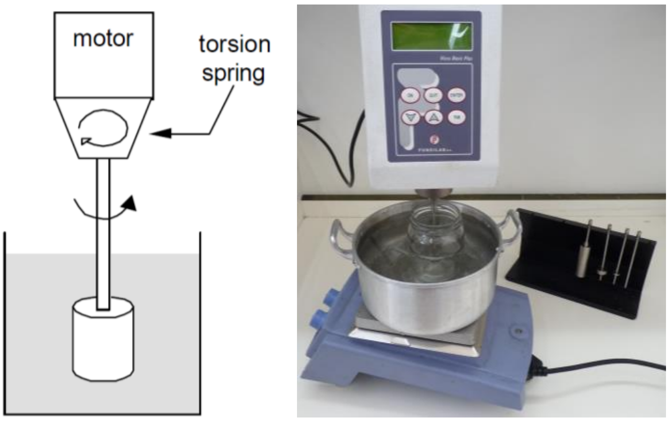

Figure 75 – Schematic representation of the rotational viscometer [245] (left) and overview of the experimental setup including the thermostatic device (right).

Rotational rheometers, on the other hand, are high-precision, continuously-varying-shear instruments in which the test sample is sheared between rotating cylinders, cones, or plates. They may operate under controlled stress or strain rate conditions. Similarly to the viscometer, the working principle of rheometer is to apply and measure the torque needed to produce a certain prescribed mechanical condition. In rheometers, however, the number of physical parameters that may be assessed is much greater due to the known constrained conditions in which the fluid is tested. In the case of a strain-controlled setup, a programmed strain rate is imposed and the stress response of the sample is measured. The known torque response of the rotating instrument gives the shear stress, while the rotational velocity and dimensions of the instrument geometry give the shear rate.

The second group of rheological characterization tests was carried out using a stress/strain control rheometer (Stresstech® from Reologica Instruments AB). In Figure 76 the schematic representation of the rotational viscometer test setup and the actual experimental apparatus are depicted. The test equipment included an oven and a heated bottom plate so that the isothermal temperatures were accurately imposed to the test samples. Since the objective was to measure the evolution of the viscosity up to a high degree of cure (past the gel point), disposable instruments were developed, adapted and calibrated into the equipment. The plate-plate geometry with 40 mm in diameter was selected due both to the easiness of manufacturing and the fact that a quasi-static shear mode was foreseen. Thus, the inexistence of a constant through-the-thickness velocity profile, as guaranteed by the cone-plate geometries, was negligible and reliable measurements were possible to achieve with this simpler geometry. A small amplitude oscillatory shear mode with strain control (2%) was programmed. Since the torque and phase angle responses of viscoelastic materials are known to depend on the applied oscillation frequency, multiple frequency experiments were conducted at 0.5 Hz, 1 Hz and 5 Hz in each sample. The applicability of these frequencies was previously determined through several frequency scans to dummy resin samples and corresponded to the plateau of the corresponding viscosity-frequency curves.

Each test sample was prepared through mixing the components (without pre-heating) and then placing it onto the bottom plate. As the top moving plate reached the set gap of 1 mm, the sample was constrained in the narrow gap between the two surfaces. The mass of sample required to properly fill the gap and barely oversize the plates diameter was previously calculated and was around 2 g. The initial time was set upon completion of the mixture.

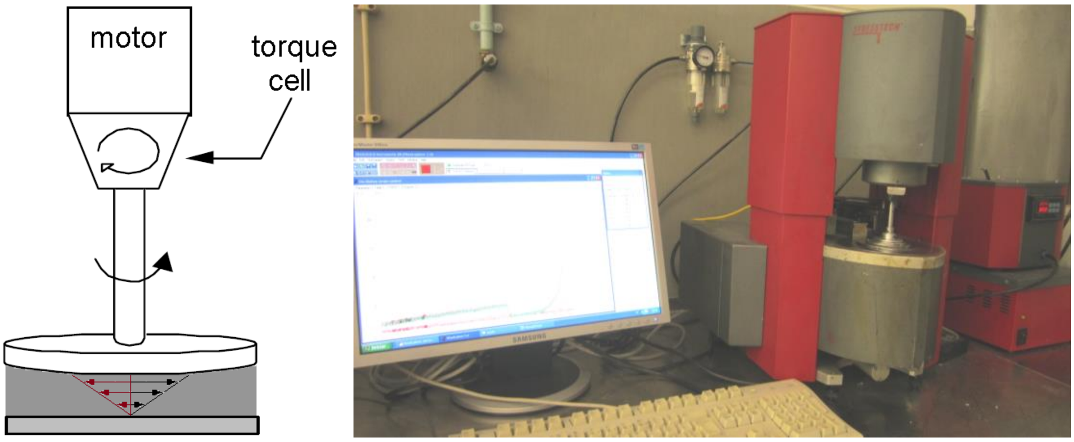

Figure 76 – Schematic representation of the rotational rheometer (left) and overview of the actual experimental setup (right).

In this experimental programme, the rheology of the two epoxy systems was assessed by means of two different experimental techniques: rotational viscosimetry and oscillatory rheometry. The information gathered in the two types of test was considerably different both in terms of quality (the precision of the viscometer was poor) and quantity. The rheometer apparatus allowed to retrieve the history of more physical parameters, thus allowing a more complete analysis. Namely, the shear stress, τ, the phase angle, δ, the storage (elastic) and the loss (viscous) moduli, G' and G'', were outputted from the rheometer integrated software. Nevertheless, the greater mass of the samples tested in the viscometer, provided interesting information on the influence of this important “real” condition which would not be reachable other way.

As proceeded in the kinetic characterization experiments, the MRCC were used for the two epoxy systems studied, since those are the applicable conditions for simulating the manufacturing conditions, particularly the ones used in the winding trials. The inclusion of initial temperature dwells correspondent to the ones verified during the manufacturing stage (near to room temperature) was also considered. The results of the experimental tests and the modelling of the rheology of the SR®1500 and Araldite® LY556 epoxies are presented in the following section.

4.2.2.2. Characterization/Modelling of Two Epoxy Systems

The two commercial epoxy resin systems selected for the experimental validation of the FW process model, SR®1500 from Sicomin Composites (France) and Araldite® LY556 from Huntsman (USA), were rheologically characterized through rotational viscosimetry and oscillatory rheometry. Four novel rheological models were developed that predict the dependence of the viscosity, μ, on the temperature, T, and degree of cure, α, of each epoxy system under two different conditions of free mass concentration. Both “real” working temperatures and mass concentration were considered in the experiments. The ability to simulate the resins behaviour in the “real” composite manufacturing conditions were evaluated and two models (one for each epoxy system) were used in the resin viscosity sub-model for the validation of the global process model. As in the kinetic studies, the MRCC were selected and applied to each test sample. The practical limitations in assessing the *in-situ* curing behaviour as well as results obtained by several authors for other comparable polymer-based composites justify the use of these experimental techniques to approach the resins behaviour within a composite laminate under manufacturing/consolidation.

The results of the conducted experiments together with the modelling approaches for each of the epoxy systems are presented and discussed hereafter.

SR® 1500

The epoxy/amine system SR®1500/SD®2505 with the weight ratio of 100:33% was tested under the MRCC, which are presented in Table 18.

Three isothermal cycles, at 30ºC (303 K), 40ºC (313 K) and 50ºC (323 K) were selected for the study of this epoxy system. Two material samples were tested at each temperature in both the viscometer and rheometer. In Brookfield-type viscometers the calibrated spindles are not disposable (consumables) and therefore measurements are typically stopped way before the gelation to avoid damages. In these experiments, the equipment’s ability was taken to the limit by extending the measurements up to the moment when resin started to gel. The spindle was then taken out from the resin sample and a fast cleaning/recovery procedure was followed each time. Thus, the duration of each test depended solely on the resin behaviour, provided that gelation always occurred prior to 14 hours, which was the maximum duration of the isothermal cycles selected and implemented in the kinetic studies previously conducted. In the rheometer, since disposable plate-plate instruments were developed and implemented, no special care was needed and extended measurements were possible.

The mass, pre-conditioning and test temperature of the tested samples for the two types of rheological characterization experiments are presented in Table 19.

Table 18 – MRCC for SR$^{®}$1500/SD$^{®}$2505 and selected curing cycles for the viscosimetry and rheometry tests.

Pre-cure	2 to 4 hours @ 20ºC
Minimum post-cure cycle	2 to 7 days @ 20ºC
Advised post-cure cycle	2 to 7 days @ 20ºC OR 12 hours @ 40ºC OR 6 hours @ 60ºC
Cycle selected for viscosimetry tests	up to gelation @ 30ºC; up to gelation @ 40ºC; up to gelation @ 50ºC
Cycle selected for rheometry tests	up to 100 Pa.s @ 30ºC; up to 100 Pa.s @ 40ºC; up to 100 Pa.s @ 50ºC

Table 19 – Mass and test condition of the samples of SR$^{®}$1500/SD$^{®}$2505 tested in viscosimetry and rheometry.

Type of Test	Sample ID	Mass [g]	Pre-conditioning	Test Temperature [ºC (K)]
Viscosimetry	SRHF101	282.3	pre-heated to test temperature	30 (303)
	SRHF102	282.3	pre-heated to test temperature	40 (313)
	SRHF103	282.4	pre-heated to test temperature	50 (323)
	SRHF104	283.8	pre-heated to test temperature	50 (323)
	SRHF105	282.5	pre-heated to test temperature	40 (313)
	SRHF106	282.1	pre-heated to test temperature	30 (303)
Rheometry	SRHF801	~2	Dry, Dark, 22ºC	30 (303)
	SRHF802	~2	Dry, Dark, 22ºC	40 (313)
	SRHF803	~2	Dry, Dark, 23ºC	50 (323)
	SRHF804	~2	Dry, Dark, 23ºC	30 (303)
	SRHF805	~2	Dry, Dark, 22ºC	40 (313)
	SRHF806	~2	Dry, Dark, 25ºC	50 (323)

The viscosity results directly outputted from both viscosimetry and rheology are graphically represented in the following figures for the three isothermal temperature conditions. The viscosimetry results are presented in Figures 77-80 and the rheometry results in Figure 81. The plots of the viscosimetry results are additionally presented separately for each isothermal condition in order to allow to percept the change in temperature that the resin samples experimented. As referred previously, the initial time, $t = 0$, corresponded to the completion of the mixture of the two constituents of this epoxy system. From these plots it became clear that the amount of resin concentrated in each sample played an important role in its macroscopic rheology.

An immediate comparison of the results obtained with the two different techniques highlighted that the values found for the initial viscosity, μ_0, were coherent with the manufacturer’s data, thus validating the measurement procedures.

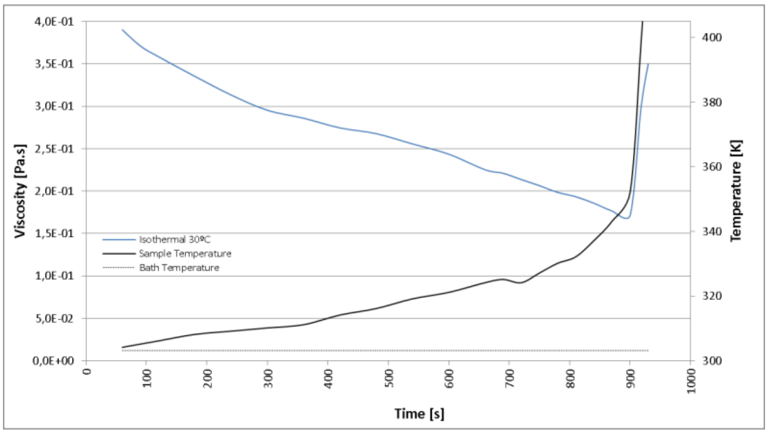

Figure 77 – Evolution of the viscosity and temperature in the sample SRHF106 during the viscosimetry test conducted at 30ºC (303 K).

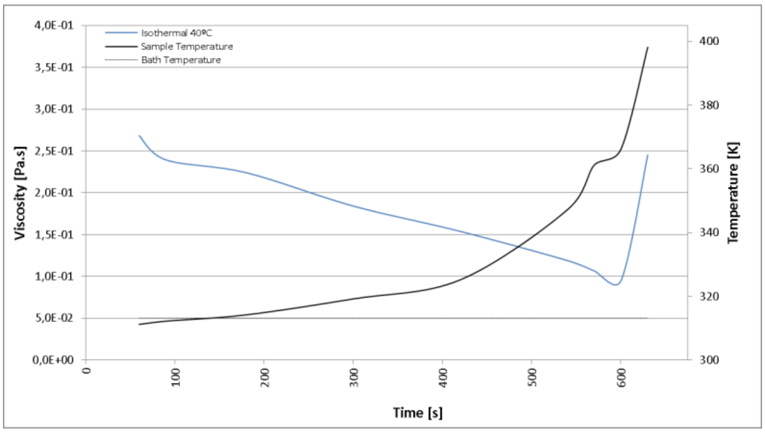

Figure 78 – Evolution of the viscosity and temperature in the sample SRHF102 during the viscosimetry test conducted at 40ºC (313 K).

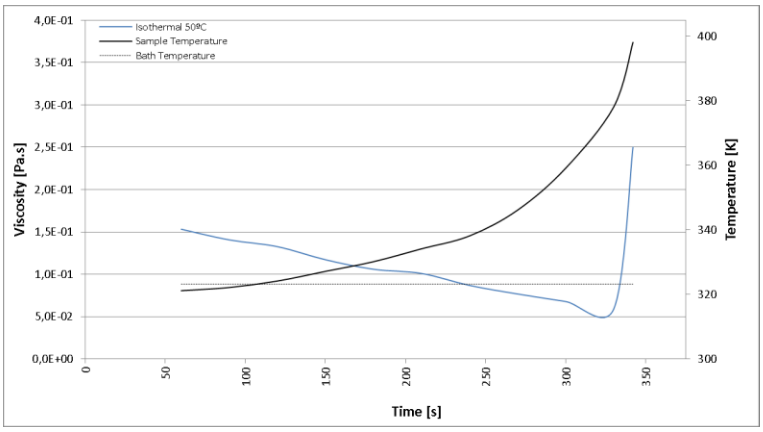

Figure 79 – Evolution of the viscosity and temperature in the sample SRHF104 during the viscosimetry test conducted at 50ºC (323 K).

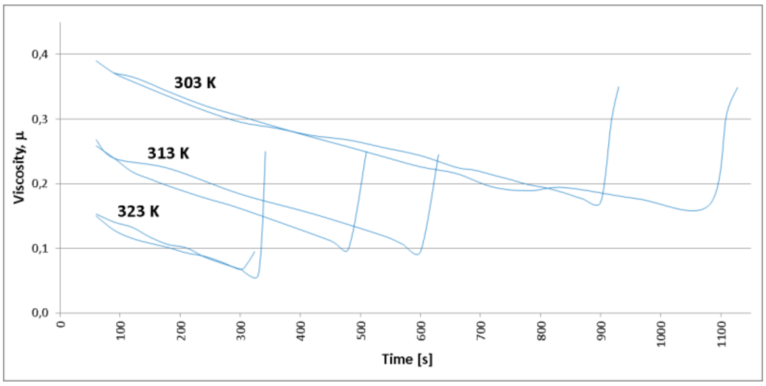

Figure 80 – Evolution of the viscosity in the samples SRHF101-106 during the viscosimetry tests conducted at 30ºC (303 K), 40ºC (313 K) and 50ºC (323 K).

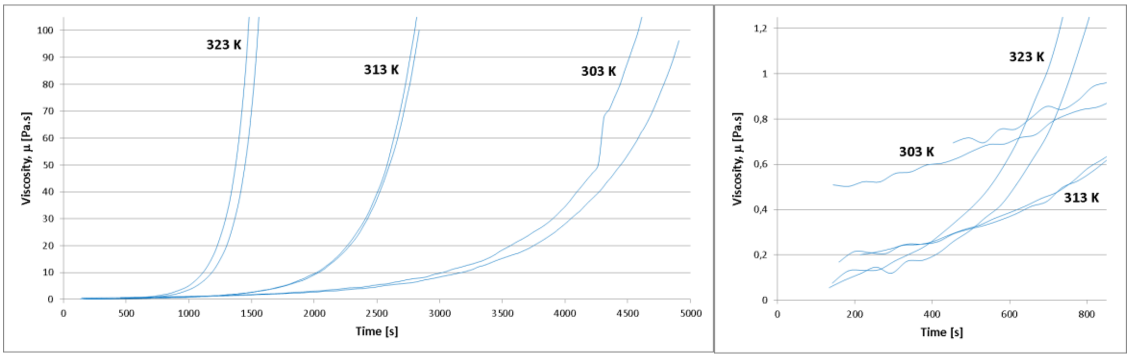

Figure 81 – Evolution of the viscosity in the samples SRHF801-806 during the rheometry tests conducted at 30ºC (303 K), 40ºC (313 K) and 50ºC (323 K). Complete view (left) and partial (zoomed) view of the initial stage (right).

In Figure 82 the initial viscosities measured at the beginning of each test are presented for all the tested samples. The resin manufacturer's data provided for the temperatures of 20ºC and 25ºC were extrapolated for the relevant test temperatures through an exponential forecast. The validity of such extrapolation was based on the widely accepted assumption that the viscosity has an Arrhenius-type dependence on the temperature. This type of dependence is widely accepted in the models reviewed in chapter 2. The values for the initial viscosity, μ_0, are compiled in Table 20.

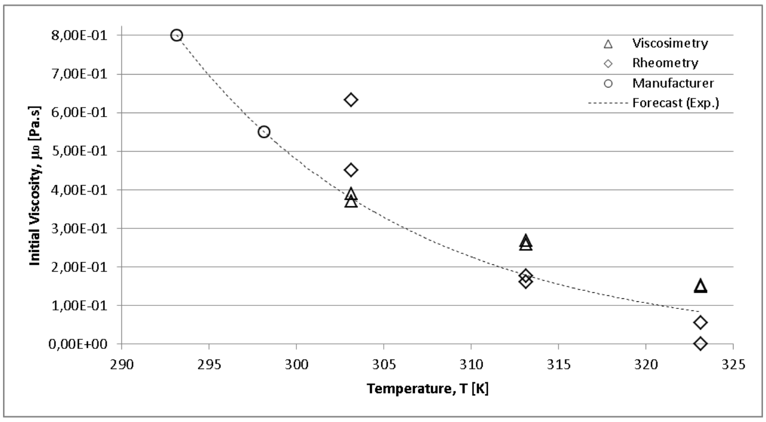

Figure 82 – Initial viscosities of the SR$^{®}$1500/SD$^{®}$2505 epoxy system measured with viscosimetry and rheometry at 30ºC (303 K), 40ºC (313 K) and 50ºC (323 K).

Table 20 – Initial viscosities of the SR®1500/SD®2505 epoxy system measured with viscosimetry and rheometry at 30ºC (303 K), 40ºC (313 K) and 50ºC (323 K).

Test Temperature [ºC (K)]	Manufacturer	Viscosimetry		Rheology	
	μ_0 [Pa.s]	μ_0 [Pa.s]	standard deviation [Pa.s]	μ_0 [Pa.s]	standard deviation [Pa.s]
20 (293)	0.800	n/a	n/a	n/a	n/a
25 (298)	0.550	n/a	n/a	n/a	n/a
30 (303)	(0.400)	0.381	0.014	0.543	0.129
40 (313)	(0.189)	0.263	0.007	0.169	0.011
50 (323)	(0.089)	0.152	0.002	0.028	0.039

The second aspect highlighted from the comparison of the two groups of results was that in the viscosity tests a consistent decrease in viscosity was observed in the early stages of the tests up to the moment where a fast gelation occurred. The rheometry tests, oppositely, outputted a monotonically increasing viscosity in all stages of the cure. The two measurement techniques were considered valid in the applicable ranges of viscosity and temperature. However, due to the different disposition of the resin samples and interaction with the measuring instruments, the two techniques actually assess the viscosity in different conditions. In the viscometer, the material sample is unconstrained, nearly steady and contains a large quantity of mass freely concentrated in a pot. Under such conditions, when the first crosslinking reactions begin, the neighbourhood receives the heat released by those exothermic reactions and is thus thermally accelerated. Due to the mobility of the reacting species, the heat cascade effect expands throughout the entire resin sample. This is the cause of the increase of temperature in the sample, as reported in Figures 77-79. Moreover, the excessive heat produced within the sample tends to be released through the upper free surface, generating a vertical thermal gradient which justifies the faster gelation from the top to the bottom of the sample. In the rheometer the sample is considerably smaller, with much less mass available and is constrained between two barely moving surfaces. Since the external heating sources coincide with those very close surfaces, no thermal gradients neither internal unreleased heat is observed in the sample. A truly isothermal condition is then obtained during the test.

In order to proceed with the development of a rheological model representative of the actual behaviour of the epoxy resin at the layer/laminate level, either one or a combination of the two test conditions should be considered. The “real” conditions of the resin within the composite laminate during the FW process are more approximated to the test conditions of the rheometer. This assumption was established because the thickness of the layers composing the laminate is very small and thus the amount of resin concentrated in each resin “pocket” among the fibres is also minimal. The fibres network through which the resin flows during the consolidation process helps heat dissipation and the room temperature isothermal condition reasonably applies to the resin. The rheometer experimental data was chosen as the best approximation to the manufacturing conditions. Nevertheless, the test conditions carried out in the viscosimeter setup are an approximation to the typical condition imposed to the resin in the impregnating bath (wet winding). Therefore, this large concentrated mass condition was further studied as well.

From the viscosimetry tests, two additional sets of data were analysed. Namely, the change in viscosity, $\Delta\mu$, and temperature, ΔT, of the samples from the test start up to the moment of the fast gelation initiation were critically investigated. In the following figures the values of these parameters are plotted. The variations of the initial, and gel start up viscosities, μ_0 and μ_{gel}, present a coherent linear dependency with the test temperature in the applicable range (Figure 83). This, a part from highlighting the consistency of the measurements, does not point towards a relevant assessment or conclusion. On the other hand, the difference between the temperatures observed at the test start and at the initiation of gelation, T_0 and T_{gel}, showed to be independent from the test temperature. Moreover, dividing the temperature difference, $T_{gel} - T_0$, by the mass of the samples, m, the same constancy was observed (Figure 84).

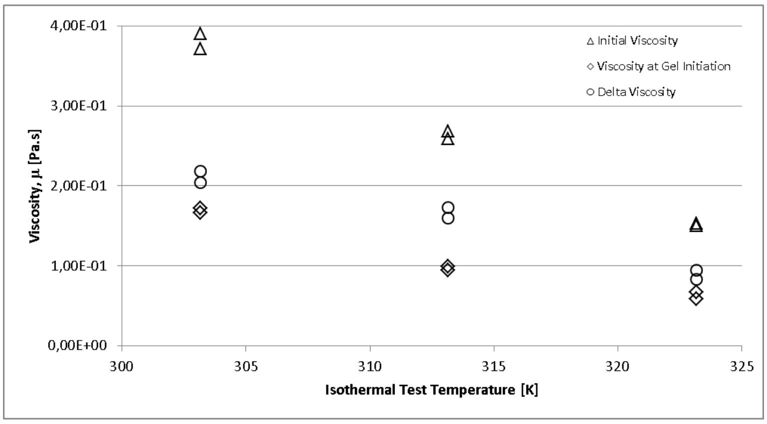

Figure 83 – Viscosities at test start and at initiation of gelation for the SR®1500/SD®2505 samples measured with viscosimetry.

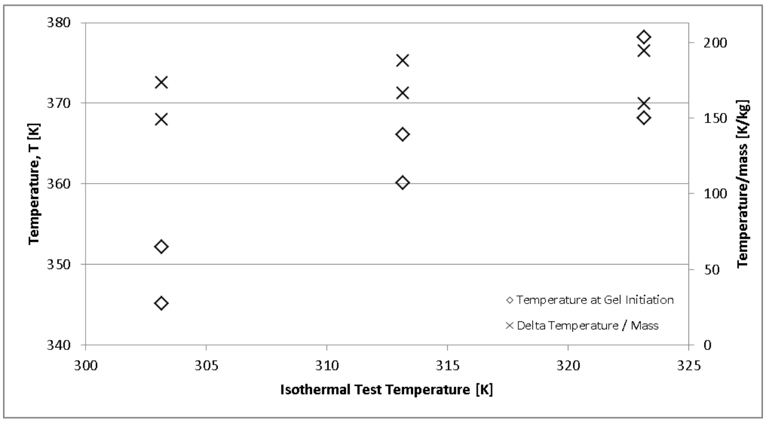

Figure 84 – Analysis of the temperature increase up to the initiation of gelation for the SR®1500/SD®2505 samples tested with viscosimetry.

Further analysis revealed that, assuming that the specific heat of the resin, C_p^m, remains constant in the temperature range under study, the specific thermal energy, E_T, generated in the resin samples from the beginning of the tests up to the gelation onset, was constant (independent from the test temperature). In the temperature range under study (room temperature up to 323 K) a value of 1200 $J\,kg^{-1}K^{-1}$ for the specific heat was considered. Devising from the energy conservation principle and heat transfer equations [246] the specific internal energy, E_T/m, associated with the heat generation within the samples as:

$$\frac{E_T}{m} = C_p^m\left(T_{gel} - T_0\right) , \tag{4.17}$$

the average value of $5.8200 \times 10^4 \ J\,kg^{-1}$ was found. The identification of a characteristic energy needed to initiate the gelation allows to estimate the change in temperatures that the resin shall experience whenever large concentrated masses and steady states are applied. This is the case of the resin impregnation bath, where resin pots of this order of mass are used upstream the winding process. More importantly, this value agrees with the value of the activation energy, $E_{a1} = 6.0067 \times 10^4 \ J\,kg^{-1}$, found in the kinetic studies, thus enhancing the validity of these analyses. However, the advantages of this knowledge are limited to this and therefore nearly irrelevant in the scope of rheological modelling. An useful relationship between the characteristic specific thermal energy, E_T/m, and the heat of reaction, H_{ISO}, previously determined in the DSC-based kinetic studies for the same isothermal conditions is far from evident.

In Figure 85, the viscosimetry experimental data is plotted for all the tests conducted with SR®1500/SD®2505 resin in terms of the viscosity, μ, *versus* degree of cure, α. The degree of cure was obtained from its correspondence with the curing time, t, through directly comparing this parameter in both the viscosimetry and kinetic experimental data for the same resin and temperature conditions. It is observable that the cure progress (conversion) achieved in each test is very low. In fact, the time range of the viscosimetry tests (up to the onset of gelation) is short and its comparison with the DSC results is barely reasonable. Again, this is due to the unbalanced internal heat generated in the viscosimetry samples, that accelerated the curing process and did not allow a truly isothermal test condition.

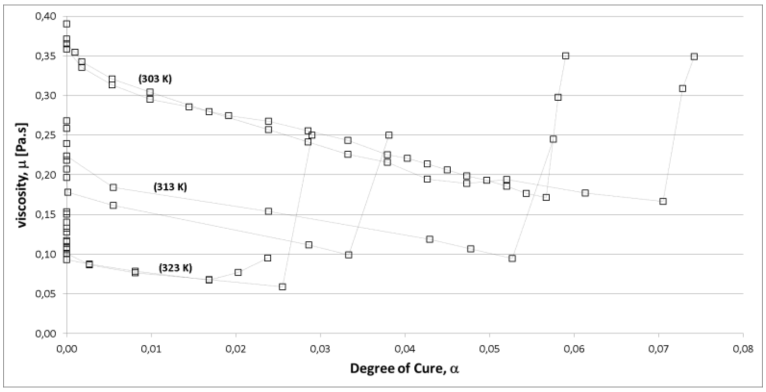

Figure 85 – Plot of the viscosity *versus* degree of cure for all the SR®1500/SD®2505 samples tested in viscosimetry.

As discussed in chapter 2, in macroscopic rheology of thermosetting resins, the viscosity, μ, is typically modelled as a function of the temperature, T, and the degree of cure, α, and several authors successfully developed models for epoxy resins [82,91,100].

In the viscosimetry experimental data, the initial decrease of viscosity opposes the typical monotonically increasing nature of exponential curves. The main phenomenological models presented and validated by other authors for thermosetting resins are set upon exponential relationships. However, given that such models have a moderate dependence on the temperature and that such dependence is the “real” cause of the initial decrease in viscosity, these models were used and applied to the experimental data. The challenge consisted, then, in selecting or establishing an adequate model in the form of equation (4.16) that would properly fit the experimental curves in the relevant domains of temperature and degree of cure. It should also represent the main physical phenomena occurred during the curing reaction, i.e., be meaningful on the parameters used.

Firstly, the three models proposed by Lee *et al.* [82], Ng *et al.* [91] and Macosko [100] were studied and fitted to the viscosimetry experimental data. These models are described in equations (2.58), (2.59) and (2.60), respectively. The three models have a similar dependence on temperature but slight different relations with the degree of cure. In Figure 86 the fitting of these models to the experimental data is presented. Although the post-gel stage could be reasonably adjusted with these models, they showed no ability to estimate the viscosity decrease as the temperature increased prior to the initiation of gelation.

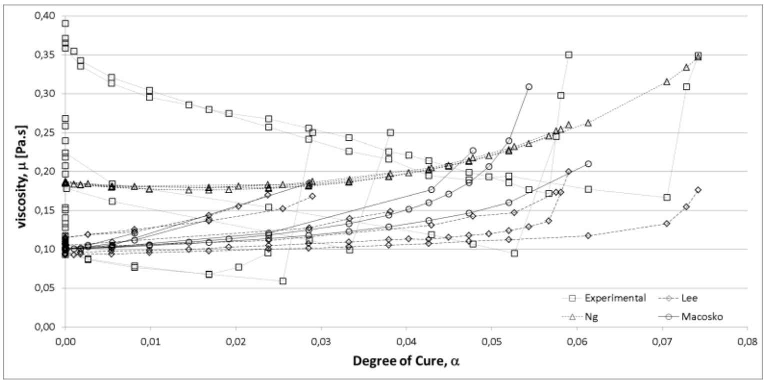

Figure 86 – Fitting of the Lee, Ng and Macosko models to the experimental viscosimetry data of SR®1500/SD®2505.

A different modelling approach was then addressed in view of enforcing the temperature dependence of the model. Based on the so-called William, Landel and Ferry equation [247] and other previous works [248,249], Kenny and Opalicki [250] proposed a model for the viscosity of a commercial epoxy in the form:

$$\mu = \mu_g e^{\frac{k_1 (T - T_g)}{k_2 + T - T_g} \left(\frac{\alpha_{gel}}{\alpha_{gel} - \alpha} \right)^n} , \tag{4.18}$$

where μ_g is the pre-exponential constant representing the viscosity of the unreacted resin at the glass transition temperature, T_g , α_{gel} is the degree of cure at the gel point and k_1 , k_2 and n are constants. This model was successfully applied to fit experimental data with similar profile to the one studied herewith, i.e., an initial stage with increase in the temperature and corresponding decrease in viscosity [242]. Following the same non-linear least squares fitting method, the model was fitted to the experimental data. The results were not satisfactory, although a negative slope for the viscosity in the initial stage of the tests was observed in the model. Unrestricted ranges for every parameters of the equation did not allow acceptable improvement. Moreover, the model is undetermined when $\alpha = \alpha_{gel}$, thus reducing its applicability domain. Nevertheless, under certain combinations of parameters, this model allowed to estimate different initial viscosities, μ_0, for different initial test temperatures, T_0, which was not possible with any of the previously fitted models. Therefore, adaptations were made and a dedicated model was developed for the case under study. A piecewise relation was considered in order to keep validity of the model for the entire domain of degree of cure. The new model was established as [251]:

$$\begin{cases} \mu = \mu_\infty e^{\frac{k_1 T - T_{gel}}{k_2 + T - T_{gel}}\left(\frac{\alpha_{gel}}{\alpha_{gel} - \alpha}\right)^n} & \alpha < \alpha_{gel} \ , \\ \mu = \mu_{gel} + \left(\alpha - \alpha_{gel}\right)^m & \alpha \geq \alpha_{gel} \end{cases} \tag{4.19}$$

where μ_∞ is the pre-exponential constant, μ_{gel} and T_{gel} are, respectively, the viscosity and the temperature at the initiation of gelation, α_{gel} is the degree of cure at the gel point and k_1, k_2, n and m are constants.

The fitting results for both the Kenny and Opalicki model and the new model (named hereafter K&O Adapted) are plotted in Figure 87. The ability of the new model to capture the different initial viscosities and their decreasing slope up to the gelation is clear. The fast increase of viscosity after initiation of gelation was also accomplished. In Table 21, the values of the parameters leading to the best model fits are listed. The parameters μ_{gel}, T_{gel} and α_{gel} were set through their linear relationships with the test temperatures, T_0, effectively observed in the experimental data.

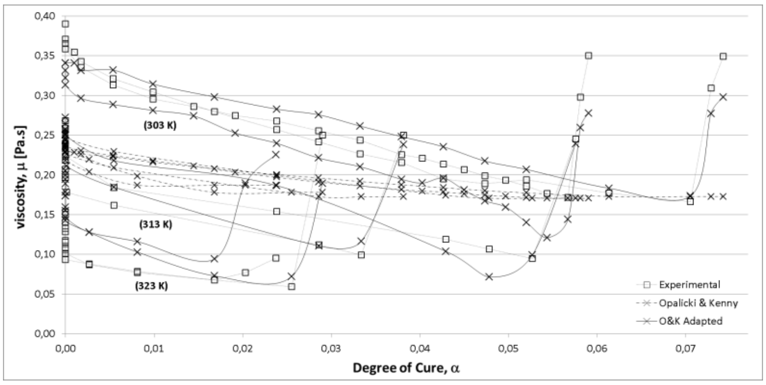

Figure 87 – Fitting of Kenny and Opalicki and the K&O Adapted models to the experimental viscosimetry data of SR®1500/SD®2505 samples tested at 30ºC (303K), 40ºC (313K) and 50ºC (323K).

Table 21 – Parameters determined for the fitting of the viscosimetry experimental curves of SR®1500/SD®2505 with the K&O Adapted rheological model.

Model Parameters	K&O Adapted $\begin{cases} \mu = \mu_\infty e^{\frac{k_1T-T_{gel}}{k_2+T-T_{gel}}\left(\frac{\alpha_{gel}}{\alpha_{gel}-\alpha}\right)^n} & \alpha < \alpha_{gel} \\ \mu = \mu_{gel} + (\alpha - \alpha_{gel})^m & \alpha \geq \alpha_{gel} \end{cases}$
μ_∞ [Pa.s]	1.7159×10^3
μ_{gel} [Pa.s]	$-0.0053T_0 + 1.7655$
k_1	-2.8662×10^{13}
k_2	1.0193×10^{15}
T_{gel} [K]	$1.225T_0 - 21.959$
n	-2.9100×10^{-3}
m	3.6603×10^{-1}
α_{gel}	$-0.0021T_0 + 0.7073$

As mentioned above, the rheometry tests conditions simulate better the “real” resin condition during the manufacturing process, mostly due to the quantity of mass involved. These results were analysed in a similar way as the one from viscosimetry. The viscosity-time curves outputted from the rheometer apparatus (Figure 81) were transformed into viscosity-degree of cure curves, through the degree of cure-time relations obtained in the DSC experiments (Figure 49). These are plotted in Figure 88.

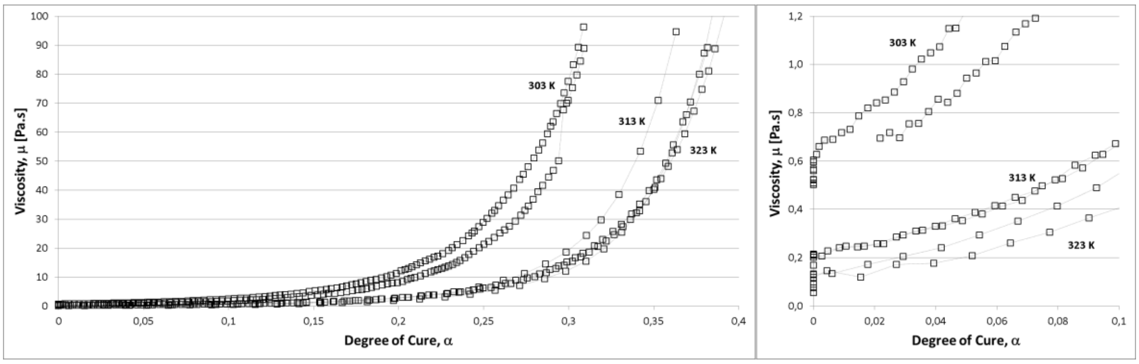

Figure 88 – Plot of the viscosity *versus* degree of cure for all the SR®1500/SD®2505 samples tested in rheometry. Complete (left) and partial (right) plots.

Both the monotonic increasing nature of the data and the wider range of conversion (degree of cure) turn these rheometry results more acceptable (comparing to the viscosimetry ones) in the scope of the process modelling. The curves were then fitted by the models proposed by Lee *et al.* [82] and Ng *et al.* [91]. The model introduced by Macosko [100] was not fitted due to its indeterminate nature at $\alpha = \alpha_{gel}$. In Figure 89 the complete view of these fittings is shown, while in Figure 90 a zoomed view of the initial ranges is shown allowing a better observation. The Lee model adjusted better to the experimental data. Compared with the Ng model, it agreed with the experimental data up to higher values of degree of cure as well as it predicted better the different initial viscosities observed for the three isothermal test temperatures.

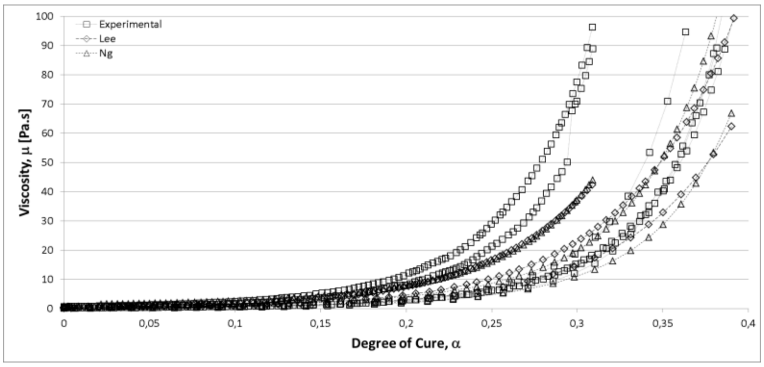

Figure 89 – Fitting of the Lee and Ng models to the experimental rheometry data of SR®1500/SD®2505.

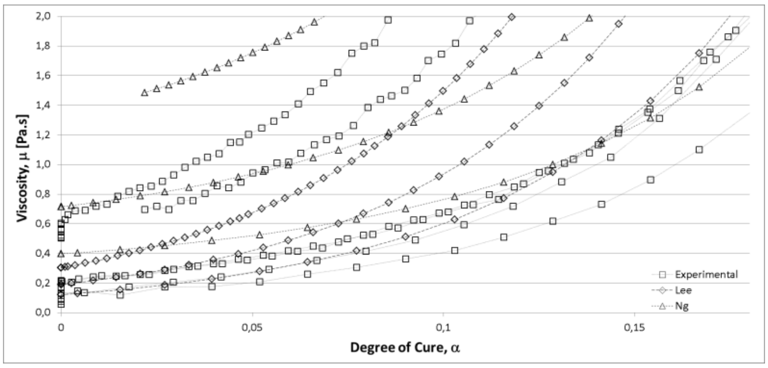

Figure 90 – Partial (zoomed) view of the Lee and Ng models fitting to the experimental rheometry data of SR®1500/SD®2505.

The main drawbacks of the model predictive ability were identified as its apparent divergence with the experimental data upon a certain degree of cure and the low dependence on temperature. The shift of the curves correspondent to different test temperatures was wider in the experimental data than in the Lee model. In order to improve the modelling results, two oriented features were developed and appended to the Lee model. Firstly, an exponent, a, was associated with the variable temperature, T, attributing greater dependence of the model on the latter. Secondly, a dependence on the gel point was introduced through the term $\alpha - b\alpha_{gel}$ so that the divergence previously observed was minimized. The new model was established as:

$$\mu = \mu_\infty e^{\frac{U}{RT^a}+k_1\left(\alpha - b\alpha_{gel}\right)}, \qquad (4.20)$$

where μ_∞ is the pre-exponential constant, U is a constant associated with the intrinsic activation energy, R is the universal gas constant, T is the temperature, α_{gel} is the degree of cure at the gel point and k_1, a and b are constants.

A proper identification of the gel point in the experimental rheometry data was needed to feed the model. In the past, a few criteria were defined to determine the gel point from physical parameters which are directly or indirectly measured during the rheometry tests. One criterion is that the gel point corresponds to the point when the two linear zones of the loss (viscous) modulus, G'', intersect (if plotted in a log scale). Another criterion is to identify the point in which the tangent of the phase angle, $\tan\delta$, is independent of the test frequency [252]. The latter criterion is only applicable when multiple frequencies are tested, as was the case of the experiments carried out. The experimental data was preliminarily analysed in light of the two criteria. The following figures show the evolution of G'' and $\tan\delta$ during the rheometry test for the three frequencies used in one of the resin samples. It is immediate to observe that both G'' and $\tan\delta$ data present great scatter up to a certain time in the experiment. After that point both parameters evolve linearly (in log scale) up to the end of the test. Despite the linearity tendency of the first stage of the loss modulus could be reasonably perceived the identification of its intersection with the second stage segment was difficult for most of the tests data. On the other hand, the identification of the point where the $\tan\delta$ curves take the same value for the three test frequencies was more evenly accessible for all tests. Thus, the second criterion to assess the gel point was used in detriment of the first criterion.

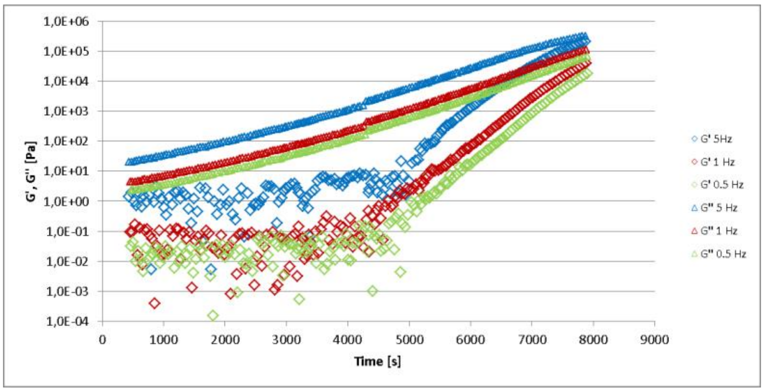

Figure 91 – Evolution of the storage (elastic) and loss (viscous) moduli during the rheometry test of resin sample SRHF801 conducted at 30ºC (303K).

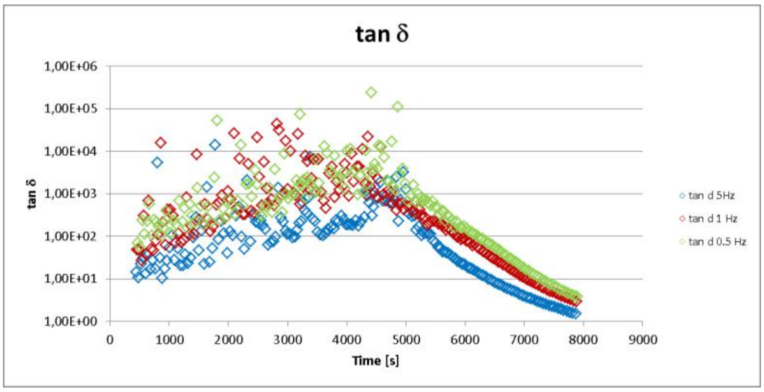

Figure 92 – Evolution of the tangent of the phase angle during the rheometry test of resin sample SRHF801 conducted at 30ºC (303K).

Upon analysis of the data in all the test samples a new criterion was developed to identify the gel point. In fact, as is clearly observed in the previous figures, the point of inflection of the $\tan\delta$ curve is coherently related with the change of slope on the G'' curves. This relation was observed for all the test samples. Moreover, such information can be assessed in single frequency rheometry tests, reducing the complexity of the experimental procedures needed. The new criterion (hereafter called $\tan\delta$ inflection) established that the gel point corresponds to the point where the tangent of the phase angle, $\tan\delta$, inflects, thus changing its tendency slope. The results obtained with the two criteria based on the $\tan\delta$ data are plotted in Figure 93 and the average values for each isothermal temperature condition listed in Table 22. The manufacturer's data is also considered for comparative analysis.

Due to the lower standard deviations of the data set from criterion 1 ($\tan\delta$ frequency independent), the better correspondence with the DSC experimental data and the technical data provided by the manufacturer, criterion 1 was chosen. Its α_{gel} values were used in the rheological model fitting. Nevertheless, the new proposed criterion outputted interesting results which allow foreseeing its applicability, mostly in experiments conducted at a single frequency.

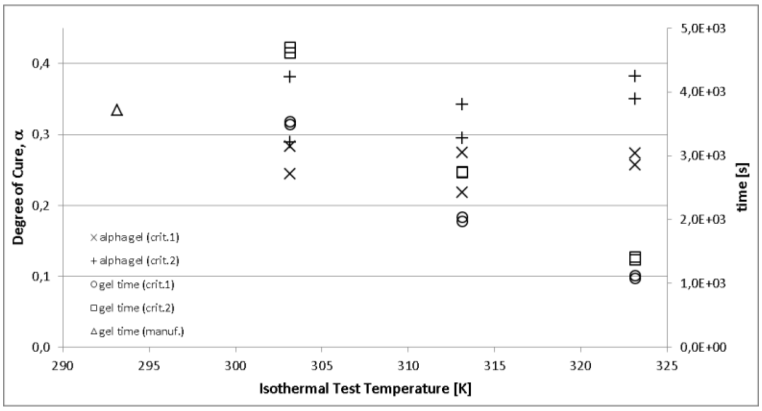

Figure 93 – Gel time and α_{gel} calculated with $\tan\delta$ frequency independent (crit.1) and $\tan\delta$ inflection (crit.2) criteria from the SR®1500/SD®2505 rheometry tests conducted at 30ºC (303 K), 40ºC (313 K) and 50ºC (323 K).

Table 22 – Gel times and α_{gel} of the SR®1500/SD®2505 at 30ºC (303 K), 40ºC (313 K) and 50ºC (323 K) calculated from rheometry tests data using different criteria.

Test Temperature [ºC (K)]	Criterion								
	manuf. data	$\tan\delta$ freq independent (criterion 1)				$\tan\delta$ inflection (criterion 2)			
	t_{gel} [s]	α_{gel}	standard deviation [s]	t_{gel} [s]	standard deviation [s]	α_{gel}	standard deviation [s]	t_{gel} [s]	standard deviation [s]
20 (293)	3722	n/a	n/a	n/a	n/a	n/a	n/a	n/a	n/a
30 (303)	n/a	0.26	0.028	3511	27.860	0.33	0.065	4655	59.185
40 (313)	n/a	0.25	0.039	2009	46.528	0.32	0.033	2744	12.445
50 (323)	n/a	0.27	0.012	1100	36.345	0.37	0.023	1388	28.143

The fitting results for both the Lee and the new model (named hereafter Lee extended) are plotted in Figure 94. In Figure 95 a zoomed view of the initial ranges is shown allowing a better observation. The Lee extended model improved considerably the prediction of the resin viscosity throughout the cure. The improvement is mostly clear for degrees of cure above $\alpha = 0.08$. Exception is noted for the case of isothermal temperature of 50ºC (323 K) in which the model behaviour quite diverge from the experimental curves. The estimation of initial viscosities is qualitatively similar to the Lee model, presenting a good agreement for the case of 40ºC (313 K) and poorer agreement for 30ºC (303 K) and 50º (323 K). However, they rapidly converge with the experimental data as the cure early progresses.

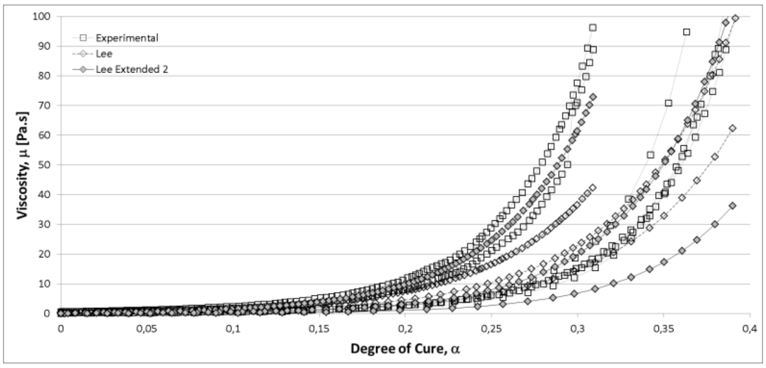

Figure 94 – Fitting of Lee and Lee Extended models to the experimental rheometry data of SR®1500/SD®2505 samples tested at 30ºC (303K), 40ºC (313K) and 50ºC (323K).

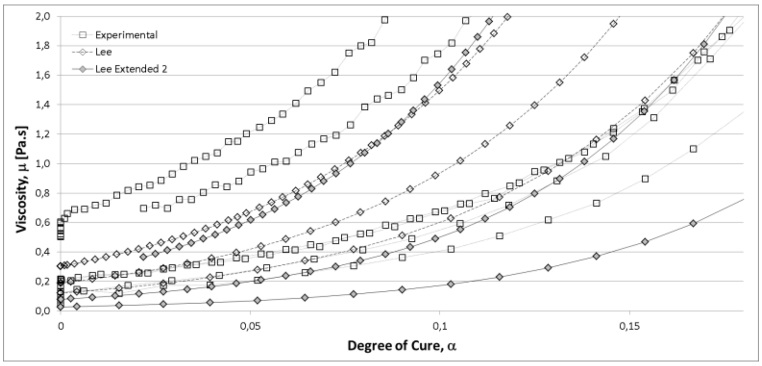

Figure 95 – Partial (zoomed) view of the Lee and Lee Extended models fitting to the experimental rheometry data of SR®1500/SD®2505 samples tested at 30ºC (303K), 40ºC (313K) and 50ºC (323K).

Table 23 – Parameters determined for the best fitting of the rheometry experimental curves of SR®1500/SD®2505 with the Ng, Lee and Lee Extended models.

Model Parameters	Rheological Model		
	Lee Extended $\mu = \mu_\infty e^{\frac{U}{RT^a}+k_1(\alpha - b\alpha_{gel})}$	Lee $\mu = \mu_\infty e^{\frac{U}{RT}+k_1\alpha}$	Ng $\mu = \mu_\infty e^{\frac{U}{RT}+k_1\alpha^2+k_2\alpha}$
μ_∞ [Pa.s]	1.3837×10^{-2}	1.1426×10^{-7}	3.9193×10^{-9}
U [J mol^{-1}]	5.0282×10^{4}	3.7276×10^{4}	4.9527×10^{4}
k_1	1.8439×10^{1}	1.6005×10^{1}	2.2795×10^{1}
k_2	n/a	n/a	4.2537
α_{gel}	0.2500	n/a	n/a
a	0.8959	n/a	n/a
b	7.0164	n/a	n/a

Summarily, the new model was able to better predict the rheological behaviour of the SR®1500/SD®2505 epoxy resin under near-to-room temperature isothermal conditions. These test conditions correspond both to the "real" manufacturing conditions and the MRCC. This model is valid for temperatures up to 40ºC and was, therefore, used as a main input to the global process model, incorporating the resin viscosity sub-model.

Araldite® LY556

The rheological study of the LY556/HY917/DY070 epoxy system followed the same procedures and analysis that the SR®1500/SD®2505. Resin samples with weight ratio of 100:90:2% (LY556:HY917:DY070) were tested under MRCC with both viscosimetry and rheometry. The MRCC selected are presented in Table 24.

Table 24 – MRCC for the LY556/HY917/DY070 epoxy system and selected curing cycles for the viscosimetry and rheometry tests.

Recommended gelation cycle	2 to 4 hours @ 80ºC OR 1 to 3 hours @ 90ºC
Recommended post-cure cycle	4 to 8 hours @ 120ºC OR 2 to 8 hours @ 140ºC OR 2 to 8 hours @ 160ºC
Cycle selected for viscosimetry tests	2 hours @ 30ºC + up to gelation @ 80ºC
Cycle selected for rheometry tests	2 hours @ 30ºC + up to 100 Pa.s @ 80ºC

The MRCC for this resin consist in two consecutive isothermal dwells, one for gelation set at 80ºC (353 K) and the other for the post-cure set at either 120ºC (393 K), 140ºC (413 K) or 160ºC (433 K). Similarly to the kinetic study of this resin, a previous near-to-room temperature isothermal dwell was added in order to simulate the "real" manufacturing stage to which the resin is subjected before the gel and post-cure cycles. Since the stop criteria in the viscosimetry and rheometry tests were established as at verification of gelation and 100 Pa.s, respectively, the actual cycle implemented in these tests consisted in a first dwell at 30ºC (303 K) and a second dwell at 80ºC (353 K). The two stop criteria were expectedly reached during the 80ºC isothermal dwell. Two material samples were tested under this cycle in both the viscometer and rheometer. The mass, pre-conditioning and test temperature of the tested samples for the two types of rheological characterization experiments is presented in Table 25.

The viscosity results directly outputted from both viscosimetry and rheology are graphically represented in the Figures 96-98 and Figures 99-101, respectively. Individual plots of each test are shown separately in order to allow to percept the correspondence of the viscosity with the change in temperature that the resin samples experienced. As referred previously, the initial time, $t = 0$, corresponded to the completion of the mixture of the three constituents of this epoxy system. From these plots no clear difference was observed between the behaviour of the resin under the two types of tests. Namely, in both viscosimetry and rheometry, the samples presented a nearly constant viscosity in the 1st dwell, a fast decrease at the transition and a fast gelation during the early stages of the 2nd dwell (80ºC).

Table 25 – Mass and pre-conditioning conditions of the samples of LY556/HY917/DY070 tested in viscosimetry and rheometry.

Type of Test	Sample ID	Mass [g]	Pre-conditioning
Viscosimetry	LYHF201	281.3	pre-heated to test temperature
	LYHF202	281.5	pre-heated to test temperature
Rheometry	SRHF901	~2	Dry, Dark, 24ºC
	SRHF902	~2	Dry, Dark, 24ºC

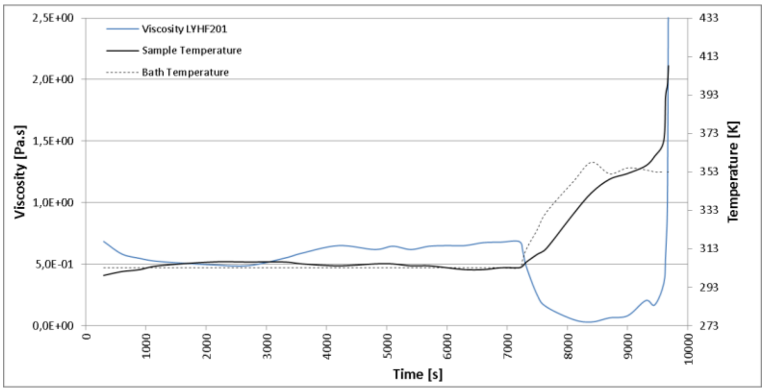

Figure 96 – Evolution of the viscosity and temperature in the sample LYHF201 during the viscosimetry test conducted at 30ºC/80ºC (303 K/353 K).

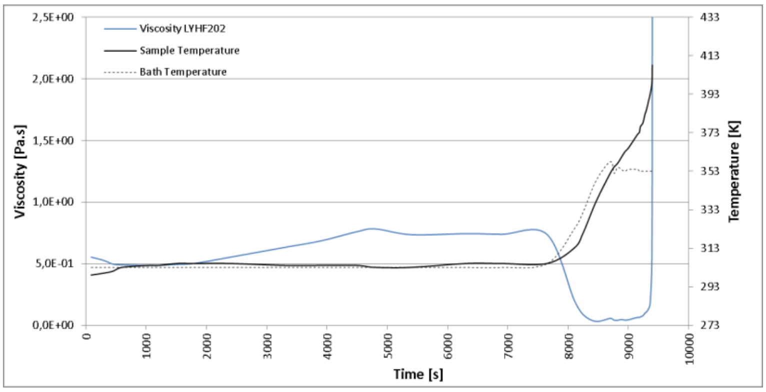

Figure 97 – Evolution of the viscosity and temperature in the sample LYHF202 during the viscosimetry test conducted at 30ºC/80ºC (303 K/353 K).

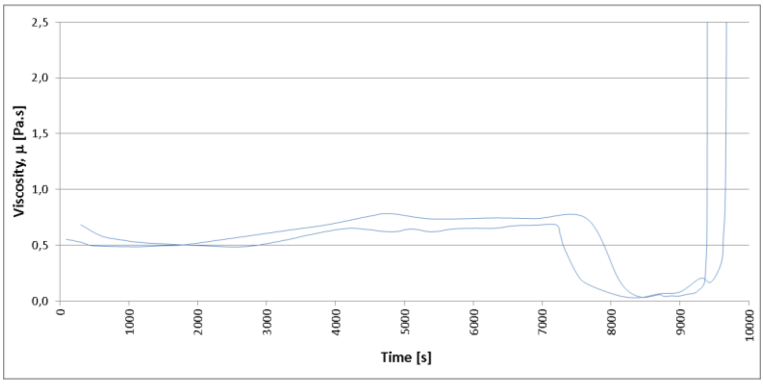

Figure 98 – Evolution of the viscosity in the samples LYHF201 and LYHF202 during the viscosimetry tests conducted at 30ºC/80ºC (303 K/353 K).

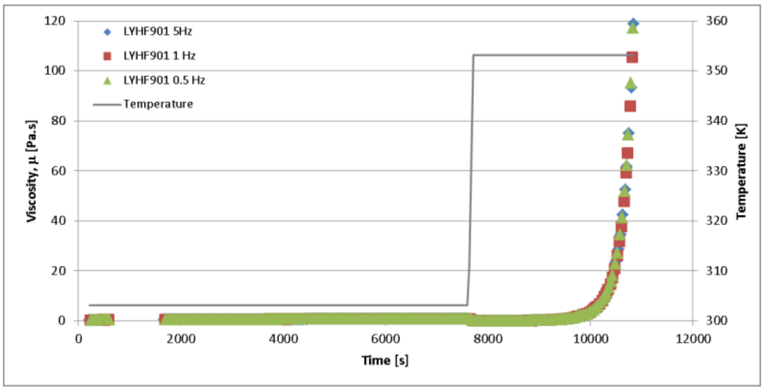

Figure 99 – Evolution of the viscosity and temperature in the sample LYHF901 during the rheometry test conducted at 30ºC/80ºC (303 K/353 K) and multiple frequencies of 0.5, 1 and 5 Hz.

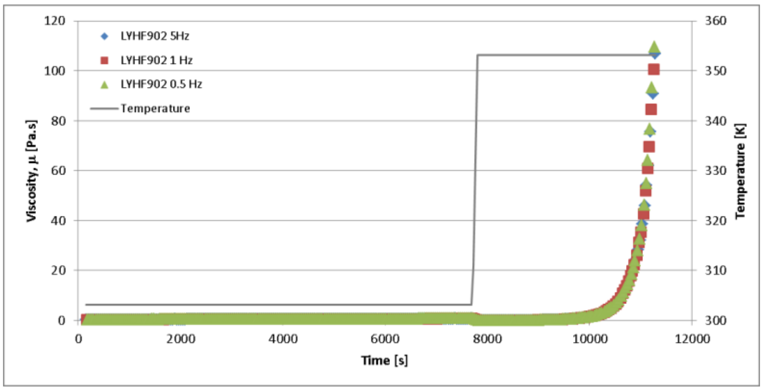

Figure 100 – Evolution of the viscosity and temperature in the sample LYHF902 during the rheometry test conducted at 30ºC/80ºC (303 K/353 K) and multiple frequencies of 0.5, 1 and 5 Hz.

In the rheometry tests, the outputs from the experiments conducted at different frequencies practically superposed, thus highlighting no dependence of the measurements on this test parameter (for the frequency range selected).

The values found for the initial viscosity, μ_0, were coherent with the manufacturer’s data, thus validating the two measurement procedures. In Figure 102 the initial viscosities measured at the beginning of each test are presented for all the samples tested by both techniques. The resin manufacturer’s data provided for the temperatures of 25ºC, 40ºC and 60ºC were used to establish the upper and lower reference limits for the expectable initial viscosity of the epoxy system, immediately after the proper mixture of its constituents. These values for the initial viscosity, μ_0, are compiled in Table 26.

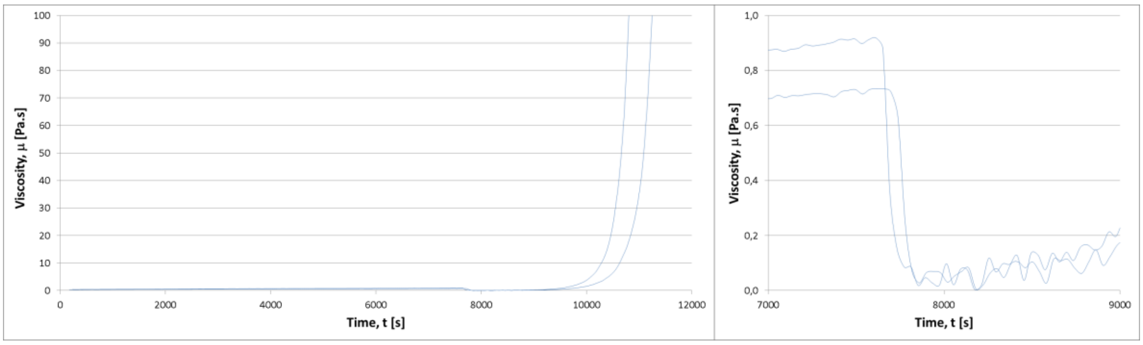

Figure 101 – Evolution of the viscosity in the samples LYHF901and LYHF902 during the rheometry tests conducted at 30ºC/80ºC (303 K/353 K). Complete view (left) and partial (zoomed) view of the initial stage (right).

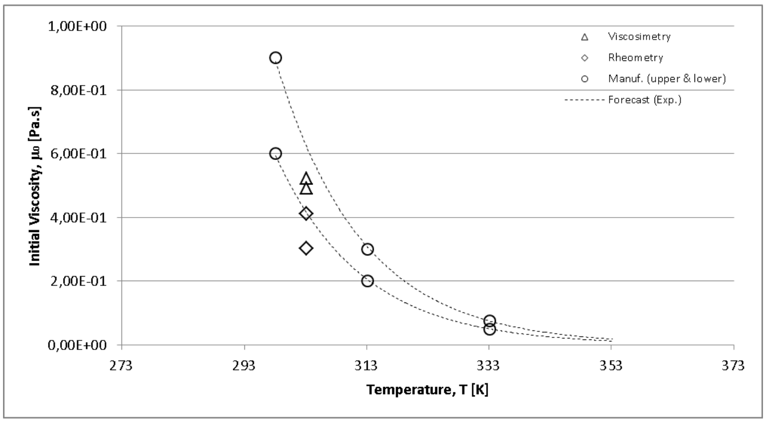

Figure 102 – Initial viscosities of the SR®1500/SD®2505 epoxy system measured with viscosimetry and rheometry at 30ºC (303 K), 40ºC (313 K) and 50ºC (323 K).

Table 26 – Initial viscosities of the LY556/HY917/DY070 epoxy system measured with viscosimetry and rheometry at 30ºC (303 K).

Test Temperature [ºC (K)]	Manufacturer	Viscosimetry		Rheology	
	μ_0 [Pa.s]	μ_0 [Pa.s]	standard deviation [Pa.s]	μ_0 [Pa.s]	standard deviation [Pa.s]
25 (293)	0.600 - 0.900	n/a	n/a	n/a	n/a
30 (303)	(0.416 - 0.625)	0.507	0.023	0.356	0.077
40 (313)	0.200 - 0.300	n/a	n/a	n/a	n/a
60 (333)	0.050 - 0.075	n/a	n/a	n/a	n/a

Analysing the overall results, as well as the initial viscosities measured, the two experimental techniques were considered valid in the applicable ranges of viscosity and temperature. Nevertheless, the two techniques actually assess the viscosity in different conditions, since they imply different amounts of concentrated mass and interactions with the measuring instruments. In spite of the similar behaviour in the 1st isothermal dwell (which correspond to the manufacturing stage), the gelation phenomenon during the 2nd dwell occurred differently in the two methods. Therefore, both were further studied and modelled.

From the viscosimetry tests, the changes in the temperature of the samples, ΔT, at the approximation of the gelation initiation were critically investigated. Similarly to the study realized with the SR®1500/SD®2505 resin, a constant value for the specific heat, $C_p^m = 1200\ J\,kg^{-1}\,K^{-1}$, was assumed and, through the equation (4.17), the averaged value for the specific thermal energy, $E_T/m = 51.000\ kJ\,kg^{-1}$, was calculated. Such value coarsely agrees with the value of the activation energy, $E_{a2} = 58.825\ kJ\,kg^{-1}$ found in the kinetic studies [238] for the 2nd dwell (Table 17).

In Figure 103 the viscosimetry experimental data is plotted in terms of the viscosity, μ, *versus* degree of cure, α. The degree of cure was obtained from the direct matching of its corresponding curing time, t, in both the viscosimetry and kinetic studies for the same resin and MRCC conditions. A maximum degree of cure of around 5% was achieved at the end of the 1st isothermal dwell (30ºC) and gelation initiated at around 25%. Oppositely to what was observed in the SR®1500/SD®2505 system, no relevant changes in viscosity occurred during the 1st dwell. Namely, no relevant decrease of viscosity nor increase of the samples temperature were measured. This indicated that the reactivity of this resin system at near-to-room temperatures is low (as expected).

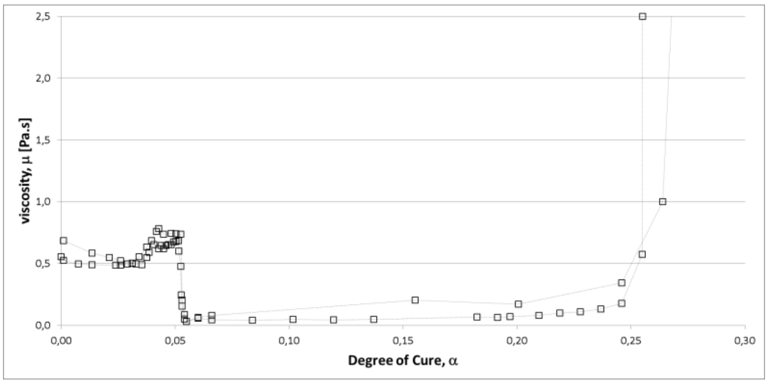

Figure 103 – Plot of the viscosity *versus* degree of cure for the LY556/HY917/DY070 samples tested in viscosimetry.

Firstly, the three models proposed by Lee *et al.* [82], Ng *et al.* [91] and Macosko [100] were fitted to the viscosimetry experimental data through non-linear least squares minimization. The best fittings are shown in Figure 104. The Macosko model presented the best agreement in both the 1st and 2nd dwell, up to the start of gelation. Recalling its description in equation (2.60), this rheological model depends on α_{gel} and is undetermined when $\alpha = \alpha_{gel}$. Therefore, adaptations were made in order to overcome this “unreal” singularity as well as to improve the prediction ability after $\alpha = \alpha_{gel}$. A dedicated model was developed for the case under study.

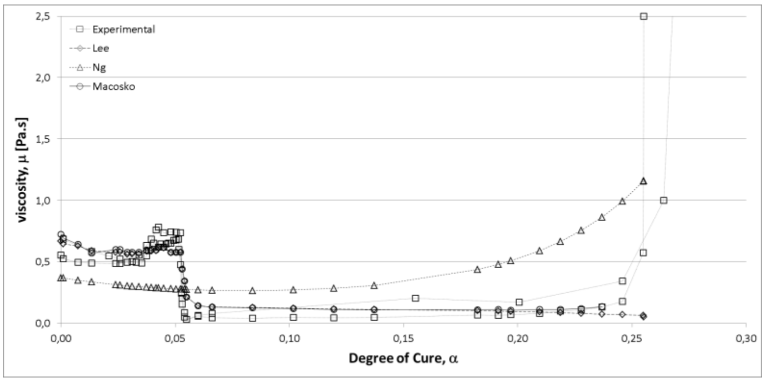

Figure 104 – Fitting of the Lee, Ng and Macosko models to the experimental viscosimetry data of LY556/HY917/DY070.

The following piecewise relation was devised in order to keep validity of the model for the entire domain of degree of cure [251]:

$$\begin{cases} \mu = \mu_\infty e^{\frac{U}{RT}\left(\frac{\alpha_{gel}}{\alpha_{gel}-\alpha}\right)^{(a+b\alpha)}} & \alpha < \alpha_{gel} \\ \mu = \mu_{gel} e^{m\left(\alpha-\alpha_{gel}\right)} & \alpha \geq \alpha_{gel} \end{cases} , \tag{4.21}$$

where μ_∞ is the pre-exponential constant, μ_{gel} and α_{gel} are, respectively, the viscosity and the degree of cure at the initiation of gelation and U, a, b and m are constants. The exponential nature of the model was kept for $\alpha \geq \alpha_{gel}$ but the temperature dependence was disregarded. This option was justified by the absence of reliable data on the temperature evolution at this stage of the cure process. It was also supported by the good agreement of this constants-based exponential function within the desired domain. The fitting results for both the Macosko and the new model (named hereafter Macosko Adapted) are plotted in Figure 105. In Table 27 the values of the parameters leading to the best model fits are listed. As one may observe, the Macosko Adapted piecewise model extended the domain of applicability of the Macosko model, keeping its description and behaviour for $\alpha < \alpha_{gel}$.

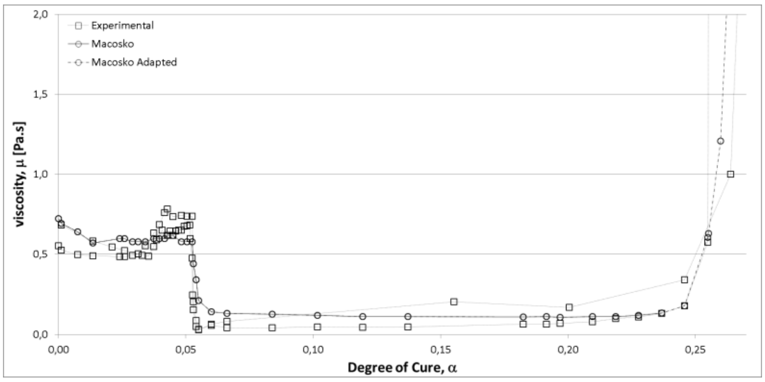

Figure 105 – Fitting of the Macosko and Macosko Adapted models to the experimental viscosimetry data of LY556/HY917/DY070 samples tested at 30ºC/80ºC (303 K/353 K).

Table 27 – Parameters determined for the fitting of the viscosimetry experimental curves of LY556/HY917/DY070 with the Macosko Adapted rheological model.

Model Parameters	Macosko Adapted $\begin{cases} \mu = \mu_\infty e^{\frac{U}{RT}\left(\frac{\alpha_{gel}}{\alpha_{gel}-\alpha}\right)^{(a+b\alpha)}} & \alpha < \alpha_{gel} \\ \mu = \mu_{gel} e^{m(\alpha-\alpha_{gel})} & \alpha \geq \alpha_{gel} \end{cases}$
μ_∞ [Pa.s]	1.5428×10^{-5}
μ_{gel} [Pa.s]	0.1790
U [J mol^{-1}]	2.6750×10^{4}
a	-1.3645×10^{-1}
b	1.6041
m	1.3500×10^{2}
α_{gel}	0.2459

The outputs of the rheometry tests were analysed in a similar way. The viscosity-time curves outputted from the rheometer apparatus (Figure 101) were converted into viscosity-degree of cure curves, through the degree of cure-time relations obtained in the DSC experiments (Figure 63). These are plotted in Figure 106.

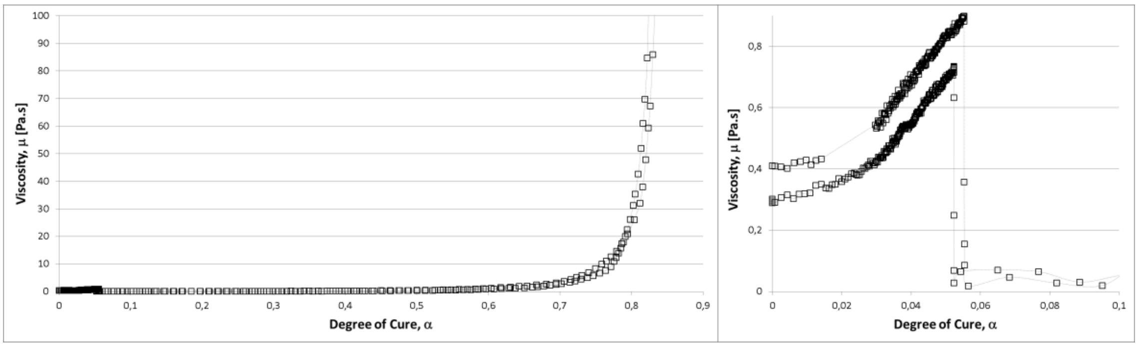

Figure 106 – Plot of the viscosity *versus* degree of cure for the LY556/HY917/DY070 samples tested in rheometry. Complete (left) and partial (right) views.

The range of viscosities and degree of cure achieved during the 1st dwell agreed reasonably with those measured in viscosimetry. In the 2nd dwell, however, the increase of viscosity was “slower”, i.e., for each degree of cure, the viscosity measured in rheometry was lower than in viscosimetry. The main reason for this was that at the transition from the 1st dwell (30ºC) to the 2nd dwell (80ºC) the temperature increasing rates imposed in the two experimental setups were considerably different. In viscosimetry, the lower temperature increasing rate conducted to a greater accumulation of energy in the sample without the corresponding matching on the advance of the conversion (degree of cure). As a result, the remaining cure behaviour (upon reaching 80ºC) is anticipated when compared to the rheometry results. Also, the greater concentrated masses in the viscosimetry samples accelerated the cure in the vicinity of the gelation. Nevertheless, the similarity of the results achieved in the 1st isothermal dwell (corresponding to the effective manufacturing stage) through the two distinct methods attributes considerable validity and confidence to its application in the process modelling.

The models proposed by Lee *et al.* [82], Ng *et al.* [91] and Macosko [100] were fitted to the rheometry curves. The results are plotted in Figure 107 (complete view of the entire domain of α) and Figure 108 (zoomed view of the initial ranges, including the transition from the 1st to the 2nd dwell).

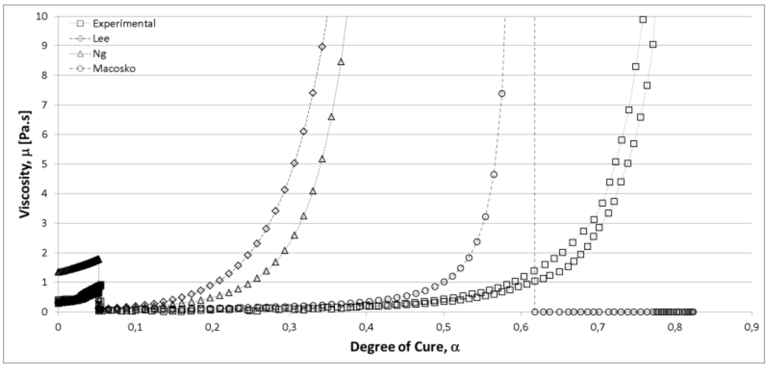

Figure 107 – Fitting of the Lee, Ng and Macosko models to the experimental rheometry data of LY556/HY917/DY070.

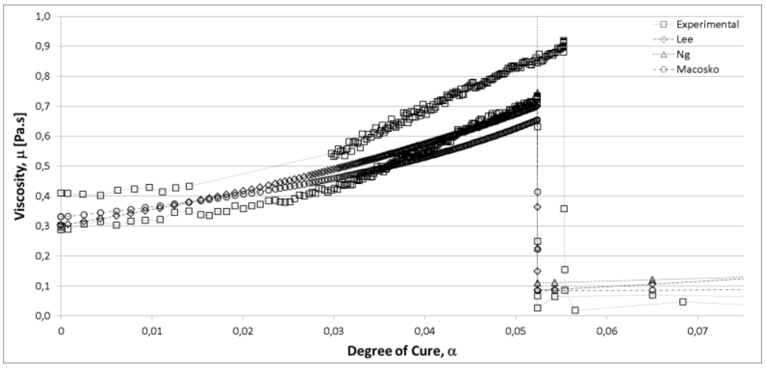

Figure 108 – Partial (zoomed) view of the Lee, Ng and Macosko models fitting to the experimental rheometry data of LY556/HY917/DY070.

The Macosko model presented greater ability to model both the 1st and 2nd dwells. Thus, a single equation model was sought to describe the rheological behaviour of the LY556/HY917/DY070 resin throughout the MRCC including an initial stage that approximates the manufacturing condition. Since the Macosko model is undetermined for $\alpha = \alpha_{gel}$, a modified equation was devised taking the form [251]:

$$\mu = \mu_\infty e^{\frac{U}{RT}} \left(\frac{\alpha^i_{\max}}{\alpha^i_{\max} - \alpha} \right)^{(a-\alpha)} \qquad i = 1,2 \ , \tag{4.22}$$

where μ_∞ is the pre-exponential constant, U is a constant associated with the intrinsic activation energy, R is the universal gas constant, T is the temperature, $\alpha^i_{\max}$ is the maximum degree of cure achieved in each isothermal dwell ($i = 1,2$) and a is a constant. The option of replacing α_{gel} by $\alpha_{\max}^{i}$ was supported by two observations: from the experimental data (1) no evidence of a singularity was observed in the curves that could be attributed to the gel point and (2) no enough data was available to determine the gel point of reference for the 1st isothermal dwell temperature (30ºC). Thus, $\alpha_{\max}^{i}$ allows to shape the model to the desired domain and avoids the undetermined result for $\alpha = \alpha_{gel}$. The constant b was disregarded since it was noted that the value $b = 1$ was common to all the acceptable combinations of parameters that minimized the error of the Macosko model. The new rheological model (hereafter called Macosko Adapted) allowed to adequately describe the behaviour of this resin for the entire domain of α, modelling both the 1st and 2nd temperature dwells with minimum error. The improvements achieved are shown in the following plots. The parameters determined for the various models are listed in Table 28.

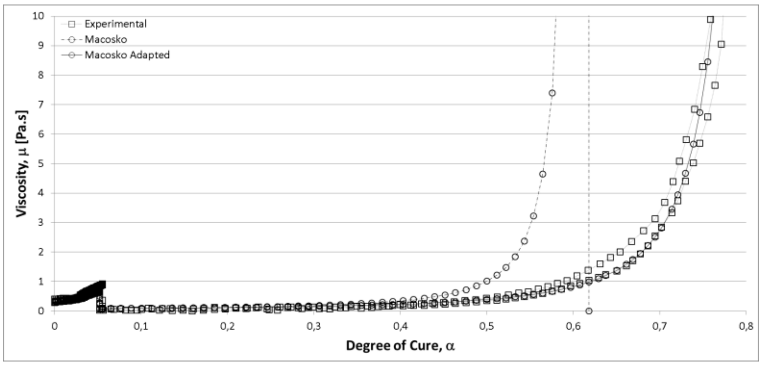

Figure 109 – Fitting of the Macosko and Macosko Adapted models to the experimental rheometry data of LY556/HY917/DY070.

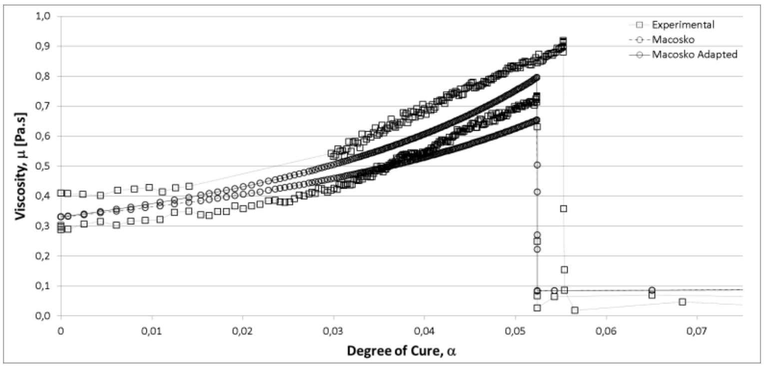

Figure 110 – Partial (zoomed) view of the Macosko and Macosko Adapted models fitting to the experimental rheometry data of LY556/HY917/DY070.

The value of the degree of cure at gelation was determined through the two alternative criteria described previously ($\tan\delta$ freq independent (criterion 1) and $\tan\delta$ inflection (criterion 2)). The gel times, t_{gel}, and α_{gel} are listed in Table 29, together with the manufacturer data available. Considerable differences on t_{gel} were observed between the effective time to gel under the MRCC conditions and the manufacturer available data for an isothermal condition at 80ºC (353 K). This is justified by the fact that the effective condition to which the resin was subjected during the rheometry tests included an initial stage at 30ºC for 2 hours in which cure and viscosity build-up were started. Thus, the resin chemo-rheological state at the beginning of the 2nd dwell (at 80ºC) was not zeroed. In order to validate the calculations of t_{gel} and α_{gel} adjusted gel times were calculated through replacing the time of the 1st dwell by the equivalent time that an isothermal condition at 80ºC would lead to a similar viscosity build-up. These agreed very well with the manufacturer's data, thus validating the assumptions taken. An interesting correspondence between the chemical (conversion) and rheological (viscosity) behaviours of this thermosetting epoxy system was, in fact, assessed.

Table 28 – Parameters determined for the best fitting of the rheometry experimental curves of SR®1500/SD®2505 with the Ng, Lee and Lee Extended models.

Model Parameters		Rheological Model			
		Macosko Adapted $\mu=\mu_\infty e^{\frac{U}{RT}}\left(\frac{\alpha^i_{\max}}{\alpha^i_{\max}-\alpha}\right)^{(a-\alpha)}$	Macosko $\mu=\mu_\infty e^{\frac{U}{RT}}\left(\frac{\alpha_{gel}}{\alpha_{gel}-\alpha}\right)^{(a-b\alpha)}$	Ng $\mu=\mu_\infty e^{\frac{U}{RT}+k_1\alpha^2+k_2\alpha}$	Lee $\mu=\mu_\infty e^{\frac{U}{RT}+k_1\alpha}$
μ_∞ [Pa.s]		1.0987×10^{-5}	1.0987×10^{-5}	3.9193×10^{-9}	1.1426×10^{-7}
U [J mol^{-1}]		2.5991×10^{4}	2.5991×10^{4}	4.9527×10^{4}	3.7276×10^{4}
k_1		n/a	n/a	2.2795×10^{1}	1.6005×10^{1}
k_2		n/a	n/a	4.2537	n/a
α_{gel}	1st dwell	n/a	(0.6086)	n/a	n/a
	2nd dwell	n/a	0.6086	n/a	n/a
$\alpha_{\max}$	1st dwell	0.1093	n/a	n/a	n/a
	2nd dwell	0.8400	n/a	n/a	n/a
a		1.2935	0.9935	n/a	n/a
b		n/a	1.0000	n/a	n/a

Table 29 – Gel times and α_{gel} of the LY556/HY917/DY070 at 80ºC (303 K) calculated from rheometry tests data using different criteria.

Test Temperature [ºC (K)]	Criterion								
	manuf. data	tanδ freq independent (criterion 1)				tanδ inflection (criterion 2)			
	t_{gel} [s]	α_{gel}	standard deviation [s]	t_{gel} [s]	standard deviation [s]	α_{gel}	standard deviation [s]	t_{gel} [s]	standard deviation [s]
80 (353)	3900-4500	0.609	0.022	effective		0.631	0.023	effective	
				2035	37.0			2069.5	71.5
				adjusted				adjusted	
				3919	71.5			3953	106.0

In summary, a new model was devised to predict the viscosity changes during the cure process for the entire domain of conversion. This model was able to describe with a single equation (only $\alpha^i_{\max}$ changes from the 1st to the second dwells) the "real" evolution of viscosity throughout the MRCC to which this resin was subjected during the manufacturing and the post-curing periods. The model was used as a main input to the global process model, incorporating the resin viscosity sub-model.

4.2.3. Resins Mixing Behaviour

In the previous sections, the kinetics and rheology of polymer matrices were studied as partially intrinsic characteristics. Specifically, two thermosetting epoxy resins were tested and modelled. The evolution of both the degree of cure, α, and the viscosity, μ, as the cure progresses govern the ability of the resin to flow through the porous fibre bed and, thus, the consolidation of the composite laminate being manufactured. The physical properties of the resin, such as the viscosity, are mostly dependent on time, since the irreversible chemical reaction starts upon mixture of its constituents. The studies conducted and discussed in the previous sections showed that other conditions like the quantity of mass and the surrounding temperature also impact significantly the kinetic and rheological behaviour. In the case of thermoplastics, the increase of the viscosity (intrinsically reversible) is set by the retrieval of the external heating source. In view of modelling the consolidation of composite laminates, the degree of cure/crystallization and viscosity should be known for each point and each moment. For the majority of the manufacturing processes, the assessment to the intrinsic behaviour of the neat resin subjected to comparable temperature and mass conditions is a very good approximation to its behaviour within the “real” laminate. In FW, however, the laminate is built-up through discontinuous deposition of the consecutive layers. As a new layer is wound it compresses the ones beneath and is invaded by their resin. Therefore, resins with different curing histories are effectively mixed in each layer. The effects of such mixture in the overall kinetics and rheology were studied and are discussed hereafter.

The two epoxy resin systems selected for the process model validation in wet FW trials were tested under different mixing conditions. In each test, two portions of the same resin system, prepared in different times, were mixed and its joint behaviour was analysed. The differences between the behaviour of this blend and the neat (unmixed) resin were then critically assessed. The study was based on the variation of two parameters: the time gap between the preparation of each portion of resin and the mixing ratio of the two portions.

Both rotational viscosimetry and oscillatory rheometry were used to measure the evolution of the viscosity of the two epoxy systems – SR®1500 from Sicomin Composites (France) and Araldite® LY556 from Huntsman (USA) – under several mixing conditions. The same MRCC previously applied in the kinetic and rheological modelling studies [238,251] were imposed in order to maintain the focus in approaching the “real” temperature conditions during manufacturing. The experimental procedures, their results and the critical analysis are presented hereafter.

4.2.3.1. Experimental Procedures

Rotational viscosimetry and oscillatory rheometry have been widely used to assess the change of viscosity in reacting polymers [243,244]. Herewith these techniques were used to have an insight to the effect of mixing portions of resin with different curing histories. As before, the use of two different experimental procedures allowed also to achieve additional cross validation of the results outputted.

Since the typical arrangements and procedures associated with these techniques are not suitable to extend the measurements up to and after the gelation of the polymer sample, special care and a few adaptations were implemented to account for this. The two experimental procedures used for the rheological characterization of the SR®1500 and LY556 epoxy systems are described hereafter.

The same measuring instruments, adapted to allow extending the test up to and after gelation, were used as for the rheological studies conducted with the neat resin samples. A Brookfield viscometer (Visco Basic Plus from Fungilab) was used in the first experiment. The setup is shown in Figure 75. In addition to the procedure implemented previously, a second set of the same resin system was pre-heated to the prescribed test temperature, then prepared (mixture of the constituents) with a time gap to the first set and finally added to the running test sample. The time gap was defined as the time interval occurred between preparation (mixing of constituents) of the first and second portions. The rheometry tests were carried out using a stress/strain control rheometer (Stresstech® from Reologica Instruments AB) with the setup shown in Figure 76. The same apparatus was used as in the rheological tests on neat samples. The relevant difference was that the blends of two portions of resin with different curing histories were produced prior to the effective start. This meant that the rheometry tests only registered the behaviour of the resin sample after the blend, thus not capturing the change of behaviour at the time of the blend. This limitation was imposed by the impracticability of changing the test sample (by adding and remixing fresh material) *in-situ*. The need of calibrating the measurement instrument at the beginning of each test was incompatible with the possibility of touching or repositioning it.

The results of the experimental tests on the SR®1500 and Araldite® LY556 epoxies are presented and critically analysed below.

4.2.3.2. Experimental Results

The characterization of the rheological behaviour of the two commercial epoxies selected under several prescribed mixing conditions was addressed through rotational viscosimetry and oscillatory rheometry. A qualitative assessment to the influence of the time gap in the curing history and the mass ratio of two blended portions of the same type of resin was pursued. The objective was to validate (or improve) the assumption introduced in the resin mixing sub-model translated in equation (3.40).

SR®1500

The epoxy/amine system SR®1500/SD®2505 with the weight ratio of 100:33% was rheologically characterized under the isothermal temperature of 30ºC (303 K), mixture mass ratios of 1:1, 2:1 and 3:1 and cure time gaps of 5min, 8min and 11min. These test conditions covered a considerable range of the comparable “real” conditions that the resin could experience during the FW process. The near-to-room temperature quite approached the “real” manufacturing temperature conditions. The selected mixing ratios and time gaps covered an interesting range of possibilities within the overall short working time window that this resin system allowed. The MRCC selected are indicated in Table 30 and the mixing conditions listed in Table 31 for the tests carried out.

The direct results outputted from the viscosimetry tests are presented in Figures 111 and 112. A reference curve of the neat resin behaviour, taken from previous measurements [251], is appended for comparison. In these plots the initial time, $t = 0$, corresponded to the completion of the preparation (mixture of the two constituents, SR®1500 and SD®2505) of the first portion of resin. The shift in the curves corresponded to the moment when the second portion of resin was blended to the first.

Table 30 – MRCC for SR$^{®}$1500/SD$^{®}$2505 and selected curing cycle for the viscosimetry and rheometry tests on mixed (blended) samples.

Pre-cure	2 to 4 hours @ 20ºC
Minimum post-cure cycle	2 to 7 days @ 20ºC
Advised post-cure cycle	2 to 7 days @ 20ºC OR 12 hours @ 40ºC OR 6 hours @ 60ºC
Cycle selected for viscosimetry tests	up to gelation @ 30ºC
Cycle selected for rheometry tests	up to 100 Pa.s @ 30ºC

Table 31 – Mixture ratio and cure time gap conditions of the SR$^{®}$1500/SD$^{®}$2505 mixed (blended) samples tested in viscosimetry and rheometry.

Type of Test	Test ID	Mass of Portion 1 [g]	Mass of Portion 2 [g]	Mixture Mass Ratio	Neat Cure Time Gap [s (min)]
Viscosimetry	SRHF501	283.4	141.3	2:1	310 (5)
	SRHF502	212.3	212.0	1:1	480 (8)
	SRHF503	213.3	212.6	1:1	300 (5)
	SRHF504	318.5	107.2	3:1	300 (5)
	SRHF505	211.9	211.9	1:1	675 (11)
Rheometry	SRHF1101	20.14	7.15	3:1	544 (9)
	SRHF1102	18.66	9.35	2:1	536 (9)
	SRHF1103	14.77	14.84	1:1	540 (9)
	SRHF1104	9.44	18.80	1:2	565 (9)
	SRHF1105	13.62	13.49	1:1	960 (15)
	SRHF1106	13.76	13.76	1:1	1500 (25)
	SRHF1107	13.60	16.31	1:1	245 (4)

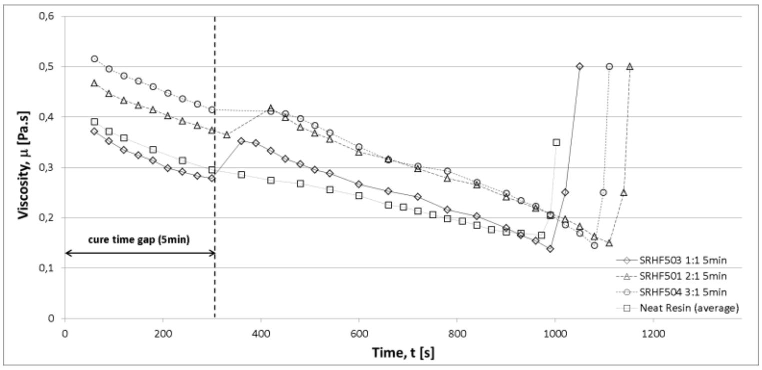

Figure 111 – Evolution of the viscosity in the SR$^{®}$1500/SD$^{®}$2505 mixed (blended) samples with mixture mass ratios of 1:1, 2:1 and 3:1 and cure time gaps of 5min during the viscosimetry tests conducted at 30ºC (303 K).

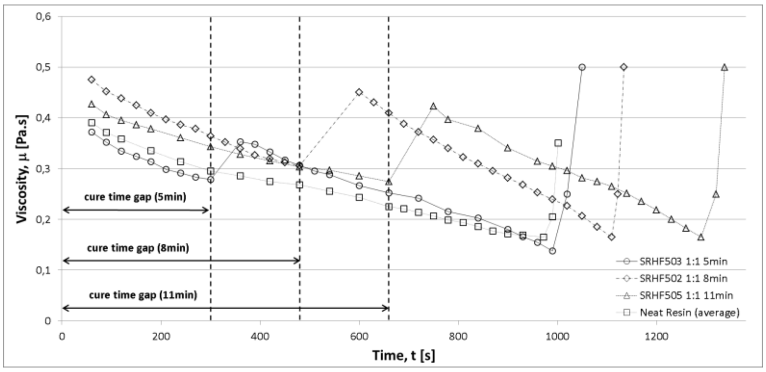

Figure 112 – Evolution of the viscosity in the SR®1500/SD®2505 mixed (blended) samples with cure time gaps of 5min, 8min and 11min and mixture mass ratio of 1:1 during the viscosimetry tests conducted at 30ºC (303 K).

Both the relative contents (mass ratio) and cure time gap of the two blended portions showed to affect the evolution of the viscosity. Actually, from these plots several preliminary conclusions could be established:

- greater relative contents of the second (added) portion led to greater shift in viscosity;
- greater cure time gaps led to greater overall times to gelation;
- time to gelation was significantly affected by the cure time gap (or the time at which the mixture of the portions was made);
- the overall viscosity immediately before gelation was nearly constant, thus being not affected by any of the parameters.

Other observations, despite less conclusive, could be made. The time to gelation seemed not to be affected by the relative content of the second portion. Also, the evolution of the viscosity after mixture seemed to consistently present higher slope.

The assumption being analysed was that, at a macroscopical level, the rheological behaviour of the blend of two portions with different curing histories could be described by a linear combination of the individual behaviours. A linear combination weighed by the relative contents of each portion was considered in chapter 3, as follows [24]:

$$\mu = \sum_{j=1}^{m} \Psi_j^m \, \mu_j \quad , \tag{3.40}$$

where μ_j are the viscosities of the individual constituents of the blend and Ψ_j^m are their relative concentrations. In order to test this relationship, it was used to estimate the virtual initial viscosity of the second portion in each test sample from the viscosity values registered immediately before and after its addition. The equation was firstly rewritten for the case under study, as:

$$\mu_{mix} = \frac{\mu_1 \, m_1 + \mu_2 \, m_2}{m_1 + m_2} \quad , \tag{4.23}$$

where μ_{mix} is the viscosity of the blend immediately after mixture, μ_1 is the viscosity of the first portion immediately before mixture, μ_2 is the viscosity of the second portion immediately after mixture and m_1 and m_2 are the masses of first and second portions, respectively. μ_2 was the only unknown for each test case and corresponded to the virtual initial viscosity of the second portion of resin. It would be expected to be similar to the initial viscosities effectively registered at the start of the each measurement. Average values of $\mu_2 = 0.455\,Pa.s$ and $\mu_2 = 0.564\,Pa.s$ were calculated, respectively, from the data of tests conducted with a cure time gap of 5min (SRHF501, SRHF503 and SRHF504) and mass ratios of 1:1 (SRHF501, SRHF502 and SRHF505). The full data for all the tests are presented in Table 32.

Table 32 – Values estimated for the initial viscosities of the second resin portions and relative errors to the effective initial viscosities of the first portions, for the viscosimetry tests of SR®1500/SD®2505 mixed (blended) samples.

Test ID	Mixture Mass Ratio	Neat Cure Time Gap [s (min)]	Initial Viscosity (portion 1) [Pa.s]	μ_1 [Pa.s]	μ_{mix} [Pa.s]	$\Delta\mu$ at Mixture [Pa.s]	μ_2 (calculated) [Pa.s]	Error [%]
SRHF501	2:1	310 (5)	0.468	0.365	0.418	0.053	0.523	11.8
SRHF502	1:1	480 (8)	0.475	0.305	0.451	0.145	0.596	25.4
SRHF503	1:1	300 (5)	0.372	0.279	0.352	0.074	0.426	14.7
SRHF504	3:1	300 (5)	0.516	0.415	0.416	0.001	0.417	19.1
SRHF505	1:1	675 (11)	0.427	0.274	0.423	0.149	0.572	34.0

The errors in the estimated values for μ_2 (corresponding to the virtual initial viscosity of the second portion composing the mixed samples) were determined by comparing these with the initial viscosities effectively measured for the first portions at the beginning of each test. The errors were partially explained by the fact that the effective initial viscosities of the first resin portions are higher than the values registered at the beginning of the tests. This was due to the time gap between preparation of the resin and the initiation of the tests. Moreover, the shift in viscosity was artificially enhanced by the test setup because after the mixture the rotating spindle had a greater contact area with the resin (the resin sample height increased) thus sensing greater resistance. However, the relative high values of the errors as well as their apparent increasing tendency with the increase of the cure time gaps between the two resin portions do not hold the assumption being studied. Nevertheless, the relation described in equation (3.40) tended to produce quite acceptable results for low cure time gaps (<5min) between the two mixing portions, which is the most often situation for adjacent layers in “real” FW conditions.

Further analysis of the experimental data was addressed aiming at both validating it and foreseeing alternative modelling approaches for the resin mixing behaviour. A clear indication of the reliability of the experimental results was retrieved from the times to gelation. Indeed, the values of the time up to initiation of gelation measured from the preparation of the first resin portion and the preparation of the second resin portion, converged for preparation time gaps equal to zero. This is better perceived in Figure 113, where the linear trend lines of the two series intercept for no cure time gap (cure time gap of zero). Additionally, the same gelation times analysed against the mixture mass ratios converge for high ratios (i.e., very low content of the second resin portion). This is plotted in Figure 114 and is intuitively correct.

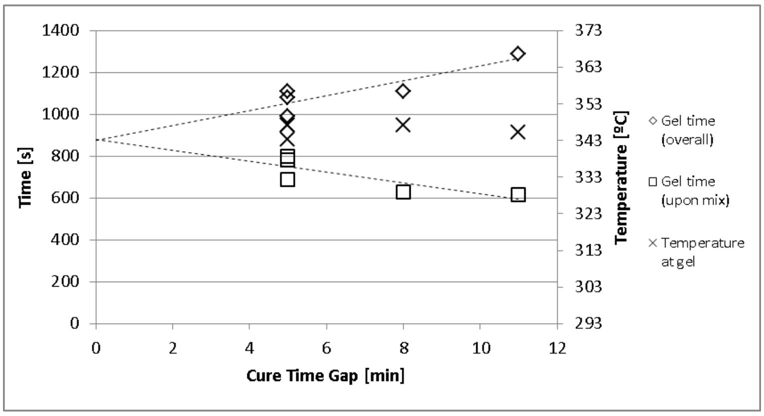

Figure 113 – Time to and temperature at gelation *versus* cure time gap for the SR®1500/SD®2505 mixed (blended) samples tested in viscosimetry at 30ºC (303 K).

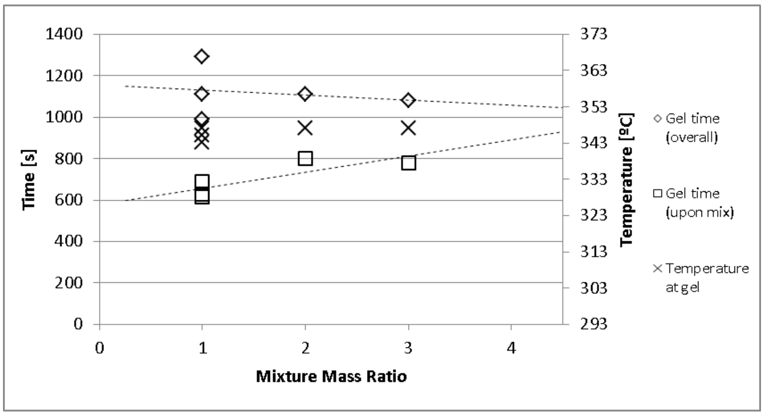

Figure 114 – Time to and temperature at gelation *versus* mixture mass ratio for the SR®1500/SD®2505 mixed (blended) samples tested in viscosimetry at 30ºC (303 K).

The consistency of the temperature measured in the samples at the initiation of gelation (together with the similar overall mass of all the samples) suggested that a characteristic value for the accumulated thermal energy required to initiate this phenomenon could be found. The same analysis addressed in the viscosimetry tests of neat resin samples would apply. However, since the addition of the second resin portions occurred when the samples temperature were still close to the test temperature (30ºC/303 K) no significant influence on the overall temperature was attributable to the mixing conditions. Therefore, besides the indicative consistency of the experimental data, no relevant information could be based on the temperature data regarding the effect of the mixture conditions on the cure or rheology of the resin system.

On the contrary, the analysis of the viscosities measured at the onset of gelation and the shift in viscosity observed at the occurrence of the mixture (second portion added to first portion) tended to support the assumption under discussion. The viscosity at gelation, μ_{gel}, showed an increasing tendency with the increase of the cure time gap and a decreasing tendency as mixture mass ratios increased. These behaviours are graphically presented in Figures 115 and 116, with solely indicative and clarifying trend lines. The former behaviour suggested that the later the fresher resin portion was added to the older one the overall mixture was gradually less able to accommodate (or “correct”) its viscosity on time for the gelation. The latter behaviour suggested that as less fresh resin was added, the overall mixture further approximated the expected viscosity at gelation of the neat resin. A rule of mixtures seemed to apply to the viscosity behaviour of these mixtures. Furthermore, a dependence on the variable time also seemed to apply.

The sudden rise of the viscosity at the mixture (second portion added to first portion) was a clear indication that the addition of a newly prepared resin affects the rheology of the new mixture. However, it was not sufficient to prove the full adequateness of the linear combination description. Nevertheless, the verification of greater shifts in viscosity for greater cure time gaps and lower mixture mass ratios (Figures 115 and 116) added a useful perception of applicability of a weighed mixing rule.

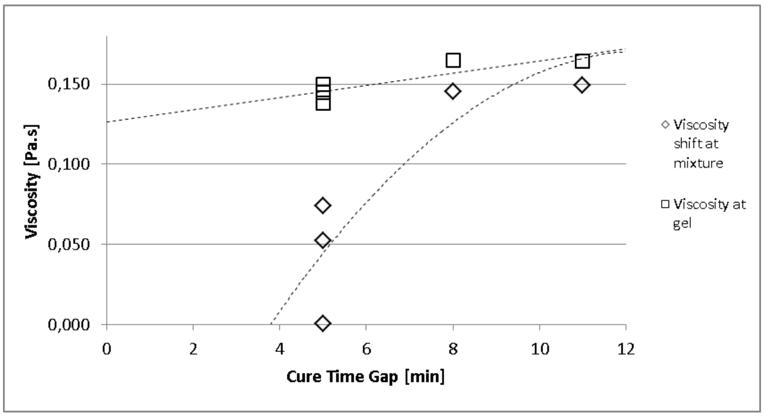

Figure 115 – Viscosity at gelation and viscosity shift at mixture *versus* cure time gap for the SR®1500/SD®2505 mixed (blended) samples tested in viscosimetry at 30ºC (303 K).

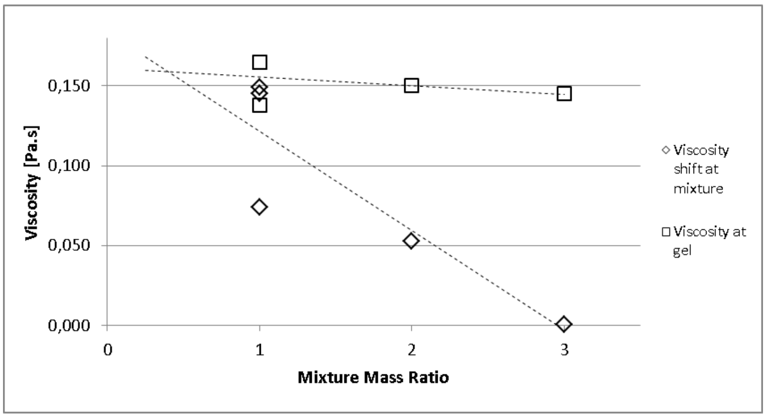

Figure 116 – Viscosity at gelation and viscosity shift at mixture *versus* mixture mass ratio for the SR®1500/SD®2505 mixed (blended) samples tested in viscosimetry at 30ºC (303 K).

The rheological behaviour of thermosetting resins is known to be intrinsically related with their kinetics. If one assumes that the gelation occurs at a characteristic degree of cure, α_{gel}, then the analysis of the time needed to achieve such state may be of interest. If upon mixture the kinetic behaviour could be described as a linear combination of the two individual behaviours, then the additional time required to reach gelation should be of the same order of the cure time gap (for 1:1 mixing ratios). This behaviour was not verified. The delay in reaching gelation was neither similar to the time gap of the curing histories of the two portions nor proportional to their mixing ratios. This is easily confirmed in the following plots. An intrinsic relationship with the kinetics of the mixed resins was not possible to draw.

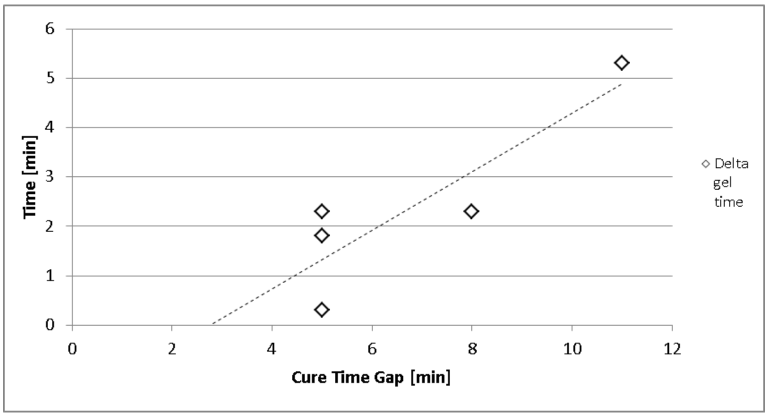

Figure 117 – Difference between the mixed and the neat resin times to gelation *versus* cure time gap for the SR®1500/SD®2505 mixed (blended) samples tested in viscosimetry at 30ºC (303 K).

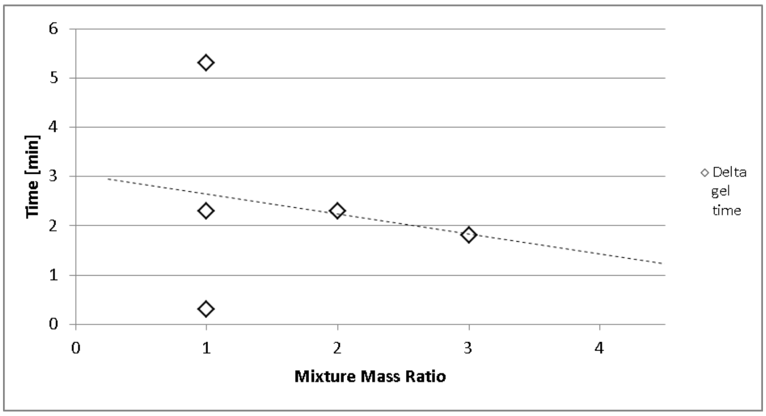

Figure 118 – Difference between the mixed and the neat resin times to gelation *versus* mixture mass ratio for the SR®1500/SD®2505 mixed (blended) samples tested in viscosimetry at 30ºC (303 K).

At the completion of the detailed analysis of the viscosimetry results three main conclusions were established:

- the equation (3.40) was adequate to estimate the viscosity of the resin blend at the moment of mixture (t=cure time gap);
- such estimation error was reduced for low cure time gaps ($\leq 5\,\text{min}$);
- the remaining rheological behaviour of the mixture (blend) after the mixture was a time-dependent combination of the two individual behaviours thus not describable through the proposed equation.

The reasonability of these conclusions was further analysed through complementary rheometry tests conducted in the same resin system.

The results of the rheometry tests are presented in Figures 119 and 120. The same test temperature of 30ºC (303 K) was applied. A reference curve of the neat resin behaviour, taken from previous measurements [251], is included in each plot for comparison. As in the case of the viscosimetry data, the initial time, $t = 0$, in each curve corresponded to the completion of the preparation of the first portion of resin (mixture of the two constituents, SR®1500 and SD®2505). The delay (time gap) in the beginning of each test curve when compared with the reference curve of neat (unmixed) resin corresponded to the sum of the cure time gap of the two portions and the time needed for their mixing. Unlike in the viscosimetry tests, in rheometry the behaviour before mixing of the two resin portions was not measured.

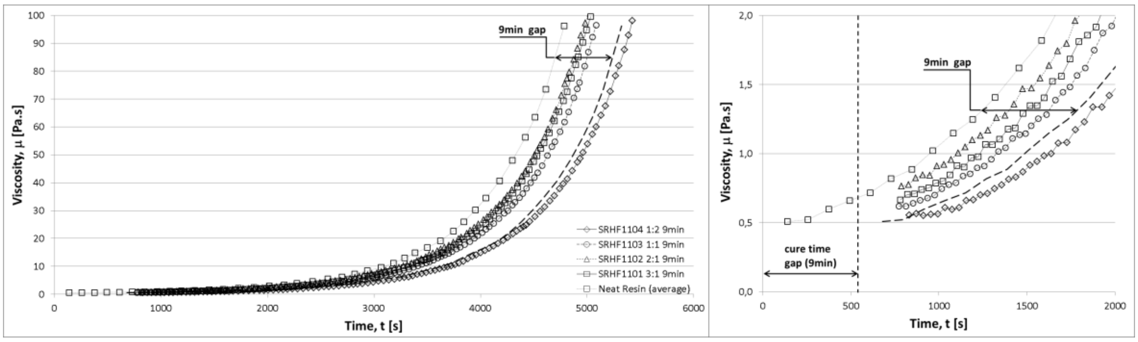

Figure 119 – Evolution of the viscosity in the SR®1500/SD®2505 mixed (blended) samples with mixture mass ratios of 1:2, 1:1, 2:1 and 3:1 and cure time gaps of 9min during the rheometry tests conducted at 30ºC (303 K).

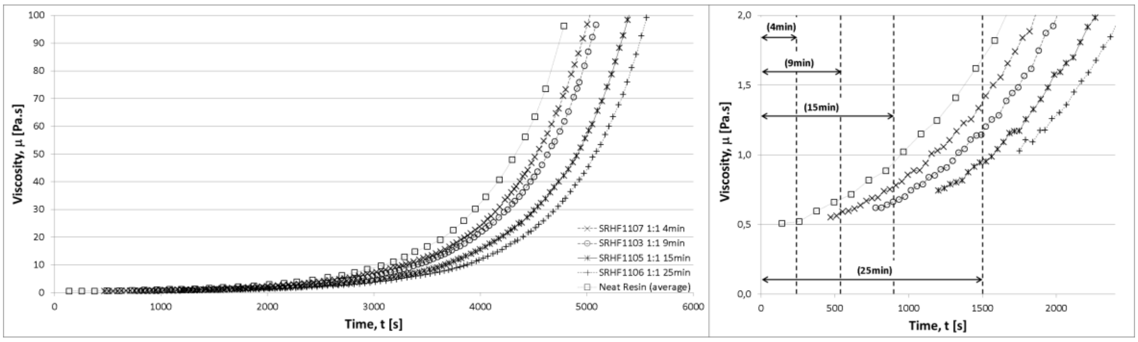

Figure 120 – Evolution of the viscosity in the SR®1500/SD®2505 mixed (blended) samples with cure time gaps of 4min, 9min, 15min and 25min and mixture mass ratio of 1:1 during the rheometry tests conducted at 30ºC (303 K).

Both the relative contents (mass ratio) and cure time gap of the two blended portions showed to affect the evolution of the viscosity. Several tendencies were observed in the curves plotted:

- the effective behaviour of the mixed blends fitted between the individual behaviours of each of the portions, thus suggesting a contribution from each to the overall behaviour;
- only greater relative contents of the second (added) portion over the first produced considerable time shift in the viscosity curve;
- greater cure time gaps led to greater overall time shifts in the viscosity curves; the time shits were, however, consistently lower than the cure time gaps of the two mixed portions.

Using the same criterion discussed along with the rheological studies (section 4.2.2) the overall times and viscosities at gelation were calculated. These are plotted in Figures 121 and 122 as function of the cure time gap and mass ratio of the two portions mixed in each sample. As in the viscosimetry results, the values of the time to gelation measured from the preparation of the first resin portion and the preparation of the second resin portion, converged for very low content of second portion (Figure 121) or preparation time gaps equal to zero (Figure 122). The overall viscosities of the samples at gelation decreased as the mass ratio increased and were nearly unchanged with cure time gaps. This suggested that, unlike the viscosimetry results, for the time gaps studied the resin mixtures were able to accommodate (or "correct") its viscosity on time for the gelation. Within the range of 1:2 to 2:1, particularly, the viscosity at gelation seems to be an intrinsic characteristic of this epoxy resin, thus not affected by the two parameters changed through the test series. The time needed to reach such characteristic viscosity, however, was consistently affected by the two parameters. The fact that the times needed to achieve gelation did not remain constant nor increased equally to the cure gap times suggested that none of the individual resin portions governed the blend behaviour.

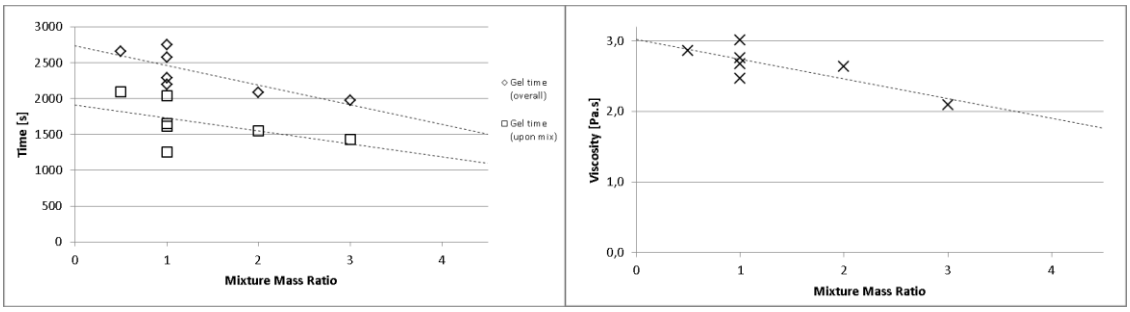

Figure 121 – Time to and viscosity at gelation *versus* cure time gap for the SR®1500/SD®2505 mixed (blended) samples tested in rheometry at 30ºC (303 K).

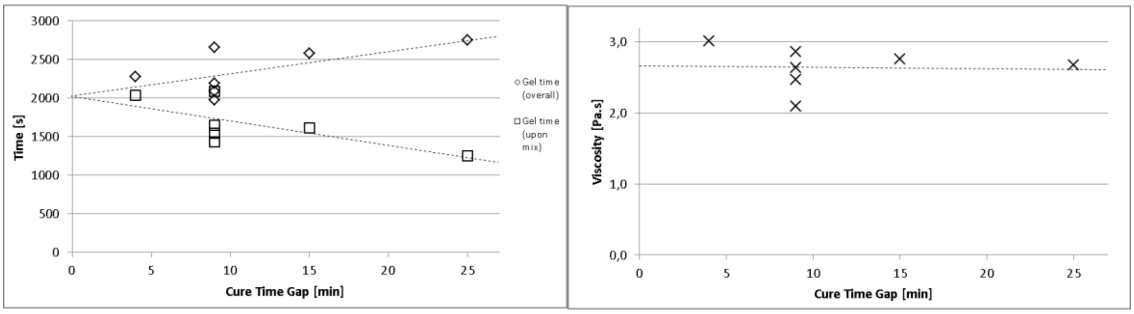

Figure 122 – Time to and viscosity at gelation *versus* mixture mass ratio for the SR®1500/SD®2505 mixed (blended) samples tested in rheometry at 30ºC (303 K).

It turned clear that, despite the rheological behaviour of the resins blend (portion 1 mixed with portion 2) should be described through a combination of the individual behaviours, the relationship itself evolved with time. This meant that the relation presented in equation (3.40), even though setting a reasonable approximation, could not describe accurately the evolution of the viscosity upon mixture of two portions with different cure histories. In graphical terms this is better visualized by noting that the viscosity curve of the mixture is not "parallel" to the two individual (idealized) curves of the neat resins, which are "parallel" to each other.

In addition, contrary to the viscosimetry data, the direct application of the linear combination mixing rules did not return consistent estimations for the idealized viscosity of the second portion at time of mixture. From the idealized viscosity of the neat first portion before mixture, the viscosity of the mixture measured immediately after mixture and the mass ratios of the portions, the idealized viscosity of the second portion was estimated through equation (4.23). The values estimated from the available experimental data are listed in Table 33. This further weakened the validity of the assumed linear combination relation.

Table 33 – Values estimated through linear combination for the initial viscosities of the second resin portions for the rheometry tests of SR®1500/SD®2505 mixed (blended) samples.

Test ID	Mixture Mass Ratio	Neat Cure Time Gap [s (min)]	Viscosity at gelation [Pa.s]	μ_1 before mix [Pa.s]	μ_{mix} [Pa.s]	μ_2 (calculated) [Pa.s]
SRHF1101	3:1	544 (9)	2.091	0.750	0.639	0.306
SRHF1102	2:1	536 (9)	2.639	0.750	0.720	0.661
SRHF1103	1:1	540 (9)	2.472	0.750	0.583	0.416
SRHF1104	1:2	565 (9)	2.858	0.750	0.520	0.404
SRHF1105	1:1	960 (15)	2.761	1.095	0.690	0.285
SRHF1106	1:1	1500 (25)	2.676	2.075	0.982	-0.112
SRHF1107	1:1	245 (4)	3.007	0.505	0.515	0.525

At the completion of the detailed analysis of the viscosimetry and rheometry results of the tests conducted on SR®1500/SD®2505 resin samples constituted by a mixture of two portions with different curing histories at near-to-room temperature, the following conclusions were established:

- the equation (3.40) showed to reasonably approximate the viscosity of the resin blend at the moment of mixture ($t \approx$cure time gap) for cure time gaps lower than 35% of the neat idealized gel time;
- the remaining rheological behaviour of the mixture (blend) after the mixture was a time-dependent combination of the two individual behaviours thus not describable through the proposed equation.

The option of using the linear combination mixing rule proposed in equation (3.40) was kept, however, due to the following reasons: (1) the behaviour of the mixture (blend) fitted within the two individual behaviour, i.e., it was describable through a combination (despite not linearly weighed nor independent of the mixing time); (2) the actual region between the two individual idealized behaviours was relatively small, i.e., the error of such linear combination would be always lower than if using one of the two ideal behaviours; (3) the typical processing conditions in wet FW imply very short delays in the deposition of adjacent layers; and (4) the practical impossibility of determining a precise model for the kinetics of the blend (upon and after mixing) did not allow to devise a precise rheological model in terms of $\mu(\alpha)$ which is the relevant relationship being used in the current process model.

4.2.4. Process Related Input Variables

Among all the FW process variables used in the model, a few relate exclusively to the physical winding setup. They typically consist of user controllable parameters. These are called process related inputs and include the fibre winding force, $F_{winding}$, the winding speed, $\dot{\beta}$, the winding angle, ϕ, the tow bandwidth, b, the mandrel radius, $r^{mandrel}$, the initial fibre volume fraction, V_0, and the processing (room) temperature, T^{pr}. Since a quasi-static condition is assumed through all the processing time, the winding speed is herewith replaced by the initial time, t_0, at which each layer is wound onto the mandrel (or the layers beneath).

A dedicated wet FW setup was developed and implemented in order to allow to measure the physical variables during the process. It was used in the series of winding trials that comprise the main part of the experimental programme. The setup is described in detail in section 4.3. Herewith the features associated with the process related inputs are, however, briefly addressed.

The winding force was controlled by a roving pre-tensioning device, shown in Figure 123. Each single roving passed through a slip-less double wheel system attached to a servo-motor with controlled binary. In this way, the tension of each roving at the remaining downstream of its path was known. In this experimental programme, similar tensions were required for every tow at each winding trial. The winding force accounted for in the model is the one actually verified at the mandrel reaching location, thus representing the “real” lay-up condition. Therefore, the winding force was firstly measured at the mandrel position for the different configurations of the whole winding setup in order to assess its value. These measurements were conducted using a portable dynamometer.

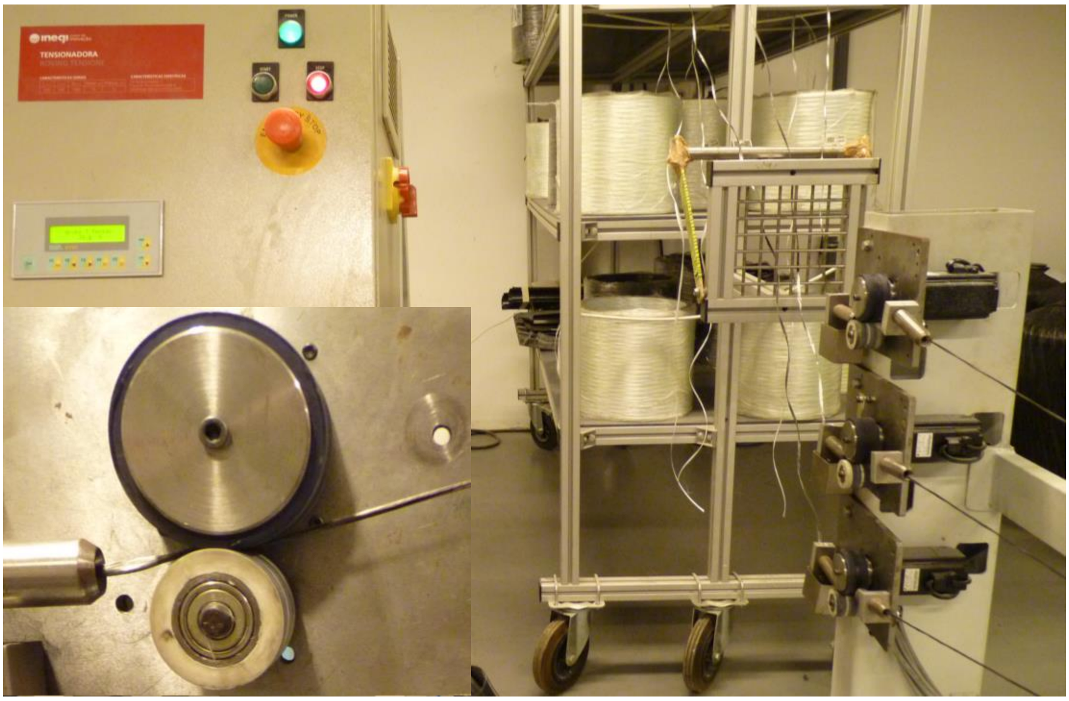

Figure 123 – Fibres tow pre-tensioning device based on a double wheel slip-less system (left bottom).

Although an ideal constant winding force would be desired through the entire FW process, it varies considerably in reality. This is observable in the majority of the industrial setups. In the setup used here, the winding force was directly influenced by three major aspects:

- The pre-tensioning device was only calibrated for static condition. It was verified that the effective dynamic tension in the rovings was different from the static one;
- The impregnation bath device (located between the pre-tensioner and the mandrel) introduced additional tension to the tows due to friction with several contact surfaces. Such friction was considerably dependent on the degree of impregnation (thus lubrication), i.e., the winding force and the initial fibre volume fraction varied in a coupled way;
- Greater winding speeds implied increased winding force.

The winding conditions used in the winding trials were settled, the pre-tensioning device was adjusted for balanced tension in the three rovings and the corresponding FW forces were measured at the mandrel position. Nevertheless, the winding force was measured at the beginning of each winding trial, assuring a better match with the real condition throughout the trial. In Table 34 the values of winding force used in the experiments and model validation are listed for all the winding conditions applied.

The initial fibre volume fraction was assessed through burn-off tests conducted on wet tow samples cut from immediately before the feeding delivery head. These samples were put into refractory crucibles and heated up to 615ºC (888 K) for 1.5 hours in a muffle as shown in Figure 124. The polymeric content was sublimated and the corresponding mass loss was registered. The burn-off tests were conducted accordingly with the standard ISO1172:1996 [253]. From the relative mass contents directly determined with this test procedure, the volume contents were calculated considering the densities of the resin and the fibres as $\rho^m = 1120.075\,kg\,m^{-3}$ and $\rho^f = 2540.000\,kg\,m^{-3}$, respectively. The values determined for each winding test condition are also listed in Table 34.

Table 34 – Winding forces and initial fibre volume contents measured and applied in the winding trials.

Winding Condition ID	No. of Specimens Wound	Winding Force [N]		Initial Fibre Volume Fraction [%]	
		AVG	STD	AVG	STD
FWC1	2	98.00	12.02	23.79	n/a
FWC2	2	102.00	12.02	35.12	n/a
FWC3	2	93.25	9.89	35.47	n/a
FWC4	1	110.00	14.14	58.32	n/a
FWC5	1	99.50	14.84	28.00	n/a
FWC6	2	150.00	15.70	23.79	n/a

The winding angle and the bandwidth were kept constant throughout the experimental programme. The former was predefined to be $\phi = 90^{\circ}$ (hoop winding) to keep the adjacent layers contact and interaction sufficiently easy to locate and analyse. Other angles would dramatically increase the complexity of the contact region and also inhomogeneous resin flow conditions throughout the spatial domain of each layer. The bandwidth was a function of the geometry of the delivery head and was set $b = 9mm$.

Figure 124 – Crucibles containing cured samples of impregnated fibre tows in the muffle oven before burn-off test start.

The mandrel used in the winding trials was a rectified aluminium tube with nominal inner and outer diameters of $130mm$ and $150mm$, respectively. In order to allow the wound specimens to be de-moulded, a slight conicity was drawn in the outer surface. Therefore, slightly different mandrel radius applied for different locations in which the specimens were manufactured and analysed. The range of inner radius registered for the several wound specimens is indicated in Table 35. The processing (room) temperature, T^{pr}, was registered and is also listed in Table 35 for all the wound specimens.

Table 35 – Inner reference (measured) radius of the wound specimens.

Wound Specimen ID	Inner Radius [mm]		Room Temperature [ºC (K)]	Wound Specimen ID	Inner Radius [mm]		Room Temperature [ºC (K)]
	AVG	STD			AVG	STD	
WS1	74.006	0.038	17.7 (291)	WS6	73.850	0.029	18.3 (292)
WS2	72.600	0.020	17.5 (291)	WS7	73.875	0.000	18.2 (291)
WS3	70.650	0.029	18.0 (291)	WS8	72.863	0.060	18.2 (291)
WS4	71.750	0.020	18.7 (292)	WS9	71.681	0.031	17.9 (291)
WS5	72.781	0.038	18.5 (292)	WS10	70.663	0.043	18.2 (291)

The winding speed was kept constant for all the wound specimens. Again, since a quasi-static condition was assumed throughout the winding process, the relevant parameter to register was the time at which each layer was wound. This time concurs with the resin cure sub-process and defines, therefore, its kinetic and rheological history (and remaining behaviour) in each region of the wound specimen. The average times for each layer to be wound (and then overwrapped by the following one) were 97s and 79s for the wound specimens WS1 and WS2, respectively and 68s for all the others.

4.2.5. Material Related Input Variables

Another group of input variables are related to the intrinsic nature of the material system being wound. The density, relative contents, geometry, physical distribution, storage conditions and/or thermochemical characteristics of the fibres and matrix have a direct and unique influence on those.

Upon establishment of the bandwidth, b, which is typically determined by the geometry of the delivery head in the FW setup, the thickness of the band is defined by the available cross-section of the tow being wound. The available cross-section is a function of the number of fibre filaments, their radius, r^f, and cross-sectional arrangement (packing) together with the resin in which the fibres are impregnated. In the winding trials, a fixed bandwidth of $b = 9\,mm$ and three tows with 4100 filaments each and $2400\,TEX$ (linear density in $g\,km^{-1}$) were used. The number of filaments was confirmed through the relations:

$$number\,of\;\,filaments = \frac{A^{tow}}{A^f}\;, \tag{4.24}$$

$$A^{tow} = \frac{TEX \times 10^{-6}}{\rho^f}\;, \tag{4.25}$$

where A^{tow} is the sum cross-sectional area of all the filaments contained in the (dry) tow, A^f is the cross-sectional area of each filament (fibre), TEX is the linear density ($g\,km^{-1}$) of the tow and ρ^f is the density of the fibres (E-glass fibres). Since $\rho^f = 2540\,kg\,m^{-3}$ and $TEX = 2400\,g\,km^{-1}$ the total area of the filaments in each tow was calculated as $A^{tow} = 9.4488 \times 10^{-7}\,m^2$. The number of filaments was determined to be 4163, which quite compares with the manufacturer's data.

The average diameter of each filament (fibre) was $17\,\mu m$, according to the manufacturer's data. This dimension was measured in the microscope setup (Figure 136) for several samples of fibres retrieved from the tows used and the value of $r^f = 8.5\,\mu m$ was confirmed and used onwards.

The initial thickness of the layers, t_0^l, being fed onto the mandrel (or previous layers) was only estimated since no adequate method was available for its reliable measurement. The reference values were computed from two idealized fibre packing patterns: the so-called square and hexagonal packing systems. Several researchers have studied these packing modes in the past [254,255]. More recently, the transversal cross-section arrangements of long-fibre reinforced composites have been modelled with random distributions [256,257] claiming good agreement with experimentally observed patterns and properties. The proper definition of the fibres neighbouring modes assume high relevance whenever precise representations are pursued. Despite all these studies focused on cured laminates, i.e., the only pattern effectively analysed was the one of the consolidated laminate, they provide interesting knowledge on how long-fibres typically accommodate to each other within a composite bundle. Herewith, the two classic patterns were considered, since they have shown to approximate reality reasonably well and are simpler to work with.

In Figure 125, the two patterns studied are schematically represented together with the representative section elements. Under such ideal maximum square or hexagonal packing conditions, the theoretical relative contents of fibres and matrix would be $V_f^{SQ\max} = 78.5\%$, $V_f^{HEX\max} = 90.7\%$ and $V_m^{SQ\max} = 21.5\%$, $V_m^{HEX\max} = 9.3\%$, respectively. These values were achieved through determination of the relative areas of fibre (grey) and resin (white) regions within the representative elements. The hexagonal packing system promotes higher compaction (thus higher fibre volume fraction, V_f) than the square system. This applies for the maximum packing condition and it shall also be observed whenever the resin content is higher than in such idealized condition.

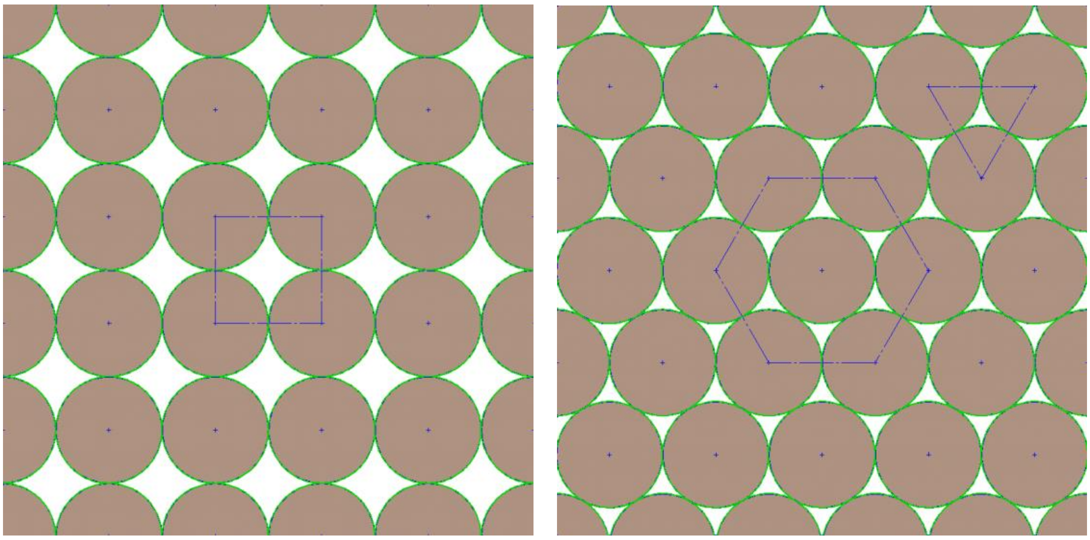

Figure 125 – Schematic cross-sectional views of idealized (maximum) packing arrangements for long-fibre composites: square packing (left) and hexagonal packing (right).

In real processing conditions, the impregnated fibre tow is fed with much greater resin content than the minimum values ($V_m^{SQ\max}$ and $V_m^{HEX\max}$) determined for the maximum packing conditions. From subtracting $V_m^{SQ\max}$ and $V_m^{HEX\max}$ to the effective resin content, V_m, the initial thicknesses of the layers, t_0^l, were estimated for square and hexagonal packing systems, respectively. The two relations between the layer thickness, t_0^l, and the initial fibre volume fraction, V_0, were finally devised as follows:

$$t_0^l = -1.2254\,V_0 + 2.1874 \;, \tag{4.26}$$

$$t_0^l = -1.1180\,V_0 + 1.8458 \;, \tag{4.27}$$

for the square and hexagonal packing assumptions, respectively. Using these relations, the estimated initial thicknesses for the layers being wound under the winding conditions applied in the winding trials were calculated and are listed in Table 36.

Table 36 – Estimated initial thickness of the layers for all the winding conditions.

Winding Condition ID	No. of Specimens Wound	Initial Fibre Volume Fraction [%]	Estimated Initial Layer Thickness [mm]		
			square packing	hexagonal packing	experimental measurements
FWC1	2	23.79	1.896	1.580	1.212
FWC2	2	35.12	1.757	1.453	1.204
FWC3	2	35.47	1.753	1.449	1.203
FWC4	1	58.32	1.473	1.194	1.105
FWC5	1	28.00	1.844	1.533	1.223
FWC6	2	23.79	1.896	1.580	1.053

The initial radial positions of each layer, r_0^{fs}, were then estimated from the sum of the thicknesses of the layers beneath. Despite the fact that the effective thickness of each of the n*th*-1 previous layers could not be assessed at the moment of deposition of the n*th* layer (all would be already compacting and resin outward flown) their added thicknesses fulfil a known value. However, this position was merely indicative and no precise calculations could be drawn from it. The eventual loss of resin during the winding (excess resin falling from the mandrel) and the fact that the layers were necessarily wound consecutively, rather than simultaneously, led to difficulties in assessing the initial radial positions of each layer.

Another material dependent input variable was the resin temperature, which was confirmed to be equal to the room temperatures (Table 35) at the time of first winding. The material temperature histories were also registered throughout the winding process. These were found to increase up to 24-27ºC (297-300K) as the thermo-chemical cure progressed. This temperature increase was considered negligible, since it was only a few degrees higher than the initial room temperature (around 18ºC) and occurred only after all layers were wound. An isothermal temperature condition was effectively observed, allowing to use the isothermal kinetic and rheological data as reference for the material state history.

4.2.6. Unmeasured Input Variables

As mentioned previously, certain process input variables were not measured nor assessed in this experimental programme, due to the unavailability of adequate resources. The initial radial position of the layers, r_0^{fs}, and the initial waviness ratio, L/a_0, are among those. The former was only estimated as explained in the previous section and the latter was virtually impossible to measure due to its inherent changing nature in both orientation and greatness. The elastic moduli of the fibres, E^f, and the elastic-apparent modulus of the resin, E^m, were not experimentally assessed as well. The fibre properties were, nevertheless, retrieved from the product data provided by the manufacturer.

A few other variables were not measured at their initial state, but only estimated or effectively assessed at their final state (upon cure/consolidation of the laminate) and will therefore be discussed in the following sections as output variables.

4.3. Experimental Validation of Model Output

In this section, the experimental setup designed and implemented to support the winding trials, allowing to evaluate the main process variables, is presented. Then, the experimental procedures conducted to assess the main variables governing each of the sub-processes are described. The experimental results are also presented and discussed in view of the process model validation.

4.3.1. Wet Filament Winding Monitoring Setup

Within the scope of conducting an experimental campaign that reproduced the FW process in all of its relevant features, a setup was developed that allowed both the advised production of wound laminate specimens and the measurement of the main process physical parameters. A setup based on the wet FW process configuration was thus implemented and is described hereafter.

The wet FW process setup is mainly divided into four functional blocks: the dry fibres creels/supply system, the impregnation bath, the delivery head and the mandrel.

The setup designed and implemented for the experimental validation of the FW process model intended to accomplish the main objective of allowing to control or assess the main process input parameters within adequate ranges. Additionally, certain variables were measured out of this physical setup, in external experimental procedures that will also be described hereafter.

The fibre creels/supply system used in the winding setup is depicted in Figure 126 together with the pre-tensioning system. Since inside-unwinding glass-fibre rovings were used in the experiments, and therefore loose tows were pulled downstream, an automated fibre pre-tensioning system was installed between the rovings stand and the resin impregnation bath. The pre-tensioner, based on a double wheel slip-less pass-through system, was earlier described in section 4.2.4. The three rovings used in each winding trial were individually pre-tensioned between 13 N and 25 N. The global winding force, $F_{winding}$, was the sum of the three individual tensions further added of the supplementary tension generated by the contact with the surfaces in the remaining setup at downstream of the pre-tensioner.

The second functional block was the resin impregnation bath. The system prepared within the setup is shown in Figure 127. It comprised two parallel paths for the fibre tows being impregnated. This feature allowed to impregnate different portions of the fibres being wound with different resin compositions. Using this facility, one specific layer was colourized differently in each wound specimen, in order to observe and measure its position and morphological changes. The transition between the two baths was processed manually by moving the fibre tows from one diving cylinder to the other aside.

Special attention was given to the colourizing conditions. Using adequate colourizing or pigments agents, thermosetting resins can remarkably change their appearance. Within this experimental campaign, three commercial colourizing agents were preliminarily tested to evaluate their applicability. A colourizing paste (high consistency and viscosity), a liquid colourizer and a powder pigment were evaluated. Similar resin samples were prepared with the different colourizers. In Figure 128 the neat and colourized resin samples are shown. The three different products were claimed compatible with epoxy-based compounds by their manufacturers.

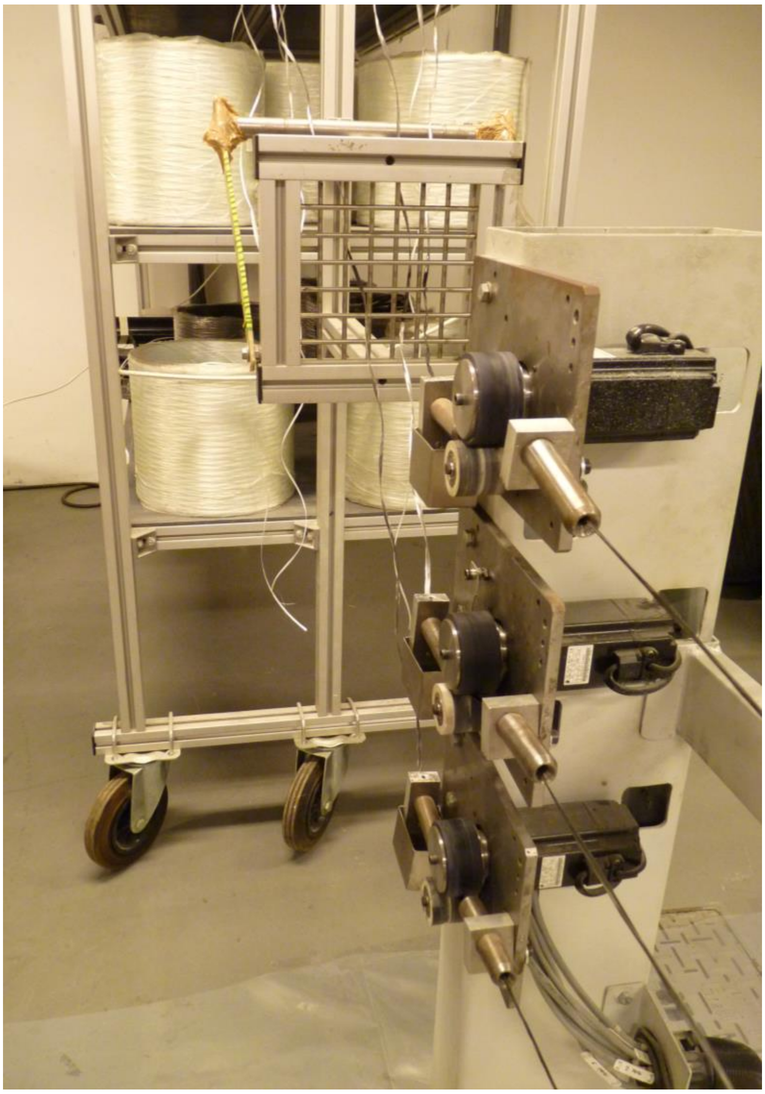

Figure 126 – Fibre roving stand and pre-tensioning system.

However, nearly no information exists on the influence of these agents in the thermo-chemical behaviour of the (curing) resin. The commercially available products typically claim their compatibility with specific chemical species (epoxy-based species, e.g.) but this is only related to the final mechanical properties and visual aspect. No studies were known addressing the inhibiting or accelerating effect that the colourizing agents have in the chemical reaction taking place in the host resin while and after their mixture.

Upon selection of the most suitable agent for the epoxy resin used in the winding trials, its influence on the cure behaviour was studied through viscosimetry tests conducted in a viscometer apparatus.

Figure 127 – Resin impregnation bath setup with double impregnation paths. Front (top) and top (bottom) views.

Figure 128 – Neat (left) and colourized resin samples. The black, blue and red samples correspond to the paste, liquid and powder colourizers, respectively.

Among the three pigmenting options, the liquid colourizer was selected due to its claimed compatibility with epoxy resins, better match in viscosity, less mass required and handling easiness. The universal dye Tintalac from Robbialac® was applied. Two epoxy resin samples of the SR®1500/SD®2505 epoxy system were prepared and tested in the viscometer. A reference sample was kept neat (uncolourized) and the other was colourized by adding the agent with a mixing ratio of 0.6% to the mass of resin. This ratio was chosen as it was considerably below the 3% limit indicated by the manufacturer and was observed to promote sufficient colour intensity, opacity and differentiation to the host material. As discussed previously, the mass and temperature conditions experienced by the resin samples in the viscosimetry tests are not fully representative of the real FW processing conditions. However, they provide relevant information on whether or not the added colourizing agent modified considerably the thermo-chemical behaviour of the epoxy system. The results of the two tests conducted are graphically presented in Figure 129. These respect to the early stages of the cure, up to the gelation. After this point, the viscometer was not able to measure the viscosity, since it increased rapidly and the motion of the rotating spindle was fastly affected. The two samples behaved similarly both in viscosity and temperature. The relative offset of the curves is actually within the error previously observed in the viscosimetry studies (section 4.2.2) conducted with this resin. This suggested that the influence of the colourizing agent in the cure behaviour of the resin system was negligible. Such assumption was enhanced by the facts that the effective mass ratio used to colourize the selected resin layer within each wound laminate was 0.2% (three times inferior to the ratio used in the viscosimetry tests) and that only one specific layer in each wound laminate had the altered resin.

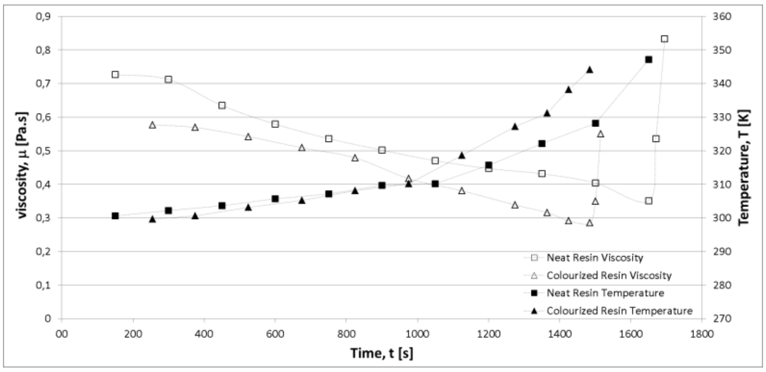

Figure 129 – Evolution of the viscosity and temperature in the neat and colourized resin samples (SR®1500/SD®2505) during the viscosimetry tests conducted at room temperature.

The main feature in the impregnation bath is the diving roller which grips resin from the container below and builds a resin film which impregnates the fibre tows contacting in the upper perimeter region. The chaotic and unpredictable nature of the resin film building phenomenon, forces one to append capability of homogenizing and controlling the amount of resin being seized and impregnating the fibre tows. Thus, the other relevant features in the resin impregnation bath system implemented were the scraper, the squeezing roller, the slalom shafts and the swinging bar. The function of the scrapper was to regulate the thickness of the resin film, thus the quantity of resin available to impregnate the fibre tows. The squeezing roller, on the other hand, was designed to promote better impregnation within each tow through their squeezing and spreading onto the resin and remove some excess resin. These two devices were adjusted and referenced in several discrete positions to correspond to different impregnation conditions. The main parameters under these winding conditions were measured and discussed in section 4.2.4. The slalom shafts further homogenized the resin distribution inside the tows. The swinging bar acted as a tension leveller since it absorbed certain unavoidable dynamic fluctuations in the winding force, $F_{winding}$, due to process velocity variations.

Following towards the mandrel, the impregnated fibre tows were guided through a converging eye and the delivery head as depicted in Figure 130. These components were solidary with the moving carriage of the FW machine. The converging eye brought the three fibre tows into one single fibre bundle. The very head was designed with two aligned eyes in which the latter defined the final bandwidth, b, of the fibre bundle being wound. This dimension was actually settled by the geometry of the delivery eye and its distance (and angle position) to the mandrel. Since these were fixed geometries, the fibre bandwidth was also kept constant throughout the winding trials.

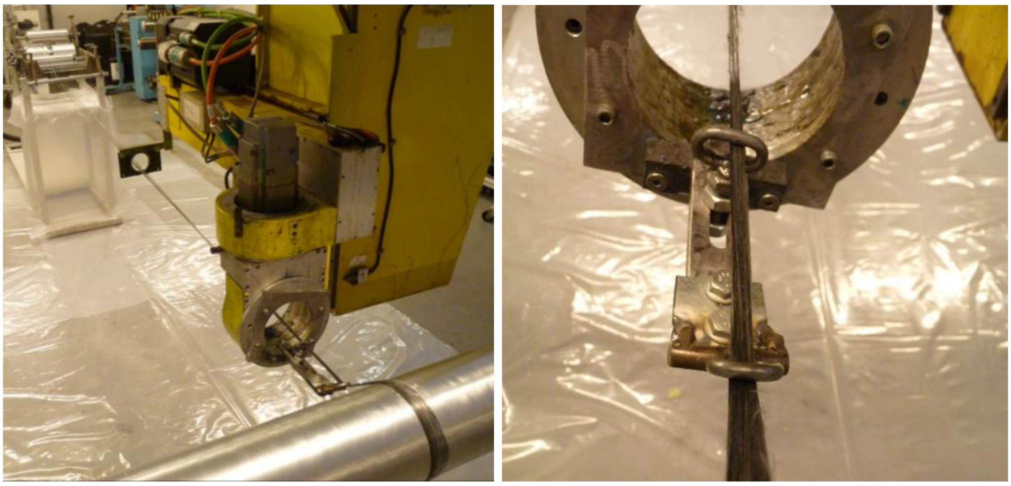

Figure 130 – Converging eye (left) and delivery head (right).

It is important to note that all the contacting surfaces that interfered with the fibre tows between the pre-tensioner and the mandrel altered significantly the effective winding force primarily generated at the former. For this reason, this physical quantity was measured at the mandrel lay-up position and not at any previous position in the setup (section 4.2.4).

The mandrel used was an aluminium cylinder with the characteristics detailed in section 4.2.4. An overview of its geometry is drawn in Figure 131. Its dimensions were defined based on the experimental requirements of a number of specimens to manufacture between each de-moulding operation and feasible handling of the wound specimens in the post-winding operations.

Figure 131 – Geometry of the mandrel and the de-moulding ring used in the winding trials.

The dedicated wet FW setup was built upon a specific automated 6-axis FW machine which supported the winding trials. The machine was a combination of a metallic frame and hardware motion structure manufactured by Pultrex® (United Kingdom) equipped with Siemens® (Germany) motors. The numerical control unit was a digital Siemens® Sinumerik® 840D that allowed the generation of the winding programs accomplishing the desired motions of the several axes to form specific winding paths. The overall FW setup is shown in Figure 132.

Figure 132 – Front (left) and back (right) views of the wet FW setup used in the winding trials.

An additional set of instruments was used to measure the temperatures in different locations of the laminates being laid-up. Namely, two thermocouples were placed in different layers as they were wound and connected to a digital thermometer (model 50D from Fluke), shown in Figure 133. Complimentary, an infrared camera setup was installed during the winding of two specimens to compare the temperature histories of the wound laminate and the same resin but without processing.

Figure 133 – Thermocouples (left) and infrared camera (right) used to measure the temperature evolution of the resin at the laminate and out of the laminate.

4.3.2. Radial Pressure

The radial pressure developed within the laminate during its cure and consolidation was not measured directly. This was mainly due to the following aspects:

- the morphology of the fibres and resin distribution within the laminate is quite complex and intrinsically changing with time;
- the pressure build-up inside the laminate is a quasi-static phenomenon;

- the pressure inside the laminate is shared by the fibres (fibres mechanical response) and the resin (hydrostatic pressure).

Thus, no sensor system was identified that could properly measure the pressure being developed inside the laminate. Such sensor system should be non-invasive so that it would not affect the fibres and resin sensitive distribution and it should be adequate to quasi-static measurements.

A monitoring system based on force sensing resistors (FSR®) was found nearly suitable. These sensors are composed of thin polymeric film where a conductive circuit is imprinted making it sensitive to force (or pressure) normal to its surface. The reduction of the electrical resistance is directly related with the force (or pressure) applied. These characteristics made it a candidate for the measurement of the pressure developed at the mandrel-composite interface. The other locations within the laminate (composite-composite interfaces) were always out of this possibility due to their tortuous and changing morphology. However, these sensors are only suitable for dynamic solicitations, since their relaxation does not allow to measure a quasi-static building of pressure. Moreover, complex signal conditioning and data-loggers are required for the useful application of these systems and this would hardly be feasible in a rotating platform as was the mandrel.

Nevertheless, the radial pressure, P^r, (also referred to as winding pressure, $p_{winding}$) was estimated from the knowledge of the winding force, $F_{winding}$, the initial and final radial positions of each layer, r_0^{fs}, and the bandwidth, b through the equations (3.2) and (3.6). The values obtained are presented in Figure 134 for all layers in the selected specimens with 16 and 20 layers ($MLayer = 16$ and $MLayer = 20$, respectively). The initial radial positions considered were those assessed from dividing the full thickness of the specimens (including the resin rich layer) by the number of layers. These were only approximated positions since an effective loss of resin (excess resin) occurred in most of the wound specimens and therefore the actual initial positions would slightly differ from these. Still, these pressure estimations represent a reasonable approximation to the effective magnitude of the radial pressures experienced at the laminate during the FW process.

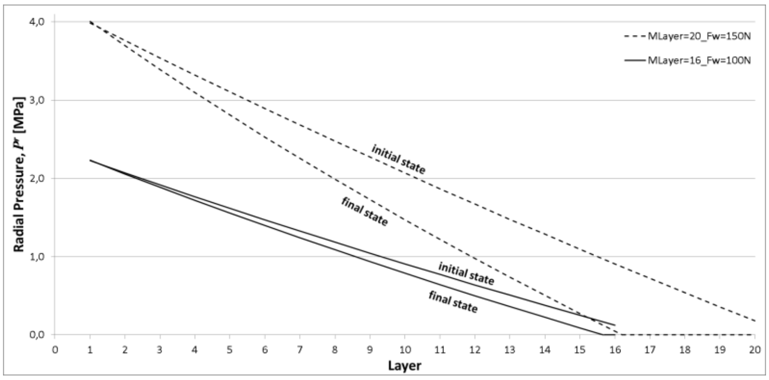

Figure 134 – Estimated radial pressure through-the-thickness of the wound specimens with total 16 and 20 layers for the initial and final winding states.

The values calculated for each layer corresponded to the pressure at its inner radius. Thus, the pressure for the first layer was actually the pressure at the mandrel-composite interface. This would be the sole value under consideration for experimental measurement when the FSR® sensing system was firstly sought.

4.3.3. Resin Flow

The resin flow was evaluated through the analysis of the final position (dispersion) of the resin belonging to a specific layer. In each wound specimen, a layer was previously selected to serve as a reference layer for later measurements. These particular layers distinguished from the others by having a different colour. Specifically, colourized resin (as discussed in section 4.3.1) was used to impregnate only the chosen layer.

The preparation of the surfaces to measure the layer's position was achieved in three steps. After cure, the wound specimens were cut and sanded at their mid-length section to allow to measure the main radial positions of the reference entities of this representative cross-section. The two operations were conducted using a band saw and a sander disc machines, respectively, and are depicted in Figure 135. In fact, since a ring was cut from each specimen due to easier handling and measurement in the remaining operations, two reference cross-sections were assessed from each specimen.

Figure 135 – Operations of transverse cutting of the wound specimens (left) and sanding of the cross-section surface (right).

In order to improve the identification of the different colours and reflectivity of the through-the-thickness entities, an additional polishing (fine sanding) was performed in each of the surfaces to be measured. This procedure is shown in Figure 136. Upon preparation of the surfaces, the ring specimens were individually placed onto a microscope setup for the accurate measurement of the positions of the colourized layer. Five locations were fully measured in each surface and therefore the averaged radial positions were taken. The measurement procedure is also depicted in Figure 136. For example, three adjacent photographs of a measuring location of one of the cross-sectional cuts are reproduced in Figure 137. These images show a colourized layer distinguishing from its vicinity which had the natural colour of the neat resin. The outward resin flow from this layer is captured by the colour gradient found at the outer region of the layer. A more detailed analysis allowed to observe the displacement of the colourized layer itself as well. Also, the overall resin rich layer (RRL) of the specimens could be identified in the outermost region of each measured section. Colour treatment of these photographs, for colour identification and/or contrast, would eventually add greater perception ability to the measuring section. This was not realized, however, and the results were directly retrieved from these observations.

Figure 136 – Polishing of the cross-section surface to enhance its readability (left) and microscopy measuring setup (right).

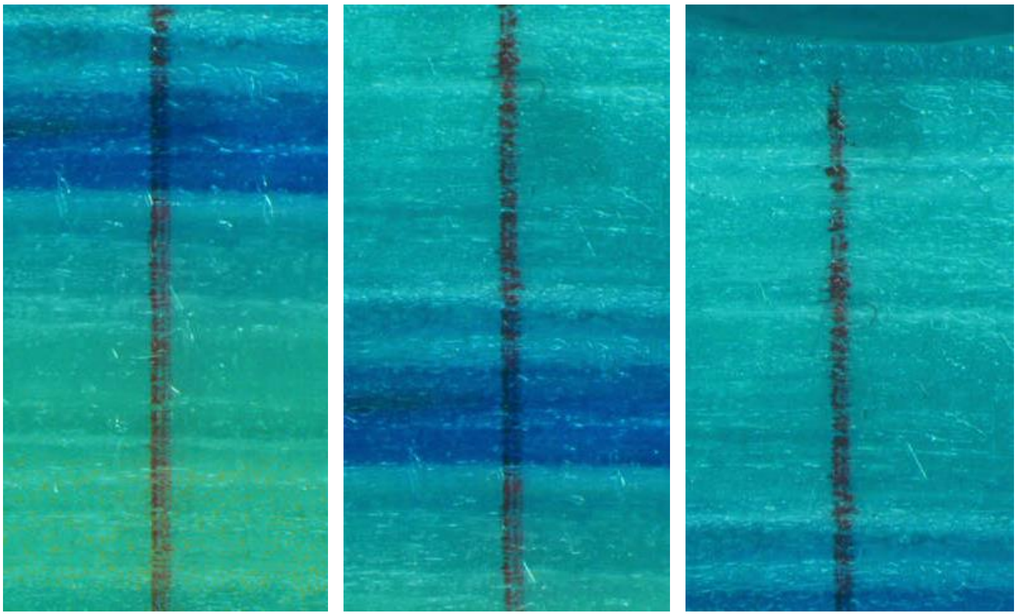

Figure 137 – Cross-sectional views of a wound specimen with one layer highlighted by its blue colourized resin. The inner (left), middle (middle) and outer (right) regions are individually shown.

The extent of resin radial flow was assessed from the measurements of the colour gradient observable at the outer radius of the colourized layer. The distance flowed by the resin initially contained in the colourized layer was firstly established as the radial distance between the outer end of the intense blue region (supposed the effective outer radius of the colourized layer) and the outer end of the blue colour gradient. The values obtained were then corrected with the knowledge of the effective average thickness of each layer within the laminate. It was noticed that the final effective outer radius of the colourized layer was smaller than the one perceived in all measurements. This meant that the outward resin flow in the vicinity of the original layer was intense. The decrease in colour intensity was only perceptible from a slightly greater radius. The results are summarized in Table 37 for all the wound specimens. Then, the radial flow distance is graphically plotted against the main process variables able to affect it, namely the winding force, $F_{winding}$, the input fibre volume fraction, V_0, the total number of layers wound, $MLayer$, and the relative through-the-thickness position of the colourized layer. Despite the scatter of the experimental measurements, the trends of the dependence of the resin flow with these process variables were possible to identify and are also plotted.

Table 37 – Inner reference (measured) radius of the wound specimens.

Wound Specimen ID	Total Thickness [mm]	Colourized Layer / No. of Layers	Outward Resin Flow Distance [mm]			Wound Specimen ID	Total Thickness [mm]	Colourized Layer / No. of Layers	Outward Resin Flow Distance [mm]		
			measured		corrected				measured		corrected
			AVG	STD	AVG				AVG	STD	AVG
WS1	20.278	11/20	1.298	53%	1.881	WS6	18.542	10/16	1.415	59%	1.914
WS2	18.469	10/16	1.417	33%	2.350	WS7	18.919	6/16	1.155	69%	2.669
WS3	18.630	10/16	1.549	29%	2.590	WS8	17.686	6/16	1.050	37%	1.482
WS4	19.042	10/16	1.731	14%	3.514	WS9	n/a	6/17	n/a	n/a	n/a
WS5	18.587	10/16	1.036	46%	1.699	WS10	19.214	6/16	1.184	16%	2.381

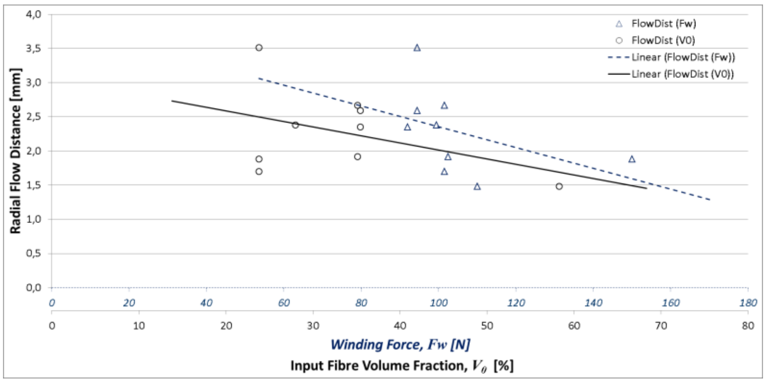

Figure 138 – Outward radial resin flow distance *versus* the winding force and the input fibre volume fraction.

Using the equation (2.17) the indicative permeability of the fibre bed was calculated for each wound specimen. Both the initial and final known values of the fibre volume content, V_0 and V_f, were used and therefore the experimental ranges were determined for the entire processing period. In Table 38 the lower, upper and averaged permeabilities are listed together with the values of the parameters used to compute them. For better understanding, the experimental permeability ranges are plotted in Figure 140 for all the wound specimens. Effectively, the values assessed from the final state data (lower limit) present lower variance due to the fact that the ultimate (final) fibre volume fraction observed in all the specimens was very similar. On the contrary, the data from the initial state promoted wider variance due to the varied input conditions. This was intuitively correct as it corresponded to the expected behaviour.

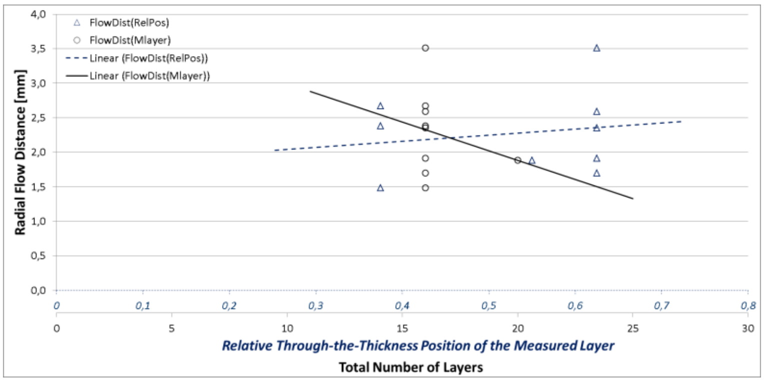

Figure 139 – Outward radial resin flow distance *versus* the relative through-the-thickness position of the measured layer and the total number of layers wound.

Table 38 – Initial and final permeabilities assessed experimentally for the wound specimens.

Wound Specimen ID	V_0 [%]	Final V_f [%]	Permeability [mm^2]			Wound Specimen ID	V_0 [%]	Final V_f [%]	Permeability [mm2]		
			initial	final	AVG				initial	final	AVG
WS1	24	58	1.14×10^{-5}	1.55×10^{-7}	5.79×10^{-6}	WS6	35	53	3.39×10^{-6}	3.79×10^{-7}	1.88×10^{-6}
WS2	35	54	3.26×10^{-6}	3.38×10^{-7}	1.80×10^{-6}	WS7	35	52	3.39×10^{-6}	4.38×10^{-7}	1.91×10^{-6}
WS3	35	53	3.26×10^{-6}	3.79×10^{-7}	1.82×10^{-6}	WS8	58	66	1.58×10^{-7}	2.75×10^{-8}	9.29×10^{-8}
WS4	24	53	1.14×10^{-5}	3.82×10^{-7}	5.91×10^{-6}	WS9	n/a	n/a	n/a	n/a	n/a
WS5	24	54	1.14×10^{-5}	3.32×10^{-7}	5.88×10^{-6}	WS10	28	51	7.28×10^{-6}	5.08×10^{-7}	3.90×10^{-6}

Common parameters		
Modified maximum fibre volume fraction at which flow stops, V'_a [%]	78.5	$S = \frac{{r^f}^2}{4k'} \frac{\left(\frac{\sqrt{V'_a}}{\sqrt{V_f}} - 1 \right)^3}{\frac{V'_a}{V_f} + 1}$
Modified Kozeny's constant, k'	0.2	
Radius of the fibres, r^f [mm]	8.5×10^{-3}	

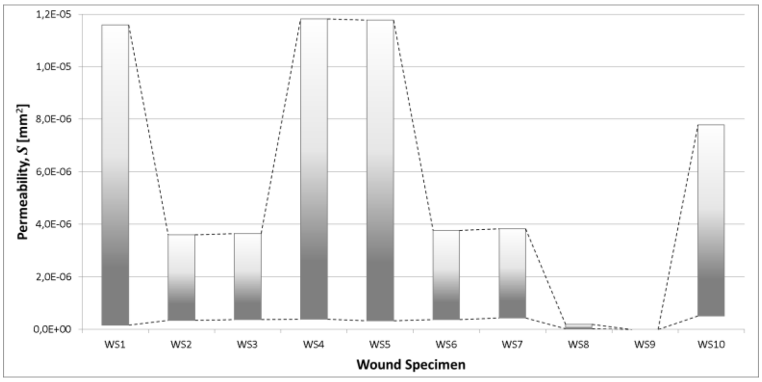

Figure 140 – Permeability ranges assessed experimentally for each wound specimen.

In Figure 141, the averaged permeabilities are plotted as a function of the winding force, $F_{winding}$, the input (initial) fibre volume fraction, V_0, and the output (final) fibre volume fraction, V_f. The exponential fittings in the case of V_0 and V_f dependences presented a quite reasonable qualitative behaviour. Indeed, the permeability is virtually null at the reaching of very high fibre volume contents (low resin content). Such value surely fits between the maximum fibre volume fraction experimentally observed, $V_f = 66\%$, and the theoretical maximum for the packing system assumed, $V_a = 78.5\%$ and $V_a = 90.7\%$ for square and hexagonal packings, respectively.

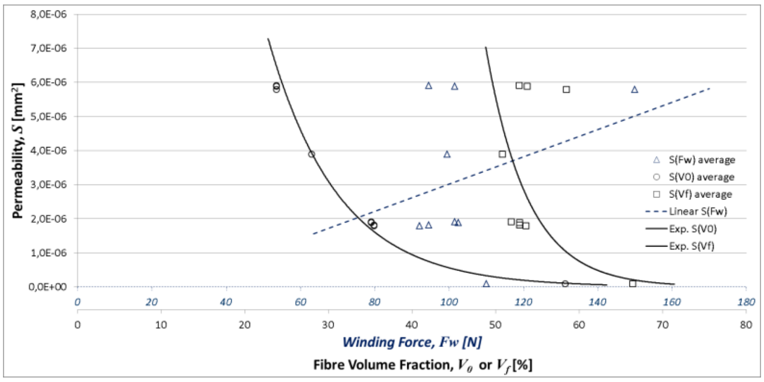

Figure 141 – Plots of average permeability *versus* winding force, input and output fibre volume contents.

Looking at the trends, the two exponential fittings, with initial and final conditions, seemed to correspond respectively to the lower and upper limits of this expected behaviour. The dependence of the permeability on the winding force, on the other hand, did not show a clear trend. Despite the fact that the linear fitting shows a positive slope, it was based on excessively scattered data series, allowing not to retrieve a clear conclusion.

4.3.4. Compaction of the Laminate

The main effect of the resin outward flow from each layer during the FW process is their compaction. This phenomenon consists in the reduction of the effective thickness of the layers and therefore an increase of the relative content of fibres. This is achieved through the overall migration of resin from the inner to the outer regions of the cylinder laminate.

In the winding trials, the initial thickness of each layer being wound was merely estimated, since no feasible means were available for its precise measurement. On the other hand, the final thickness was measured in the cured ring sample extracted from each wound specimen using the operations presented in section 4.3.1. Thus, the variation of the radial position of each layer was experimentally assessed and is registered in Table 39. As expected, greater initial layer thickness resulted in greater relative reduction during the winding process. In fact, as the final thicknesses were quite similar for all specimens, the differences in the initial ones were “corrected” through outward flow of resin. Greater initial resin content generally promoted greater reduction of the layer thickness up to a nearly converging value. Nevertheless, whenever the winding force changed significantly these conditions changed as well. Greater winding forces also promote greater reduction of layer thickness, since increased pressure gradients were formed and thus greater resin outward flow was observed. These tendencies are shown in Figure 142.

Table 39 – Averaged layer thickness variations and resin rich layer content for all wound specimens.

	Initial Thickness, r_0^l [mm]	Final Thickness, r^l [mm]	Thickness Variation [mm]	Relative Thickness Variation [%]	Thickness of Resin Rich Layer [mm]	Relative Volume of Resin Rich Layer [%]
WS1	1.580	1.014	-0.566	-35.82	0.777	4.31
WS2	1.449	1.154	-0.295	-20.36	0.722	4.37
WS3	1.449	1.164	-0.285	-19.67	0.685	4.12
WS4	1.580	1.190	-0.390	-24.68	0.664	3.91
WS5	1.580	1.162	-0.418	-26.46	0.498	2.99
WS6	1.453	1.159	-0.294	-20.23	0.573	3.44
WS7	1.453	1.182	-0.271	-18.65	0.403	2.97
WS8	1.194	1.105	-0.089	-7.45	0.000	0.00
WS9	(1.007)	n/a	n/a	n/a	0.000	0.00
WS10	1.533	1.201	-0.332	-21.66	0.349	2.04

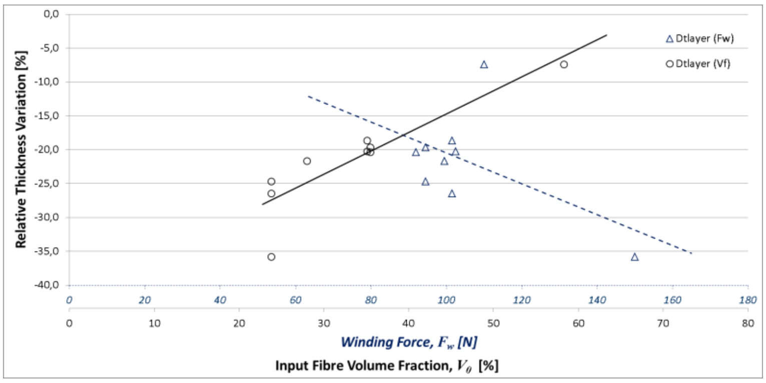

Figure 142 – Plots of relative layer thickness variations *versus* winding force and input fibre volume content.

As the laminates compact, during the winding and consolidation processes, the resin is successively transferred outwards throughout the layers and ultimately squeezed to the outermost region of the cylinder. In this region, the resin rich layer is formed. It is then intuitive that if greater compaction of the generic layers is promoted, more resin will be squeezed up to this outer resin rich layer. This behaviour was observed in the experiments and is highlighted in Figure 143 as a function of the winding force. In the same chart, the dependency of these two thicknesses (generic and resin rich layers) on the initial fibre volume content is also plotted but no matching behaviour was found. These data showed, however, that above a certain value of fibre relative content there was not sufficient resin being squeezed to form a resin rich layer. This results was intuitively correct as well.

Despite the intrinsic relationship between the quantity of resin lost by the layers compacted and the resin available in the resin rich layer, the latter presented an apparent maximum that could distort such analysis. In fact, when computing the relative fraction of resin rich layer over the total laminate (retrieved from thickness of RRL over total laminate thickness) it was noticed that a maximum value of around 4.4% was several times achieved but never overpassed. This was related with the effective loss of excess resin, which was consistently observed during the winding trials. Due to the liquid-viscous nature of the resin during the winding process, a limited quantity was able to be kept in the outermost perimeter of the rotating mandrel and laminate. This evidence is graphically represented in Figure 144. Between the two extreme conditions – no enough resin to form a RRL or a maximum amount of resin able to sustain in rotating surface – the dependence of this amount on the winding force and initial fibre volume content was unclear.

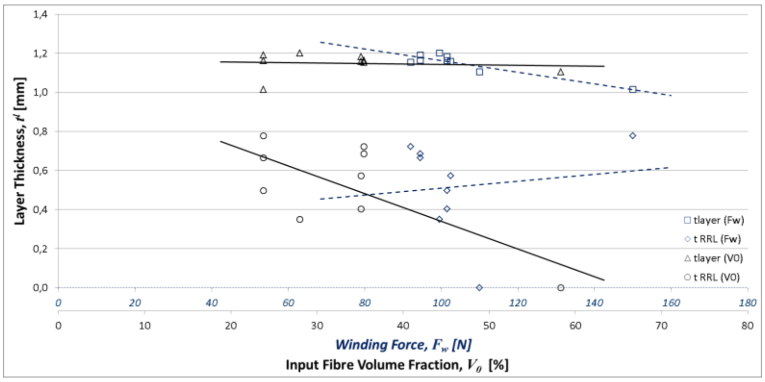

Figure 143 – Plots of the final thickness of the generic and resin rich layers *versus* winding force and input fibre volume content.

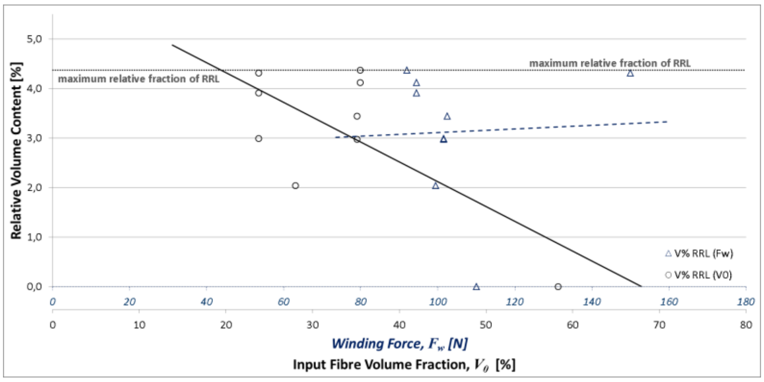

Figure 144 – Plots of the final relative fraction of RRL over the entire laminate *versus* winding force and input fibre volume content.

A natural consequence of the resin outflow from each layer is the ability of the layers above it to approach its radial position through the outflowing resin. The resin invades the new layer while its fibres encounter the ones below. This compaction phenomenon is traduced into an effective displacement of the layers. The initial radial positions of each layer were estimated and their final positions were measured. The former correspond to the hypothetical positioning of each and every layer in the moment of delivery onto the mandrel (or previous layers) if one assume that all layers were simultaneously wound. In reality, since the layers are successively wound with time delays between consecutive layers, by the time of deposition of a certain layer the ones beneath had already early progressed in their own compaction process. In addition, part of the excess resin generated at the compaction of the layers beneath might already been lost. Therefore, the actual initial radial position of each layer accounted with the previous compaction and resin flow from its preceding layers. Depending on the winding conditions, this can be negligible in face of the total compaction time and process. In the absence of the actual values accounting for these phenomena, the assumption of a simultaneous deposition of layers was used. The values estimated and measured are listed in Table 40 for certain wound specimens and layers as for reference. Again, as expected, greater displacements were achieved in the specimens with more favourable winding conditions, namely higher winding force and initial resin content (lower fibre content).

Table 40 – Displacement of the layers within the wound specimens from their initial to final radial position.

Specimen	WS1		WS2		WS8		WS10	
Layer	Initial Radial Position, r_0^{fs} [mm]	Final Radial Position, r^{fs} [mm]	Initial Radial Position, r_0^{fs} [mm]	Final Radial Position, r^{fs} [mm]	Initial Radial Position, r_0^{fs} [mm]	Final Radial Position, r^{fs} [mm]	Initial Radial Position, r_0^{fs} [mm]	Final Radial Position, r^{fs} [mm]
Layer 1	74.006		72.600		72.863		70.663	
Layer 2	75.902	75.020	74.353	73.754	74.335	73.968	71.885	71.863
Layer 6	83.486	79.076	81.364	78.371	80.226	78.390	76.776	76.667
Layer 10	91.069	83.131	88.375	82.989	86.117	82.811	81.667	81.470
Layer 11	92.965	84.145	90.128	84.143	87.590	83.917	82.890	82.671
Layer 16	102.440	89.215	98.891	89.914	94.954	89.444	89.003	88.675
Layer 20	110.030	93.271	105.900	n/a	n/a	n/a	n/a	n/a

4.3.5. Relative Phases Content

The variation of the relative contents of the two phases composing the composite laminate, fibres and resin, is a consequence of the resin outflow and the fibre bed compaction. Although the initial conditions in which the impregnated tows are fed onto the mandrel affects the history of this parameter, the fact is that the two phases within the laminate tend to an equilibrium that is mainly function of other process parameters such as the winding force and/or mandrel radius, the winding speed, the resin viscosity and the number of layers.

The input (initial) fibre volume fractions were measured through burn-off tests as described in section 4.2.4. The output (final) ones were measured using the same experimental procedure, but on material samples collected from the cured wound specimens.

Three material samples weighing between 3 and 6 g were measured to obtain the averaged overall fibre mass/volume content in each wound specimen. Since a through-the-thickness pressure gradient was developed in the laminates as the layers were successively wound, different resin flow rates and thus different relative contents could be achieved along the thickness. In order to assess this result additional material samples were extracted from the inner, middle and outer regions of the specimens thickness. The outer samples nearly corresponded to the two outermost layers, including the resin rich layer whenever present. The results obtained are summarized in Table 41. The experimental values for the overall fibre content (full thickness) are plotted in Figure 145 and show the expected increasing tendency with both the winding force, $F_{winding}$, and input fibre volume content, V_0.

Table 41 – Final fibre volume contents measured in the wound specimens.

Wound Specimen ID	Winding Force [N]	Initial Fibre Volume Fraction [%]	Final Fibre Volume Fraction [%]							
			Full Thickness		Inner Layers		Middle Layers		Outer Layers	
			AVG	STD	AVG	STD	AVG	STD	AVG	STD
WS1	150.0	23.79	58.44	0.61	58.84	0.68	57.75	2.24	52.07	1.25
WS2	92.0	35.47	53.65	0.05	51.36	0.23	55.43	n/a	51.26	0.28
WS3	94.5	35.47	52.88	0.56	52.73	0.64	54.23	0.08	44.78	1.05
WS4	94.5	23.79	52.83	0.67	51.21	0.46	55.55	0.53	46.95	0.13
WS5	101.5	23.79	53.76	0.28	51.17	0.45	55.30	0.28	49.47	0.90
WS6	102.5	35.12	52.87	0.24	48.87	0.17	53.31	0.15	50.18	2.91
WS7	101.5	35.12	51.87	0.52	49.30	1.12	52.45	0.87	50.06	0.77
WS8	110.0	58.32	66.41	1.13	n/a	n/a	n/a	n/a	n/a	n/a
WS9	83.5	n/a	n/a	n/a	n/a	n/a	n/a	n/a	n/a	n/a
WS10	99.5	28.00	50.82	1.07	47.30	0.42	53.23	0.80	44.93	2.62

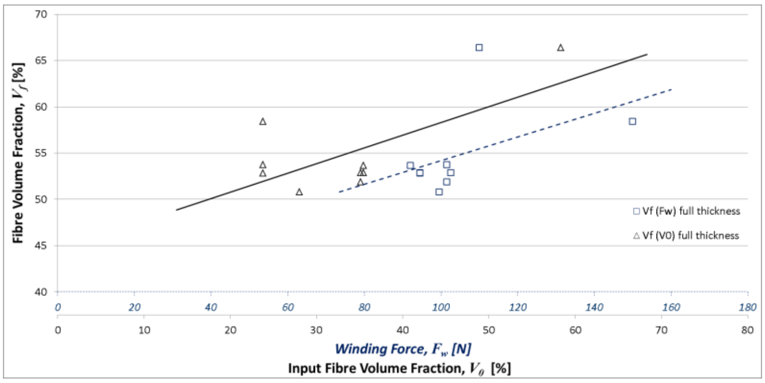

Figure 145 – Plots of the overall final fibre volume fraction *versus* winding force and input fibre volume content.

The through-the-thickness variation of the relative contents is plotted twice for better perception. In Figure 146 the overall, inner, middle and outer fibre volume fractions are displayed for each wound specimen. Here, one may observe that the outer layers presented consistently lower relative fibre content (higher resin content), which was mainly due to the presence of a resin rich layer. Unexpectedly, however, in some specimens the inner layers presented lower fibre volume fraction than in the neighbouring region (middle). This is also observable in Figure 147, where the data is plotted against the winding force and initial fibre volume fraction. When analysing the dependence on the winding force, it becomes clear that the unexpected behaviour in the inner layers occurred only for lower winding forces. Still, this was unexpected.

Due to the limited number of specimens wound, all with nearly the same number of layers (16), no analysis was produced on the dependence of the final fibre volume fraction on the number of layers. This analysis would, in any case, strongly depend on other winding conditions, such as the winding speed, since this clearly would affect the ability of the layers to out-squeeze the excess resin before new layers were added to the winding laminate.

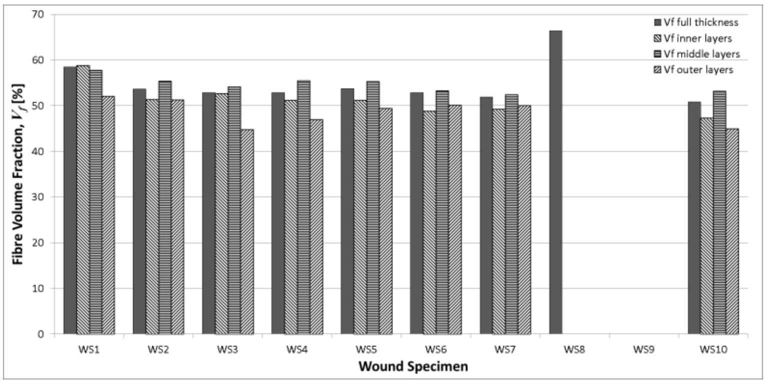

Figure 146 – Plots of the overall, inner, middle and outer (from left to right columns) fibre volume fraction for all the wound specimens.

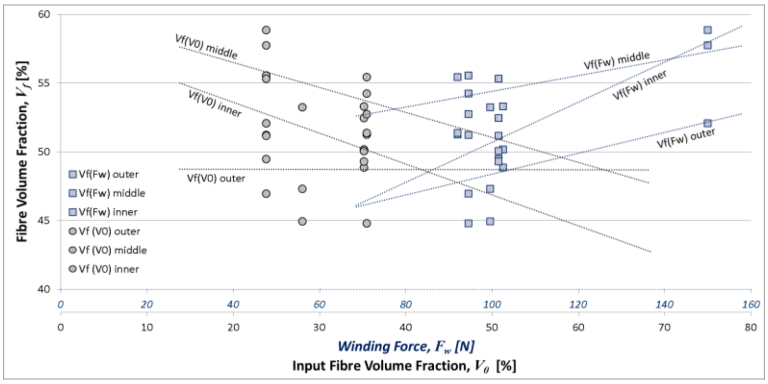

Figure 147 – Plots of the inner, middle and outer fibre volume fractions *versus* winding force and input fibre content.

4.3.6. Resin Mixing

The resin mixing is a very particular characteristic of the FW process. In fact, it is negligible in most composite manufacturing processes. In the FW process, however, it may significantly affect the final morphology of the laminate due to the incremental nature of the winding procedure. Whenever the winding time is comparable to the thermochemical cure of the resin, its influence is widened to the ability of the resin to flow throughout the newly wound layers and therefore the laminate's compaction is affected.

In the winding trials conducted herewith, the overall winding time was a reasonably high fraction of the gelation time of the thermosetting resin used. This meant that at the final stages of the winding procedure, the resin viscosity was different from the early stages. However, no evidence of relevant changes in the flowing ability during the winding stage was observed during the trials.

In section 4.2.3 the resin mixing rheological behaviour was extensively treated upon the rheometry tests conducted on resin samples. Hereafter, the effective extension of the resins mixing between adjacent layers is discussed upon the measurements of the wound specimens.

From the flow distance measured for the colourized layers and the layers final thickness, an estimative of the number of adjacent layers crossed (trespassed) by the resin of the colourized layer was drawn. The dependences on the winding force, $F_{winding}$, initial fibre volume fraction, V_0, total number of layers wound, $MLayer$, and relative through-the-thickness position of the measured layer are plotted hereafter. The limited range of winding conditions enforced, together with the significant scatter in the data does not allow to conclude on the trends. Nevertheless, in most cases the number of adjacent layers being affected by the resin flow was approximately 2 and this value was shown to fit within 1 and 3. Therefore, the order of magnitude of adjacent layers being affected with resin mixing was experimentally assessed with these data.

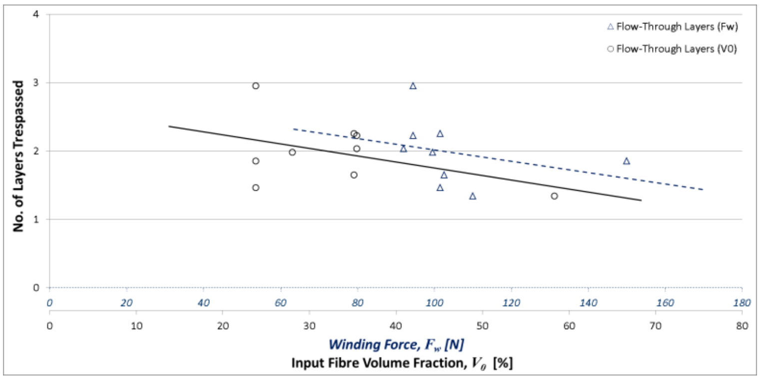

Figure 148 – Plots of the number of layers flowed-through as functions of the winding force and input fibre content.

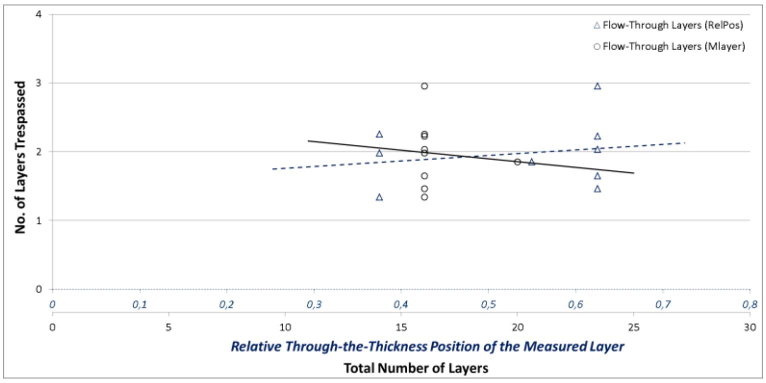

Figure 149 – Plots of the number of layers flow-through as functions of the relative through-the-thickness position of the measured layer and the total number of layers wound.

The experimental procedure did not allow, however, to evaluate precisely the quantity of resin transferred from one layer to the others. It allowed only to assess the ultimate flow distance and thus the number of layers crossed by. Upon several limiting assumptions, the gradient of resin content from a certain *j*th layer into the *j*th+1, *j*th+2, … layers could be computed. This is treated at the comparison with the model results.

4.3.7. Fibre Waviness

Upon observation of the cross-sections of the wound specimens a few waviness defects were identified. Specifically, two types of waved patterns were found: isolated waviness spot and circumferentially-oriented semi-continuous patterns. Both patterns were co-existing in several specimens and they were characterized through measuring the typical wave length, L, and amplitude, a, thus calculating the typical waviness ratio, L/a. These data are presented in Table 42. The two relevant assessments provided with these experimental data were that the typical waviness ratio was of the order of $L/a = 20$ and that whenever higher winding forces and/or relative fibre content were applied, no waviness defects were visible in the cured specimens. These results tend to support the thesis that the waviness is a process-related phenomenon. In other words, it is promoted by the processing conditions during the winding operation rather than by the eventual fibre tension release upon completion of the winding stage.

Table 42 – Waviness measurements on the wound specimens.

Wound Specimen ID	Visible Waviness	Location	Waviness Pattern					
			length, L		amplitude, a		ratio, L/a	
			AVG	STD	AVG	STD	AVG	STD
WS1	no	n/a	n/a					
WS2	yes	mid outer	15.258	0.337	0.949	0.391	17.500	6.860
WS3	yes	mid outer	12.751	0.526	0.482	0.515	62.922	68.292
WS4	yes	mid outer	9.803	0.023	0.614	0.247	17.368	6.963
WS5	no	n/a	n/a					
WS6	yes	mid outer	10.953	0.604	0.456	0.079	24.271	2.891
WS7	yes	outer	9.098	0.644	0.473	0.343	25.467	17.121
WS8	no	n/a	n/a					
WS9	n/a	n/a	n/a					
WS10	yes	mid inner	10.705	1.856	0.589	0.150	19.129	5.998

4.4. Remarks

The experimental results achieved gathered extensive and reliable sets of data. These results globally show the ability to measure most of the main process parameters and variables. Such level of integration of procedures, covering a wide range of physical phenomena, from chemo-rheological to mechanical interactions, was not made aware of by prior authors or publications. Therefore, it substantiates, itself, increments to the actual state of the art regarding FW and even correlated manufacturing processes.

However, these results *per se*, do not validate the process model under analysis. With this aim, a numerical code was devised and several simulations were run, in an attempt to reproduce pre-selected experimental conditions. This is fully addressed in next chapter.

CHAPTER 5

NUMERICAL IMPLEMENTATION AND VALIDATION

5.1. Objectives and Methods

Due to the multi-physical nature of the FW process model developed in this work, it accounts for various inter-dependent analytical descriptions of physical phenomena. The inter-dependence arises from the effective coupling of the different sub-processes modelled by the referred descriptions. Despite the analytical modelling methodology applied was based on the modular and decoupled study and description of every particular phenomenon, their real behaviour is obviously coupled by sharing common variables. Therefore, a numerical code incorporating discretized formulations of the several phenomena was devised to allow simulating the global process with incremental evolutions of the variables through their flow and exchange between related sub-models.

The discretization of the differential equations was mostly achieved by backwards or forwards finite-difference schemes, accordingly with the domain and the available data for each specific case. Both spatial and temporal discretizations were operated.

The numerical code built upon these discrete formulations of each physical phenomenon was structured with as many sub-routines as the sub-models earlier presented in chapter 3. A root main routine was responsible for the variables flow between the called sub-routines, as well as for the necessary external updates and formal actions from the programming view point.

In the following sections the discretization of the main analytical equations and the overall numerical model scheme are described. Also, sensitivity and compatibility tests conducted to analyse the modelling abilities of the written code are presented. Finally, full winding conditions were simulated and the results for the main process variables were compared with the experimental ones. This last analysis intended to evaluate the overall validity of the FW process model developed.

5.2. Discretization of the Analytical Descriptions

Herewith, the discretizations in the time and/or spatial variables of the analytical formulations developed are presented. For the analytical equations not explicitly depending on time and/or spatial variables, as well as those of non-differential form, no specific discretization procedure was implemented. Only the analytical descriptions requiring translation to algebraic formulation are treated hereafter. In each sub-process, highlight is given to the fundamental equations.

5.2.1. Resin Flow Sub-Model

The resin flow modelling was set upon the Darcy's type equation, and is substantiated in equation (2.11). It was discretized and numerically implemented in the form:

$$\frac{\Delta u}{\Delta t} = -\frac{S}{\mu}\frac{\Delta p}{\Delta r} \ , \tag{5.1}$$

where Δu is the radial distance flown by the resin during the time increment Δt, Δp is the pressure spatial gradient in the radial position interval Δr and S and μ are the permeability of the fibre bed and the resin viscosity, respectively. For the *j*th layer, the incremental discrete formulation to calculate the updated position in instant $t + \Delta t$ is:

$$u_{t+\Delta t}^{j} = u_t^{j} - \frac{S^j}{\mu^j}\frac{p_t^{j+1} - p_t^{j}}{r_t^{j+1} - r_t^{j}}\Delta t \ , \tag{5.2}$$

where the subscripts and superscripts refer to time and layer, respectively.

5.2.2. Fibre Bed Compaction Sub-Model

The main equation settling the compaction of the fibre sheet is equation (3.9) which was discretized for the *j*th layer, similarly to the above equation, into:

$$u_{t+\Delta t}^{j} = u_t^{j} - \frac{S^j}{\mu^j}\frac{\sigma_{11}^{f\,j}}{r^{fs\,j}}\sin^2\phi^j\,\Delta t \ , \tag{5.3}$$

where σ_{11}^{f} is the fibre's stress in the local on-axis longitudinal direction, r^{fs} is the radial position of the fibre sheet and ϕ is the winding angle. As in the previous equation, the subscripts and superscripts refer to time and layer, respectively.

5.2.3. Heat Transfer Sub-Model

The one-dimensional heat transfer, defined in equation (2.26) was used to calculate the temperature, T , in the following algebraic form:

$$T_{t+\Delta t}^{j} = T_{t}^{j} + \frac{1}{\rho C}\left[\frac{k_r{}^{j}}{r^{j}}\frac{T^{j+1} - 2T^{j} + T^{j-1}}{\left(r^{j+1} - r^{j}\right)^{2}} + \rho^{m}\dot{Q}\right]\Delta t \ , \tag{5.4}$$

where r is the radial position, ρ and ρ^m are is the densities of the composite and resin, respectively, C is the specific heat of the composite, k_r is the thermal conductivity in radial direction and $\dot{Q}$ is the rate at which heat is generated by the curing or crystallizing resin. A central finite-difference scheme was used to discretize the 2nd order spatial derivative of the temperature.

The term $\rho^m\dot{Q}$ was defined in equations (2.27) and (2.32) which contain time-differential 1st order derivatives. These are, however, specifically treated in the following section.

5.2.4. Resin Cure/Crystallization Sub-Model

The kinetic behaviour of the resins was modelled through analytical descriptions of the types indicated in equations (3.53) and (3.54). The derivatives of the degree of cure, $d\alpha/dt$, or crystallization, dc/dt, are explicit functions of the degree of cure, α, or degree of crystallization, c, respectively, and temperature, T. For the discretization and calculation of the updated α or c the following formulations were set:

$$\alpha_{t+\Delta t} = \alpha_t + f(\alpha_t, T_t)\Delta t \ , \tag{5.5}$$

$$c_{t+\Delta t} = c_t + f(c_t, T_t)\Delta t \ , \tag{5.6}$$

and applied for the dedicated models included in the library for each specific resin system.

5.3. Numerical Code

A numerical code was written to implement the FW process model into a finite element platform. A VUMAT® user routine coded in FORTRAN® was devised and applied to an ABAQUS® explicit code. The main root routine was co-structured into several child sub-routines, each corresponding to a sub-model of the overall process model developed. A global simplified scheme of the model structure is depicted in Figure 150. In it, the interactions between the different sub-models are expressed through the flow of the main process variables. The flow and/or update of the fibre volume fraction, V_f, the radial positions, r^{fs}, the temperature, T, the resin velocity, $\dot{u}^r$, the degree of cure or crystallization, α or c, the "chemical" and effective viscosities, μ_{ch} and μ, the stresses, σ, strains, ε, and stiffness components, C, are specifically drawn.

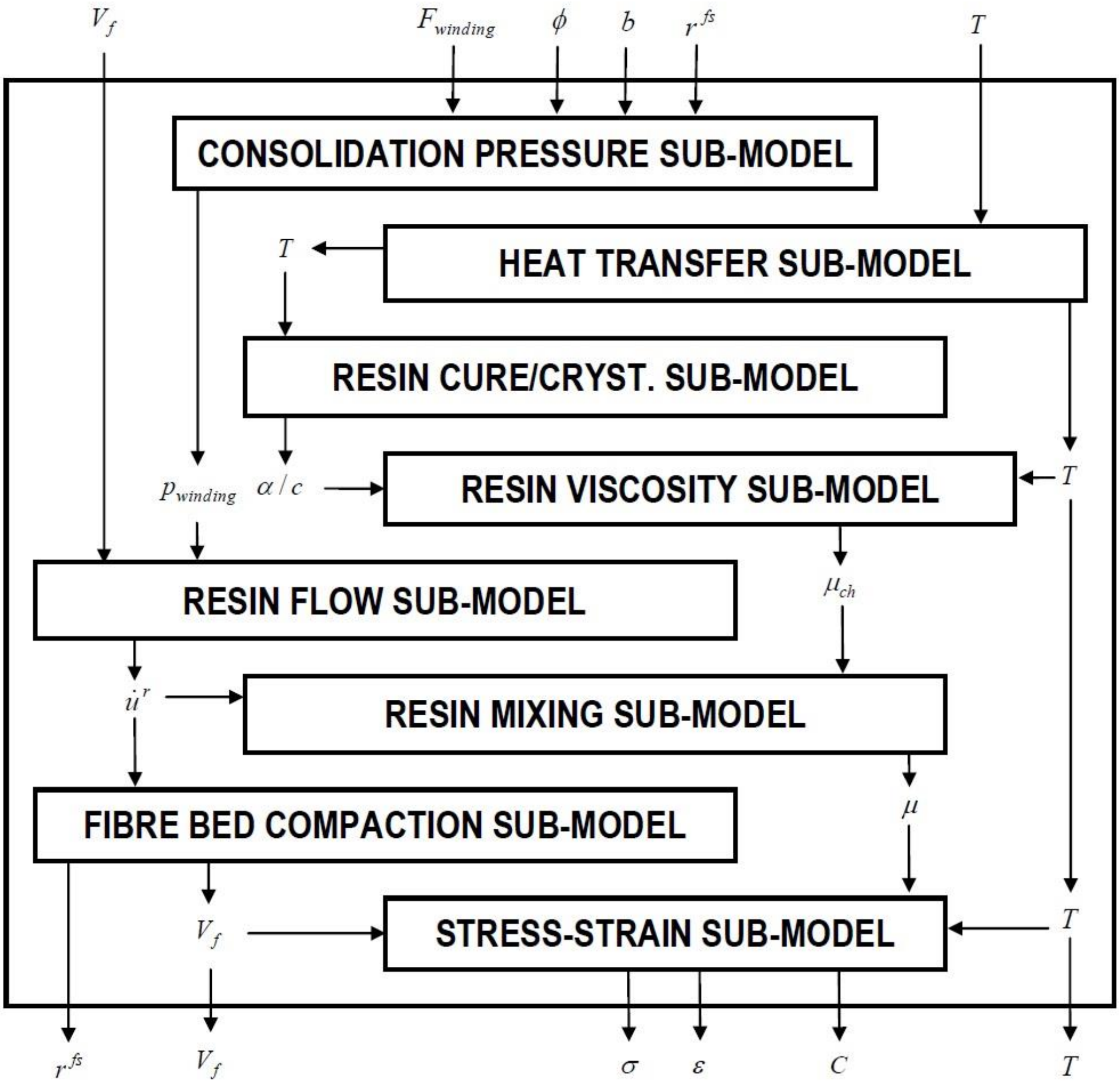

Figure 150 – Overall main scheme of the FW process model.

5.4. Sensitivity and Compatibility Tests

After setting the numerical code, it was tested under specific inputs in order to evaluate its sensitivity to pre-determined conditions and qualitative behaviour. In this section, the first difficulties found at the early debugging tests as well as later evaluations related with specific flow restrictions are presented.

5.4.1. Early Code Debugging

The first series of numerical tests had the sole objective of early detecting significant errors in the code and/or programming in order to debug it. Two major unexpected errors were initially impeding the useful application of the model, and therefore, are briefly discussed hereafter.

Several unexpected errors occurred in the first testing stages. Namely, hardware-software incompatibilities (previously unknown) such as the limitation of the finite elements commercial software used to 32-bit platforms when running explicit analysis. Several 32-bit platforms were purposely kept during the period of intensive usage of the first version of the code, in order to guarantee the compatibility with the required versions of the software. Such drawback is not a problem anymore, since newer versions of the software released in past two years overcame this limitation. Other difficulty arose with the existence of very large and very small numbers in the code. Numerical instabilities were observed and non-systematic errors inhibited the correct running of the program. This problem was solved by using “double precision” form which duplicates the bytes available for each variable value allocation. Complementarily, scaled dummy variables were set to avoid the worst case combinations. This problem is reported because the multi-physical nature of the process model favours such numerical instabilities. In fact, by including variables and quantities of very different nature in the same algorithm, the possibilities of promoting algebraic operations which encounter both very high and very small numbers increase substantially. Several other minor errors were successively detected and solved, but with no relevant relationship with the nature or technical features of the process model.

The two major unexpected errors abovementioned are, however, presented hereafter, since they represent relevant difficulties associated with the type of model and numerical program selected.

The first series of tests with the devised code, were carried out with a single finite element (2D quadrilateral, CPE4 from the ABAQUS® library) subjected to the four load cases depicted in Figure 151. The aim was to excite different stress and strain states and evaluate the outputs under such conditions. The first results achieved showed unexpected and perturbed behaviours. Due to the explicit dependence on time, the numerical program was devised and used in time-explicit mode. This meant that eventual dynamic effects should have been attained. The material mechanical properties defined within the process model, were based on the elastic-apparent properties, i.e., no viscous or damping properties were considered. The instantaneous application of the load, generated waved sinusoidal responses. Since no damping properties were known for the composite material system that could be applied without undesired effects on the other properties, the problem was solved through applying a smoothing function to the load. This function, of sigmoidal type, affected the initial stages of the load application, allowing to achieve the prescribed level of load only after a certain number of time steps. In Figure 152 both results (ModEFil code without and with smoothening function) are plotted. The effect of the restriction applied was clear and satisfactory.

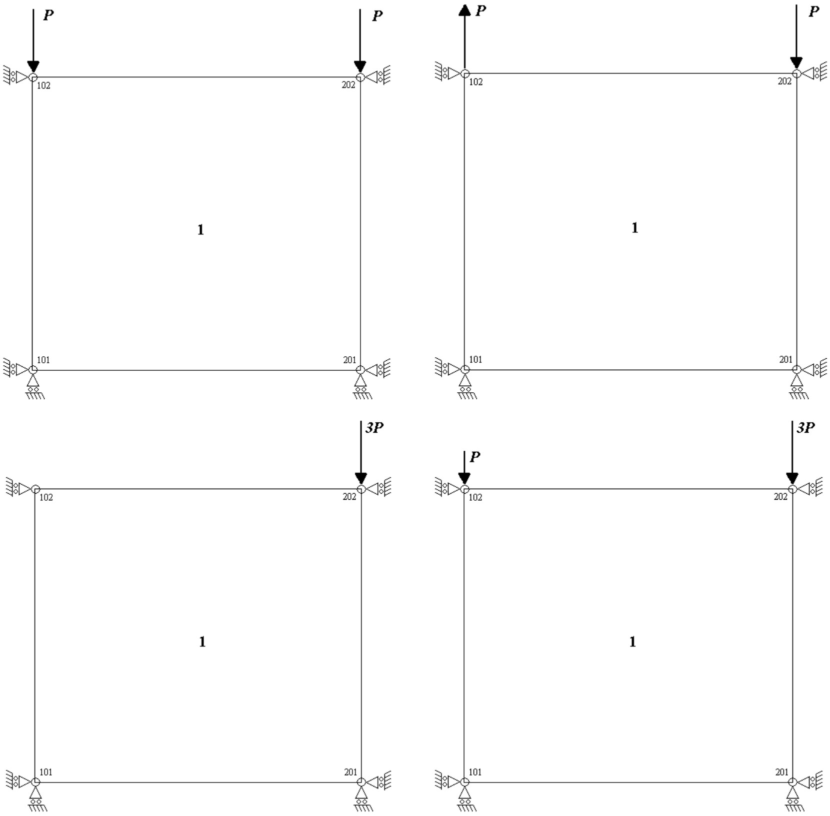

Figure 151 – Boundary conditions and load cases used to test the stress-strain behaviour of the model. UD compression (top left), pure shear (top right), 1-sided compression (bottom left) and unbalanced compression (bottom right).

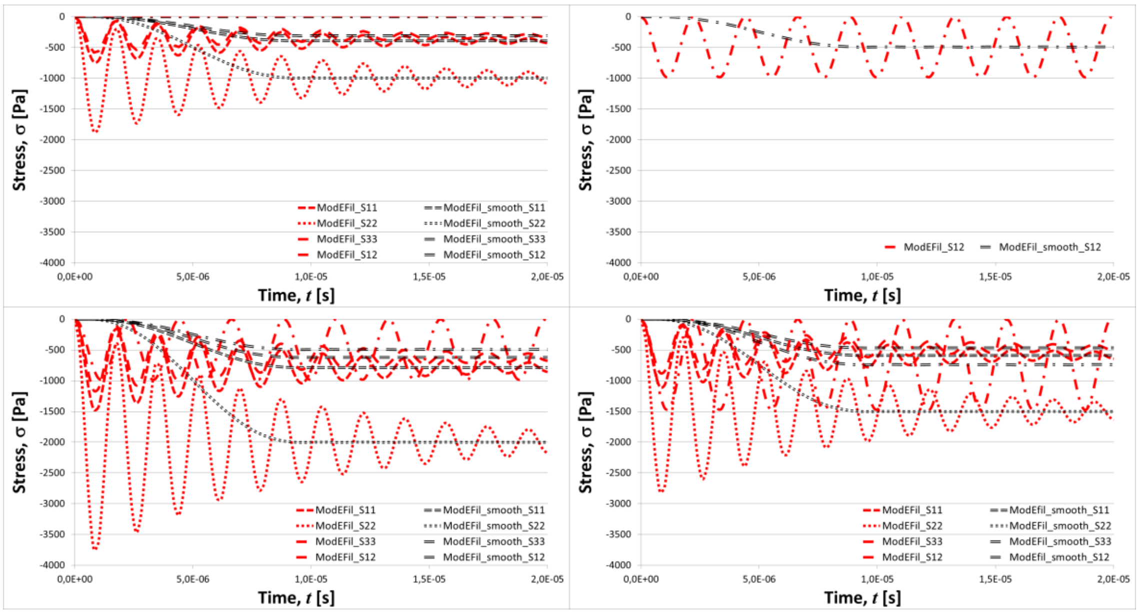

Figure 152 – Stress results of the ModEFil with and without smooth load function, for the four load cases: UD compression (top left), pure shear (top right), 1-sided compression (bottom left) and unbalanced compression (bottom right).

The second major error found was related with the need of artificially define a different material set of properties (dummy material) for the first time increment of each analysis. This limitation was correlated with the lack of definition of material properties to build the stiffness tensor at the artificial instant $t = -\Delta t$ which is required within the frame of the finite element code initiation. In order to overcome this, a dummy material (isotropic, purely elastic) was defined in the VUMAT® specifically for the first time that ABAQUS® requested the user material properties. At the second increment (starting effectively at $t = 0$) , the adequate composite properties were introduced, thus making the analysis converge with the desired material properties.

Upon completion of the main debugging tasks, a draft reference version of the numerical code was set. Further tests were realized over this reference baseline.

5.4.2. Qualitative Behaviour Evaluations

The qualitative behaviour of the process model was firstly assessed through a test series in which specific boundary conditions were applied to enforce certain expectable results. In this way, a preliminary validation of the model and/or the numerical code devised would be achieved. Herewith, the two tests dedicated to enforce specific resin flow restrictions are discussed. These were chosen by being representative of a characteristic feature of the FW process, since they relate with the unique geometry and the lay-up mechanism of the winding. The two tests were carried out using a lay-up of 18 layers. The code was modified only locally. Since the aim was to evaluate results in specific variables, the others are not detailed or listed here.

Within the first test, two configurations for the winding angles distribution were approached:

- Winding angle of 0º in a mid-section (10th layer);
- Winding angle gradients from the mid-section layer (10th layer) to both inner (1st layer) and outer (2nd layer).

In the first configuration, the winding angle was kept constant ($\phi = 40^{\circ}$) in all the 18 layers, except for the mid-section layer (10th layer) where it was enforced $\phi = 0^{\circ}$. In the second configuration, the winding angle was made different for each layer, keeping it equal to 0º for the mid-section layer (10th layer). Two “symmetric” winding angles gradients were set. In Figure 153 these two particular distributions are graphically depicted.

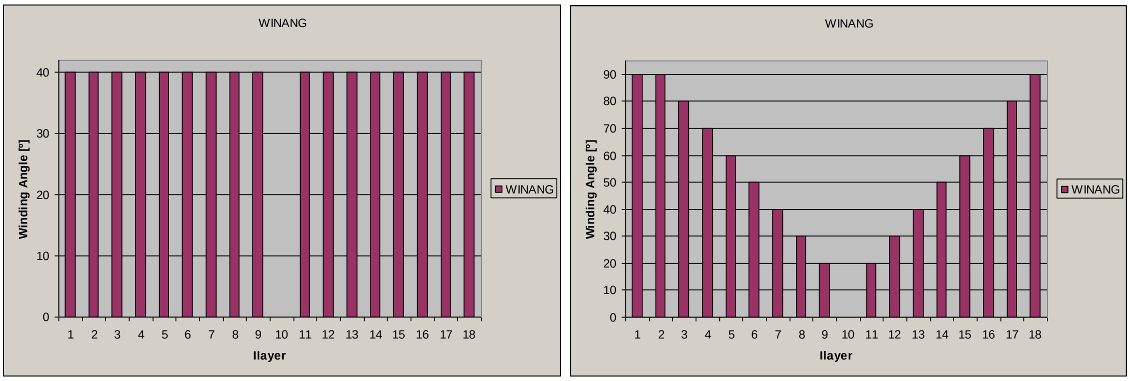

Figure 153 – Winding angles distribution for the two test configurations.

The expected outcome was the absence of resin flow in the mid-section layer. This is imposed by the equation (3.8) where, for $\phi = 0^{\circ}$, the radial pressure developed upon the winding force is null. Therefore, no pressure gradient would exist throughout the thickness of the selected layer and, from equation (2.11), no flow should occur.

The pressure distributions for several time instants are depicted in Figure 154. It is observable the absence of pressure gradient at the mid-section layer.

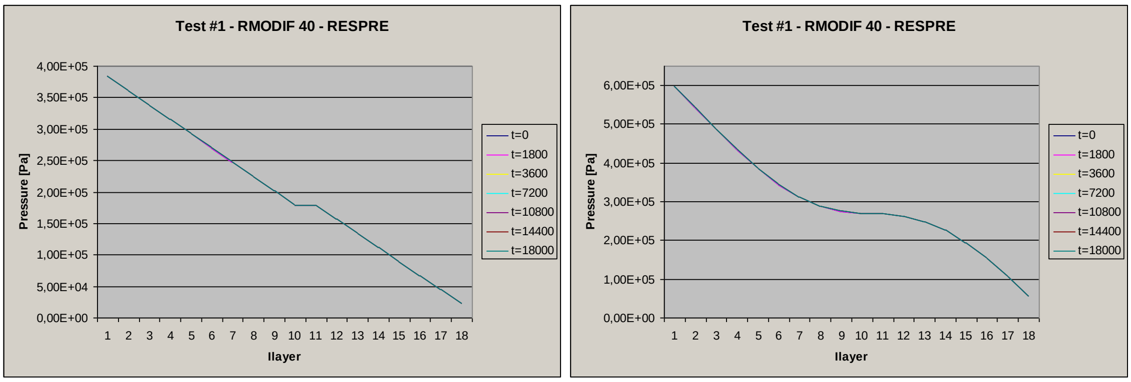

Figure 154 – Through-the-thickness pressure distribution for the two test configurations: constant (left) and varying (right) winding angles.

The results for the radial resin velocity and the fibre volume fraction are plotted below. The resin flow was zeroed at the selected layer, as expected. As a consequence of those interruptions described above, the fibre volume fraction evolved differently for layers 10 and 18. For layer 10 the decrease of fibre volume fraction is due to the impossibility of letting the reaching resin (from the layers beneath) pass and flow to the upper layers, thus accumulating resin. For layer 18, the reason is the predicted constitution of a laminate's global resin rich layer.

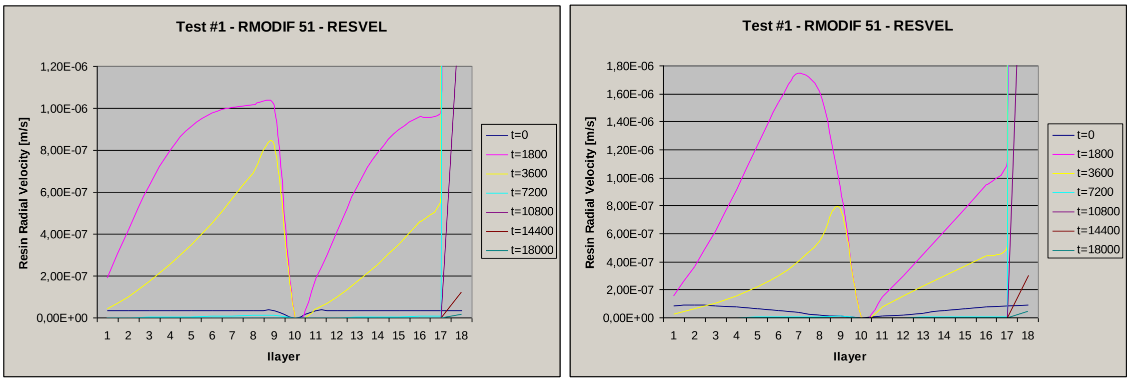

Figure 155 – Through-the-thickness distributions of resin velocity for the two test configurations: constant (left) and varying (right) winding angles.

The results have shown an adequate and intuitively correct behaviour of the model predictions regarding the flow mechanisms.

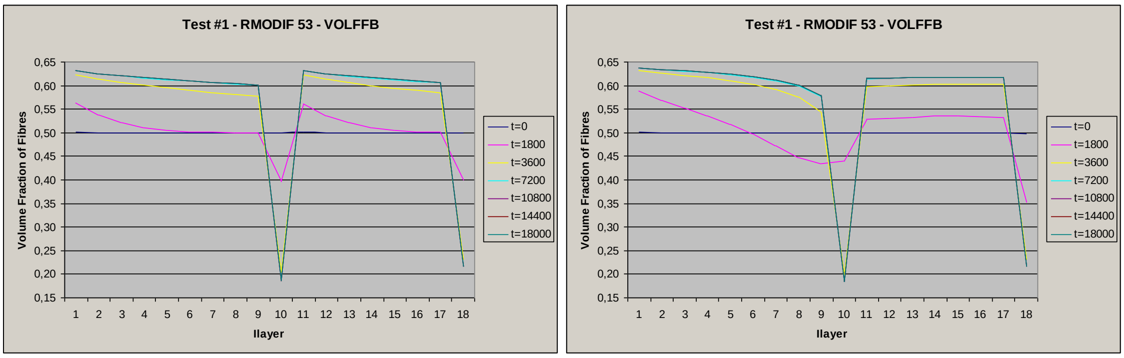

Figure 156 – Through-the-thickness distributions of fibre volume fraction for the two test configurations: constant (left) and varying (right) winding angles.

In the second test, zero permeability ($S = 0$) was enforced for all layers. The obvious consequence would be the total flow inability throughout the laminate. The expected results were, then, no resin flow and constant fibre volume fractions. These results are plotted below, and fully agree with the prediction.

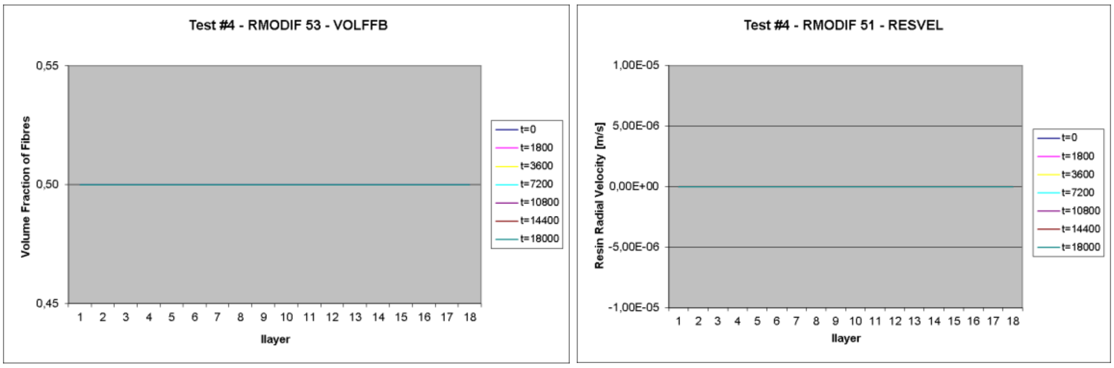

Figure 157 – Through-the-thickness distributions of fibre volume fraction (left) and velocity (right) for the zero permeability test.

One shall recall that the objective was to test the qualitative behaviour of the model, using several specific restrictions that should produce intuitively known results. The quantitative and more relevant evaluations were conducted after the conclusion of these preliminary sensitivity tests.

5.5 Validation of the Process Model

After the conclusion of the experimental test procedures, which covered the main physical phenomena of the FW process, a series of numerical simulations were carried out to reproduce the experimental results. The aim was to validate the process model for a limited range of known conditions, thus allowing to infer its wider applicability and validity. In the following sections, the process conditions tested and the comparison between experimental and numerical results is addressed. The validity of the process model together with the main limitations and the assumptions made are discussed in detail.

5.5.1. Comparison of Experimental and Numerical Results

Four winding conditions, corresponding to the wound specimens WS1, WS2, WS8 and WS10, were selected for the numerical simulations. These represent reasonably different processing conditions within the range experimentally tested. The main input conditions differing from one to another are summarized in Table 43. For the constant parameters their values were initialized and kept throughout the entire simulation. In the case of variable parameters, these were initialized with the values presented and then evolved and updated by the respective sub-routines as the simulations progressed. Many other properties are not summarized here, due to the fact that they either are calculated from the properties shown or do not differ from one simulation to another.

Table 43 – Main input conditions (initializations) for the various numerical simulations, for the selected wound specimens WS1, WS2, WS8 and WS10.

Parameter / Property	History	Specimen			
		WS1	WS2	WS8	WS10
Total Number of Layers	constant	20	16	16	16
Winding Force [N]	constant	150.00	93.25	110.00	99.50
Layer Winding Time [s]	constant	97	79	68	68
Room Temperature [ºC (K)]	constant	17.7 (291)	17.5 (291)	18.2 (291)	18.2 (291)
Radius of the Mandrel [mm]	constant	74.006	72.600	72.863	70.663
Layer Thickness [mm]	variable	1.580	1.449	1.194	1.533
Fibre Volume Fraction [%]	variable	23.79	35.47	58.32	28.00
Degree of Cure [%]	variable	3.86	3.58	4.93	3.56

In order to further approach the real winding conditions, within each numerical test, the layers were incrementally wound (added), according to the “real” layer winding time used in the winding trials. This configuration was named sequential (SEQ) winding as opposed to simultaneous (SIM) winding.

Herewith, the numerical results, from both simultaneous and sequential winding simulations, are presented and directly compared with the corresponding experimental results. These comparisons are addressed for all the main multi-physical parameters of the FW process studied. Namely, the evolutions of the radial pressure, P^r, the degree of cure, α, the viscosity, μ, the temperature, T, the resin radial velocity, $\dot{u}^r$, the radial positions, r^{fs}, the layers' thicknesses, t^{l}, the fibre volume fraction, V_f, and the permeability, S, are analysed and compared.

The radial pressure (consolidation pressure) was applied in a single step in the case of simultaneous winding simulations, and incrementally in the sequential winding cases. The pressure history results are plotted in Figure 158 for the four winding conditions (wound specimens) selected. For the sake of readability, in each chart only the inner most, the middle and the outer most layers were selected and plotted. These were representative of the through-the-thickness variations of properties. Also, due to the fact that the most relevant evolutions occurred in the early stages of the winding (up to the deposition of the last layer), a logarithmic time scale was used, thus enhancing its visualization. In each chart, the experimental results obtained in the winding trials were added for comparison.

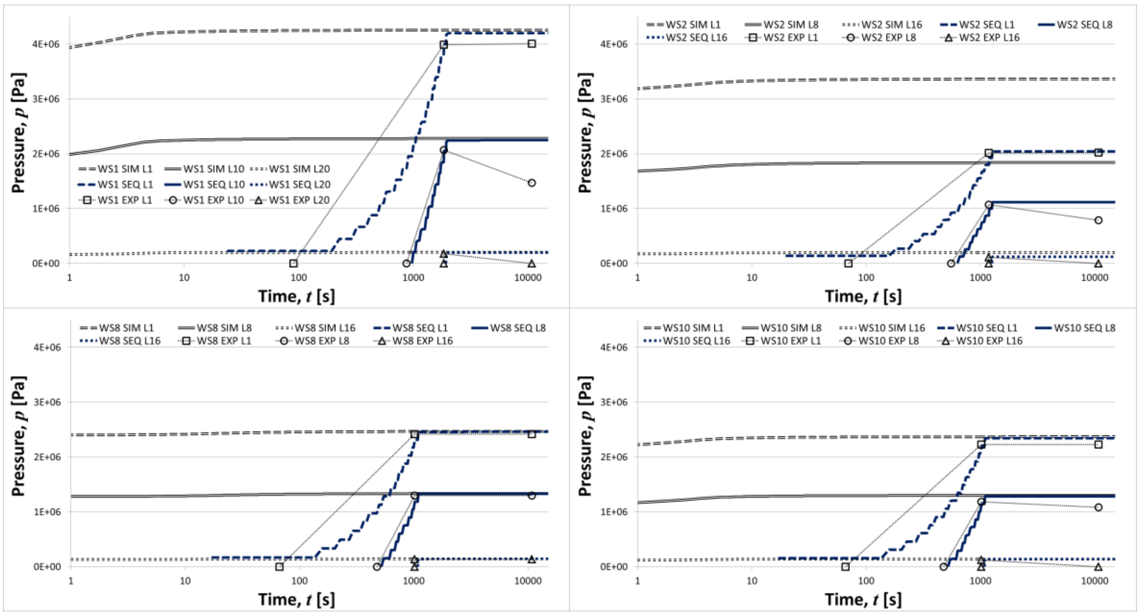

Figure 158 – Radial pressure history (numerical simultaneous/sequential and experimental) for the four winding cases tested in the inner-most, middle and outer-most layers.

The first clear output was the consistent convergence of both simultaneous and sequential simulations as the last layer was wound. This behaviour was actually observed for the other properties/variables being analysed hereafter. The experimental values were retrieved from the direct relationship between the measured winding force and the radial pressure (equation (3.2)). They are graphically represented with linear segments between each effective discontinuous data point for visual reference only, since no continuous measurements were actually made and, therefore, the type of evolution is not experimentally known. The numerical results agree with the experimental data for the initial moments, i.e., until the last layer is wound. After this moment, the numerical models kept nearly constant values for each layer. In the algorithms used, the update of the pressure was solely dependent on the change of the radial position, which had no relevant influence in the overall pressure. However, the final radial positions measured for each layer, together with the increasing stiffness of the laminate (resin curing), suggested that a relaxation term should apply (equation (3.8)). This term was used in the determination of the ultimate experimental values, and, as one can see, they diverge after the initial agreement. Exception was noted for the WS8 case, since in this case no inward movement of layers was observed, and therefore, no relaxation occurred as well. In this latter condition, the numerical models fully agree with experimental data for the entire time range (even after all layers' deposition).

The degree of cure, α, had a particular condition to be accounted in its initialization. In fact, the initial extent of cure, i.e., the cure state at the first deposition/winding time, varied from layer to layer since all were wound/deposited at different times. The different values for every layer were found through linearly interpolating the estimated $\alpha(t)$ curve at room temperature, for the corresponding winding times (multiples of the unitary layer winding time). The linear relations achieved for the determinations of each layer's initial degree of cure, α_0^{ilayer}, were written as:

$$\alpha_0^{ilayer} = a \times ilayer + b \ , \tag{5.7}$$

where $ilayer$ is the layer being attributed an initial value and a and b are constants. These constants are listed in Table 44 for the four selected simulation cases.

Table 44 – Values for the constants a and b in the linear relation determining the initial degree of cure for each layer within the laminate being wound and simulated.

Wound Specimen	constant	
	a	b
WS1	0.00289	0.03568
WS2	0.00235	0.03342
WS8	0.00202	0.04729
WS10	0.00202	0.03354

The evolutions of the degree of cure in the four winding cases are plotted in Figure 159. The numerical simultaneous and sequential windings are directly compared with the experimentally estimated $\alpha(t)$ curve at room temperature. This estimation was achieved by exponentially extrapolating to the applicable room temperature the experimental curves obtained for six samples tested in DSC at three higher temperatures (303K, 313K and 323K).

From the plots one can observe that the different layers tend to a common final degree of cure and that the simultaneous winding simulations lasted longer, as expected, to converge with the experimental curves. In fact, in the simultaneous winding simulations, the initial degree of cure of all layers except the first one (inner-most) were "artificially" set at $t = 0$ instead at the moment of each one's winding. In all the cases, an initial overestimation and final underestimation of the expected degree of cure by the numerical models were found. Nevertheless, since the experimental data was estimated by a different method than the kinetic model equation developed for this resin and implemented in the numerical code, and also that the effective temperatures experienced during the winding and curing stages were non-isothermal, the numerical and experimental results can only be qualitatively compared. Such qualitative comparison shows reasonable agreement for the relevant time domain. The differences observed from intermediate degree of cure onwards are justified later in the discussion of similar behaviours for other variables.

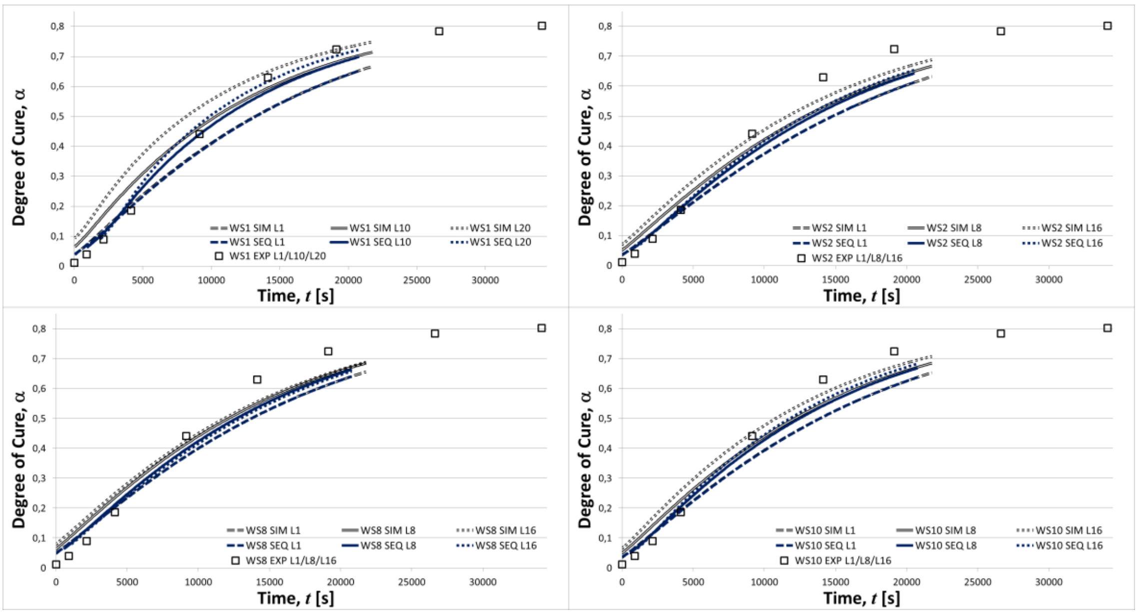

Figure 159 – Evolutions of the degree of cure (numerical simultaneous/sequential and experimental) for the four winding cases tested in inner-most, middle and outer-most layers.

Similarly to the degree of cure, also the initial viscosities of the several layers at their deposition/winding time are expectedly different, since $\mu = f(\alpha, T)$. However, these were not initialized in the same way of α, because the model calculates viscosities in a sub-sequent sub-routine. The specificity of the viscosity sub-model is that it accounts for the possibility of mixture of resins from adjacent layers. This is a major aspect of the FW process governed by the outward resin flow as discussed in previous chapters. Therefore, two resin histories were written and analysed: the so-called "chemical" viscosity, μ_{ch}, which corresponds to the plain evolution of the viscosity without external mixing effects, and the effective viscosity, μ, resulting from eventual mixings. The "chemical" viscosities are plotted in Figure 160 where they are also compared with the experimental curves obtained with neat (unmixed) resin at the nearest possible temperature (303K). In Figure 161 the effective viscosities are plotted. Since the range of viscosities experienced by the resin is very wide, and that, again, the main mixing events occurred in early stages of the process, log-log scales are used for better visualization.

Despite differences were observed between "chemical" and effective viscosity numerical data, these were minimal. This was mainly due to the fact that the viscosities of the adjacent layers exchanging resin, through its flow, were very similar. In other words, the resins being mixed were very similar (similar degrees of cure and viscosities) and no relevant mixing effects were visible in these four cases selected. Longer winding times would need to be implemented to allow observing stronger mixing effects.

Under these conditions, the main physical factor influencing the evolution of viscosity, a part from time, was the temperature. This is the reason why the "chemical" viscosities of the layers being wound later were also affected at the early stages of their winding. Heat transfer with the layers beneath promoted sudden increase of temperature and consequent variations of viscosity at and immediately after the deposition of each layer. This was particularly observable in the WS1 case at the outer-most layer.

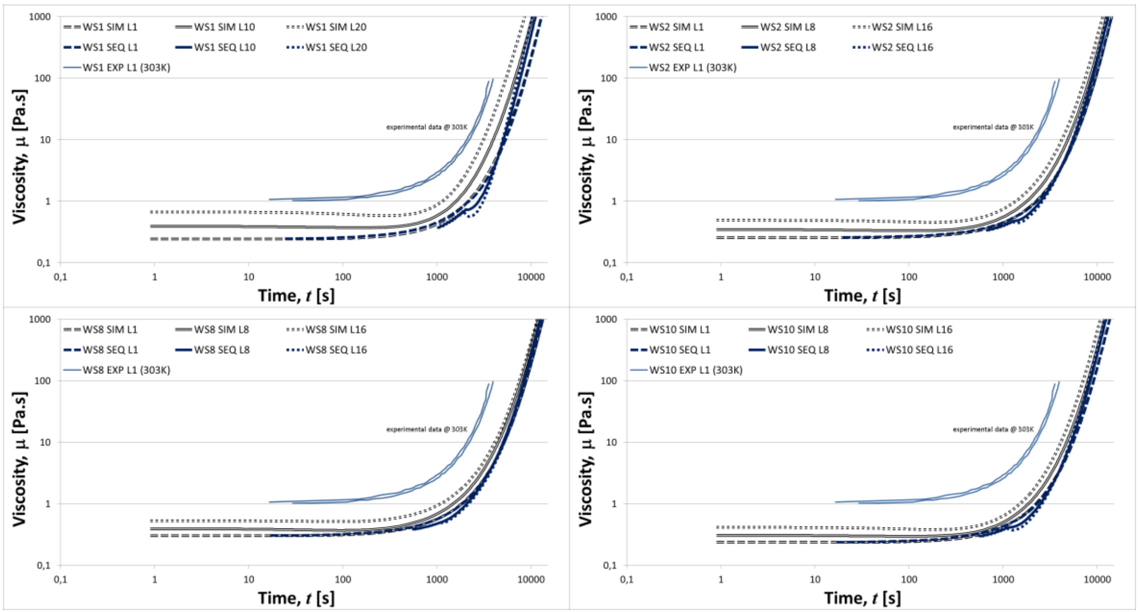

Figure 160 – Evolutions of the "chemical" viscosities (numerical simultaneous/sequential and experimental) for the four winding cases tested in inner-most, middle and outer-most layers.

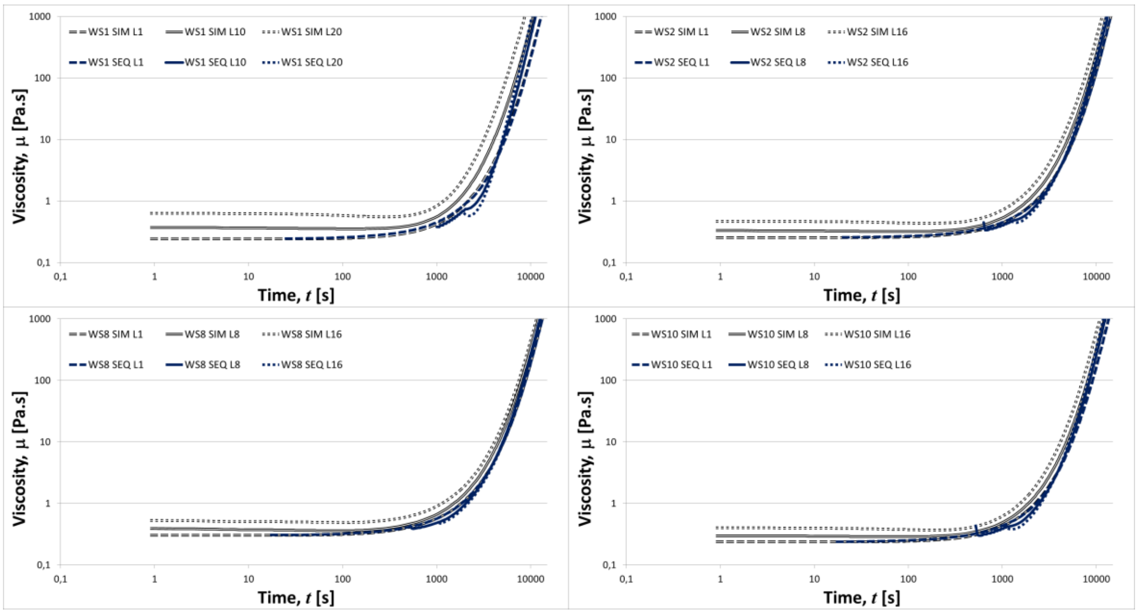

Figure 161 – Evolutions of the effective viscosities (numerical simultaneous/sequential) for the four winding cases tested in inner-most, middle and outer-most layers.

The simultaneous and the sequential winding simulations results converged for times after the deposition and accommodation of the last layer. The realistic perturbations that the sequential winding promoted in the viscosity of the layers at the first moments of their winding were, however, a noticeable difference between the two results, since the variations in viscosity directly affected the resin flow ability.

The evolution of viscosities compares well with the experimental data (obtained at different temperature), although no accurate nor direct comparison could be addressed.

The temperatures, T , experienced by the composite layers during the winding and post-winding stages, are plotted in Figure 162.

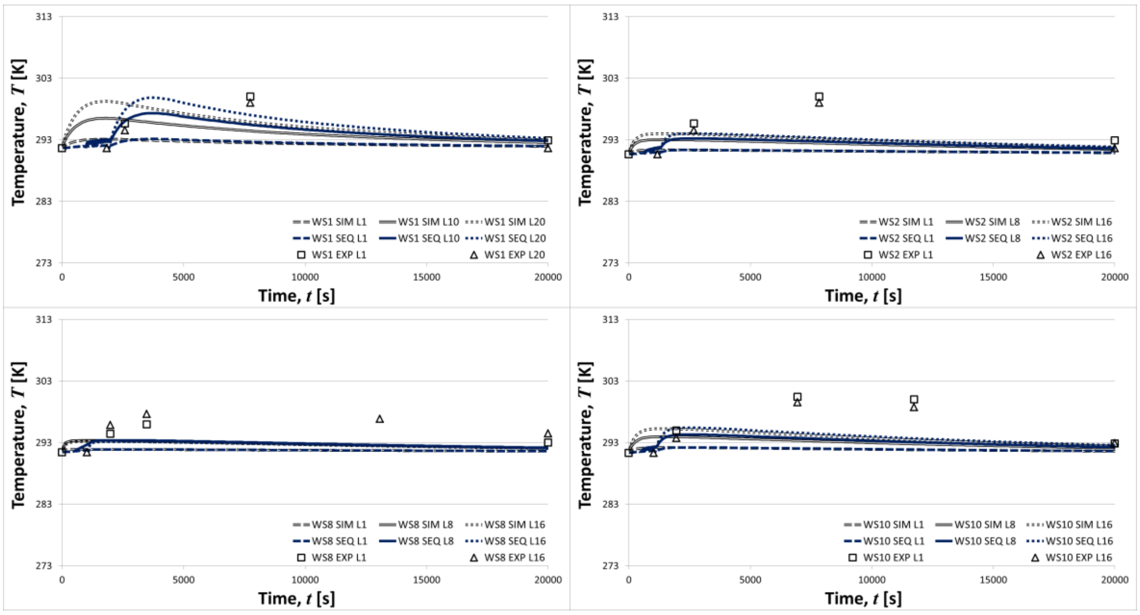

Figure 162 – Evolutions of the temperature (numerical simultaneous/sequential and experimental) for the four winding cases tested in inner-most, middle and outer-most layers.

As one can see, the experimental data showed considerably different evolution than the one predicted by the models. Such differences are justifiable by two main aspects: (1) the effectively inadequate (unrealistic) material thermal properties inputted to the numerical model, and/or (2) the underestimation of the intrinsic heat generation of the resin during its curing process. The latter aspect was attained during the formulation of the heat transfer sub-model, which accounted for the effectively measured heat generation term. However, different mass concentrations may apply between the DSC and the real winding conditions, and thus different values could be applicable. Further thermo-chemical characterizations of the resin should be addressed under more realistic mass and neighbouring conditions. This was largely discussed earlier in section 4.2.

The resin radial velocity was modelled as well and is plotted in Figure 163. Log-log scales were used to enhance readability of the data. The experimental data is reduced to an average velocity determined from the measured flow distances and the known winding and consolidation times.

In all the cases tested, the velocity nearly ceased after 10000 s. Also, the outer-most layer presented much higher velocities than the others. This substantiates the process-intrinsic characteristic that the outer-most layer receives all the excess resin flowing from the fibre bed beneath. Later we will discuss the implications of this phenomenon in the numerical results.

The simultaneous and sequential winding results converged for the intermediate and outer layers upon deposition of the last layer. However, such convergence was not observed for the inner-most layer (except for the WS8 case). This was due to the fact that, in the sequential winding configuration, the pressure build-up occurred later and therefore the resin flow presented a time delay in accordance. The range of velocities predicted by the simulations was in line with the average velocity estimated from the experimental measurements. Since these measurements were only made in the coloured layers (sections 4.3.1 and 4.3.3), which were typically at the mid-thickness, results shall be compared with the middle layer's numerical data (continuous lines).

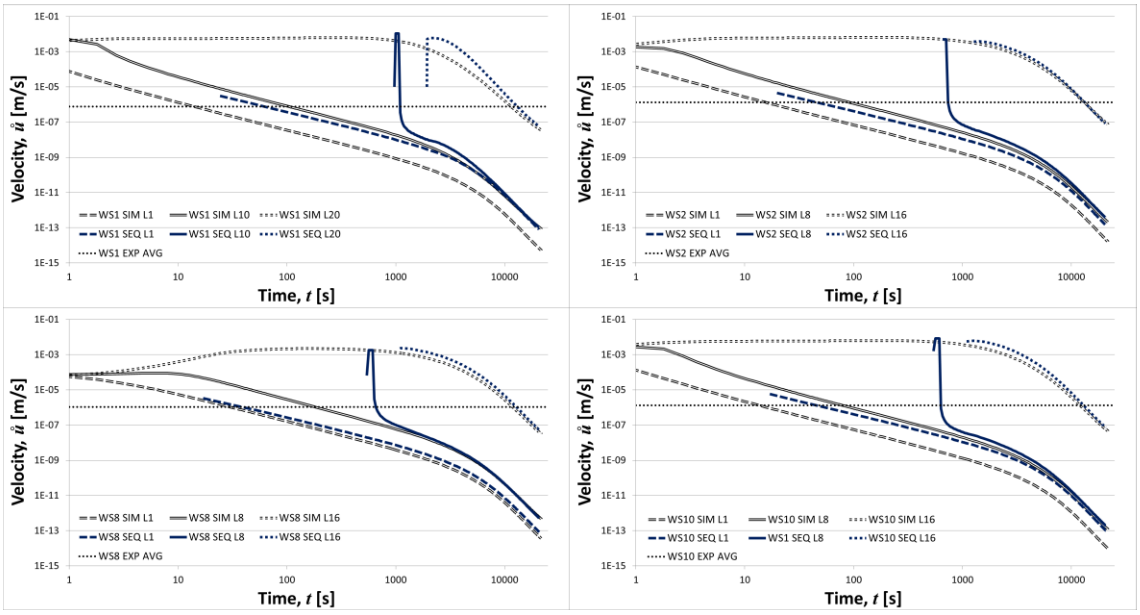

Figure 163 – Evolutions of resin radial velocity for each winding case (numerical simultaneous/sequential and experimental) at inner-most, mid and outer-most layers.

The radial positions of the layers (radial distance from the mandrel rotation axis to the inner border of each layer within the laminate) are presented in Figure 164. For the same reasons above logarithmic time scales were used.

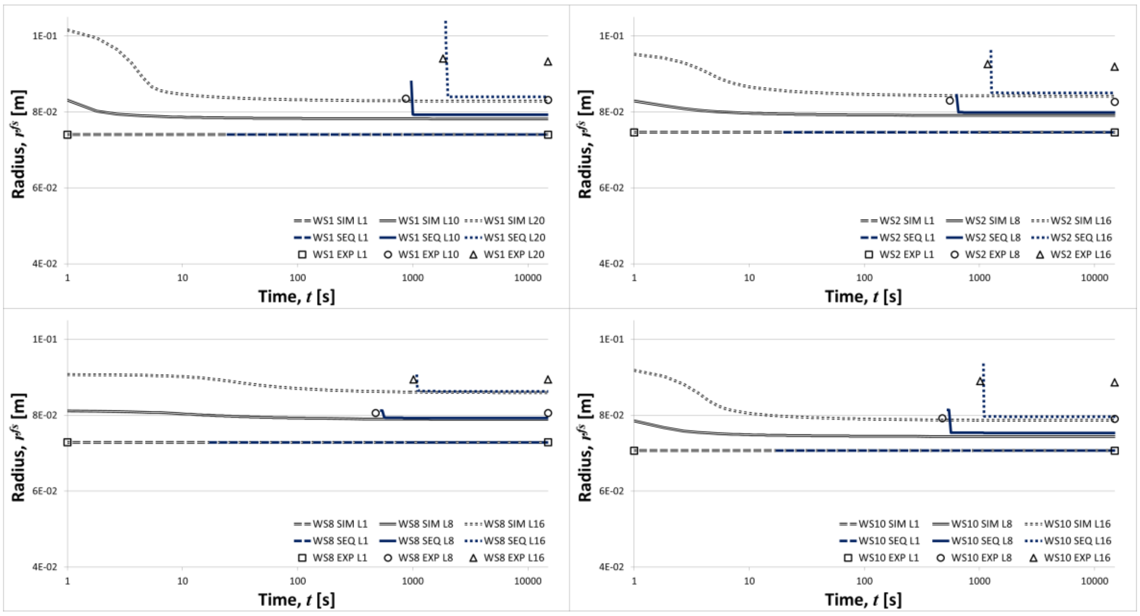

Figure 164 – Evolutions of radial positions (numerical simultaneous/sequential and experimental) for the four winding cases at inner-most, mid and outer-most layers.

The radial position of the inner-most layer is constant and equal to the radius of the rigid mandrel surface. This constraint was applied to the numerical simulations and therefore, the experimental and numerical results were equal as well for these layers. However, such matching between the experimental and numerical results was not observed for all other layers. The initial and final values were, respectively, overestimated and underestimated by the numerical simulations when compared with the experimental estimations. The underestimation of the final radial positions was due to modelling aspects (excessive resin flow), focused in the end of this section. The disagreement in the initial radial positions had, however, another known reason. In the real winding trials, considerable resin loss was observed during each experiment. Such phenomenon was a natural consequence of the resin outward flow and its excessive accumulation in the outer region of the laminate being wound. The excess resin which could not be kept there, due to its weight, viscous nature and the mandrel cylindrical geometry, was effectively lost from the composite specimen. In order to highlight this specific feature/characteristic of the wet FW process, the experimental radial positions at the beginning of the winding were estimated from the measurements of the full thickness of the specimens, thus ignoring the lost resin. In other words, the real thickness of the resin rich layer (outer layer) was considerably lower than the one calculated in the numerical simulations, because in these the resin is fully “stored” in the last (outer) layer and no losses are considered. This aspect is further depicted in Figure 165 where the evolutions of the layer thicknesses are presented. Due to the different magnitudes of the thickness of the last (outer) layer and the others, log-log scales were used.

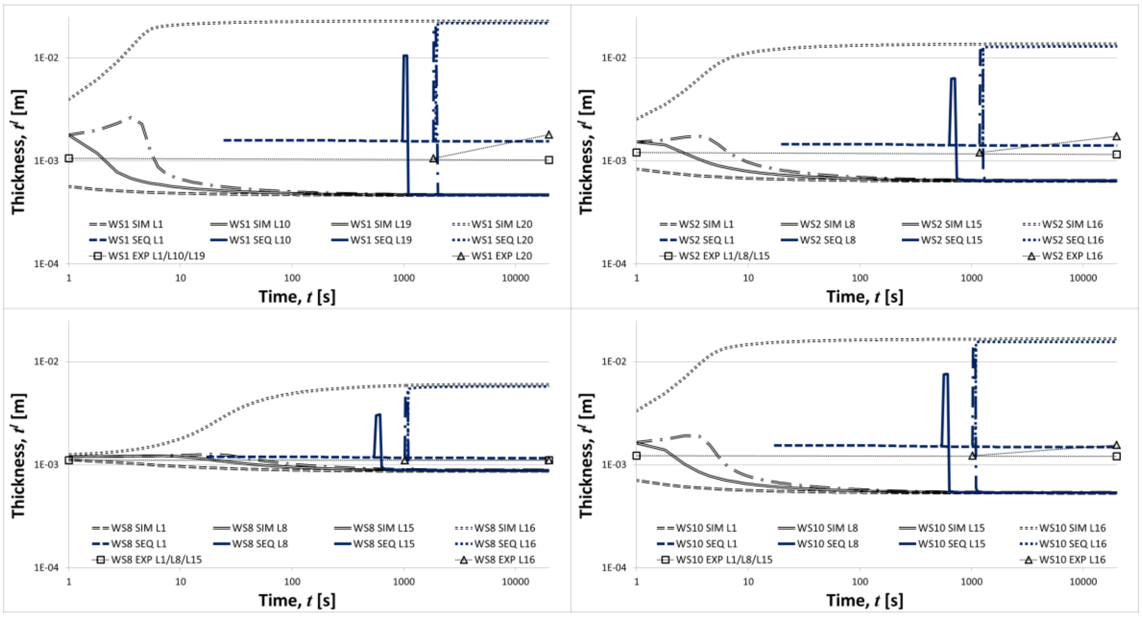

Figure 165 – Evolutions of the layer thickness (numerical simultaneous/sequential and experimental) for the four winding cases tested for the inner-most, middle, next to outer-most and outer-most layers.

As expected, the results of the layer thicknesses are affected in a similar way to the ones of radial positions, given their intrinsic relationship. What is clearer from the layer thickness results, is that the numerical simulations generally underestimated the final thicknesses of all layers but the outer-most. In fact, the resin quantity accumulated in the outer-most layer (which includes the so-called resin rich layer) is clearly overestimated. Two reasons concurred to this, namely the fact that the numerical code was not prepared to allow loss of resin and the fact that the experimental measurement did not include the amount of resin effectively lost. Further support to this evidence lies in the fact that the results for WS8 (less resin available) presented better experimental-numerical agreement. In this winding case the relative amount of resin was minimal and therefore no resin loss occurred nor resin rich layer was formed. Under such conditions, the numerical predictions hold realistic.

In Figure 166 the evolutions of the fibre volume fraction (relative fibre content) are plotted for the four wound cases simulated. It can be observed, similarly to the thickness variable, that the behaviour of the outer-most layer is qualitatively and quantitatively different from all other layers, including the penultimate (next to outer-most) layer. The numerical model showed to allow higher resin flow (in both simultaneous and sequential winding configurations) and thus overestimated the changes in the radial positions, layers' thicknesses and fibre volume fractions. The influence of the resin outward flow is clearly observed by the behaviour of the penultimate layers. In these, the relative content of fibres initially reduces (as the resin from the layers beneath invades and passes through it) and then inverts this trend and converges with the other layers. Only the outer-most layer reduced its relative content of fibres, due to the accumulation of resin (incorporating the resin rich layer).

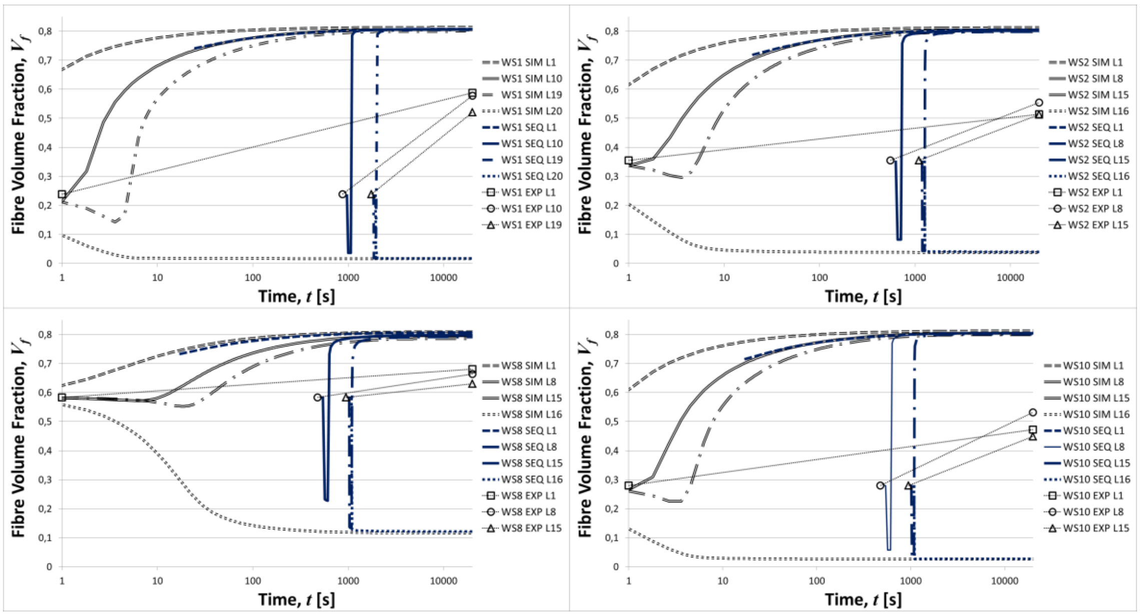

Figure 166 – Evolutions of the fibre volume fraction (numerical simultaneous/sequential and experimental) for the four winding cases tested for the inner-most, middle, next to outer-most and outer-most layers.

Although not measured directly, the transverse permeability of the saturated fibre bed was retrieved from the experimental data by applying the equation (2.17) to the known initial and final fibre volume contents. The empirical constants were assumed equal to the ones earlier determined by Gutowski *et al.* [16]. The initial and final averaged values could be determined and were compared with the numerical results for this parameter. These are plotted in Figure 167, showing the expected trend (reduction in all layers except the outer-most) and that the averaged experimental value reasonably fits the average of the range numerically evolved.

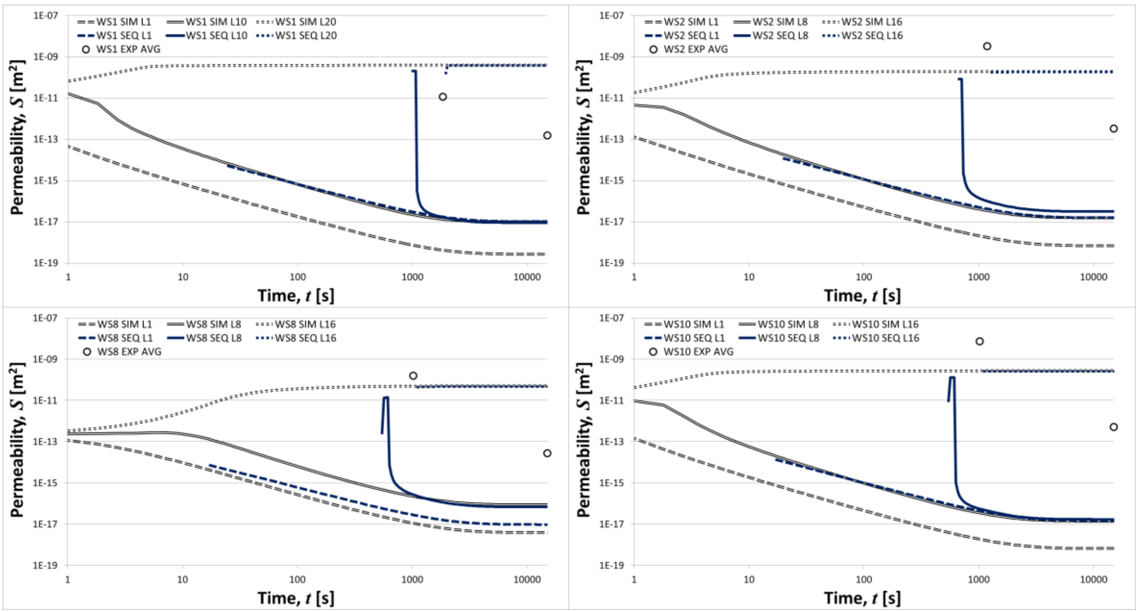

Figure 167 – Evolutions of the transverse (radial) permeability of the saturated fibre bed (numerical simultaneous/sequential and experimental) for the four winding cases tested for the inner-most, middle and outer-most layers.

These comparisons globally showed that both the simultaneous and sequential winding simulation configurations were able to qualitatively predict the behavipur of the main physical phenomena of the wet FW process. Moreover, the two simulation schemes typically converged after the deposition/lay-up of the last (outer-most) layer, meaning that both are applicable to predict the ultimate distributions and properties of the laminates being wound. Nevertheless, the sequential winding model scheme showed to better simulate reality, since the history of variables in each layer was coherently more close to the expected behaviour. The early evolutions of fibre volume fractions and permeability in layers near to the outer-most region, showing inversion of trends upon resin flow pass-through, are good examples of this.

Also clear was that the WS8 case was better simulated since no relevant resin flow actually occurred and therefore its erroneous modelling did not govern the overall results.

5.5.2. Advantages/Disadvantages of the Adopted Methodology

As first enunciated in the introduction to this chapter, the validation strategy for the FW process model was based on a comprehensive experimental programme, aiming at measuring the main physical variables of the process. The desirable independent validation of each sub-model (sub-process phenomena) was assessed through several dedicated tests and procedures. Then, numerical results were produced using the experimental chemo-rheological and mechanical data as inputs to simulate the winding and consolidation conditions selected for comparison.

The main advantages of this methodology were:

- the deeper understanding and insight to each of the relevant physical phenomena interacting during the process, since these were specifically studied and tested;
- the development of novel chemo-rheological models for the resins studied;

- the understanding of main physical phenomena which are also present in other composites manufacturing process;
- the possibility of identifying the cause-effects relations between the various parameters (process- and material-intrinsic) and their influence at a greater detail level, due to the restricted ambit of each sub-model and corresponding tests/measurements;
- the comprehensive evaluation of the process modelling analytical descriptions, by adding reliable experimental data for the analysis.

As for the disadvantages, the main were:

- the pronounced variety of different physical phenomena being studied independently, not allowing to deepen each one as desirable for greater understanding and/or accuracy in the parametric analyses;
- the absence of a dedicated strategy for the experimental validation of the stress-strain relations, due to the inherent difficulty in assessing these quantities during the process;
- the difficulties in assessing the history of the main process variables, being only discretely assessed at the initial and final conditions;
- the need for estimation of some input quantities, such as the initial layer's thickness, due to the mentioned difficulty in assessing or measuring these at the winding location, during the winding trials.

The approach drawn was, nevertheless, unique, comprehensive and proved to allow achieving very useful and even innovative results, thus enhancing its validity.

5.5.3. Assumptions and Limitations

Two major weaknesses were highlighted throughout the comparison of the numerical and experimental results: no stress-strain measurements were carried out that could compare and/or validate the model predictions/assumptions and no pressure release term was included in the numerical runs (despite analytically modelled in chapter 3). The former limitation was due to the lack of experimental means to measure stresses and/or strains accurately at local level during the process. These specific measurements were not included in the experimental campaigns, since their complexity justified a dedicated and deep specific study. The latter was specifically detected in Figure 158, where the numerical results suggested a constant pressure level in every layer after lay-up of the last one, which both experience and experimental evidence opposed. The pressure release is effectively present in the FW process, since the inward displacement of the layers (upon the resin outward flow) lead to a gradual decrease of the circumferential tension promoted by the winding force. Nevertheless, this effect was included in the process model (chapter 3) and was also treated in the chapter 4 along with the experimental pressure estimations.

The main assumptions and limitations of the process model itself have been focused in previous chapters.

5.5.4. Process Model Validity

The validity of the multi-physical model developed to represent the FW process was assessed through comparison of experimental and numerical data for selected winding conditions. This validity was analysed both in general and specific terms, i.e., both the global ability to model the overall evolutions of the main physical variables and the particular results of each group of phenomena were observed.

As shown by the experimental-numerical comparisons, the evolutions of the main process variables were qualitatively correct. In other words, the trends were logical and correspondent with the observed reality. Furthermore, the predictions of the final states of the main parameters reasonably agreed with the experimental data. The possibility of replicating the real incremental nature of the lay-up mechanism further enhanced the model ability and utility.

The two exceptions to the accurate predictions were the predictions of the temperature and the resin flow history, which disagreed from the experimental evidence. The former did not produce any relevant influence in the remaining results, since the interval of temperatures experienced was nearly negligible in both numerical and experimental tests. Nearly isothermal conditions could apply. The latter, however, propagated severe influence on the other outputs, like radial positions, thicknesses, fibre volume fractions and permeability of the layers. It is easy to observe that the overestimation of the resin flow, in both magnitude and time duration, affected the global results for all cases where this parameter governed the consolidation. This was the case of WS1, WS2 and WS10 in which the high relative amount of resin available to flow promoted such predominance. As referred previously, in WS8 the flow conditions were minimal and thus the overall results returned correct and realistic. Based on the Darcy's type flow formulation, the analytical and numerical descriptions of the resin flow, settled by equations (2.11) and (5.2), respectively, depended on the pressure gradient, the resin viscosity and the permeability of the saturated media. Since the pressure gradients and the resin viscosity were independently validated by the experimental results, the factor influencing the flow behaviour seemed to be the apparent permeability. This parameter is itself modelled as a function of the fibre volume fraction and "external" empirical constants, by equation (2.17). Since the evolution of the fibre volume fraction is directly dependent of the permeability and consequent flow (the multi-physical phenomena are actually coupled), the reasonable improvements to promote were on those empirical constants. These should be determined by dedicated permeability tests, which are documented in literature and were reviewed in chapter 2. Due to the limited time and resources, these tests were not programmed and therefore, this improvement was not addressed. The alternative of "adjust" the constants value until numerical and experimental results would match was not addressed as well, due to the main universal principle that governed this study: all the data used as inputs to the model were either collected experimentally within this study or retrieved from consensual and consolidated studies from other authors. This principle was justified by the objective of keeping high control of the sub-processes modelling and model-reality close relations throughout the model development and testing phases. The quality of the results achieved hold this principle successfully accomplished.

CHAPTER 6

CONCLUSIONS

6.1. Objectives *vs* Results

The work conducted and presented throughout this thesis was structured in view of accomplishing the several objectives initially drawn. These were briefly identified in chapter 1 and detailed in chapters 3 and 5, along with the analytical modelling and validation discussions, respectively. The principal objective of developing and validating a multi-physical process model for the FW manufacturing process was further complemented with partial objectives during the realization of the work. These aimed at addressing specific aspects of the manufacturing technique, thus increasing the depth and utility of the study itself.

In brief, the main objectives established were the following:

- Develop and validate a global FW process model;
- Comprise both thermosetting and thermoplastic process configurations;
- Model the effect of manufacturing features intrinsically related to FW:
    - through-the-thickness gradients on pressure, flow and stiffness;
    - misaligned pattern of the fibres at lay-up and compaction;
    - incremental lay-up;
- Develop experimental procedures for the measurement of main process parameters and input/output variables;
- Analyse and evaluate the model through parametric tests;
- Foresee wider and useful applications of the process model to several configurations of FW and/or to other FW-related techniques.

From chapters 2 to 5 the pursuing of these objectives was described in detail through a comprehensive identification of the “problems”, proposition of both methods and solutions, and their validation.

Despite several modifications were introduced in the course of the work, the main scope and aims were kept and drove the decisions made. Such modifications mostly referred to difficulties encountered to strictly fulfil the initial plan. Namely, the early difficulties in establishing fully functional draft version of the numerical code, the lack of validated data in literature to produce complete comparisons of the model, the need of introducing and anticipating the chemo-rheological experimental program to develop reliable input sub-models and the unmanageable logistics to set an experimental program dedicated to the stresses and strains online measurements. Nevertheless, the objectives listed above remained referential to evaluate the results achieved. Also, the accuracy and applicability of the model can be discussed. This evaluation is addressed next, point by point.

Development and Validation of Global FW Process Model

This main objective was early accomplished, since the analytical descriptive sub-models dealing with the several physical phenomena identified as crucial within the process, were developed in the first stage of the study. The validation, however, was only concluded much later, with the comparisons of the experimental and numerical results.

The validation was not fully accomplished as initially planned, due to the remarkable difficulties in operating in-situ measurements of strains (and/or stresses) during the FW process. These were not included in the experimental program becoming, in fact, the main weakness on the model validation produced. The stress-strain sub-model was not directly validated through dedicated experiments, but rather only through the overall analysis of the consistency of the results. This sub-model, in particular, remains as a proposed approach. All the other relevant sub-processes were validated through either dedicated experimental measurements and tests or comparison with previously published models.

Nonetheless, the results achieved have shown the ability of the process model to predict the behaviour of the main input/output variables and parameters, meaning that it covered the essential physics of the manufacturing processes. This statement is supported by the fact that no relevant parameter was identified during the “real” winding trials that was not included in the model. Even the options of not including the mandrel thermo-mechanical effects or the possibility of voids formation became partially validated by the consistency of the results.

The results achieved, allow to conclude for the successful accomplishment of the main objective initially drawn.

Inclusion of Both Thermosetting and Thermoplastic Process Configurations

This objective was established in order to enhance the utility of the present model. It arose from several evidences: there is an increasing trend to use thermoplastic matrices; there are almost no process models dealing with thermoplastics; many industrial facilities are capable of using both thermosetting (wet or prepreg) and thermoplastic (prepreg) FW process configurations.

In order to attain this key objective, the model was developed in a modular way. The two advantages envisaged were the possibility of developing decoupled sub-models, easy to study and improve independently, and the possibility of using the same model for either thermosetting or thermoplastic resins, by simply adapting the thermo-chemical sub-models (heat transfer, resin cure/crystallization and resin viscosity). Through the correct definition of the input parameters, the model was able to consider both process configurations. This objective was, thus, successfully achieved.

Model the Effect of FW Intrinsic Manufacturing Features

Among the composites manufacturing techniques, FW presents unique features and specificities which required special attention. The three identified (listed above) were the incremental nature of the winding lay-up, the gradients developed across the laminate’s thickness and the twisted/waved pattern of the fibres roving fed onto the laminate. These characteristic features were explicitly modelled.

The discrete and incremental building of the laminate (winding lay-up) was attained in the numerical implementation of the process model, since the analytical descriptions were kept generic. The results have shown the specific influence of this phenomenon in several outputs.

The gradients across the laminate’s thickness formed naturally upon the correct definitions of the correlated parameters and/or process variables. Namely, the pressure gradients generated flow gradients. These produced, in the end, through-the-thickness gradients of fibre relative contents, and, thus, stiffnesses. This is, in fact, one major output of the current model.

The misaligned patterns of the fibres were modelled, through assuming sinusoidal paths and including these in the determination of the stress-strain constitutive relations. In fact, the constitutive stiffness matrix for each material point was calculated from wave-transforming the local on-axis stiffness matrix components. These were then averaged for one wavelength. In this way, the waved orientation of the fibres was modelled and coherently affected the stress-strain states. The possibility of no-waviness was considered as well, thus making the stress-strain descriptions universal. The existence and measurement of the waved orientations of the fibre tows was validated experimentally. Its particular parametric effect in the stress or strain states, as well as in other eventual outputs, was not specifically validated, though.

Overall, the identified specificities of the FW process, distinguishing it from other composites manufacturing techniques, were successfully addressed and included in the analyses and results presented.

Experimental Procedures for the Assessment to Process Input/Output Variables

As extensively treated in chapter 5, a comprehensive experimental program was designed and carried out for the validation of the several sub-models. This program included several experimental procedures typically associated with different fields of expertise. Namely, differential scanning calorimetry (DSC), typically used by thermo-analysts, viscosimetry and rheology, used by polymer and/or product engineers, burn-off calcination and morphological microscopy, typically used by materials scientists, and infrared thermography, transversal to many engineering applications. These procedures were used for the experimental evaluation of specific quantities. Since they are quite established among the scientific community, they were firstly studied and introduced by expert colleagues and then conducted following the existing recommendations. Beyond the obvious enrichment of the overall validation results, the use of such wide variety of procedures consisted itself in clear added value for the practical knowledge put in service for the current model as well as for the expected upcoming studies.

The main experimental technique used was, however, the FW. The conduction of several winding trials, in which the main input/output variables were measured (either in-situ or through one of the previously mentioned techniques), introduced a realistic analysis in the whole process modelling approach. The prior expertise in this particular process, allowed to further introduce reliable tools and sub-techniques to gather relevant measurements. Namely, the ability to measure the winding tension in different points of the setup, the development of a novel technique to measure the resin flow distance and layer’s compaction, the online temperature measurement, the precise programming and control of the lay-up sequence and the un-damaging de-moulding capability, were some of the specific techniques developed and implemented throughout the trials. These efforts also increased the available know-how.

In summary, both established and novel techniques and procedures were used in the experimental program, aiming at enhancing the completeness of the model validation. This objective was, then, successfully achieved as the results document.

Model Evaluation Through Parametric Tests

Upon the establishment of a fully functional and process-representative numerical code, the model was tested under several predetermined conditions. These conditions typically consisted in artificially imposing a certain history for a selected variable, such as winding angle, permeability, temperature, or winding force. From there, the specific influence of that variable in the results was assessed. Qualitative evaluations were made through comparing the evolutions of the relevant variables accordingly with prior experience or evidence. These early tests are partially discussed in chapter 4. Later, at the experimental program, the main process inputs, like winding force, number of layers and initial fibre relative contents, were varied in ranges representing the typical conditions used in real process applications. Therefore, the model validation included parametric analyses as well. These are discussed in chapter 5. Despite deeper analyses would be desired, the results achieved have shown trends and evolutions of the main process outputs with the known variations of the main inputs, thus accomplishing the main purpose of this objective.

Foresee Broader Applications for the Process Model

The wider and/or universal application of the current process model to other manufacturing processes cannot be claimed entirely. As mentioned above, several features relate exclusively to FW. However, several mechanisms governing physical phenomena involved are common to other processes. These were, typically, initially studied from literature related to those processes, as is clear in chapter 2. The range of applications in which the model developed is of added value may be divided into two main groups: the range of different applications within FW and the applicability to other correlated processes.

Within FW, several process configurations may exist. The use of either thermosetting or thermoplastic resins is one major differentiating aspect. The model accounted for both possibilities, but only the wet thermosetting configurations was effectively tested and validated. Increasing complexity, different geometries (non-axissymmetric) could be explored. The model is of local nature, i.e., the variables are defined at the material point. Therefore, the applicability of this model to any laminate geometry is virtually unlimited, provided that the adequate transformations from local to global definitions are implemented.

Strong limitation is seen in special cases. If, for example, a FW configuration is considered that includes unfilled regions (promoted by bridging tows in concave surfaces, e.g.), no clear applicability is obvious for all the sub-models. This and other special (but also uncommon) situations, may introduce serious difficulties to the application of the current process model.

Regarding other processes, immediate correlations exist with tow placement of fibre placement techniques. The same fundamental physical phenomena are present and interact in a similar way to the one observed in FW. Although specific features, such as direct contacts promoting consolidation pressure, would need to be further studied and implemented, the overall applicability of this model is clear. Many other processes could benefit from this modelling strategy, and even the sub-models as they are defined. However, processes like autoclave consolidation or resin transfer moulding, have ben deeply studied by several groups of researchers and use typically only part of the multi-physics modelled herewith. On the other hand, other processes, like pultrusion, have been far less studied and would clearly accept many of the sub-modelling approaches used in this model. Novel applications for improved versions of the process model can be foreseen.

Concluding, the multi-physical model developed in this study has shown consistent and coherent results when compared with reliable and dedicated experimental data. The degree of validation for the winding conditions pre-selected is reasonably high, thus suggesting a correct approach and methodology. The model was capable of wisely relate the input with the output relevant parameters of this process, thus allowing to foresee reliable design and controls of the FW manufacturing process for each application. The modular structure and the comprehensive experimental validation carried out further enhance the utility of the model developed. All the main objectives were successfully accomplished and novel techniques and sub-models were established.

6.2. With Respect to the State of the Art

After conclusion of this study, several contributions to the improvement of the state of the art were settled and are identified henceforth. The global main contribution substantiated with the multi-physical process model was always pursued and identified from the early stages of this program. It is, naturally, the overall and more relevant contribution to the state of the art. In addition, the knowledge gathered throughout the developments will allow profitable and improved outcomes in the continuation of the present work. However, several other contributions were made.

Within the scope of the analytical modelling, a novel definition of the radial pressure release due to the inward motion of the fibre bed was developed and proposed. This novel definition couples the winding force-pressure relation with the incremental mechanical compressive state to which the layers are subjected during the referred inward motion. The formulation, set in equation (3.8), is unique and novel, since no previous author included such description in the several process models and sub-models studied and analysed. This definition replaces complex descriptions proposed by previous authors for the fibre motion [23,24], and showed to comply with reality.

Other innovative approach was set in the stress-strain sub-model, due to the unique combination of the Mori-Tanaka [214] (and/or other methods for calculation of the homogenized composite elastic-apparent properties) with the Hsiao & Daniel [114] stress-strain constitutive relations including waviness. The novelty is the integrative application of these methods to the FW process. Not only these two complementary methods had not been combined before, as also none was previously applied to a laminate's consolidating state, but rather only to fully cured/consolidated parts. In fact, the stress-strain sub-model contains another differentiating aspect regarding the consideration of orthotropic laminate properties, instead of the commonly used definition of transversely isotropic. Although not specifically compared or validated experimentally, the definitions used are supported in the discussion set in chapter 3.

The inclusion of a sub-model dedicated to the resin mixing phenomenon is also an improved approach. This had been previously addressed by Banerjee *et al.* [24], but without critical analysis or experimental confirmation. In this work, the resins mixing behaviour was studied in detail through rheological tests, and the linear combination rule for the overall viscosity estimation was criticized. The validity of this study was further substantiated by its publication [258] in a specialized journal. The tests implemented allowed to confirm the incorrect results of such rule, although it was used in absence of a better model for the mixture behaviour. Further studies, based on this one, may now progress the knowledge from the critical analysis drawn.

The fibre bed compaction was modelled in a unique simplified way, when compared to previous authors [23,24,34]. Namely, the continuity condition established in equation (3.52) further simplified the analysis, with similar results. The coherent definition of the inward movement of the fibres as symmetrical to the resin outward flow, set in equation (3.48) also attributed uniqueness to the present modelling approach.

In the cure modelling, two novel kinetic models were proposed for the two resin systems pre-selected. These are expressed in equations (4.8) and (4.15). These models were achieved through oriented fitting of the experimental data, in accordance with the best practices applied by several authors from both chemical and physical fields.

Meaningful models were developed with unique features, such as the consideration of “real” manufacturing conditions and near-to-room temperatures. The interesting results were published in a relevant journal in the field of polymers [238].

The viscosity modelling also included the full characterization and meaningful modelling of two thermosetting resins. Dedicated viscosimetry and rheometry procedures were implemented, with specific adaptions to extend the measurements up to an after gelation, thus retrieving complete data. The four models developed, expressed in equations (4.19) to (4.22), together with the unique features of the setups were published as well [251].

Overall, the methods and results achieved, presented several relevant contributions to the actual knowledge on composites multi-physical process modelling, as well as for the research line being enforced on manufacturing processes. It is believed that these contributions are valuable *per se*, but also of strategic importance to the present and future activity of several research groups, naturally including the one in which these thesis inserts in. None of these aspects were neglected during the realization of the work.

6.3. Future Work

The overall reliability and utility of the process model developed suggests that the approach is globally kept and that further improvements may be implemented over it. Hereafter, several improvements to be made are identified. These relate to either corrections or enrichments of the model, thus approaching its accurate and real applicability.

The first action to take will be the calibration of the current model to improve the matching with experimental results. These "regulation" will focus on the material-dependent constants which were assumed a certain value, without experimental evidence. Parameters like thermal conductivity, chemical shrinkage, or constants like the Kozeny's or the maximum available fibre volume fraction at which resin flow stops, affect considerably the final results. However, their values were used in accordance with empirical proposition from previous authors and might not agree with required conditions. This first series of improvements will allow to achieved nearly perfect match on the main process physical variables and also to determine the coherent values for those implicative empirical parameters.

Among the options and assumptions taken during the model development, the negligibility of the mandrel thermo-mechanical interactions with the consolidating laminate was not specifically proven. This interaction was previously considered by other authors and might introduce relevant thermal and mechanical loadings when higher temperatures are used. This improvement is considered of interest, although not crucial.

More importance is given to the simplifying assumption that no void formations existed. This phenomena actually exists (the assumption made was that it did not produce relevant effects, as was consistently proven in the experimental tests for thermosetting wet winding) and might assume relevant expressions when thermoplastics are used. Other process conditions could favour such formation as well, such as higher viscosities and winding tensions. This phenomenon is to be addressed in the future through either validating its negligible effects or specifically modelling it.

During the experimental program, only thermosetting resins were tested and sub-modelled. Therefore, the applicability of the process model to thermoplastic configurations should be studied, in view of validating such extension.

Also, more complex laminate configurations and wider ranges of input conditions shall be addressed. These include different angles, irregular thicknesses, longer winding times, resins requiring elevated consolidation temperatures, etc. These studies will potentially highlight difficulties which, at being solved, will widen the model robustness and universality.

A specific improvement is thought for the accounting of the possibility of resin loss at the resin rich layer. This was discussed earlier in chapter 5 and is not truly relevant. However, a correct modelling of the resin "drop" conditions would allow to understand its physics of interaction with itself and the moving laminate (mandrel rotation).

Main activities like the adaptation of part or the entirety of this model to different manufacturing processes is obviously envisaged in the continuation of the work.

Bibliography

[1] *Composite Engineering Materials: Guide to Composites*, GTC-1-1098, SP Systems, Newport, 1999.

[2] S. Lee, G. S. Springer, *Filament Winding Cylinders: III. Selection of the Process Variables*, Journal of Composite Materials, vol.24 (1990), pp.1344-1366.

[3] M. Clairaut, *Theorie da la Figure de la Terre, Tirée des Principes de l'Hydrostatique*, Académie Royale des Sciences, London Royal Society Ed., 1743, Paris.

[4] J. A. O. Simões, *O Enrolamento Filamentar*, Department of Mechanical Engineering and Industrial Management Engineering, Faculty of Engineering of University of Porto

[5] S. Koussios, O. K. Bergsma, A. Beukers, *Filament Winding. Part 1: Determination of the Wound Body Related Parameters*, Composites Part A, vol.35 (2004), pp.181-195.

[6] S. Koussios, O. K. Bergsma, A. Beukers, *Filament Winding. Part 2: Generic Kinematic Model and Its Solutions*, Composites Part A, vol.35 (2004), pp.187-212.

[7] E. V. Morozov, *The Effect of Filament-Winding Mosaic Patterns on the Strength of Thin-Walled Composite Shells*, Composite Structures, vol.76 (2006), pp.123-129.

[8] N. J. Pagano, J. M. Whitney, *Geometric Design of Composite Cylindrical Characterization Specimens*, Journal of Composite Materials, vol.4 (1970), pp.360-378.

[9] M. S. Babu, G. Srikanth, S. Biswas, *Composite Fabrication by Filament Winding - An Insight*, TIFAC, India.

[10] H. Blok, J. J. van Rossum, The Foil Bearing – A New Departure in Hydrodynamic Lubrication, Lubrication Engineering, vol.9 no.6 (1953), pp.316-320.

[11] A. Eshel, H. G. Elrod, *The Theory of the Infinitely Wide, Perfectly Flexible, Self-Acting Foil Bearing*, ASME Journal of Basic Engineering, vol. 87 (1965), pp.831-836.

[12] J. T. S. Ma, *An Investigation of Self-Acting Foil Bearings*, ASME Journal of Basic Engineering, vol. 87 (1965), pp.837-846.

[13] K. L. Knox, T. L. Sweeney, *Fluid Effects Associated with Web Handling*, Industrial & Engineering Chemistry Process Design and Development, vol.10 no.2 (1971), pp.201-206.

[14] P. J. Bates, J. Kendall, D. Taylor, M. Cunningham, *Pressure Build-up During Melt Impregnation*, Composite Science and Technology, vol.62 (2002), pp.379-384.

[15] P. J. Bates, J. M. Charrier, *Pulling Tension Monitoring During the Melt Impregnation of Glass Roving*, Journal of Polymer Composites, vol.21 (2000), pp.104-113.

[16] Z. Cai, T. Gutowski, S. Allen, *Winding and Consolidation Analysis for Cylindrical Composite Structures*, Journal of Composite Materials, vol.26 (1992), pp.1374-1399.

[17] W. B. Young, *Compacting Pressure and Cure Cycle for Processing of Thick Composite Laminates*, Composite Science and Technology, vol.54 no.3 (1995), pp.299-306.

[18] Pascal Hubert; Anoush Poursartip, *A Method for Direct Measurement of the Fibre Bed Compaction Curve of Composite Prepregs*, Composites: Part A, vol.32 (2001) pp.179-187.

[19] V.A.F. Costa, A.C.M.Sousa, *Modelling of Flow and Thermo-Kinetics During the Cure of Thick Laminated Composites*, International Journal of Thermal Sciences, vol.42 (2003), pp.15-22.

[20] Daniel D. Shin, H. Thomas Hahn, *Compaction of Thick Composites: Simulation and Experiment*, Journal of Polymer Composites, vol.25 no.1 (2004), pp.49-59.

[21] Min Li, Yizhuo Gu, Zuoguang Zhang, Zhijie Sun, *A simple Method for the Measurement of Compaction and Corresponding Transverse Permeability of Composite Prepregs*, Journal of Polymer Composites, vol.28 no.1 (2007), pp.61-70.

[22] Pascal Hubert; Reza Vaziri, Anoush Poursartip, *A Two-Dimensional Flow Model For the Process Simulation of Complex Shape Composite*, International Journal for Numerical Methods in Engineering, vol.44 (2011), pp.1-26.

[23] S. Lee, G. S. Springer, *Filament Winding Cylinders: I. Process Model*, Journal of Composite Materials, vol.24 (1990), pp.1270-1298.

[24] A. Banerjee, L. Sun, S. C. Mantell, D. Cohen, *Model and Experimental Study of Fibre Motion in Wet Filament Winding*, Composites: Part A, vol.29 (1998), pp.251-263.

[25] Katherine A. Mackenzie, *Measurement of Resin Pressure in Composite Laminates During Cure*, MSc Thesis, University of British Columbia, 1993.

[26] T. G. Gutowski, T. Morigaki, Z. Cai, *The Consolidation of Laminate Composites*, Journal of Composite Materials, vol.21 (1987), pp.172-188.

[27] Z. Cai, T. Gutowski, *The 3-D Deformation Behaviour of a Lubricated Fibre Bundle*, Journal of Composite Materials, vol.26 no.8 (1992), pp.1207-1237.

[28] T. G. Gutowski, G. Dillon, *The Elastic Deformation of Lubricated Carbon Fiber Bundles: Comparison of Theory and Experiments*, Journal of Composite Materials, vol.26 no.16 (1992), pp.2330-2347.

[29] R. Dave, J. L. Kardos, M. P. Duduković, *A Model for Resin Flow During Composite Processing: Part1 - General Mathematical Development*, Journal of Polymer Composites, vol.8 no.2 (1987), pp.29-38.

[30] R. Dave, J. L. Kardos, M. P. Duduković, *A Model for Resin Flow During Composite Processing: Part 2 – Numerical Analysis for Unidirectional Graphite/Epoxy Laminates*, Journal of Polymer Composites, vol.8 no.2 (1987), pp.123-132.

[31] Z.Cai, T.Gutowski, *Fibre Distribution and Resin Flow in the Laminate Molding Process*, Proceedings of the 7th International Conference on Composite Materials ICCM-7 (1991), Hawaii.

[32] A. Agah-Tehrani, H. Teng, *Analysis of Fibre Motion During Wet Filament Winding of Composite Cylinders with Arbitrary Thickness*, International Journal of Solid Structures, vol.29 (1992), pp.2649-2668.

[33] M. Hojjiati, S. V. Hoa, *Curing Simulation of Thick Thermosetting Composites*, Composites Manufacturing, vol.5 no.3 (1994), pp.159-171.

[34] T. G. Gutowski, Z. Cai, S. Bauer, D. Boucher, J. Kingery, S. Wineman, *Consolidation Experiments for Laminate Composites*, Journal of Composite Materials, vol.21 no.7 (1987), pp.650-669.

[35] Gregory David Smith, *Modelling and Experimental Issues in the Processing of Composite Laminates*, MSc Thesis, University of British Columbia, 1992.

[36] C. M. Ó Brádaigh, G. B. McGuiness, R. B. Pipes, *Numerical Analysis of Stresses and Deformations in Composite Materials Sheet Forming: Central Indentation of a Circular Sheet*, Journal of Composites Manufacturing, vol.4 no.2 (1993), pp.67-83.

[37] P. Hubert, A. Pourtsartip, *A Review of Flow and Compaction Modelling Relevant to Thermoset Matrix Laminate Processing*, Journal of Reinforced Plastics and Composites 17 4 (1998), pp. 286-318.

[38] C. P. Kyan, D. T. Wasan, R. C. Kintner, *Flow of Single-Phase Fluids Through Fibrous Beds*, Industrial & Engineering Chemistry Fundamentals, vol.9 no.4 (1970), pp.596-603.

[39] J. Thomas Lindt, *Consolidation of Circular Cylinders in a Newtonian Fluid. I. Simple Cubic Configuration*, Journal of Rheology, vol.30 no.2 (1986), pp.251-269.

[40] J. Bear, *Dynamics of Fluids in Porous Media*, Dover Publications (1988), New York.

[41] Henry Darcy, *Les Fointaines Publiques de la Ville de Dijon*, Victor Dalmont Ed. (1856), Paris.

[42] A. J. E. J. Dupuit, *Etudes Théoriques et Pratiques sur le Mouvement des Eaux dans les Canaux Découverts et à Travers les Terrains Perméables*, Victor Dalmont Ed. (1863), Paris.

[43] P. Forchheimer, *Wassernewengung durch Boden*, Zeitschrift des Vereines Deuts Ingenieure, vol.45 (1901), pp.1736-1741,1781-1788.

[44] L. Skartsis, J. L. Kardos, B. Khomami, *Resin Flow Through Fiber Beds During Composite Manufacturing Processes. Part I: Review of Newtonian Flow Through Fiber Beds*, Journal of Polymer Engineering and Science, vol.32 no.4 (1992), pp.221-230.

[45] O. Rahli, L. Tadrist, M. Miscevic, *Experimental Analysis of Fibrous Porous Media Permeability*, AIChE journal, vol.42 no.12 (1996), pp.3547-3549.

[46] J. Kozeny, *Uber Kapillare Leitung das Wassers im Boden*, Sitzungsberichte Wiener, vol.136 no.2 (1927), pp.271-276.

[47] T. G. Gutowski, Z. Cai, S. Bauer, D. Boucher, *Consolidation Experiments for Laminate Composites*, Journal of Composite Materials, vol.21 (1987), pp.650-669.

[48] R. R. Sullivan, K. L. Hertel, *The Flow of Air Through Porous Media*, Journal of Applied Physics, vol.11 (1940), pp.761-765.

[49] Alfred C. Loos; George S. Springer, *Curing of Epoxy Matrix Composites*, Journal of Composite Materials, vol.17 (1982), pp.135-168.

[50] R. C. Lam, J. L. Kardos, *The Permeability of Aligned and Cross-Plied Fiber Beds During Processing of Continuous Fiber Composites*, Proceedings of the Third Technical Conference of the American Society for Composites, Technomic Publishing Co. Inc. (1986), pp.13-22.

[51] G. S. Springer, *Resin Flow During the Cure of Fibre Reinforced Composites*, Journal of Composite Materials 17 (1982), pp.400-410.

[52] S. Kuwabara, *The Forces Experienced by Randomly Distributed Parallel Circular Cylinders or Spheres in a Viscous Flow at Low Reynolds Numbers*, Journal of the Physical Society of Japan, vol.14 (1959), pp.527-532.

[53] H. Hasimoto, *On the Periodic Fundamental Solutions of the Stokes Equations and their Application to Viscous Flow Past a Cubic Array of Spheres*, Journal of Fluid Mechanics, vol.5 (1959), pp.317-328.

[54] J. Happel, H. Brenner, *Low Reynolds Number Hydrodynamics*, Prentice-Hall Englewood Cliffs Ed. (1962), New Jersey.

[55] A. Sangani, A. Acrivos, *Slow Flow Past Periodic Arrays of Cylinders with Applications to Heat Transfer*, International Journal of Multiphase Flow, vol.8 (1982), pp.193-206.

[56] B. R. Gebart, *Permeability of Unidirectional Reinforcements for RTM*, Journal of Composite Materials, vol.26 no.8 (1992), pp.1100-1133.

[57] M. Sahraoui, M. Kaviany, *Slip and No-Slip Velocity Boundary Condition at Interface of Porous, Plain Media*, International Journal of Heat and Mass Transfer, vol.35 no.4 (1992), pp.927-943.

[58] M. Bruchke, S. Advani, *Flow of Generalized Newtonian Fluids Across a Periodic Array of Cylinders*, Journal of Rheology, vol.37 no.3 (1993), pp.479-498.

[59] G. W. Jackson, D. James, *The Permability of Fibrous Porous Media*, Canadian Journal of Chemical Engineering, vol.64 (1986), pp.364-374.

[60] D. Mehri, V. Michaud, L. Kämpfer, P. Vuilliomenet, J.-A. E. Manson, *Transverse Permeability of Chopped Fibre Bundle Beds*, Composites: Part A, vol.38 (2007), pp.739-746.

[61] R. E. Sherrer, *Filament-Wound Cylinders with Axial-Symmetric Loads*, Journal of Composite Materials, vol.1 no.4 (1967), pp.344-355.

[62] N. Epstein, J. Masliyah, *Creeping Flow Through Clusters of Spheroids and Elliptical Cylinders*, Journal of Chemical Engineering, vol.3 (1972), pp.169-175.

[63] F. R. Phelan, G. Wise, *Analysis of Transverse Flow in Aligned Fibrous Porous Media*, Composites: Part A, vol.27 no.1 (1996), pp.25-34.

[64] S. Ranganathan, F. R. Phelan, S. G. Advani, *A Generalized Model for the Transverse Fluid Permeability in Unidirectional Fibrous Media*, Journal of Polymer Composites, vol.17 no.2 (1996), pp.222-230.

[65] T. D. Papathanasiou, E. M. Gravel, S. C. Barwick, E. D. Dendy, *Non-Isotropic Structured Fibrous Media: The Permeability of Arrays of Fibre Bundles of Elliptical Cross-Section,* Journal of Polymer Composites, vol.23 no.4 (2002), pp.520-529.

[66] B. Markicevic, T. D. Papathanasiou, *An Explicit Physics-Based Model for the Transverse Permeability of Multi-Material Dual Porosity Fibrous Media*, Journal of Transport in Porous Media, vol.53 no.3 (2003), pp.265-280.

[67] J. K. Woods, P. D. M. Spelt, P. D. Lee, T. Selerland, C. J. Lawrence, *Creeping Flows of Power-Law Fluids Through Periodic Arrays of Elliptical Cylinders*, Journal of Non-Newtonian Fluid Mechanics, vol.111 no.2-3 (2003), pp.211-228.

[68] L. N. Hjellming, J. S. Walker, *Thermal Curing Cycles for Composite Cylinders with Thick Walls and Thermoset Resins*, Journal of Composite Materials, vol.23 (1989), pp.1048-1064.

[69] H. Cheng, S. Chiao, *Fibre Consolidation in The Filament Winding Process: Modelling with Undulating Channels*, Composite Science and Technology, vol.56 (1996), pp.1161-1169.

[70] Avella, M., Martuscelli, E., Pascucci, B. and Raimo, M. (1992), *Transcrystallinity Phenomena in Fiber-Reinforced Polypropylene. II: Morphology, Thermal and Mechanical Properties Relationships*, Journal of Polymer Engineering & Science, vol.32 (1992), pp.383-391.

[71] J. L. Thomason, A. A. Van Rooyen, *Transcrystallized Interphase in Thermoplastic Composites*, Journal of Materials Science, vol.27 (1992), pp.889-896.

[72] D. Campbell, M. M. Qayyum, *Melt Crystallization of Polypropylene: Effect of Contact with Fiber Substrates*, Journal of Polymer Science: Polymer Physics Edition, vol.18 (1980), pp.83-93.

[73] C. Wang, L. M. Hwang, *Transcrystallization of PTFE Fiber/PP Composites (I) Crystallization Kinetics and Morphology*, Journal of Polymer Science Part B: Polymer Physics, vol.34 (1996), pp.47-56.

[74] J. A. Martins, J. J. C. Cruz Pinto, *Evaluation of the Instantaneous Nucleation Density in the Isothermal Crystallization of Polymers,* Polymer, vol.43 no.14, (2002), pp.3999-4010.

[75] J. Varga, J. Karger-Kocsis, *The Difference Between Transcrystallization and Shear-Induced Cylindritic Crystallization in Fibre-Reinforced Polypropylene Composites*, Journal of Materials Science Letters, vol.13 (1994), pp.1069-1071.

[76] G. Sala, D. Cutolo, *Heated Chamber Winding of Thermoplastic Powder-Impregnated Composites: Part 1. Technology and Basic Thermo-chemical Aspects*, Composites: Part A, vol.27 (1996), pp. 387-392.

[77] G. Sala, D. Cutolo, *Heated Chamber Winding of Thermoplastic Powder-Impregnated Composites: Part 1. Influence of Degree of Impregnation on Mechanical Properties*, Composites: Part A, vol.27 (1996), pp.393-399.

[78] N Ersoy, K D Potter, M R Wisnom, M J Clegg, *An Experimental Method to Study the Frictional Processes During Composites Manufacturing*, Composites: Part A, vol.36, (2005), pp.1536-1544.

[79] E. P. Calius, G. S. Springer, *A Model of Filament Wound Thin Cylinders*, International Journal of Solids and Structures, vol.26 (1990), pp.271-297.

[80] Liyang Zhao, Susan C.Mantell, David Cohen, Reed McPeak, *Finite Element Modeling of the Filament Winding Process*, Composite Structures, vol.52 (2001), pp.499-510.

[81] Kuang-Ting Hsiao, Rex Little, Omar Restrepo, Bob Minaie, *A Study of Direct Cure Kinetics Characterization During Liquid Composite Molding*, Composites: Part A, vol.37 (2006), pp.925-933.

[82] W. I. Lee, A. C. Loos, G. S. Springer, *Heat of Reaction, Degree of Cure, and Viscosity of Hercules 3501-6 Resin*, Journal of Composite Materials, vol.16 (1982), pp.510-520.

[83] J. Mijovic, H. T. Wang, *Modeling of Processing of Composites Part II -Temperature Distribution During Cure,* SAMPE Journal , vol.24 (1988), pp.42-55.

[84] Woo Il Lee, George S. Springer, *A Model of the Manufacturing Process of Thermoplastic Matrix Composites*, Journal of Composite Materials, vol.21 (1987), pp.1017-1055.

[85] K. Horie, H. Hiura, M. Sawada, I. Mita, H. Kambe, *Calorimetric Investigation of Polymerization Reactions. III. Curing Reaction of Epoxides with Amines*, Journal of Polymer Science Part A-1: Polymer Chemistry, vol.8 (1970), pp.1357-1372.

[86] F. Heba, M. Mouzali, M. J. M. Abadie, *Effect of the Crosslinking Degree on Curing Kinetics of an Epoxy-Acid Copolymer System*, Jounal of Applied Polymer Science, vol.90 (2003), pp.2834-2839.

[87] C.-S. Chern, G. W. Poehlein, *A Kinetic Model for Curing Reactions of Epoxides with Amines*, Polymer Engineering & Science, vol.27 (1987), pp.788-795.

[88] K. C. Cole, J. J. Hechler, D. Noel, *A New Approach to Modeling the Cure Kinetics of Epoxy/Amine Thermosetting Resins. 2. Application to a Typical System Based on bis[4-(diglycidylamino)phenyl]methane and bis(4-aminophenyl) sulfone*, Macromolecules, vol.24 no.11 (1991), pp.3098-3110.

[89] L. Sun, I. I. Negulescu, S.-S. Pang, A. M. Sterling, *Characterization of Epoxy Prepreg Curing Process*, Journal of Adhesion, vol.82 (2006), pp.161-179.

[90] S. Sourour, M.R. Kamal, *Differential Scanning Calorimetry of Epoxy Cure: Isothermal Cure Kinetics*, Thermochemica Acta, vol.14 (1976), pp.41-59.

[91] S. J. Ng, R. Boswell, S. J. Claus, F. Arnold, A. Vizzini, *Degree of Cure, Heat of Reaction, and Viscosity of 8522 and 977-3 HM Epoxy Resin*, Technical Report, Naval Air Warfare Center Aircraft Division (2000), Maryland.

[92] E. M. Pearce, J. Mijovic, *Final Report to NASA-Ames Research center on Characterization-Curing-Property Studies of HBRF-55A Resin Formulations*, Technical Report, NASA-CR-175836 (1985), Moffett Field.

[93] N. Ersoy, K. Potter, M. R. Wisnom, M. J. Clegg, *Development of Spring-in Angle During Cure of a Thermosetting Composite*, Composites: Part A, vol.36 (2005), pp.1700-1706.

[94] A. Yousefi, P.G.Lafleur, *Kinetic Studies of Thermoset Cure Reactions: A Review*, Polymer Composites, vol.18 no.2 (1997), pp.157-167.

[95] S. C. Mantell, G. S. Springer, *Manufacturing Process Models for Thermoplastic Composites*, Journal of Composites Materials, vol.26 no.16 (1992), pp.2348-2377.

[96] A. M. Maffezzoli, J. M. Kenny, L. Nicolais, *Welding of PEEK/Carbon Fiber Composite Laminates*, SAMPE Journal, vol.25 no.1 (1989), pp.35-39.

[97] J. C. Seferis, C. N. Velisaris, *Modeling-Processing-Structure Relationships of Polyetheretherketone (PEEK) Based Composites*, Materials Sciences for the Future. SAMPE (1986), pp.1236-1252.

[98] C. N. Velisaris, J. C. Seferis, *Heat Transfer Effects on the Processing-Structure Relationships of Polyetheretherketone (PEEK) Based Composites*, Polymer Engineering and Science, vol.28 (1988), pp.583-591.

[99] S. J. Hwang, C. L. Tucker III, *Heat Transfer Analysis of Continuous Fiber/Thermoplastic MatrixComposites During Manufacture*, Journal of Thermoplastic Composite Materials, vol.3 (1990), pp.41-51.

[100] C. W. Macosko, *Rheology: Principles, Measurements and Applications*, Wiley VCH Ed., 1994.

[101] N. J. L. van Ruth, J. F. Vega, S. Rastogi, J. Martinez-Salazar, *Viscoelastic Behaviour During the Crystallisation of Isotactic Polypropylene*, Journal of Materials Science, vol.41 no.12 (2006), pp.3899-3905.

[102] G. V. Vinogradov, N. V. Prozorovskaya, *Rheology of Polymers. Viscous Properties of Polypropylene Melt*, Rheologica Acta, vol.3 no.3 (1964), pp.156-163.

[103] B. Wunderlich, *Macromolecular Physics*, Academic press, New York, Vol.1-3, 1973.

[104] Y. Long, Z. H. Stachurski R. A. Shanks, *A Practical Guide to Study Kinetics of Polymer Crystallization*, Progress in Polymer Science, vol.20 (1995), pp.651-701.

---

[105] G. Bogoeva-Gaceva, A. Grozdanov, *Crystallization of Isotactic Polypropylene: The Effect of Fiber Surface*, Journal of the Serbian Chemical Society, vol.71 no.5 (2006), pp.483-499.

[106] N. Ersoy, T. Garstka, K. D. Potter, M. R. Wisnom, D. Porter, M. J. Clegg, G. Stringer, *Development of the Properties of a Carbon Fibre Reinforced Thermosetting Composite Through Cure*, Composites: Part A, vol.41 (2010), pp.401-409.

[107] A. Caiazzo, M. Orlet, H. McShane, L. Strait, C. Rachau, *The effects of Marcel Defects on Composite Structural Properties*, Composite Structures: Theory and Practice ASTM-STP 1383, Ed. Peter Grant and Carl Q. Rousseau, 1999.

[108] H. G. Rai, E. V. Honein, M. I. Najjar, *Mechanics of Laminated Composite Containing Marcel Defects*, Key Engineering Materials, vols.334-335 (2007), pp. 13-16.

[109] H. M. Hsiao, I. M. Daniel, *Elastic Properties of Composites with Fiber Waviness*, Composites: Part A, vol.27, (1996), pp.931-941.

[110] J. T. Hofeditz, *Structural Design Considerations for Fibrous Glass Pressure Vessels*, Modern Plastics, vol.41 (1964), pp.127-146.

[111] R. M. Jones, *Mechanics of Composite Materials*, McGraw-Hill Ed., Chapter 2, 1975.

[112] S. W. Tsai, *Composites Design*, 3rd edition, Think Composites, Chapter 2, Dayton, OH, 1987.

[113] J. R. Vinson, R. L. Sierakowski, *Behavior of Structures Composed of Composite Materials*, 2nd edition, Kluwer Academics Publishers, 2002.

[114] H. M. Hsiao, I. M. Daniel, *Elastic Properties of Composites with Fiber Waviness*, Composites: Part A, vol.27 (1996), pp.931-941.

[115] T. Garstka, N. Ersoy, K. D. Potter, M. R. Wisnom, *In Situ Measurements of Through-the-Thickness Strains During Processing of AS4-8552 Composite*, Composites: Part A, vol.38 (2007), pp.2517-2526.

[116] T. A. Bogetti, J. W. Gillepse Jr, *Process Induced Stress and Deformation in Thick-Section Thermoset Composite Laminates*, Journal of Composite Materials, vol.26 no.5 (1992), pp.627-660.

[117] D. W. Radford, *Cure Shrinkage Induced Warpage in Flat Uni-Axial Composites*, Journal of Composites Technological Resolutions, vol.15 no.4 (1993), pp.290-296.

[118] Y. K. Kim, S. R. White, *Cure-Dependent Viscoelastic Residual Stress Analysis of Filament-Wound Composite Cylinders*, Mechanics of Composite Materials Structures, vol.5 (1998), pp.327-354.

[119] L. G. Stringer, R. J. Hayman, M. J. Hinton, R. A. Badock, M. R. Wisnom, *Curing Stresses in Thick Polymer Composite Componets. Part II. Management of Residual Stresses*, Proceedings of the 12th International Conference on Composite Materials, 1999, Paris.

[120] Andrew A. Johnston, *An Integrated Model of the Development of Process-Induced Deformation in Autoclave Processing of Composite Structures*, PhD Thesis, University of British Columbia, 1997.

[121] A. Johnston, R. Vaziri, A. Poursartip, *A Plane Strain Model for Process-Induced Deformation of Laminated Composite Structures*, Journal of Composite Materials, vol.35 no.16 (2001), pp.1435-1469.

[122] R. B. Prime, *Thermal Characterization of Polymer Materials*, Academic Press: New York (1982), pp.435-569.

[123] L. J. Ernst, C. van 't Hof, D. G. Yang, M. S. Kiasat, G. Q. Zhang, H. J. L. Bressers, J. F. J. Caers, A. W. J. den Boer, J. Janssen, *Determination of Visco-Elastic Properties During the Curing Process of Underfill Materials*, Proceedings of the Electronic Components and Technology Conference, 2000.

[124] Y. K. Kim, S. R. White, *Stress Relaxation Behavior of 3501-6 Epoxy Resin During Cure*, Polymer Engineering and Science, vol.46 no.23 (1996), pp.2852-2862.

[125] J. Lange, S. Toll, J. E. Manson, A. Hult, *Residual Stress Build-up in Thermoset Films Cured Below Their Ultimate Glass Transition Temperature*, Polymer, vol.38 no.4 (1997), pp.809-815.

[126] J. Lange, S. Toll, J. E. Manson, A. Hult, *Residual Stress Build-up in Thermoset Films Cured Above Their Ultimate Glass Transition Temperature*, Polymer, vol.36 no.16 (1995), pp.3135-3141.

[127] T. Sproewitz, T. Wille, M. Kleineberg, J. Tessmer, *Spring-In – Simulation in Fiber-Composite Manufacturing*, Proceedings of the 13th European Conference on Composite Materials, June 2nd – 5th, 2008, Stockholm.

[128] M. Li, C. L. Tucker, *Optimal Curing for Thermoset Matrix Composites: Thermochemical and Consolidation Consideration*, Polymer Composites, vol.23 no.5 (2002), pp.739-757.

[129] S. T. Bhi, R. S. Hansen, B. Wilson, E. P. Calius, G. S. Springer, *Degree of Cure and Viscosity of Hercules HBRF-55 Resin*, Proceedings of the 32nd International SAMPE Symposium, pp.1114-1118.

[130] C. Dispenza, J. T. Carter, P. T. McGrail, G. Spadaro, *Cure Behaviour of Epoxy Resin Matrices for Carbon Fibre Composites*, Polymer Composites, vol.48 (1999), pp.1229-1236.

[131] M. J. Perry, L. J, Lee, *Online Cure Monitoring of Epoxy / Graphite Composites Using a Scaling Analysis and a Dual Heat Flux Sensors*, Journal of Composite Materials, vol.26 no.2 (1992), pp.274-292.

[132] Brian E. Spencer, *Prediction of Manufacturing Stresses in Thick-Walled Orthotropic Cylinders*, PhD Thesis, University of Nebraska, 1988.

[133] M. G. Maximovich, R. M. Galeos, *Rheological Characterization of Advanced Composite Prepreg Materials*, Proceedings of the 28th National SAMPE Symposyum, April 12th-14th, 1983, pp.569-580.

[134] G. Ikonomopoulos, M. Marchetti, *Filament Winding Technology: A Numerical Simulation and Experimental Validation of the Winding and Curing Phases*, Science and Engineering of Composite Materials, vol.7 no.3 (1998), pp.215-222.

[135] Kurt S. Olofsson, *Temperature Predictions in Thick Composite Laminates at Low Cure Temperatures*, Applied Composite Materials , vol.4 (1997), pp.1-11.

[136] Kurt S. Olofsson, *Stress Development in Wet Filament Wound Pipes*, Journal of Reinforced Plastics and Composites, vol.16 no.4 (1997), pp.372-390.

[137] A. C. Loos, W. T. Freeman Jr., *Resin Flow During Autoclave Cure of Graphite-Epoxy Composites*, High Modulus Fiber Composites in Ground Transportation and High Volume Applications, ASTM STP 873, D. W. Wilson Ed., Philadelphia, 1985, pp.119-130.

[138] P. -J. Shih, A. C. Loos, *Heat Transfer Analysis of the Thermoplastic Filament Winding Process*, Journal of Reinforced Plastics and Composites, vol.18 no.12 (1999), pp.1103-1112.

[139] Y. M. P. Toso, P. Ermanni, D. Poulikakos, *Thermal Phenomena in Fiber-Reinforced Thermoplastic Tape Winding Process: Computational Simulations and Experimental Validations*, Journal of Composite Materials, vol.38 no.2 (2004), pp.107-135.

[140] Xiaolan Song, *Modeling of Thermoplastic Composite Filament Winding*, MSc Thesis, Virginia Polytechnic Institute and State University, 2000.

[141] Gregory David Smith, *Modelling and Experimental Issues in the Processing of Composite Laminates*, MSc Thesis, University of British Columbia, 1992.

[142] C. Xin, Y. Gu, M. Li, Y. Li, Z. Zhang, *Online Monitoring and Analysis of Resin Pressure Inside Composite Laminate During Zero-Bleeding Autoclave Process*, Polymer Composites, vol.32 no.2 (2011), pp.314-323.

[143] K. Lynch, P. Hubert, A. Poursartip, *Use of a Simple, Inexpensive Pressure Sensor to Measure Hydrostatic Resin Pressure during Process of Composite Laminates*, Polymer Composites, vol.20 no.4 (1999), pp.581-593.

[144] Y. Gu, Z. Zhang, M. Li, *Resin Pressure Measuring System for Hot Pressing of Composites*, Acta Mater. Compos. Sin., vol.24 no.2 (2007), pp.23-27.

[145] R. C. Lam, J. L. Kardos, *The Permeability and Compressibility of Aligned and Cross-Plied Fiber Beds During Processing of Composites*, ANTEC, vol.89 (1989), pp.1408-1412.

[146] Y. R. Kim, S. P. McCarthy, J. P. Fanucci, *Compressibility and Relaxation of Fiber Reinforcements During Composite Processing*, Polymer Composites, vol.12 no.1 (1991), pp.13-19.

[147] L. Skartsis, J. L. Kardos, *Resin Flow Through Fiber Beds During Composite Manufacturing Processes. Part II: Numerical and Experimental Studies of Newtonian Flow Through Ideal and Actual Fiber Beds*, Journal of Polymer Engineering and Science, vol.32 no.4 (1992), pp.231-239.

[148] N. Pierce, J. Summerscales, *The Compressibility of a Reinforcement Fabric*, Journal of Composites Manufacturing, vol.6 no.1 (995), pp.15-21.

[149] R. A. Saunders, C. Lekakou, M. G. Bader, *Compression and Microstructure of Fibre Plain Woven Cloths in the Processing of Polymer Composites*, Composites: Part A, vol.29 (1998), pp.443-454.

[150] J. T. Gotro, B. K. Appelt, T. L. Ellis, *Characterization of Resin Flow in Composites*, Society of Plastic Engineers, Proceedings of the 44th Annual Technical Conference, 1986, pp.371-374.

[151] A. Poursartip, G. Riahi, L. Frederick, X. Lin, *A Method to Determine Resin Flow During Curing of Composite Laminates*, Polymer Composites, vol.13 no.1 (1992), pp.58-65.

[152] S. Thomas, C. Bongiovanni, S. R. Nutt, *In Situ Estimation of Through-hickness Resin Flow Using Ultrasound*, Composites Science and Technology, vol.68 (2008), pp.3093-3098.

[153] N. Pearce, F. Guild, J. Summerscales, *A Study of the Convergent Flow Fronts on the Properties of Fibre Reinforced Composites Produced by RTM*, Composits: Part A, vol.29 (1998), pp.141-152.

[154] T. Stöven, F. Weyrauch, P. Mitschang, M. Neitzel, *Continuous Monitoring of Three-Dimensional Resin Flow Through a Fiber Preform*, Composites: Part A, vol.34 (2003), pp.475-480.

[155] X. Wu, J. Li, *A New Method to Determine Fiber Transverse Permeability*, Journal of Composite Materials, vol.41 no.6 (2007), pp.747-756.

[156] A. Endruweit, P. Glover, K. Head, A. C. Long, *Mapping of the Fluid Distribution in Impregnated Reinforcement Textiles Using Magnetic Resonance Imaging: Methods and Issues*, Composites: Part A, vol.42 (2011), pp.265-273.

[157] O. Rahli, L. Tadrist, R. Santini, J. Pantaloni, *Fluid Flow and Heat Transfer Analysis in Fibrous Porous Media*, Proceedings of the 3rd World Conference on Experimental Heat Transfer, Fluid Mechanics and Thermodynamics, Vol. 2, Honolulu, 1993, p.1577.

[158] S. Scholz, J. W. Gillespie, D. Heider, *Measurement of Transverse Permeability Using Gaseous and Liquid Flow*, Composites: Part A, vol.38 (2007), pp.2034-2040.

[159] O. Elbouazzaoui, S. Drapier, P. Henrat, *An Experimental Assessment of the Saturated Transverse Permeability of Non-crimped New Concept (nc2) Multiaxial Fabrics*, Journal of Composite Materials, vol.39 no.13 (2005), pp.1169-1193.

[160] M. J. Buntain, S. Bickerton, *Compression Flow Permeability Measurement: A Continuous Technique*, Composites: Part A, vol.34 (2003), pp.445-457.

[161] S. Comas-Cardona, C. Binetruy, P. Krawczak, *Unidirectional Compression of Fibre Reinforcements. Part 2: A Continuous Permeability Tensor Measurement*, Composites Science and Technology, vol.67 no.3-4 (2007), pp.638-645.

[162] R. Arbter *et al.*, *Experimental determination of the permeability of textiles: A benchmark exercise*, Composites: Part A, vol.42 (2011), pp.1157-1168.

[163] G. Morren, M. Bottiglieri, S. Bossuyt, H. Sol, D. Lecompte, B. Verleye, S. V. Lomov, *A Reference Specimen for Permeability Measurements of Fibrous Reinforcements for RTM*, Composites: Part A, vol.40 (2009), pp.244-250.

[164] R. Labreque, *The Effects of Fiber Cross-Sectional Shape on the Resistance to the Flow of Fluids Through Fiber Mats*, TAPPI, vol.51 (1968), pp.8-15.

[165] V. Feuillade, *Etude de l'Influence da la Formulation de l'Ensimage des Fibres de Verre sur la Qualité de Surface des Composites SMC de Type Classe A*, PhD Thesis, University of Montpelier II, 2003.

[166] J-. Y. Chen, S. V. Hoa, C.-K. Jen, H, Wang, *Fibre-Optic and Ultrasonic Measurements for In-Situ Cure Monitoring of Graphite/Epoxy Composites*, Journal of Composite Materials, vol.33 (1999), pp.1860-1881.

[167] A. Atarsia, R. Boukhili, *Relationship Between Isothermal and Dynamic Cure of Thermosets Via the Isoconversion Representation*, Polymer Engineering and Science, vol.40 No.3 (2000), pp.607-620.

[168] Loleï Khoun, Pascal Hubert, *Cure Shrinkage Characterization of an Epoxy Resin System by Two in Situ Measurement Methods*, Polymer Composites, vol.31 no.9 (2010), pp.1603-1610.

[169] Loleï Khoun, Geneviève Palardy, Pascal Hubert, *Relation Between Volumetric Changes of Unsaturated Polyester Resin and Surface Finish Quality of Fiberglass/Unsaturated Polyester Composite Panels*, Polymer Composites, vol.32 no.9 (2011), pp.1473-1480.

[170] E. S. Freeman, B. Carrol, *The Application of Thermoanalytical Techniques to Reaction Kinetics: The Thermogravimetric Evaluation of the Kinetics of the Decomposition of Calcium Oxalate Monohydrate*, Journal of Physical Chemistry, vol.62 no.4 (1958), pp.394-397.

[171] L. Sun, S. Pang, A. M. Sterling, I. I. Negulescu, M. A. Stubblefield, *Dynamic Modeling of Curing Process of Epoxy Prepreg*, Journal of Applied Polymer Science, vol.86 (2002), pp.1911-1923.

[172] H. E. Kissinger, *Reaction Kinetics in Differential Thermal Analysis*, Analytical Chemistry, vol.29 no.11 (1957), pp.1702-1706.

[173] T. Ozawa, *Kinetic analysis of Derivative Curves in Thermal Analysis*, Journal of Thermal Analysis and Calorimetry, vol.2 no.3 (1970), pp.301-324.

[174] H. J. Borchardt, F. Daniels, *The Application of Differential Thermal Analysis to the Study of Reaction Kinetics*, Journal of the American Chemical Society, vol.79 no.1 (1957), pp.41-46.

[175] W. Chen, P. Li, Y. Yu, X. Yang, *Curing Kinetics Study of an Epoxy Resin System for T800 Carbon Fiber Filament Wound Composites by Dynamic and Isothermal DSC*, Journal of Applied Polymer Science, vol.107 (2008), pp.1493-1499.

[176] K.-T. Hsiao, R. Little, O. Restrepo, B. Minaie, *A Study of Direct Cure Kinetics Characterization During Liquid Composite Molding*, Composites: Part A, vol.37 (2006), pp.925-933.

[177] Gordana Bogoeva-Gaceva, Anita Grozdanov, *Crystallization of Isotactic Polypropylene: The Effect of Fiber Surface*, Journal of Serbian Chemical Society, vol.71 (2006), pp.483-499.

[178] H. G. Kim, D. G. Lee, *Dielectric Cure Monitoring for Glass/Polyester Prepreg Composites*, Composite Structures, vol.57 no.1-4 (2002), pp.91-99.

[179] D. L. Woerdeman, J. K. Spoerre, K. M. Flynn, R. S. Parnas, *Cure Monitoring of the Liquid Composite Molding Process Using Fiber Optic Sensors*, Polymer Composites, vol.18 no.1 (1997), pp.133-50.

[180] H. T. Hahn, *Application of Ultrasonic Techniques to Cure Characterization of Epoxies*, Nondestructive Methods for Material Property Determination, C. O. Rudd and R. E. Green Jr. Ed., Plenum Press, 1984, pp.315-326.

[181] B. Fanconi *et al.*, *Assessment of the State of the Art for Process Monitoring Sensors for Polymer Composites*, NISTIR 4514, 1991, pp.1-20.

[182] N. Oshima, K. Inoue, S. Motogi, T. Fukuda, *Cure Monitoring of Composite Materials by Using Impedance Changes of Piezoelectric Ceramics*, Proceedings of the Dynamics and Design Conference, 2002, pp.439-442.

[183] S. H. Eum, K. Kageyama, *et al.*, *Structural Health Monitoring Using Fiber Optic Distributed Sensors for Vacuum-Assisted Resin Transfer Molding*, Smart Materieals and Structures, vol.16 no.6 (2007), pp.2627-35.

[184] S. Kobayashi, R. Matsuzaki, A. Todoroki, *Multipoint Cure Monitoring of CFRP Laminates Using a Flexible Matrix Sensor*, Composites Science and Technology, vol.69 (2009), pp.378-384.

[185] M. Giordano, A. Laudati, J. Nasser, L. Nicolais, A. Cusano, A. Cutolo, *Monitoring by a Single Fiber Bragg Grating of the Process Induced Chemo-Physical Transformations of a Model Thermoset*, Sensors and Actuators, vol.A113 (2004), pp.166-173.

[186] E. Chehura, A. A. Skordos, C-. C. Ye, S. W. James, I. K. Partridge, R. P. Tatam, *Strain Development in Curing Epoxy Resin and Glass Fibre/Epoxy Composites Monitored by Fibre Bragg Grating Sensors in Birefringent Optical Fibre*, Smart Materials and Structures, vol.14 (2005), pp.354-362.

[187] P. Casari, C. Lupi, P. –A. Morvan, D. Leduc, N. Daher, *Sensing strain Gradients with Embedded Bragg Gratings Across the Width of a Composite Laminate*, Proceedings of the CompTest2008 - 4th International Conference on Composites Testing and Model Identification, 2008, Dayton, October 20th-22nd.

[188] L. Khoun, R. de Oliveira, V. Michaud, P. Hubert, *Investigation of Process-Induced Strains Development by fibre Bragg Grating Sensors in Resin Transfer Moulded Composites*, Composites: Part A, vol.42 no.3 (2011), pp.274-282.

[189] Y. J. Rao, *Recent Progress in Applications of In-Fibre Bragg Grating Sensors*, Optics and Lasers in Engineering, vol.31 (1999), pp.297-324.

[190] S. W. James, M. L. Dockney, R. P. Tatam, *Simultaneous Independent Temperature and Strain Measurement Using In-Fibre Bragg Grating Sensors*, Electronics Letters, vol.32 (1996), pp.1133-1134.

[191] C. M. Lawrence, D. V. Nelson, E. Udd, T. Bennett, *A Fibre Optic Sensor for Transverse Strain Measurement*, Experimental Mechanics, vol.39 no.3 (1999), pp.202-209.

[192] E. Udd, W. Schulz, J. Seim, E. Haugse, A. Trego, P. Johnson, T. Bennett, D. Nelson, A. Makino, *Multidimensional Strain Field Measurements Using Fibre Optic Grating Sensors*, Proceedings of SPIE 3986, 2000, pp.255-262.

[193] T. Liu, D. Brooks, G. Fernando, *A Multimode Extrinsic Fabry Perot nterferometer Strain Sensor*, Smart Materials and Structures, vol.6 (1997), pp.464-469.

[194] A. Kalmakarov, S. Frotzgerald, O. Mac Donald, *The Use of Fabry Perot Fiber Optic Sensors to Monitor Residual Strains During Pultrusion of FRP Composites*, Composites: Part B, vol.30 (1999), pp.167-175.

[195] B. Yates, B. A. McCalla, L. N. Phillips, D. M. Kingston-Lee, K. F. Rogers, *The Thermal Expansion of Carbon Fibre-Reinforced Plastics*, Journal of Materials Science, vol.14 (1979), pp.1207-1217.

[196] I. M. Daniel, T.- M. Wang, D. Karalekas, J. T. Gotro, *Determination of Chemical Cure Shrinkage on Composite Laminates*, Journal of Composite Technologic Resolutions, vol.12 no.3 (1990), pp.172-176.

[197] J. D. Russell, *Cure Shrinkage of Thermoset Composites*, SAMPE Quarterly vol.24 no.2 (1993), pp.28-33.

[198] P. Prasatya, G. B. Mckenna, S. L. Simon, *A Viscoelastic Model for Predicting Isotropic Residual Stresses in Thermosetting Materials: Effect of Processing Parameters*, Journal of Composite Materials, vol.35 no.10 (2001), pp.826-848.

[199] B. Bilyeu, W. Brostow, K. P. Menard, *Determination of Volume Changes During Cure Via Void Elimination and Shrinkage of an Epoxy Prepreg Using a Quartz Dilatometry Cell*, Polimery, vol.46 no.11-12 (2001), pp.799-802 .

[200] M. Zarrelli, I. K. Partridge, A. D’Amore, *Warpage Induced in Biomaterial Specimens: Coefficient of Thermal Expansion, Chemical Shrinkage and Viscoelastic Modulus Evolution During Cure*, Composites: Part A, vol.37 no.4 (2006), pp.565-570.

[201] C. Li, K. Potter, M. R. Wisnom, G. Stringer, *In-situ Measurement of Chemical Shrinkage of MY750 Epoxy Resin by a Novel Gravimetric Method*, Composites Science and Technology, vol.64 (2004), pp.55-64.

[202] M. Haider, P. Hubert, L. Lessard, *Cure Shrinkage Characterization and Modeling of a Polyester Resin Containing Low Profile Additives*, Composites: Part A, vol.38 no.3 (2007), pp.994-1009.

[203] M. A. Stone, B. K. Fink, T. A. Bogetti, J. W. Gillespie Jr, *Thermo-Chemical Response of Vinyl-Ester Resin*, Polymer Engineering and Science, vol.40 no.12 (2000) pp.2489-2497.

[204] F. Flores, J. W. Gillespie Jr, T. A. Bogetti, *Experimental Investigation of the Cure-Dependent Response of Vinyl Ester Resin*, Polymer Engineering and Science, vol.42 no.3 (2002), pp.582-590.

[205] A. Johnson, K. Sherwin, *Foundations of Mechanical Engineering*, Nelson Thornes Ltd, 2001, United Kingdom.

[206] eFunda, Inc., *Thin-Walled Pressure Vessels* (n.d.), eFunda.com, Retrieved October 26th, 2011 from http://www.efunda.com/formulae/solid_mechanics/mat_mechanics/pressure_vessel.cfm

[207] J. T. Evans, A. G. Gibson, *Composite angle ply laminates and netting analysis*, Royal Society of London Proceedings Series A, vol.458 (2002), pp.3079-3088.

[208] John T. Hofeditz, *Structural Design Considerations for Fibrous Glass Pressure Vessels*, Proceedings of 18th Annual Conference of the Society of the Plastics Industry, Chicago, 1963.

[209] C. C. Chamis, G. P. Sendeckyj, *Critique on Theories Predicting Thermoelastic Properties of Fibrous Composites*, Journal of Composite Materials, vol.2 (1968), pp.332-358.

[210] Stephen W. Tsai, *Structural Behaviour of Composite Materials*, National Aeronautics and Space Administration - CR-71, Washington, 1964.

[211] W. Voigt, *Ueber die Beziehung Zwischen den Beiden Elasticitätsconstanten Isotroper Körper*, Annalen der Physik, vol.274 (1889), pp.573-587.

[212] A. Reuss, *Berechnung der Fließgrenze von Mischkristallen auf Grund der Plastizitätsbedingung für Einkristalle*, ZAMM - Zeitschrift für Angewandte Mathematik und Mechanik, vol.9 (1929), pp.49-58.

[213] Z. Hashin and B.W. Rosen, *The Elastic Moduli of Fiber Reinforced Materials, Journal of Applied Mechanics*, vol.31 (1964), pp.223-232.

[214] T. Mori and K. Tanaka, *Average Stress in Matrix and Average Elastic Energy of Materials with Misfitting Inclusions*, Acta Metallurgica, vol.21 (1973), pp.571-574.

[215] Y. Benveniste, *A New Approach to the Application of Mori-Tanaka's Theory in Composite Materials*, Mechanics of Materials, vol.6 (1987), pp.147-157.

[216] G. J. Dvorak, *Plasticity theories for fibrous composite materials. Metal Matrix Composites, Vol. 2: Mechanisms and Properties*, R. K. Everett and R. J. Arsenault, eds, Boston: Academic Press, 1990.

[217] Carl T. Herakovich, *Mechanics of Fibrous Composites*, John Wiley & Sons, 1998.

[218] Yu. M. Tarnopol'skii, G. G. Portnov, I. G. Zhigun, *Effect of Fiber Curvature On the Modulus of Elasticity for Unidirectional Glass-Reinforced Plastics in Tension*, Polymer Mechanics, vol.3 (1967), pp.161-166.

[219] T-W. Chou, K. Takahashi, *Non-linear Elastic Behaviour of Flexible Fibre Composites*, Composites, vol.18 (1987), pp.25-34.

[220] C-M. Kuo, K. Takahashi, T-W. Chou, *Effect of Fiber Waviness on the Nonlinear Elastic Behavior of Flexible Composites*, Journal of Composite Materials, vol.22 (1988), pp.1004-1025.

[221] L. C. Brinson, W. S. Lin, *Comparison of Micromechanics Methods for Effective Properties of Multiphase Viscoelastic Composites*, Composite Structures, vol.41 (1998), pp.353-367.

[222] B. Gommers, I. Verpoest, P. Van Houtte, *The Mori-Tanaka Method Applied to Textile Composite Materials*, Acta Metallurgica, vol.46 (1998), pp.2223-2235.

[223] A. J. Duncan, T. G. Mackay, A. Lakhtakia, *On the Homogenization of Orthotropic Elastic Composites by the Strong-Property-Fluctuation Theory*, Journal of Applied Mahematics, vol.74 (2009), pp.507-532.

[224] S. Vyazovkin, A. K. Burnham, J. M. Criado, L. A. Perez-Maqueda, C. Popescu, N. Sbirrazzuoli, *ICTAC Kinetics Committee Recommendations for Performing Kinetic Computations on Thermal Data*, Thermochimica Acta, vol.520 (2011), pp.1-19.

[225] *For Better Thermal Analysis and Calorimetry*, 3rd Edition, ICTAC Ed. (1991).

[226] *TA Instruments – Thermal Analysis*, T-2006A – DSC Products Brochure, retrieved May 07th, 2012, from http://www.tainstruments.co.jp/products/dsc/pdf/dsc_bro.pdf

[227] M. Tarr, *Properties of Laminates*, Advanced Microelectronics for Industrialists, retrieved May 07th, 2012, from http://www.ami.ac.uk/courses/topics/0140_pl/

[228] A. Atarsia, R. Boukhili, *Relationship Between Isothermal and Dynamic Cure of Thermosets Via the Isoconversion Representation*, Polymer Engineering and Science, vol.40 (2000), pp.607-620.

[229] V. A. Beloshenko, M. K. Pacter, B. I. Beresnev, V. I. Zaika, T. P. Zaika, *Structural and Kinetic Aspects of Hydrostatic Pressure Effect on Polymer Network Formation*, High Pressure Research, vol.6 (1991), pp.203–212.

[230] J. A. Ramos, N. Pagani, C. C. Riccardi, J. Borrajo, S. N. Goyanes, I. Mondragon, *Cure Kinetics and Shrinkage Model for Epoxy-Amine Systems*, Polymer Polymer, vol.46 (2005), pp.3323–3328.

[231] R. B. Prime, *Differential Scanning Calorimetry of the Epoxy Cure Reaction*, Polymer Engineering & Science, vol.13 (1973), pp.365–371.

[232] M. R. Kamal, S. Sourour, *Kinetics and Thermal Characterization of Thermoset Cure*, Polymer Engineering & Science, vol.13 (1973), pp.59–64.

[233] P. I. Karkanas, I. K. Partridge, D. Attwood, *Modelling the Cure of a Commercial Epoxy Resin for Applications in Resin Transfer Moulding*, Polymer International, vol.41 (1996), pp.183–191.

[234] S. Sourour, M. R. Kamal, *Differential Scanning Calorimetry of Epoxy Cure: Isothermal Cure Kinetics*, Thermochemica Acta, vol.14 (1976), pp.41-59.

[235] J. Fournier, G. Williams, C. Duch, G. A. Aldridge, *Changes in Molecular Dynamics during Bulk Polymerization of an Epoxide-Amine System As Studied by Dielectric Relaxation Spectroscopy*, Macromolecules, vol.29 (1996), pp.7097-7107.

[236] C.-S. Chern, G. W. Poehlein, *A Kinetic Model for Curing Reactions of Epoxides with Amines*, Polymer Engineering & Science, vol.27 (1987), pp.788-795.

[237] K. C. Cole, J. J. Hechler, D. Noel, *A New Approach to Modeling the Cure Kinetics of Epoxy/Amine Thermosetting Resins. 2. Application to a Typical System Based on bis[4-(diglycidylamino)phenyl]methane and bis(4-aminophenyl) sulfone*, Macromolecules, vol.24 no.11 (1991), pp.3098-3110.

[238] H. Faria, C. M. C. Pereira, F. M. A. Pires, A. T. Marques, *Kinetic Models for the SR1500 and LY556 Epoxies under Manufacturing Recommended Cure Cycles*, European Polymer Journal, (2013) submitted.

[239] G. Van Assche, A. Van Hemelrijck, H. Rahier, B. Van Mele, *Modulated Differential Scanning Calorimetry: Isothermal Cure and Vitrification of Thermosetting Systems*, Thermochimica Acta, vol.268 (1995), pp.121-142.

[240] N. Rabearison, Ch. Jochum, J. C. Grandidier, *A Cure Kinetics, Diffusion Controlled and Temperature Dependent, Identification of the Araldite LY556 Epoxy*, Journals of Materials Science, vol.46 (2011), pp.787-796.

[241] A. Somwangthanaroj, *Rheology and Polymer Characterization*, Chulalongkorn University, September 20th, 2010, retrieved July 11th, 2012, from http://pioneer.netserv.chula.ac.th/~sanongnl/course.html.

[242] A. Maffezzoli, A. Trivisano, M. Opalicki, J. Mijovic, J. M. Kenny, *Correlation Between Dielectric and Chemorheological Properies During Cure of Epoxy-based Composites*, Journal of Materials Science, vol.29 (1994), pp.800-808.

[243] J. Stabik, A. Dybowska, M. Szczepanik, Ł. Suchoń, *Viscosity Measurements of Epoxy Resin Filled with Ferrite Powders*, Archives of Material Science and Engineering, vol.38 (2009), pp.34-40.

[244] K. Hyun, M. Wilhelm, C. O. Klein, K. Soo Cho, J. G. Nam, K. H. Ahn, S. J. Lee, R. H. Ewoldt, G. H. McKinley, *A Review of Nonlinear Oscillatory Shear Tests: Analysis and Application of Large Amplitude Oscillatory Shear (LAOS)*, Progress in Polymer Science, vol.36 (2011), pp.1697-1753.

[245] V. A. Hackley, C. F. Ferraris, *Guide to Rheological Nomenclature: Measurements in Ceramics Particulate Systems - Special Publication 946*, National Institute of Standards and Technology, U.S. Department of Commerce, 2001.

[246] F. P. Incropera, D. P. DeWitt, T. L. Bergman, A. S. Lavine, *Fundamentals of Heat and Mass Transfer*, 6th Edition, John Wiley & Sons, 2006, USA.

[247] M. L. Williams, R. F. Landel , J. D. Ferry, *The Temperature Dependence of Relaxation Mechanisms in Amorphous Polymers and Other Glass-forming Liquids*, Journal of American Chemical Society, vol.77 (1955), pp.3701-3707.

[248] N. F. Sheppard, S. D. Senturia, *Dielectric Properties of Bisphenol-a Epoxy Resins*, Journal of Polymer Science. Part B: Polymer Physics, vol.27 (1989), pp.753-762.

[249] W. W. Bidstrup, S. D. Senturia, *Monitoring the Cure of a Composite Matrix Resin with Microdielectrometry*, Polymer Engineering & Science, vol.29 (1989), pp.290-294.

[250] J. M. Kenny, M. Opalicki, *Influence of the Chemorheology of Toughened Epoxy Matrices on the Processing Behavior of High Performance Composites*, Makromolekulare Chemie. Macromolecular Symposia, vol.68 (1993), pp.41-56.

[251] H. Faria, F. M. A. Pires, A. T. Marques, *Modelling the Rheology of SR1500 and LY556 Epoxies under Manufacturer's Recommended Cure Cycles After Viscosimetry and Rheometry Characterization*, Polymer Engineering & Science, in press.

[252] D. Harran, A. Laudouard, *Caractérisation de la Gélification d'une Résine Thermodurcissable par Méthode Rhéologique*, Rheologica Acta, vol.24 (1985), pp.596-602.

[253] ISO 1172:1996 – Textile-glass-reinforced plastics -- Prepregs, moulding compounds and laminates -- Determination of the textile-glass and mineral-filler content -- Calcination methods, International Organization for Standardization, Geneva, Switzerland.

[254] N. Pan, *Theoretical Determination of the Optimal Fiber Volume Fraction and Fiber-Matrix Property Compatibility of Short Fiber Composites*, Polymer Composites, vol.14 (1993), pp.85-93.

[255] S. Li, *General Unit Cells for Micromechanical Analyses of Unidirectional Composites*, Composites: Part A, vol.32 (2000), pp.815-826.

[256] A. R. Melro, P. P. Camanho, S. T. Pinho, *Generation of Random Distribution of Fibres in Long-fibre Reinforced Composites*, Composites Science and Technology, vol.68 (2008), pp.2092-2102.

[257] J. Zangenberg, J. B. Larsen, R. C. Østergaard, P. Brøndsted, *Methodology for Characterisation of Glass Fibre Composite Architecture*, Plastics, Rubber and Composites, vol.41 (2012), pp.187-193.

---

[258] H. Faria, F. M. A. Pires, A. T. Marques, *Identification of the Combined Rheology of Mixtures of Epoxy Resins With Different Initial Curing States*, Applied Rheology, vol.23 (2013), 42413.